University of Lille: Doctoral School SPI-ENGSYS

Ph.D. in ELECTRONICS, MICROELECTRONICS, NANOELECTRONICS AND MICROWAVES

Metamaterial absorbers with transverse gradients

Xhoandri Lleshi

Presented on: November 22nd 2021

Examination committee:

Mr. André de Lustrac	Université Paris Nanterre	Chairman
Mr. Didier Lippens	Université de Lille, IEMN	Academic supervisor
Ms. Habiba Hafdallah Ouslimani	Université Paris Nanterre	Reviewer
Mr. Fabien Ferrero	Université Cote d'Azur	Reviewer
Mr. Davide Ramaccia	Università di Roma Tre	Examiner
Mr. Xavier Begaud	Université Telecom ParisTech	Examiner
Mr. Philippe Pouliguen	DGA	Examiner / DGA supervisor
Ms. Thi Quynh Van Hoang	Thales Research & Technology	Examiner / Industrial supervisor
Ms. Isabelle Le Roy Naneix	Thales DMS	Invited
Ms. Carole Jégou	DGA	Invited / DGA supervisor

Université de Lille: École Doctorale SPI-ENGSYS

Thèse de doctorat en Electronique, microélectronique, nanoélectronique et micro-ondes

Absorbeurs métamatériaux à gradients transversaux

Xhoandri Lleshi

Présentée et soutenu le 22 Novembre 2021

Devant le jury:

Pr. André de Lustrac	Université Paris Nanterre	Président du jury
Pr. Didier Lippens	Université de Lille, IEMN	Directeur de thèse
Pr. Habiba Hafdallah Ouslimani	Université Paris Nanterre	Rapporteur
Pr. Fabien Ferrero	Université Cote d'Azur	Rapporteur
Pr. Davide Ramaccia	Università di Roma Tre	Examinateur
Pr. Xavier Begaud	Université Telecom ParisTech	Examinateur
HDR. Philippe Pouliguen	DGA	Directeur de thèse DGA
Dr. Thi Quynh Van Hoang	Thales Research & Technology	Encadrant industriel Thales
Dr. Isabelle Le Roy Naneix	Thales DMS	Invité
Dr. Carole Jégou	DGA	Invité / Encadrant DGA

Acknowledgements

I address my sincere thanks to Prof. Habiba Hafdallah Ouslimani and Prof. Fabien Ferrero for the honor they gave me by accepting to review my Ph.D. work.

Special thanks to professors André de Lustrac, Xavier Begaud, Davide Ramaccia, and to Isabelle Le Roy Naneix that accepted to be part of my jury as examiners and invited.

Many thanks to Thi Quynh Van Hoang and Didier Lippens, my industrial and academic supervisors, for their exchanges and help over these years. Thank you for your guide with the manuscript redaction and defense presentation.

Thank you very much to Philippe Pouliguen, Carole Jegou, and Sylvain Gransart, my DGA supervisors, for the various reunions we had together that have constantly pushed me to give more and helped me understand every physical aspect of my work on a deeper level.

Many thanks to professors Davide Ramaccia, Filiberto Bilotti, and Alessandro Toscano of Antennas & Metamaterials Research Lab of the University of Roma Tre who proposed this three-year position to me that completely changed my life.

Many thanks to Brigitte Loiseaux, manager of LCDT lab, who always provided me with wise guidance and constantly checked up on me throughout the years.

Many thanks to everyone at the LCDT lab starting, in office order, from Giuseppe Bellomonte, who first introduced me to characterization and I can call now a true friend. Jean-François Allaeys with his deep knowledge of antennas and measurements as well as his typical sense of humor. Erika Vandelle with the various discussions over coffee time and with whom I began climbing. Thanks to Aude Leuliet for her positive attitude daily, as well as Quentin Lévesque and Sebastien Heron for always listening to my ideas and providing feedback, we had some unforgettable discussions about the physical nature of all phenomena. Thank you to Anne Delboulbe for her pleasant conversations about Paris, art, and cinema, as well as Laure Mane Si Lee and Claude Prevot for sharing their expertise in optics, electronics, thermodynamics, and other fields with me. Thank you to Matthieu Bertrand for our discussions in Italian and Matthieu Le Baillif for our general and specific dialogues. Thank you so much to Jules Billuart, who was my first friend in Paris and helped me to understand French reality. Special thanks to Louiza Hamidouche, with whom I shared my office for the past year and a half, who encouraged me to stay focused on my ultimate goal by reminding me of it every day. You know how helpful our conversations and your positive attitude were to me, I hope I was able to do the same for you.

I would like to thank everyone in the GRTM group for their practical assistance in the Ph.D., especially Lilia Qassym, Shama Enouz-Verenne, Paolo Martins, and Laurent Divay. A big thank you to Shailendra Bansropun for welcoming me into the group. Thanks to Christophe Galindo, Richard Lebourgeois, Jaafar Saied, Paolo Bondavalli, Patrick Garabedian, Raphael Guillemet, Dominique Carisetti, Wilson Maia, and everyone else with whom I have spent a pleasant time over the years.

Many thanks to Lorenzo Beccacece, Simone Magaletti and Pablo Helio Zapata Cano with who I shared part of my and their Ph.D., our dialogues in Italian have always made me feel at home, our friendship will never end.

For the final thanks, I would like to start with my entire family for always being there for me in times of need, giving me the strength to keep going no matter what.

Special thanks to Luca Castiglione and Matteo Montefiore, the distance has never changed our friendship and never will.

I would like to thank all members of the Maximus group for integrating me in Paris, you are now part of my family.

Last but not least, I want to thank the most important person in my life: Barbara Gilquin, who constantly inspires me to be a better person and to improve any day of my life, your smile helps me every day.

Summary

List of figures

List of abbreviations

2D	Two dimensions
3D	Three Dimensions
A	Absorptivity
ABS	Acrylonitrile Butadiene Styrene
CAA	Circuit Analog Absorber
CBMMA	Chess-Based Metamaterial Absorber
CCA	Capacitive Circuit Absorber
CT	Computed Tomography
DGA	Direction Générale de l'Armement
DMS	Defense Mission Systems (Thales)
EBG	Electrical Band Gap
EM	Electromagnetic
EMI	Electromagnetic Interference
F. F.	Far Field
FB	Fractional Bandwidth
FDM	Fused Deposition Modeling
FSS	Frequency Selective Surface
HIS	High Impedance Surface
H-pol.	Horizontal polarization
IEMN	Institut d'Electronique, de Microélectronique et de Nanotechnologie
ISAR	Inverse Synthetic Aperture Radar
LoS	Line of Sight
MIM	Metal-Insulator-Metal
MM	Metamaterial
MMA	Metamaterial Absorber
NiCr	Nikel Chrome
PCB	Printed Circuit Board
PEKK	PolyEtherKetoneKetone
PLA	Polyactic Acid
PMA	Perfect Metamaterial Absorber
R	Reflectivity
RAM	Radar Absorbing Material
RCS	Radar Cross Section
RF	Radio Frequency
SLMMA	Stair-Like Metamaterial Absorber
SUT	Sample Under Test
T	Transmissivity
TE	Transverse Electric
TLM	Transmission Line Model
TM	Transverse Magnetic
TRT	Thales Research & Technology – France
VNA	Vector Network Analyzer
V-pol.	Vertical polarization

Introduction

Nowadays, microwave absorbers have to fulfill exigent needs regarding RF functionality, integrability, and industry constraints. The required functionalities of such structures vary from a wideband behavior to insensitivity to polarization and robustness to oblique incidence. The integrability is connected to an "on-chip world" with complex structures where low-profile is mandatory. The industry constraints are linked to the necessity to fabricate "in-house" prototypes for strategic reasons, maintaining easy-to fabricate and low-cost structures.

In this context, I began my Ph.D. project at Thales Research & Technology – France (TRT), Palaiseau, and Institut d'Electronique, de Microélectronique et de Nanotechnologie (IEMN), Lille (France). The Direction Générale de l'Armement (DGA), a division of the French Armed Forces Ministry whose mission is to prepare the future of French defense systems, equip the French armed forces and promote French defense industry exports, partly funded this thesis (DGA01D18048780/DS/MRIS number: 2018864).

Thales, IEMN and DGA decided to concentrate the Ph.D. project on 3D-printed absorbers since they have experience and know-how in new printable filaments high-performance radar absorbing materials. TRT goal was to develop new absorbers via additive manufacturing (3D printing), which enables the creation of complex shapes on non-planar geometries, at a relatively low cost, in small quantities, while simplifying the fabrication of multi-material structures compared to other fabrication techniques. Additionally, the research into the development of 3D-printed specific materials is very active. As a result, it is a versatile and promising technique for designing and manufacturing RF components with unique properties and in ways that other techniques cannot.

To address the interests of Thales, IEMN, and DGA, my research work was divided into three main points I investigated in these three years:

1. To design and characterize metamaterial absorbers with an absorption level greater than 90% over a broad range of radio frequency bands, preferably from 2 to 18 GHz (or more than one decade), with a thickness less than 1 cm, which is polarization-insensitive and robust to oblique incidences.
2. To identify and evaluate “ad-hoc” materials and concepts focusing on new printable filaments for absorbers operating in the low-frequency band (from 1 to 4 GHz).
3. To design and characterize RF absorber prototypes with an absorptivity gradient, which means that the incident electromagnetic wave is absorbed gradually from 0% to 100% along the structure, in the X-band (8 – 12 GHz), and with a thickness less than 1 cm.

In this presented framework, my objective was to answer these three issues.

In Chapter 1, an overview of the absorption mechanisms is presented, clarifying how and why a structure can absorb. Additionally, the necessity of conductive, dielectric, or magnetic losses is emphasized from the Poynting theorem. A state of the art on RF absorbers is also presented following the reduction of the absorbers profiles. The other chapters aim to answer the previous points.

In Chapter 2, I presented the study on a metamaterial absorber composed of multilayer conductive and dielectric layers, which had been started during an internship at Thales. The metamaterial absorber design was completed during the internship while I carried out the characterization of the fabricated prototype. I performed various retro-simulations to understand the discrepancy between the simulation and characterization, identifying the issue of the dielectric constant values, which are different between the initial solid filament and the printed sample. This prototype allowed validating Fused Deposition Modeling technology as a promising manufacturing process and demonstrating the good performance of the metamaterial absorber.

In Chapter 3, due to the strong interest in studying these multilayer and multi-material stair-like absorbers and the goal to design new structures to be polarization-insensitive and to be more robust to oblique incidences for a different frequency band, I optimized, characterized, and retro-simulated metamaterial absorbers that could satisfy these criteria. I presented the full-wave analysis of two prototypes, each with a distinct permittivity value, to demonstrate that using high permittivity filaments can improve angular robustness. Additionally, a circular section was chosen to be polarization-insensitive and to minimize manufacturing process imperfections. Moreover, I completed a study of such metamaterial absorbers, considering the major issues that could arise and the rules to follow to design these absorbers.

In Chapter 4, different structures were studied aiming at a total absorption at a low-frequency range (from 1 to 4 GHz) that was an important point for the DGA. For this chapter, it was pointed out that the optimal solution would be to utilize magneto-dielectric materials. To address the second point required for the Ph.D., I presented the absorbing performances of structures using advanced electromagnetic properties of a new printable filament that does not exist yet. Then, I proposed a structure that answers the first question of ultra-wideband absorptivity by using a cylindrical full-dielectric basic cell with a chess-based configuration. The objective was dual: on one hand, to increase the absorption level across a broad frequency band, and on the other hand, to create a lighter structure compared to an absorber with full magnetic materials.

In the final year of my Ph.D., I concentrated on the third point of the absorber with an absorptivity gradient, whose results are presented in Chapter 5. To address the necessity of a gradient absorber in the X-band, I proposed using conventional elemental resistive sheet absorbers, each able to exhibit a different absorptivity level. The originality of this proposal is the use of Salisbury-like structures to obtain the controlled absorption levels. This point has not previously been seen in the literature to the best of our knowledge. To demonstrate the validity of the proposal, a studied proof-of-concept is reported based on numerical simulation, along with experimental assessment of three prototypes.

Chapter 1: A Literature Review

This chapter presents the general principles that an electromagnetic absorber must satisfy to avoid reflection and transmission while maintaining unitary absorptivity. The physical mechanisms of the absorption are discussed in connection with the constitutive properties of a material. An exhaustive state of the art on Radio Frequency (RF) absorbers is presented, beginning with the earliest implementations and concluding with metamaterial absorbers aimed at presenting low-profile, ultra-broadband, polarization-insensitive, and high angle robust absorbers along with a description of their advantages and disadvantages.

1.1 General principles, absorption mechanism, and figures of merit

1.1.1 General principles

When an electromagnetic wave impinges on a structure, it can be reflected, transmitted, or absorbed. An electromagnetic absorber can avoid reflection and transmission, converting all the incoming energy into thermal energy through dissipation. To describe this phenomenon, the energy law is introduced by (1.1a):

$$A = 1 - R - T \tag{1.1a}$$

where *A* is the absorbance, *R* is the reflectance, and *T* is the transmittance.

Within this dissertation, all the designed absorbers are bounded by a metallic plate at the bottom that cancels all transmission, which means T = 0, reducing (1.1a) to (1.1b):

$$A = 1 - R \tag{1.1b}$$

Thus, to obtain total absorption, the condition of zero reflection is required. This condition is known as *impedance matching*[1].

To avoid misunderstanding, let us remind that *R* is the reflectance corresponding to the power ratio between the reflected and incident waves. It can be written in terms of complex reflection coefficient Γ, as in (1.2a), or complex reflection coefficient described by the scattering parameter S_{11}, as in (1.2b) [2]. Both Γ and S_{11} are expressed as voltage ratios.

$$R = |\Gamma|^2 \tag{1.2a}$$

$$R = |S_{11}|^2 \tag{1.2b}$$

Considering equation (1.2), equation (1.1b) can be written as:

$$A = 1 - |\Gamma|^2 = 1 - |S_{11}|^2 \tag{1.3}$$

[1] In Chapter 2, the so-called "critical coupling" condition, which is equivalent to the impedance matching one, is derived [1].

To understand the impedance matching condition, we assume the case of a plane wave traveling in free space under normal incidence and reaching a medium above a metal plate, as depicted in Figure 1.

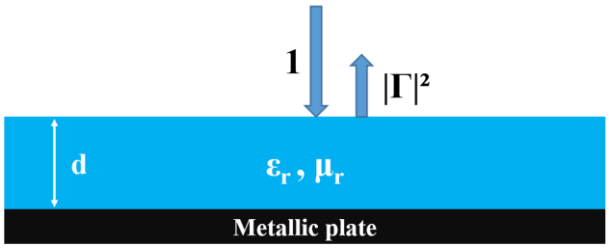

Figure 1. Geometry of a single dielectric slab placed on a metallic plate. 1 is the unitary incident power that can be either reflected or absorbed. The metallic plate assures zero transmission.

Since the transmission is zero below the metal plate, unitary absorptivity described by (1.3) is achieved through material losses when the reflection coefficient in equation (1.4) vanishes [3]:

$$\Gamma = \frac{\eta - \eta_0}{\eta + \eta_0} \tag{1.4}$$

where η is the intrinsic impedance of the medium and η_0 is the intrinsic impedance of the free space (air) equal to 377 Ω. When $\eta = \eta_0$, the impedance matching condition is satisfied since the reflection coefficient (Γ) is zero.

The intrinsic impedance of a generic material η is dependent only on the constitutive parameters of the medium as described in (1.5):

$$\eta = \sqrt{\frac{\mu}{\varepsilon}} = \sqrt{\frac{\mu_0 \mu_r}{\varepsilon_0 \varepsilon_r}} = \eta_0 \sqrt{\frac{\mu_r}{\varepsilon_r}} \tag{1.5}$$

where μ and ε are complex values corresponding to the permeability and permittivity, respectively, and are described by equations (1.6a) and (1.6b), respectively.

$$\mu = \mu_0 \, \mu_r = \mu_0 \, (\mu_r' - j\mu_r'') \tag{1.6a}$$

$$\varepsilon = \varepsilon_0 \, \varepsilon_r = \varepsilon_0 \, (\varepsilon_r' - j \, \varepsilon_r'') \tag{1.6b}$$

The imaginary part of the constitutive parameters is associated with the dissipation of energy into the medium. Thus, the magnetic and dielectric losses of a given medium are expressed in terms of loss tangent by equations (1.7a) and (1.7b), respectively:

$$tg\delta_m = \frac{\mu_r''}{\mu_r'} \tag{1.7a}$$

$$tg\delta_e = \frac{\varepsilon_r''}{\varepsilon_r'} \tag{1.7b}$$

Ideally, a perfect absorber is obtained when $\varepsilon_r = \mu_r$ since equation (1.5) is satisfied. This condition is challenging to satisfy, especially over wide frequency bands, but it could be implemented for narrowband absorbers.

By describing the previous electromagnetic field analysis employing a transmission line model (voltage and current approach), we can consider two cases, lossless and lossy, for the medium described in Figure 1 and analyze the input impedance at the air/absorber interface [2].

The lossless medium is exploited in Chapter 5 to answer the need of an RF absorber with absorptivity gradient by introducing resistive sheets on the top of the lossless medium. The input impedance seen by an incident wave on a grounded lossless medium of thickness *d* can be written as follows:

$$Z_{in} = j\,\eta\,tan(kd) \tag{1.8a}$$

where η is the intrinsic impedance of the lossless material (imaginary parts of permittivity and permeability are zero) and *k* is the wave vector in the medium.

For a lossy medium, one has to consider the imaginary parts of the constitutive parameters. Equation (1.8a) becomes (1.8b), which is exploited in Chapter 4:

$$Z_{in} = \eta\,tanh\left(j\frac{2\pi}{\lambda_0}\sqrt{\mu\varepsilon}d\right) = \eta_0\sqrt{\frac{\mu_r' - j\,\mu_r''}{\varepsilon_r' - j\,\varepsilon_r''}}\,tanh\left(j\frac{2\pi}{\lambda_0}\sqrt{(\mu_r' - j\,\mu_r'')(\varepsilon_r' - j\,\varepsilon_r'')}\,d\right) \tag{1.8b}$$

where λ_0 is the wavelength in free space and η is a complex value.

For both lossless and lossy medium, perfect absorption is obtained with the condition of $Z_{in} = \eta_0$, and it may be achieved by varying the thickness *d* and the real parts ε_r' and μ_r' in (1.8a) and (1.8b), and the imaginary parts ε_r'' and μ_r'' in (1.8b).

We gave here several fundamental equations to study the absorbance of a given structure. In the next section, an insight into the physical absorption mechanisms will be provided.

1.1.2 Absorption mechanisms

Energy loss occurs in a medium illuminated by electromagnetic waves due to damping forces acting on polarized atoms and molecules. Vector calculus can be used to write an electromagnetic conservation-of-energy equation, referred to as the complex Poynting vector theorem that relates the power flow into a volume V, via a closed surface S, to the electromagnetic fields and material properties contained within the volume. The real power flowing in such a surface is the dissipated (absorbed) power. To illustrate this statement, we report below the conservation-of-energy equation given by (1.9) derived from [3].

$$\begin{aligned} -\frac{1}{2}\iiint_V (\boldsymbol{H}^* \cdot \boldsymbol{M_i} + \boldsymbol{E} \cdot \boldsymbol{J_i^*})dv = {} & \oiint_S \left(\frac{1}{2}\boldsymbol{E} \times \boldsymbol{H}^*\right) \cdot d\boldsymbol{s} + \frac{1}{2}\iiint_V \sigma \mid \boldsymbol{E} \mid^2 dv \\ & + j2\omega \iiint_V \left(\frac{1}{4}\mu \mid \boldsymbol{H} \mid^2 - \frac{1}{4}\varepsilon \mid \boldsymbol{E} \mid^2\right) dv \end{aligned} \tag{1.9}$$

Where $\boldsymbol{H}$ is the magnetic field intensity (in A/m), $\boldsymbol{M_i}$ is the impressed (fictitious source) magnetic current density (in V/m²), $\boldsymbol{E}$ is the electric field intensity (in V/m), $\boldsymbol{J_i}$ is the impressed

(source) electric current density (in A/m²), σ is the conductivity (in S/m), ε is the complex permittivity (in F/m), and μ is the complex permeability (in H/m)

Equation (1.9) can be written as (1.9a)

$$P_S = P_e + P_d + j2\omega\,(\bar{W}_m - \bar{W}_e) \tag{1.9a}$$

where

$$P_S = -\frac{1}{2}\iiint\,(\boldsymbol{H}^* \cdot \boldsymbol{M_i} + \boldsymbol{E} \cdot \boldsymbol{J_i^*})\,dv\text{: supplied complex power (W)} \tag{1.9b}$$

$$P_e = \oiint_S \left(\frac{1}{2}\boldsymbol{E} \times \boldsymbol{H}^*\right) \cdot d\boldsymbol{s}\text{: excited complex power (W)} \tag{1.9c}$$

$$P_d = \frac{1}{2}\iiint_V \sigma\ |\ \boldsymbol{E}\ |^2\ dv\text{: dissipated real power (W)} \tag{1.9d}$$

$$\bar{W}_m = \iiint_V \left(\frac{1}{4}\mu\ |\ \boldsymbol{H}\ |^2\right)\ dv\text{: time-average magnetic energy (J)} \tag{1.9e}$$

$$\bar{W}_e = \iiint_V \left(\frac{1}{4}\ \varepsilon\ |\ \boldsymbol{E}\ |^2\right)\ dv\text{: time-average electric energy (J)} \tag{1.9f}$$

While P_S and P_e are in general complex and P_d is real, the last two terms are always imaginary and represent the reactive power associated with magnetic and electric fields. It should be emphasized that for complex permeability and permittivity, the contribution of their imaginary parts of the integrals of (1.9e) and (1.9f) should be combined with (1.9d), as both represent losses associated with the permeability and permittivity as described in (1.9g).

$$P_d = \frac{\omega}{4}\iiint_V \left(\mu''\ |\ \boldsymbol{H}\ |^2 + \ \varepsilon''\ |\ \boldsymbol{E}\ |^2 + \frac{\sigma}{\omega}\ |\ \boldsymbol{E}\ |^2\right)\ dv \tag{1.9g}$$

As a result, one can conclude that when the impedance matching condition is satisfied, to have total absorptivity, one or a combination of conductivity (σ), imaginary permittivity (ε''), and imaginary permeability (μ'') must be exploited. This remark is of prime importance for the structures considered in the present work. For instance, two prototypes are manufactured in 3D printing using relatively low conductive layers compared to PCB technology structures with high conductive layers.

1.1.3 Figures of merit

The most common figure of merit to qualify a broadband absorber is the fractional bandwidth (FB), given by (1.10):

$$FB = \frac{f_{max} - f_{min}}{f_c} = 2\frac{f_{max} - f_{min}}{f_{max} + f_{min}} \tag{1.10}$$

where f_{max} and f_{min} are the extreme frequencies of the band in which an absorption coefficient of more than 90% is obtained, and f_c is the center frequency.

Three points have to be underlined at this point that are considered throughout this thesis:

- FB is always referred to as an absorption level above 90% unless otherwise specified.

- The presented results are expressed in terms of the frequency dependence of the absorbance. Sometimes, the reflection coefficient in terms of scattering parameter S_{11} in decibel (dB) is exploited. For the absorption level of 90% (0.9), the corresponding S_{11} has a value of -10 dB.
- An absorber is classified as wideband if its fractional bandwidth exceeds 0.67, which corresponds to one octave.

As the last point, an overview of the frequency bands of interest linked to this Ph.D. are listed in Figure 2.

Frequency Range	Wavelength Range	Band Name
3-30 MHz	10-100 m	HF
30-300 MHz	1-10 m	VHF
300-1000 MHz	0.3-1 m	UHF
1-2 GHz	15-30 cm	L-band
2-4 GHz	7.5-15 cm	S-band
4-8 GHz	3.75-7.5 cm	C-band
8-12 GHz	2.5-3.75 cm	X-band
12-18 GHz	1.67-2.5 cm	Ku-band
18-24 GHz	1.11-1.67 cm	K-band
24-40 GHz	0.75-1.11 cm	Ka-band

Figure 2. Radar frequency bands from HF (High Frequency) to K_a-band. For this dissertation, we are mainly interested in the bands from L to K_u (1 – 18 GHz).

1.2 State of the art on RF absorbers

We continue our literature analysis by looking at the state of the art on absorber technology, starting with the first developments in this research field. We also analyze the evolution of the various absorber elements by seeking in particular a thickness reduction for low-profile total absorbers. To this aim, we start with the radar application context, which is where RF absorber research began.

1.2.1 Beginning of RF absorbers

A RADAR (Radio Detection and Ranging) is a system that can calculate distances, directions of arrival, and velocity of objects. For example, the transmitting and receiving towers of the British coastal radar stations that were of critical importance during the Second World War (WWII) are shown in Figure 3(a). As illustrated in Figure 3(b), a radar emits an electromagnetic wave with a directivity. This incident wave can be reflected in many directions by an object. The wave reflected in the same direction as the incident one can be detected by the radar. For stealth application, this "echo" has to be avoided as far as possible with a figure of merit called Radar Cross Section (RCS).

Consequently, the object considered as a target must have low RCS, and the reduction of this figure of merit is usually associated with EM absorbers.

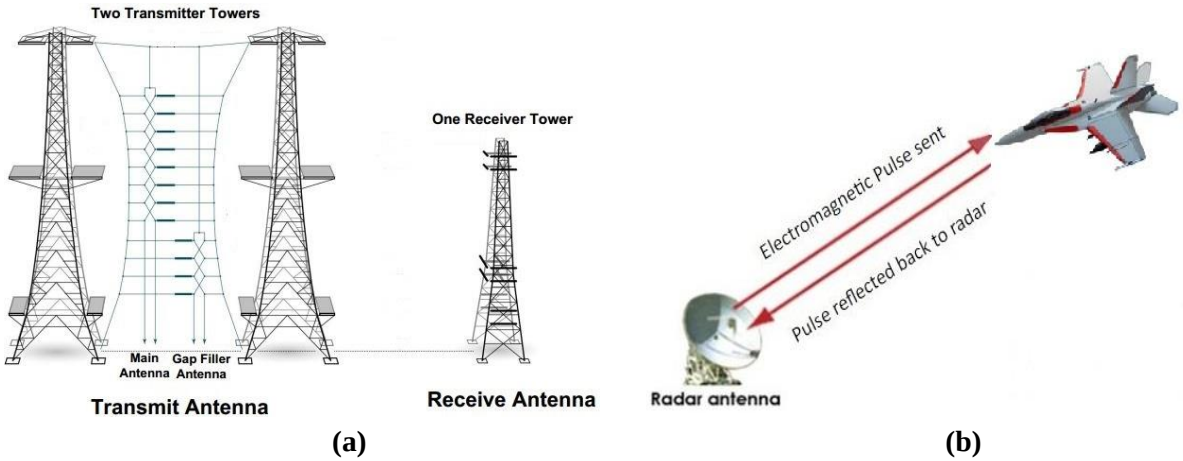

Figure 3. (a) Chain Home Transmit & Receive Antennas in 1940, and (b) radar echo scattered from an object [the pictures are taken from the web].

As described in detail in [4], the first patent on EM absorbers, suggesting a structure with a narrowband absorption at 2 GHz composed of carbon black powder and TiO_2 to achieve a high dielectric constant and low-profile, was developed by Naamlooze Vennootschap Machinerieen in 1936 [5]. Some years later, during WWII, radar material absorbers were the subject of intense researches in Germany and the United States. In Germany, a project named "Schornsteinfeger", which means chimney sweep, allowed developing two absorbers: one was known as Wesh material, a 7.6 mm-thick rubber sheet loaded with carbonyl iron powder with a resonant frequency at 3 GHz. The other was a multilayered structure composed of resistive sheets called Jauman absorber [6] with a reflection coefficient of -20 dB for 2 - 15 GHz (FB of 1.53) and a thickness of 76.2 mm. In the US, a project was conducted at the M.I.T. Radiation Laboratory to develop two absorbers operating in X-band. The most relevant result was the homonymous Salisbury screen [7] with a patent published in 1952 for strategic reasons. The structure is similar to the Jauman screen, with only one resistive layer whose surface impedance equals to that of the free space. Both Jauman and Salisbury screens are described in detail in Section 1.2.3. A more detailed history of the electromagnetic wave absorbers can be found in [4] and [8].

In the next section, we analyze the different classes of EM absorbers by taking as a common thread, namely the thickness of the absorber. Three principal classes will be reported: absorbers with a thickness of several wavelengths (1.2.2), quarter-wavelength absorbers (1.2.3), and thin absorbers with thickness much less than a wavelength (1.2.4).

1.2.2 Impedance Matching Absorbers

As outlined in section 1.1, the main requirement for perfect absorption is to satisfy the impedance matching condition that suppresses any reflection at the air/absorber interface. An impedance matching absorber has its characteristic impedance that progressively matches the free space one [9]. The materials used are electrically resistive, and the energy absorption is obtained through ohmic losses (conductive losses). In Figure 4, three kinds of impedance matching absorbers, pyramidal, tapered loading, and matching layer, are illustrated. All structures adapt their intrinsic impedance by loading Polyurethane foams, usually with lossy powder, typically carbon, in different percentages.

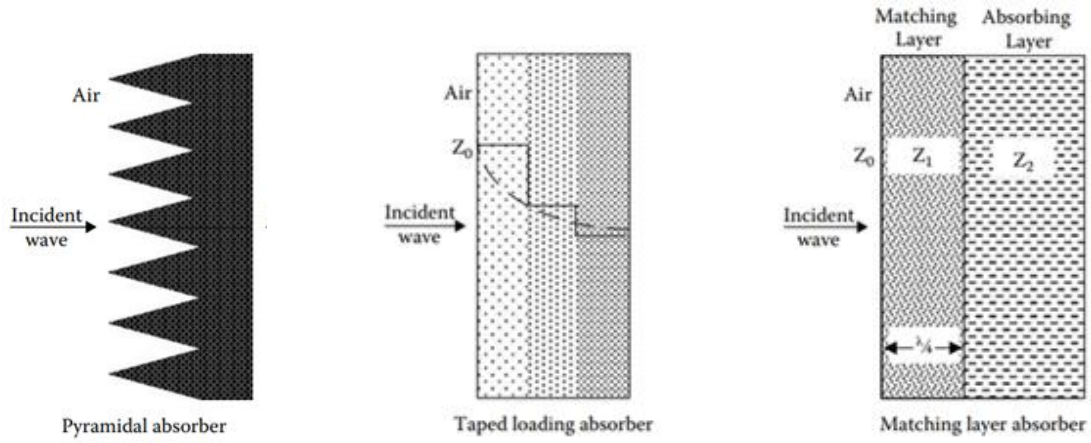

Figure 4. Geometries of impedance matching absorbers. (a) Pyramidal geometry, (b) Tapered loading geometry, and (c) Matching layer geometry [9].

1.2.2.1 Pyramidal foam absorbers

Pyramidal foam absorbers [10] are thick structures with pyramidal or conical shapes with a symmetry axis toward the incident wave direction, as seen in Figure 4(a). The wideband behavior that provides a reflectivity of -50 dB (or more) is obtained thanks to the material losses and multiple reflections inside the triangular geometries, as shown in Figure 5. For instance, a wideband pyramidal absorber with an absorptivity greater than 99% for the frequency range from1 GHz to 18 GHz (FB = 1.79) for a total height of 90 mm is presented in [11]. The drawbacks of such absorbers are a significant thickness [8], [12] and their tendency to be fragile.

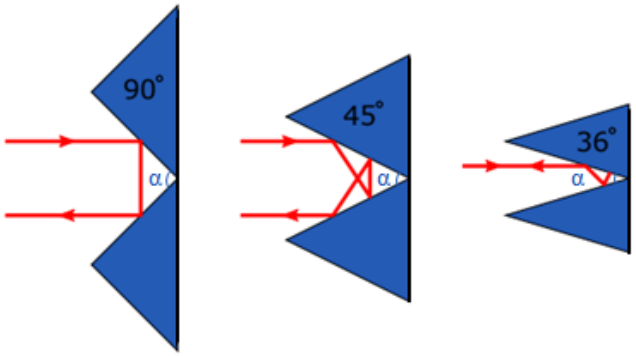

Figure 5. Multiple reflections in a pyramidal absorber with different α angles of 90°, 45°, and 36° [pictures from the web].

1.2.2.2 Tapered loading absorbers

A tapered loading absorber is an absorber with a planar structure composed of more than one layer, as in Figure 4(b). Unlike foam pyramidal absorbers, with a triangular-shaped cross-section that progressively changes its intrinsic impedance providing gradual transition in impedance, as in Figure 6(a), the tapered absorber has a discrete intrinsic impedance value for each layer, as shown in Figure 6(b). Compared to the pyramidal absorbers, the advantages of these structures are a lower profile and a planar geometry, while the downside is a smaller FB.

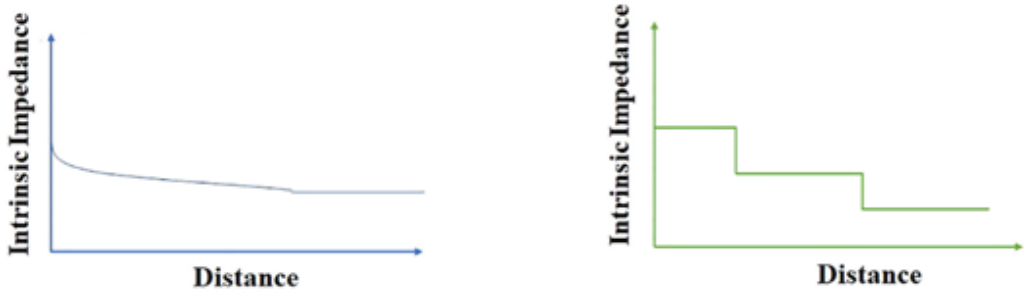

Figure 6. (a) Smooth change of the intrinsic impedance as for pyramidal absorbers, and (b) discrete values of the intrinsic impedance as for tapered loading absorbers.

1.2.2.3 Matching layer absorbers

Matching layer absorbers are composed of one matching layer above a lossy dielectric slab, as depicted in Figure 4(c). The matching layer acts as a quarter-wave transformer, with a thickness $\lambda_g/4$, whose characteristic impedance Z_1 is described as follows:

$$Z_1 = \sqrt{Z_0 Z_2} \tag{1.11}$$

where Z_0 is the free space impedance (η_0), and Z_2 is the impedance of the absorbing layer. Since Z_1 is matched at one frequency, this absorber is usually narrowband.[2]

1.2.3 Absorber with quarter-wavelength dielectric thickness condition

These resonant absorbers work with the quarter-wave condition of the dielectric thickness. In order, we present the Dallenbach screen that relies on dielectric and/or magnetic losses, the Salisbury absorber, and the Jauman absorber that rely on conductive losses. In addition, some examples of absorbers that exploit Frequency Selective Surface (FSS) to reduce the absorber thickness with values less than $\lambda_g/4$ are also shortly described [13].

1.2.3.1 Dallenbach screen

The Dallenbach absorber is composed of two layers, a lossy slab above a metallic plate [8]. Let us recall that to have zero reflection, Z_{in} of equation (1.8b) has to be equal to the free space impedance of 377Ω. The trivial solution is to have $\mu_r = \varepsilon_r$ for which the impedance matching condition is satisfied while the imaginary parts of the complex permittivity and permeability are responsible for the absorption mechanisms. The results investigating the importance of the dielectric and magnetic losses in achieving low reflectivity are displayed in Figure 7(a,b) [14].

For a non-magnetic material ($\varepsilon_r = 16$, $\mu_r = 1.0$), equation (1.8b) is satisfied when the thickness of the structure is $\lambda/4$, as depicted in the solid line in Figure 7(a). When only magnetic properties is exploited ($\varepsilon_r = 1.0$, $\mu_r = 16$), the zero reflection condition occurs when the material thickness increases toward $\lambda/2$, as shown in Figure 7(b). All other configurations must be analyzed in detail since the

[2] Nowadays with the developing of new materials, it is important to notice that the performances of impedance matching absorbers (all the three types) could be significantly improved in terms of fractional bandwidth and low thickness.

thickness criterion of multiple of λ/4 is no longer satisfied [15]-[16] as for the results plot in dashed lines in Figure 7(a,b).

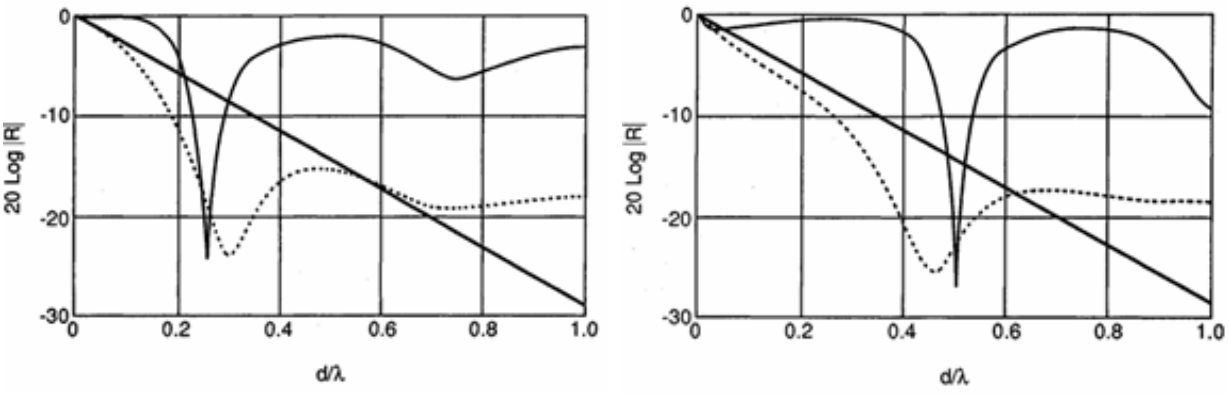

Figure 7. (a) Reflectivity for: Solid line is for ε_r = 16, μ_r = 1, $tg\delta_\varepsilon$ = 1.52 and $tg\delta_\mu$ = 0. Dashed line is for ε_r = 25, μ_r = 16, $tg\delta_\varepsilon$ = 1.54, $tg\delta_\mu$=1.52, Diagonal line is for ε_r = μ_r = 4, $tg\delta_\varepsilon$ = $tg\delta_\mu$ = 1.50. (b) Reflectivity for: Solid trace is for ε_r = 1, μ_r = 16, $tg\delta_\varepsilon$ = 0 and $tg\delta_\mu$ = 1.47. Dashed trace is for ε_r = 16, μ_r = 25, $tg\delta_\varepsilon$ = 1.52, $tg\delta_\varepsilon$ = 1.54, Diagonal trace is for ε_r=μ_r=4, $tg\delta_\varepsilon$ = $tg\delta_\mu$ =1.50. R is here the reflection coefficient [14].

The main drawback of the Dallenbach screen is the thickness of the lossy slab, and for the magneto-dielectric layer, the weight increase. It should be emphasized that such issues could be alleviated by developing new materials with higher permittivity and permeability values and by implementing lower mass density material to reduce their weight.

1.2.3.2 Salisbury screen

The Salisbury screen (patented in 1952 [7]) is a resonant absorber composed of three layers: a metallic layer acting as a ground plane, a dielectric spacer (that could be air) with a thickness d, and a purely resistive sheet with a surface resistance R_s that matches free space impedance on top of it, as depicted in Figure 8(a). When an electromagnetic wave impinges onto the 377 Ω resistive sheet under normal incidence, it passes through it without being reflected, forming a standing wave with the 180° phase-shifted wave reflected from the ground plane. This condition assures that the two waves are in phase at λ/4 apart from the metal plate with the **E**-field being twice as intense as the initial field [2], [8]. Since the resistive sheet is placed at this point, the power of the wave is entirely dissipated by the resistive losses [17].

Therefore, two conditions are required for total absorption:

- The ideal lossless dielectric spacer must be $\lambda_g/4$-thick, where λ_g is the wavelength of the absorbed frequency in the dielectric, as shown in Figure 8(a).
- The resistive sheet must have a surface impedance R_S of 377 Ω/square[3] to match the free space impedance.

If both requirements are satisfied, the impedance matching condition is fulfilled. In fact, by using (1.8a), the input impedance Z_{in} of the $\lambda_g/4$-thick dielectric slab terminated by a metallic plate seen from an incoming wave is infinite. When the resistive sheet is placed at this point, the incoming wave sees the parallel configuration between the sheet resistance and Z_{in}, which reduces to 377 Ω. Consequently, impedance matching is achieved between the free space and the absorber. More details are given in Chapter 5 where this concept is widely exploited.

[3] Ω/square (or Ω/□) is dimensionally equal to Ω but it is extensively used for surface resistances [18].

The surface resistance of the resistive sheet in relation to its thickness and conductivity can be calculated as follows:

$$R_S = \frac{1}{\sigma t} = \frac{\rho}{t} \tag{1.12}$$

where σ is the conductivity (in S/m), t is the thickness (in m) of the resistive layer and ρ is the resistivity (in Ωm).

Figure 8(b) presents the simulation result of the S_{11} parameter for a Salisbury screen, operating at 10 GHz, for a resistive sheet with R_S of 377Ω and a 7.5 mm-thick air dielectric spacer. The scattering parameter S_{11} is lower than -10 dB between 6.2 GHz and 13.6 GHz (FB = 0.75).

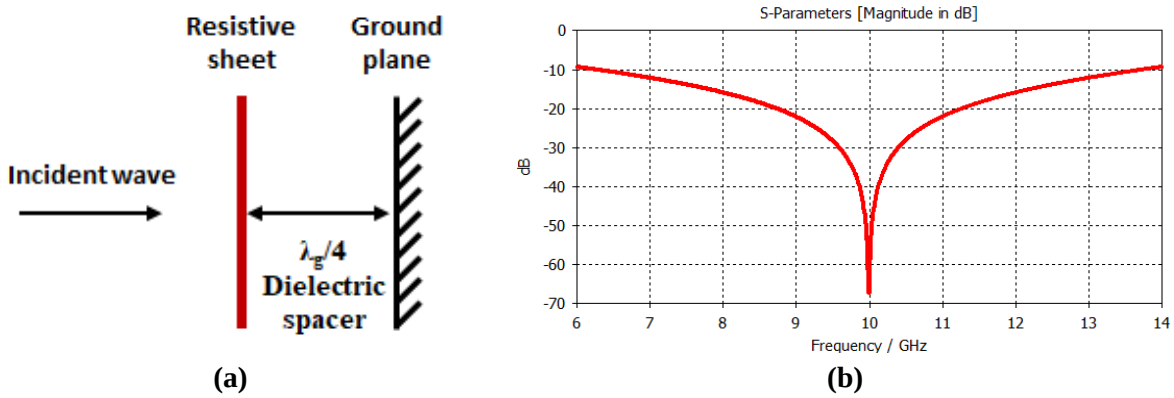

Figure 8. Salisbury screen: (a) schematic of the absorber composed of a ground plane, a $\lambda_g/4$-thick dielectric spacer, and a resistive sheet with surface impedance R_S. (b) Simulation of the S_{11} parameter considering a R_S of 377 Ω, and an air spacer of 7.5 mm.

The main drawback of the Salisbury screen is related to its thickness (λ/4). For practical applications, a low-profile is required and the λ/4-thickness condition is not suitable. A dielectric with high permittivity could be used to reduce the thickness at the expense of a reduced absorption bandwidth.

1.2.3.3 Jauman screen

Jauman screen is a multilayer version of Salisbury absorber. By vertically stacking multiple resistive layers (Figure 9(a) [6]), the absorption bandwidth is enhanced. Figure 9(b) presents the frequency dependence of the modulus of S_{11} parameter for a Jauman screen composed of two resistive layers, equidistantly spaced of 7.5 mm, with R_{S1} = 266 Ω/square and R_{S2} = 1287 Ω/square [19]. The -10 dB-bandwidth is obtained from 3.8 GHz to 14 GHz, corresponding to a FB of 1.15. This high FB value greater than 1 is achieved at the expense of a total thickness of 15 mm.

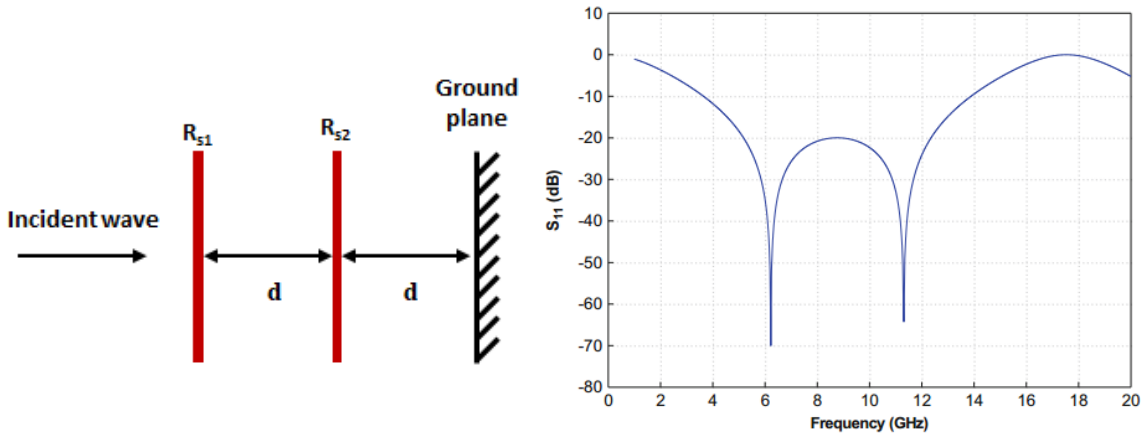

Figure 9. Jauman screen: (a) structure composed of two resistive screens with surface impedances R_{S1} and R_{S2} equispaced of the same d, and (b) simulation of S_{11} parameter for R_{S1} = 266 Ω and R_{S2} = 1287 Ω, from [19].

A Jauman absorber is a complex structure, and its study for a targeted fractional bandwidth requires adjusting different parameters as dielectric thicknesses, constitutive parameters of the dielectric slabs, and the number of resistive screens along with their resistances. Different algorithms were developed to achieve the best performances aiming to the lowest possible profile [20]-[22]. In fact, as for the Salisbury screen, the drawbacks of the Jauman screen are the thickness and the weight that make the structure unsuitable for many practical applications. In the next section, a solution to the thickness issue is proposed by exploiting Frequency Selective Surfaces (FSS) to reduce the $\lambda_g/4$ dielectric thickness condition.

1.2.3.4 Frequency Selective Surface

A frequency selective surface (FSS) is a periodic structure composed of an assembly of identical elements arranged in one or two-dimensional infinite array. Single elements can be designed with different metallic patterns or slots. Figure 10 illustrates typical patterns used in the FSS layout [13].

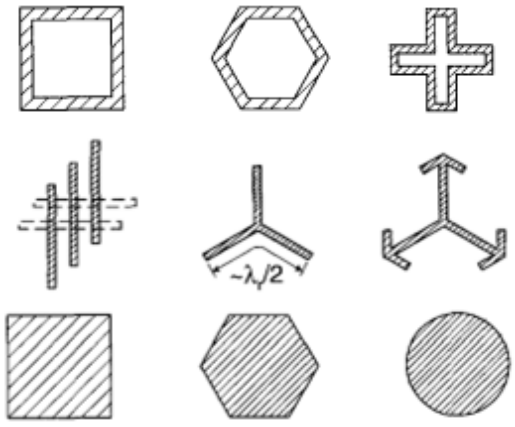

Figure 10. Typical element patterns for an FSS (Frequency Selective Surface) [13].

The basic elements periodically arrayed can be analyzed with an equivalent circuit model with two examples of element patterns, and their equivalent circuits that are depicted in Figure 11.

Physically, a distributed inductance can be associated with the straight part of a metallic pattern, and a capacitance element can be related to the gap between two adjacent metal strips.

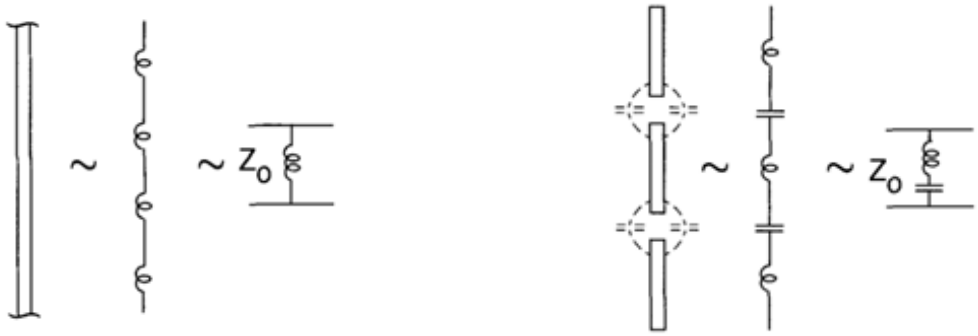

(a) **(b)**

Figure 11. (a) Infinitely long rod and its equivalent circuit, (b) periodic rectangular strip and its equivalent circuit [13].

FSSs are exploited in many applications, such as filtering structures in quasi optics applications or antennas arrays. Their use here in the framework of full absorber technology is motivated by the possibility to cancel the imaginary part of the input impedance for a distance between the FSS and the ground plane lower than the conventional criterion $d = \frac{\lambda}{4}$. Under this condition, the input impedance seen by the impinging wave is purely real and can be adjusted to fit the 377 Ω free space impedance.

As examples, two absorbers known as Circuit Analog Absorber (CAA) and Capacitive Circuit Absorber (CCA) are analyzed in the two following sections. Both structures are composed of a metallic ground plane, a dielectric substrate, and an FSS. They differ with a cross type pattern for the first example, while in the second case, a patch-like structure is used corresponding to a capacitive selective surface.

1.2.3.4.1 Circuit Analog Absorber (CAA)

An example of the so-called Circuit Analog absorber (CAA) with the periodic arrangement of cross basic is shown in Figure 12(a), where the structure and the FSS equivalent LC circuit are depicted. The equivalent circuit of a generic FSS at a distance $d < \lambda_g/4$ from a ground plane is an RLC series configuration as in the right part of Figure 12(b), from which the name "Circuit Analog" is derived. The resonant frequency of the RLC circuit corresponds to the central frequency of the absorption window. The intrinsic FSS reactive elements allow canceling the inductive behavior term due to the ground plane. Moreover, compared to a Salisbury screen, it can be shown that a larger bandwidth can be obtained [23].

To sum up, two key points can be pointed out with this configuration:

- The FSS is placed at a distance *d* less than $\lambda_g/4$.
- The bandwidth is increased.

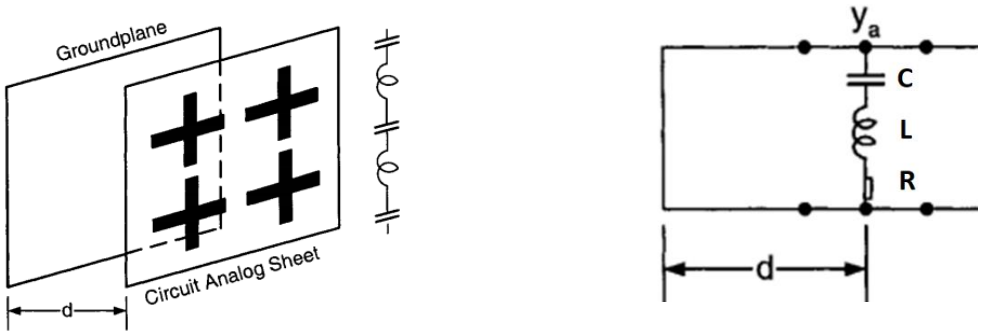

(a) **(b)**

Figure 12. Example of a circuit analog absorber (CAA): (a) Design composed of a ground plane, a dielectric spacer with thickness $d < \lambda_0/4$, and the FSS circuit analog sheet with its equivalent circuit. (b) Model of the equivalent transmission line loaded by a short circuit and at the distance d the equivalent circuit of the FSS composed of capacitance (C), inductance (L), and resistance (R) [13].

Another example of an absorber that exploits two circuit analog sheets [13] is presented in Figure 13(a), while in Figure 13(b), the equivalent transmission line model with two complex admittance values of y_{a1} and y_{a2} is described. As noted before, the absorbed frequencies f_{a1} and f_{a2}, depicted in Figure 13(c), corresponding to the resonant frequencies of the first and second RLC circuits, respectively.

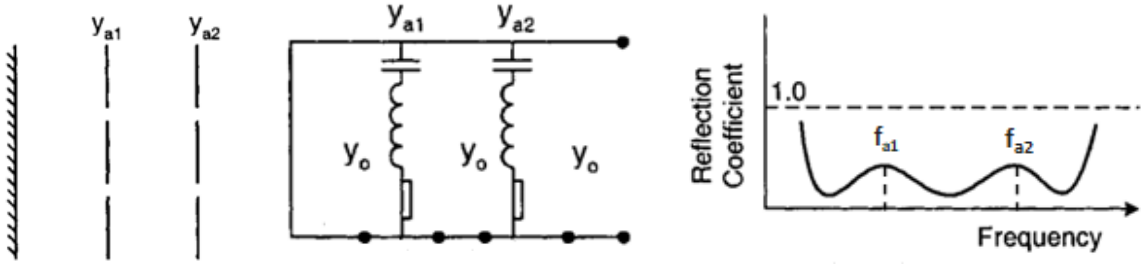

(a) **(b)** **(c)**

Figure 13. CAA: (a) Geometry of an absorber made of two circuit analog sheets of admittances y_{a1} and y_{a2}. (b) Equivalent network model of the structure (y_0 is the free space admittance), and (c) a typical reflection coefficient over the frequency of this kind of absorber [13].

The absorption spectra displayed corresponds to normal incidence. Before considering the Capacitive Circuit Absorber in the next section, let us mention that several publications in the literature address the robustness of such FSS–type absorber as a function of the incidence angle. For example, an exhaustive study on the response of the CAA for oblique incidences is presented in [24] and [25].

1.2.3.4.2 Capacitive Circuit Absorber (CCA)

A significant difficulty in the design of a CAA is retrieving the resonant equivalent lumped elements. A possible simplification is implementing a low-pass filter configuration instead of a band-pass filter one. This kind of absorber is Capacitive Circuit Absorber (CCA), forming an RC circuit shown in Figure 14(a,b). The work presented in [26] demonstrated that a CCA achieves a better response compared to the Salisbury screen (Figure 14(c)) in terms of bandwidth and similar response when compared to a CAA (Figure 14(d)) with the advantage of simple design rules without the inductance term in the FSS equivalent circuit.

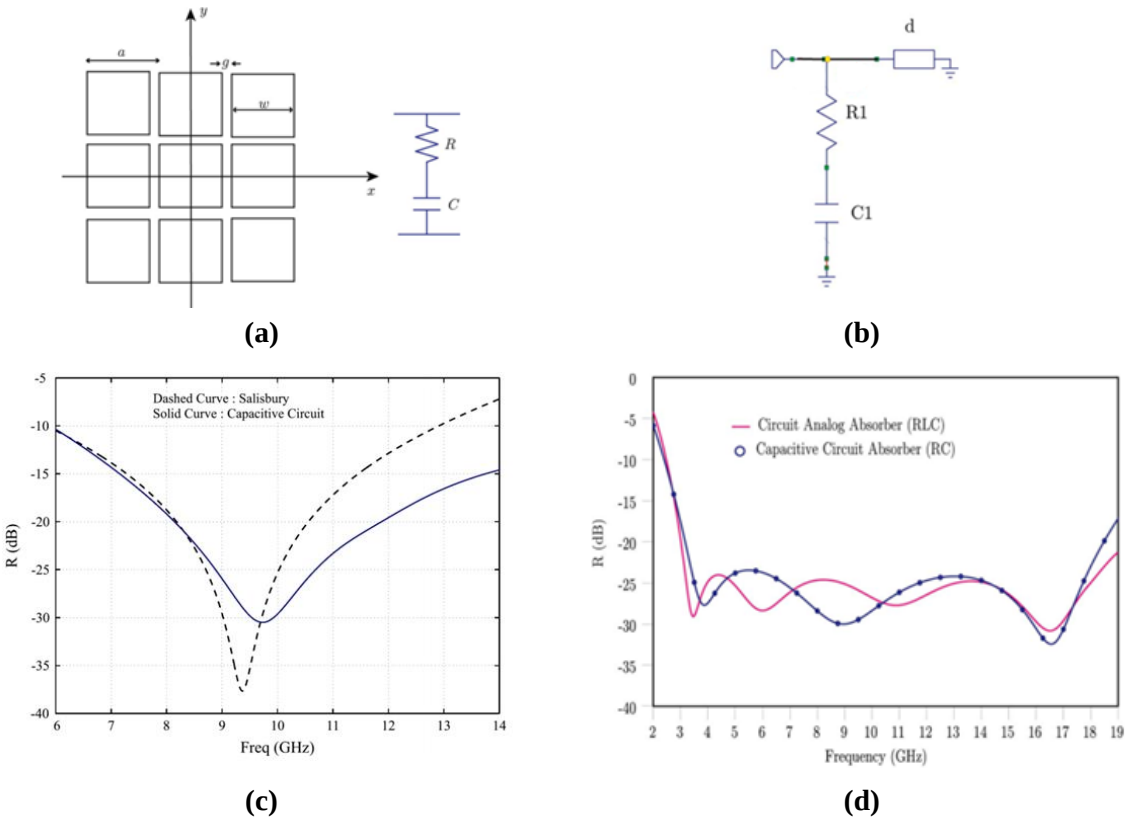

Figure 14. Capacitive Circuit Absorber (CCA): (a) geometry of the FSS and its equivalent RC circuit. (b) Equivalent circuit model: starting from the ground plane on the right, the transmission line with thickness d and the FSS equivalent circuit (RC circuit) (c) Comparison of the reflectivity versus frequency between a CCA (in blue) and a Salisbury screen (in black dashed line). (d) Comparison of the reflectivity over the frequency between a CCA (in blue) and a CAA (in rose) [26].

In conclusion, the operating principle of CCA absorbers is based on the cancellation of the inductance due to the metal plate by the FSS equivalent capacitance, allowing a reduction of the dielectric layer and opening the way for the design of low-profile absorbers ($d < \frac{\lambda}{4}$). In addition, both CCA and CAA absorbers can be tuned for changing the targeted frequency band.

We now consider further reduction of the dielectric substrate thickness to obtain absorber structures with total thickness much smaller than a wavelength at operating frequency ($d << \lambda$). In the next section, how ultra-thin absorbers can be designed by exploiting the so-called metamaterial technology are discussed.

1.2.4 Metamaterial Absorbers

The definition of metamaterial (MM), given by the Virtual Institute (VI) that was given after the Network of Excellence NoE METAMORPHOSE is: “a metamaterial is an arrangement of artificial structural elements, designed to achieve unusual electromagnetic properties”. The most common meaning given to the prefix ‘‘meta’’ in metamaterials is ‘‘beyond”. Following this signification, metamaterials may be defined as artificially engineered materials exhibiting unique or abnormal properties that cannot be found in natural materials at the frequencies of interest [27].

One can consider that the article of Veselago [28] published in 1968 about negative refraction ($\mu_r < 0$ and $\varepsilon_r < 0$), and the theoretical demonstration of the possibility to focus a divergent beam through a flat lens in 2000 by Pendry, notably considering the possibility of a perfect lens [29] are

the seminal works in this field. Nowadays, one can find plenty of applications in all the electromagnetic frequency ranges [30].

For a homogeneous medium composed of atoms and molecules, the scattering with an electromagnetic field can be analyzed through the constitutive parameters [3]. In the same way, for a 3D arrangement composed of "artificial atoms" that can be considered as composite elemental structures (metamaterial), or for a 2D configuration (metasurface), the interaction with the electromagnetic wave can be described with the *effective* constitutive parameters [31] or equivalent surface impedance [32]. An important condition for this analysis is that the relevant dimensions of the elemental structure, for instance, composed of metal and dielectric materials such as the Split Ring Resonator (SRR) proposed by Pendry [33], are much smaller than the operating wavelength. Under this condition, one can interpret the scattering of the impinging EM wave as an interaction with an effective homogeneous medium field. As a result, the great advantage of metamaterial–inspired structures is their small dimensions compared to the wavelength.

Hereafter, we present some key articles published in this field, paying attention to the achievement of ultra-thin absorbing structures, emphasizing their advantages in terms of dimension and their drawbacks in particular concerning their frequency selectivity.

1.2.4.1 First structures

To the best of our knowledge, one of the first theoretical works about the possibility to design a full absorbing screen with $d << \lambda$ was proposed by Engheta in 2002 [34]. As shown in Figure 15, this structure consists of three layers: a metallic plate, a metamaterial surface at a distance d much less than $\lambda_g/4$ ($d << \lambda$), and a resistive sheet on top of the MM. The metamaterial surface and the conductive ground plane form a High Impedance Surface (HIS) [35]. Considering a plane wave coming from the top, the HIS reflection is unitary with zero phase shift and a maximum of the tangential component of the **E**-field. The electric field energy is dissipated within the resistive losses in the resistive sheet placed above the equivalent High Impedance Surface. The main advantage of this structure proposed by Engheta is that the absorber thickness is close to the physical limitation of the thickness to bandwidth ratio of radar absorbers introduced by Rozanov in [36]. As demonstrated by Bilotti et al. in 2011, using MMs permits to reach closer values with respect to this theoretical limit [37].

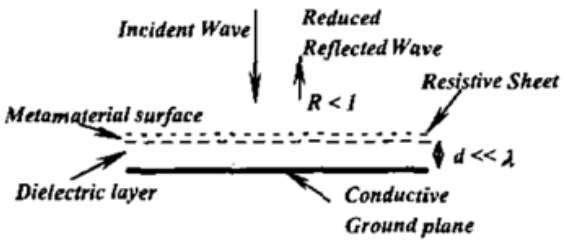

Figure 15. Geometry of the three layers metamaterial absorber proposed in [34] composed of a ground plane, a metamaterial surface at the distance d from the ground plane (with $d << \lambda$) equivalent to a HIS (High Impedance Surface) and a resistive sheet on top of this metasurface.

From the experimental side, Landy et al. proposed in 2008 the first fabricated metamaterial absorber operating at X-band with an overall thickness of 0.72 mm ($\lambda_0/36$) and hence in deep subwavelength technology [38]. This article published in Physical Review letters can be considered as the seminal work on Perfect Metamaterial Absorbers (PMA). The basic cell geometry is presented in Figure 16(a). The top layer is composed of a so-called Electric Ring Resonator (ERR) allowing an

electric response when coupled to an incident electric field at the resonance frequency. The metal strip, printed onto the substrate backside, contributes to the overall response by a magnetic coupling via a current loop (conduction and displacement currents) between this strip and the ERR center metal branch. Consequently, this design allows for tuning both electric and magnetic responses. Figure 16(b) compares the frequency dependence of the absorbance between simulation and characterization that were reported in this publication for normal incidence. It can be noticed that 96% of absorbance for the simulation (in red) and 88% for the measurements (in blue) at 11.5 GHz are achieved. Its successful design with maxima of absorbance close to unity was based on the retrieval of the effective constitutive parameters according to [39] aiming to satisfy the impedance matching condition ($\eta = \eta_0$, so $\varepsilon_{r,eff} = \mu_{r,eff}$). The absorption window is quite selective, with a fractional bandwidth of the order of 4%.

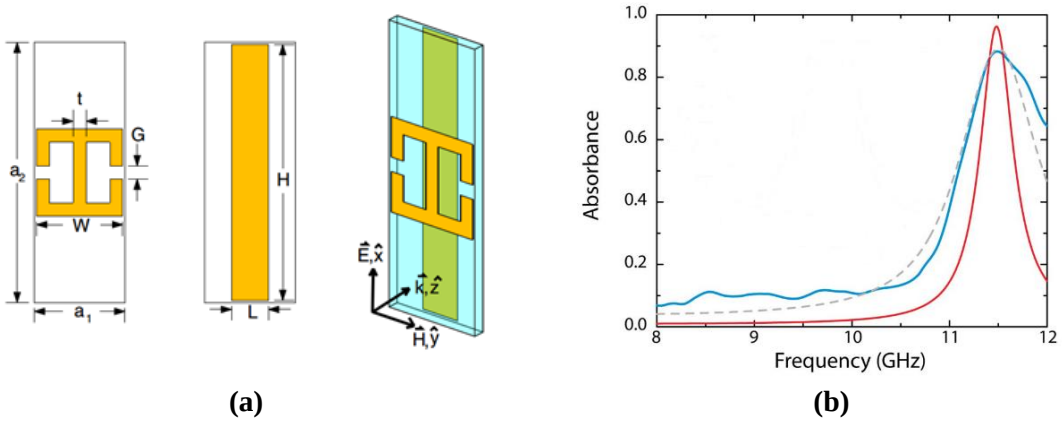

Figure 16. Perfect metamaterial absorber (PMA) (a) basic cell geometry that resonates at 11.5 GHz. (b) Frequency dependence of the absorbance over the range 8 GHz – 12 GHz (measurements in blue and simulations in red). The gray dashed absorbance curve is a Gaussian weighted average that approximates assembly error of the metamaterials absorber, as described in [38].

Another metamaterial with narrowband absorption is presented by the Metal-Insulator-Metal (MIM) cavities that confine the field inside a lossy dielectric layer. The absorption process is similar to the preceding PMA since it relies on simultaneous electric and magnetic resonances. Anti-parallel currents are excited by the incidence magnetic field, resulting in a magnetic dipole resonance. For illustration, the MIM-type array structure operating at NIR proposed by Padilla's group in 2010 exhibits an absorptivity of 88% for the wavelength of 1.58 μm [40].

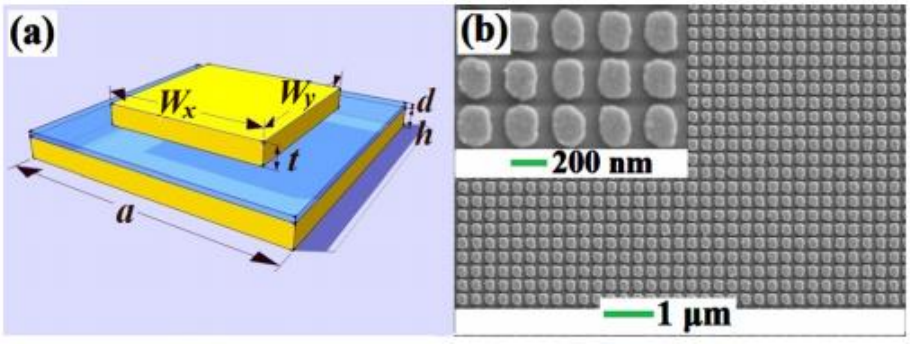

Figure 17. Illustration of NIR MIM metamaterial absorber: (a) design of the 310 × 310 × 100 nm³ elementary structure composed of metallic gold layers (in yellow) and a dielectric Al_2O_3 layer (in blue). (b) Fabricated periodic structure with relevant dimensions [40]

The main drawback of the metamaterial absorber mentioned above, which can be appropriately scaled in frequency, is their intrinsic narrowband with a fractional bandwidth of a few percent. We will consider in the following part how various concepts have been proposed to increase the absorption bandwidth, notably by integrating multiscale resonator array either in planar or vertical integration techniques.

One way to increase the bandwidth is using the so-called *dispersive control MMs* that manipulate the dispersive behavior as presented in [41]-[42]. Ye et al. exploited in [41] the resonances of four Split Ring Resonators (SRRs [43]) and four resistances, one in each corner of each SRR, as depicted in Figure 18(a). Different resistance values were used to obtain a flat behavior in the frequency band between 1 GHz and 2 GHz (L-band). Figure 18(b) illustrates how the dispersive control is handled with different configurations of resistance values used to retrieve the condition at which the effective permittivity matches the effective permeability. Nearly perfect absorption is obtained for the L-band (FB = 0.67) as shown in Figure 18(c), where $\varepsilon_{r,eff}$ matches $\mu_{r,eff}$. The main drawbacks are the complexity in fabricating the structure, and the absorber is fragile. Moreover, the integration of external discrete components such as resistors could be tricky for applications in harsh environment.

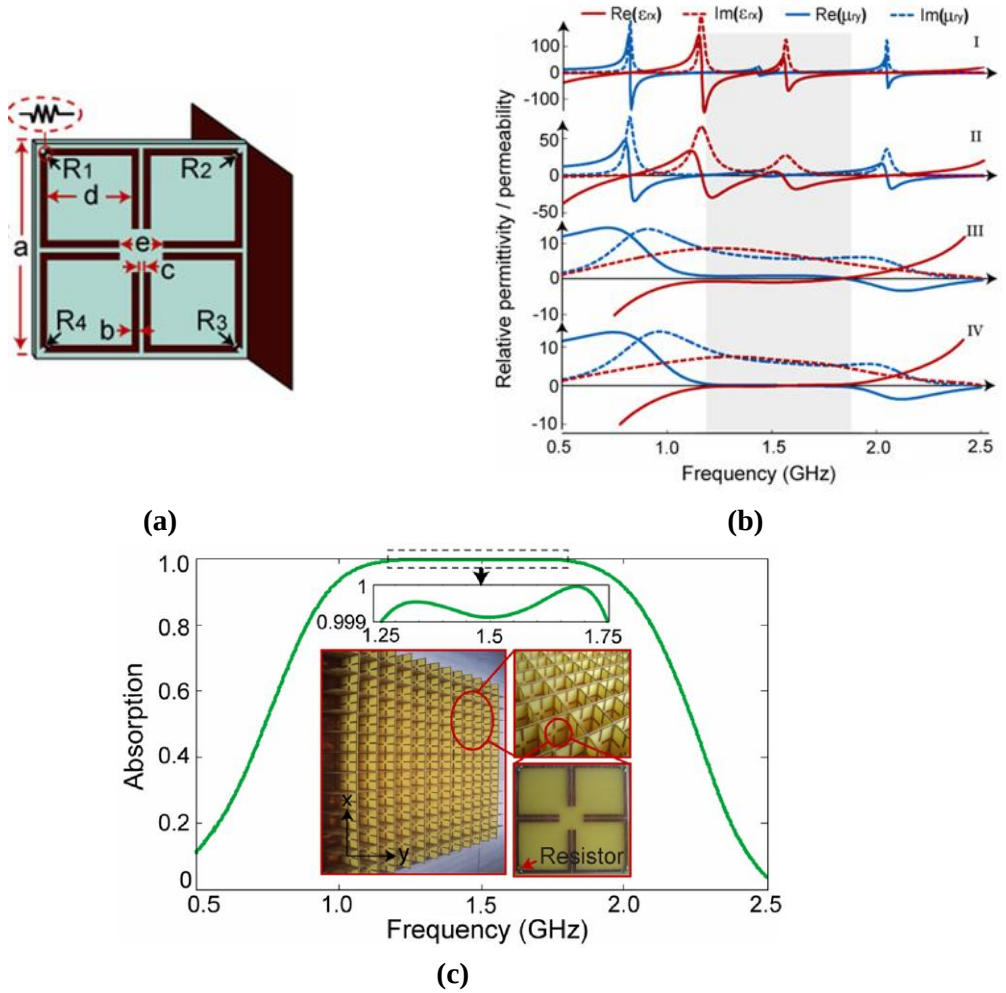

Figure 18. (a) Design of the unit cell of the absorber, (b) values of the effective permittivity and permeability considering: (I) four resistances at 1Ω, (II) four resistances at 10Ω, and (III) four resistances at 100Ω. (IV) Optimized resistance values of 203Ω, 122Ω, 39Ω, and 63Ω for R_1, R_2, R_3, and R_4 respectively. (c) Absorption level of the metamaterial over the frequency range 0.5 GHz – 2.5 GHz. In the inset, the manufactured MMA is presented [41].

Another way published in the literature to broaden the absorption bandwidth is to exploit various resonant elements in the same transverse plane [44]-[48]. Yahiaoui and Ouslimani

implemented a MIM patch structure, adding an etched cut wire to generate two absorption peaks [49]. The $\lambda_0/20$-thick absorber is polarization-insensitive up to oblique incidences of 75°. An absorptivity above 80% is shown for the frequency range from 7.4 GHz to about 10.4 GHz (FB = 0.34), which remains stable up to incident angles of 30°. At last, using the same concepts, Beeharry et al. demonstrated that a U-shaped resonator with a thickness of $\lambda_0/13$ offers a simulated absorption bandwidth from 5.6 GHz to 9.1 GHz (FB = 0.48) thanks to three broad resonances [50]. However, the MMA has an aborbance above 90% up to incidence angles of 20°, the absorptivity drops above this angle.

1.2.4.2 Salisbury metamaterial absorber

The conventional Salisbury screen was already introduced in paragraph 1.2.3.2. Hereafter, we present two designs that enhance the absorption bandwidth of such structures by exploiting the metamaterial technology [51]-[52].

The resonance condition of the Salisbury screen depends on the dielectric substrate thickness *l*, as depicted in Figure 19(a) that was published in 2017 [51]. To achieve unitary absorptivity, one has to satisfy the phase shift condition in (1.13):

$$\frac{4\pi f l}{c} + \psi = 2\pi \tag{1.13}$$

where *f* is the resonant frequency, *l* is the distance between the ground layer and the resistive sheet, *c* is the speed of light, and ψ is the phase shift introduced by the backside mirror-like layer (equal to180° for a metal plate). This condition is satisfied only for one frequency *f* with a given ψ. However, by changing ψ, one can satisfy (1.13) for different frequencies as suggested in [51], and thus achieve 85% of absorptivity over a wide frequency range between 6 and 30 GHz (FB = 1.33). In this paper, Whou et al. used a metasurface that replaces the ground plane and thus allowed for different phase reflections ψ, as depicted in Figure 19(b). In Figure 19(c), the Metamaterial Salisbury Screen (MSS) composed of the elements in Figure 19(d) is presented, while Figure 19(e) shows the comparison between the MSS and a Conventional Salisbury Screen (CSS). The great advantage of using such a metamaterial-inspired backside layer is the significant increase of absorption bandwidth, while the main drawback is that this structure does not allow reducing the thickness of the overall structure.

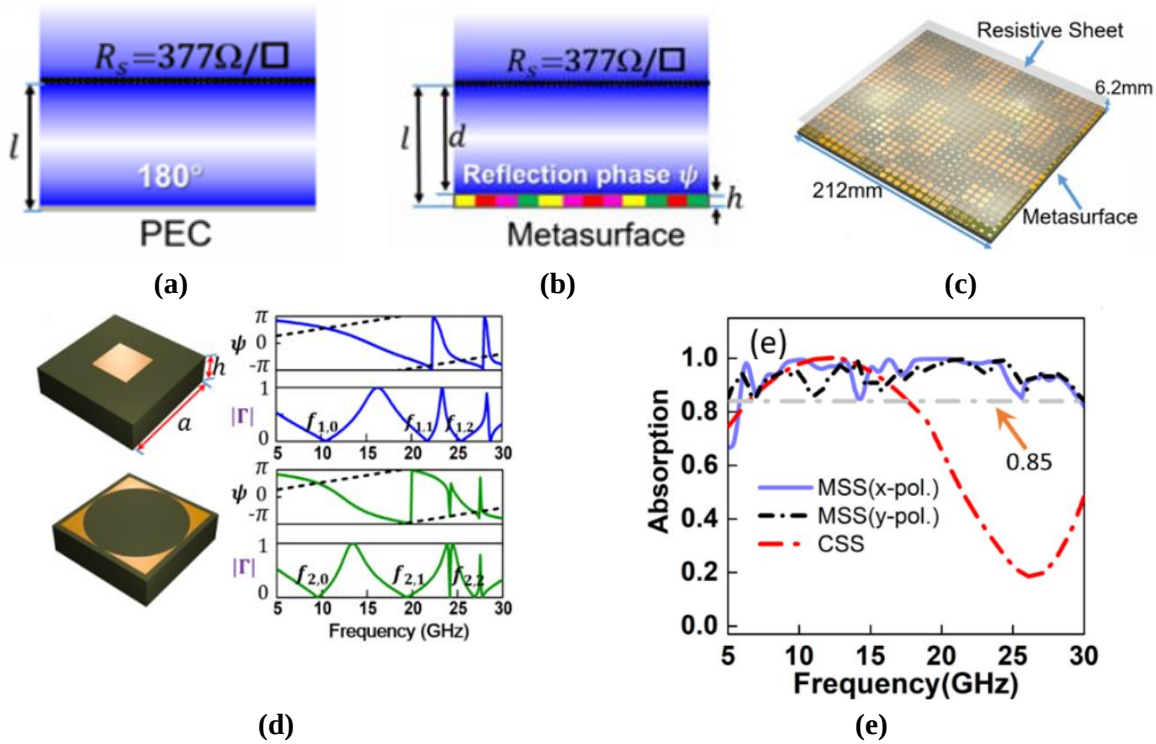

Figure 19. (a) Schematic of a Conventional Salisbury screen (CSS), (b) schematic of a Metamaterial Salisbury screen (MSS), (c) design of the metamaterial Salisbury screen and, (d) designs of two of the four particles that compose the metasurface layer with the phase shift and the reflection coefficient introduced. (e) Comparison of the frequency dependence of the absorbance under normal incidence between the MSS in vertical polarization (in blue solid line) and horizontal polarization (in black dashed line) and Classic Salisbury Screen (CSS) (in red dashed line) [51].

In the second publication [52], a frequency selective surface was sandwiched between the resistive sheet of R_s = 377 Ω/□ and a metallic plate. In this configuration, the authors exploited the so-called miniaturization technique [53]-[56] of the resistive screen, obtaining -10 dB of reflectivity (90% of absorptivity) for 5.4 - 18.0 GHz (FB = 1.07). This technique exploits long metal path patterns, which allows the resonance of low frequencies and their absorbance with quite small unit cells [57].

1.2.4.3 Pyramidal metamaterial absorber

Pyramidal metamaterial absorbers exploit the superposition of MIM structures described in paragraph 1.2.4.1 to increase the fractional bandwidth. The superposition of MIM absorber forms hyperbolic MMs, which have a hyperbolic dispersion relation [58]- [59].

In 2012, a V-grooved hyperbolic metamaterial absorber, with a total thickness of 1.02 μm, operates in the optical regime composed of 20 gold layers (conductor) and 20 germanium layers (dielectric), stacked along the z-direction, as depicted in Figure 20(a), was studied by Fang et al. for optical frequencies [60]. In this key publication, it was numerically demonstrated that a plane wave under normal incidence and hence with a wave vector along the –z-direction is trapped and absorbed in the layer whose transverse dimensions correspond to half of the wavelength of the impinging wave (resonance condition). Because each pair of layers is responsible for the absorption at a specific frequency, an increase in the absorption bandwidth is obtained by stacking multiple pairs of layers of different sizes, according to the aforementioned resonant condition. In Figure 20(b), we report the absorption spectra taken from this publication that was calculated by full-wave analysis and by assuming an equivalent homogeneous *anisotropic* metamaterial slab with the parallel and

perpendicular permittivity tensor elements ($\varepsilon_{//}$ *and* $\varepsilon_{\perp}$ in inset of this figure). A wide broadband with absorption above 80% ranging from 3 to 6 μm can be noticed in Figure 20(b), while in Figure 20(c), the results for different incident angles from 0° (normal incidence) to 85° with the red line corresponding to an absorption of 90% are presented.

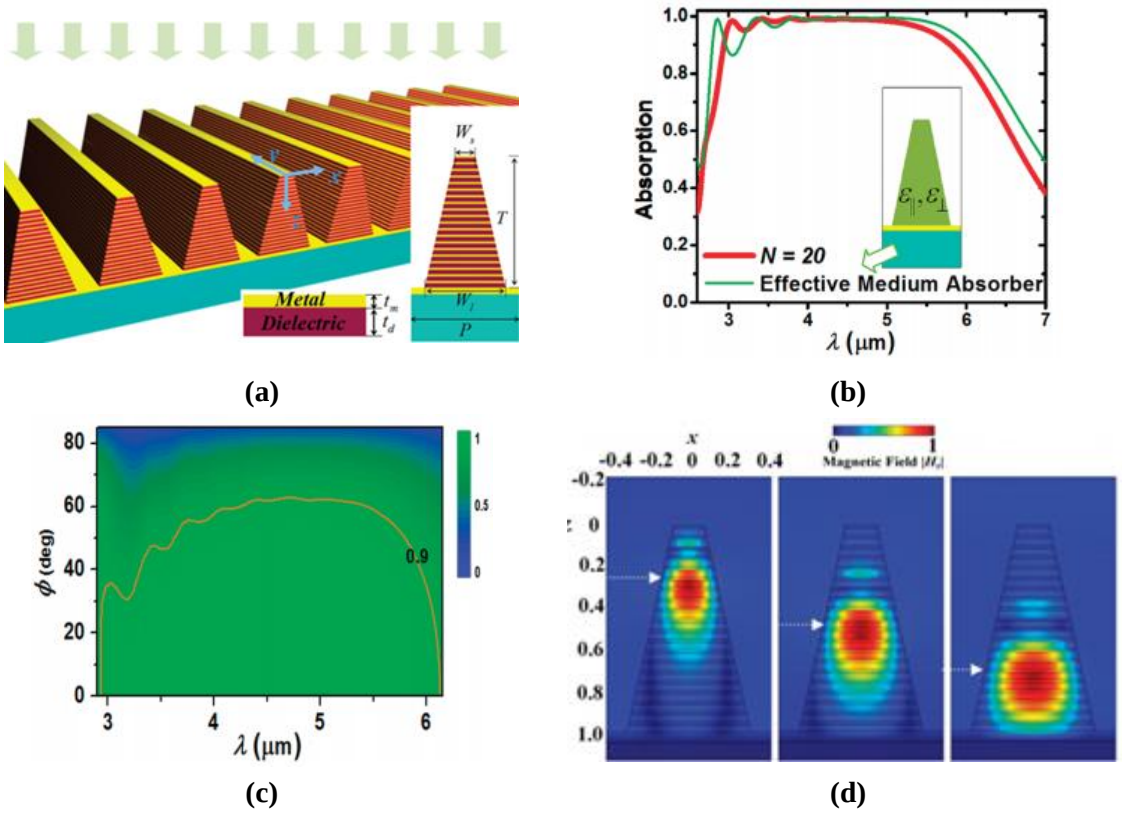

Figure 20. Pyramidal metamaterial absorber: (a) designed structure composed of metal layers (in yellow) and dielectric layers (in violet), (b) absorption comparison between full-wave simulation and anisotropic effective medium approximation, (c) absorption spectra for different incident angles and, (d) magnetic field maps at λ_0 = 3.5 μm, λ_0 = 4.5 μm, and λ_0 = 5.5 μm (left, center and right respectively) [60].

Similar pyramidal-shaped structures can be scaled for operating at microwave range with a proper choice of the bilayered materials and dimensions. From the simulation side, it can be shown that while for the optical frequency, the resonance mechanisms occur in multiple layers as can be noted in Figure 20(d), at microwaves, the field is mainly confined within one pair of dielectric and metallic layers[4]. The best way to study this relatively strict confinement seems to be the cavity model [61]. From the technological side, He et al. proposed in 2012 a pyramidal metamaterial absorber operating between 8 and 14 GHz [62]. The periodic array consists of unit cells, each composed of the stacking of 20 metallic square layers of copper (with $\sigma = 5 \times 10^7$ S/m) and 20 dielectric layers of FR4 ($\varepsilon'_r = 4.4$ and tgδ = 0.02) as shown in Figure 21(a). In Figure 21(b), one can observe on the simulation curve (in blue) around 20 absorbed peaks corresponding to 20 resonance frequencies from 20 pairs of metal-dielectric layers. The experimental result confirms an absorptivity above 90% for 7.8 - 14.7 GHz (FB = 0.61). The magnetic field maps calculated for four distinct frequencies are shown in Figure 21(c). This structure will be further analyzed in Chapter 2.

[4] At microwave frequency the metal can be considered as a good conductor (i.e. copper at 1 GHz has a skin depth δ of 2.06 μm so that the EM field cannot penetrate through the metal layer with thickness of few tens of microns).

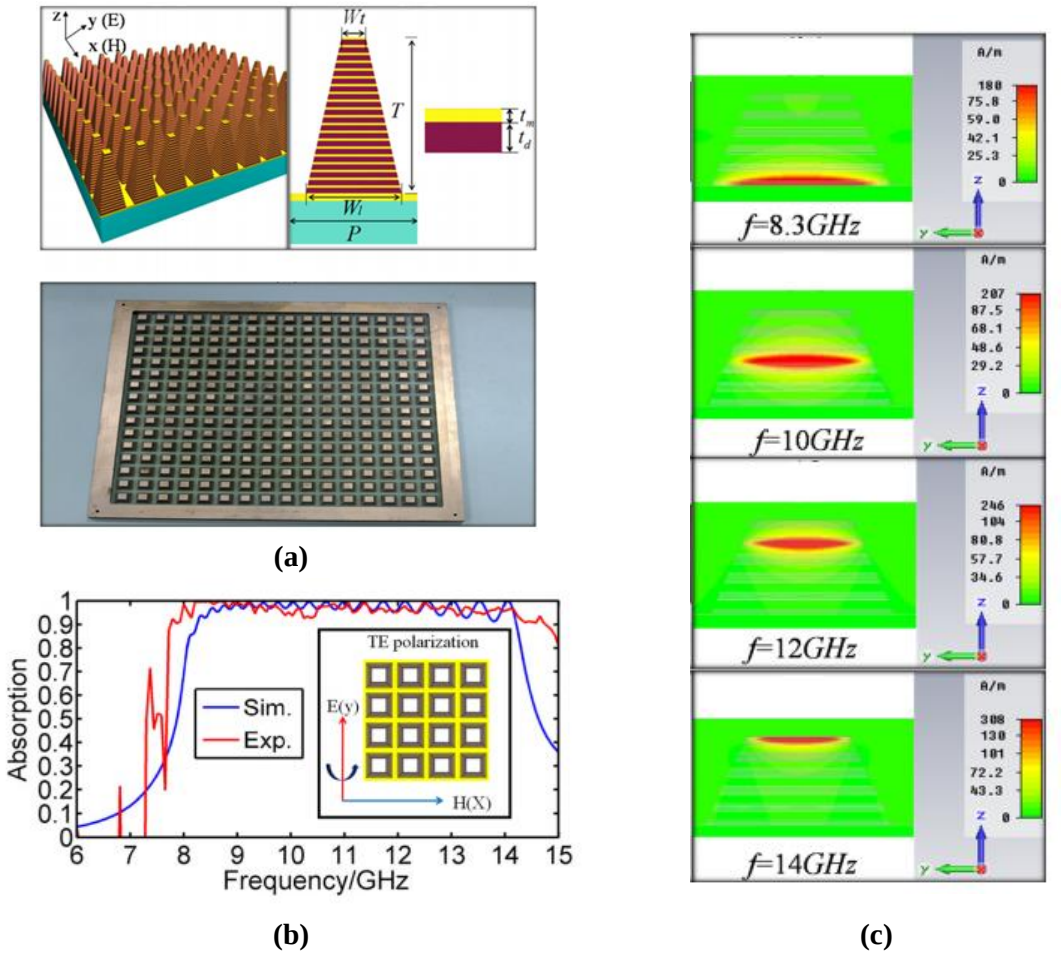

Figure 21. Pyramidal metamaterial absorber at microwave: (a) top: design of the structure composed of 20 metallic layers (in yellow) and 20 dielectric layers (in violet), bottom: fabricated structure in printed circuit board (PCB) technology, (b) comparison of the absorption for normal incidence between the simulation (in blue) and the measurements (in red) and, (c) magnetic field maps at 8.3 GHz, 10 GHz, 12 GHz, and 14 GHz [62].

At last, to further increase the bandwidth, it is possible to combine vertical and horizontal multi-resonance effects as exploited in [63]-[64]. In [64], two different pyramidal metamaterial absorbers were integrated into the same array. By this means, it demonstrated an enhancement of the bandwidth extending from 2.3 GHz to 40 GHz (FB = 1.78) at the expense of some frequencies that do not have an absorptivity above 90%. In [65], an absorptivity above 90% in the frequency range of 7 – 21.5 GHz (FB = 1.02) was achieved by exploiting 4 different-sized Cu-FR4 pyramids in a single unit cell.

While the increase of the fractional bandwidth is evident when exploiting such concepts, two drawbacks in connection with the PCB fabrication technique can be pointed out, which severely limit the use of such technology in practice. The first issue is related to the multi-stack structure machining required for the challenging fabrication of pyramidal shape structures. The second is the limited number of constitutive materials available in PCB technology. In Chapter 2, these two issues are further commented with some proposals for solving these difficulties via FDM technology.

As a last comment about the material issue, one can find other types of metamaterial in the literature as described in the general overview published by the Padilla and Tretyakov groups [66] and [67].

1.2.5 3D Printing Absorbers

Most of the structures illustrated in the previous sections were fabricated using PCB technology that is a 2D structuring technique by essence. Beyond the fabrication of planar structures, the complexity of using such a technique significantly increases when considering multilayer geometries with arbitrary thicknesses. This problem can be solved with the 3D printing technology that is one of the techniques in the context of the so-called additive manufacturing.

In the next section, we report three examples from the literature representing the current effort devoted to 3D printing technology. These studies are based on the 3D printing process and point out the advantages of additive manufacturing. In addition, it is worth mentioning that many studies are currently in progress for the development of new printable materials dedicated to microwave components such as high permittivity dielectrics [68]-[69], conductive filaments [70], and magnetic materials [71]. Several 3D-printed microwave components have been experimentally verified since the first 3D-printed absorber was patented in 2016 [72], making additive manufacturing a promising technology for the future generation of RF and microwave devices [73]-[80].

1.2.5.1 First 3D-printed absorber

One of the first implemented 3D-printed absorbers was reported in 2016 by Kronberger et al. [73]. It consists of a flat and thin Frequency Selective Surface (FSS) absorber operating at the X-band. The structure, which is fully 3D-printed with Brassfill filament ($\varepsilon'_r = 8.15$, $tg\delta_e = 0.015$, $\mu'_r = 1.25$, $tg\delta_m = 0.2$ at 10 GHz), is composed of a periodic array with circular etched slots above a Rohacell foam spacer ($\varepsilon'_r = 1.09$ and $tg\delta = 0.0038$ at 10 GHz), as illustrated in Figure 22(a), for a total thickness of 6.21 mm ($\approx\lambda_0/5$). The absorber was designed to exhibit a maximum absorption around 10 GHz (corresponding to a minimum reflection of about -28 dB with respect to the 0 dB reference at 9.95 GHz in the experiment), as it can be noticed in Figure 22(b).

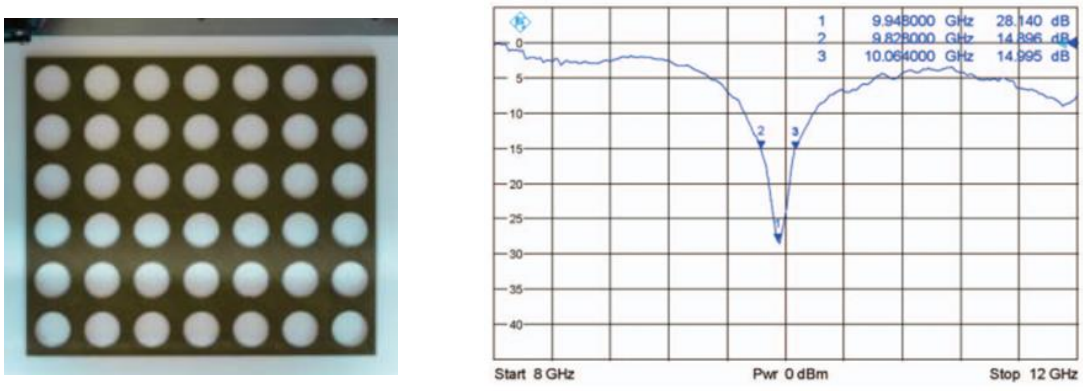

(a) **(b)**

Figure 22. (a) 3D-printed absorber manufactured with Brassfill filament, (b) Modulus of the reflectivity over the frequency for normal incidence [73].

1.2.5.2 3D-Printed impedance matching absorber

A Radar Absorbing Metamaterial composed of three Carbonyl Iron Powder (CIP) layers, printed with the Selective Laser Sintering (SLS) technique and placed above a metallic ground plane,

is presented in 2017 [74]. The schematic of this stair-like three-layered structure is reported in Figure 23(a), while the dispersion characteristics of the complex constitutive parameters over the 2-18 GHz frequency band are presented in Figure 23(b). A picture of the manufactured structure is shown in Figure 23(c); successful impedance matching was achieved with an intrinsic impedance of 360Ω, 190Ω, and 150Ω from the top layer to the bottom one. This gradual matching between the impedance of free space and the one of the metal plate allows a decrease of the reflectivity of more than 10 dB in the frequency range of 8 –18 GHz (FB = 0.77) as shown in Figure 23(d), for a total height of 2.89 mm.

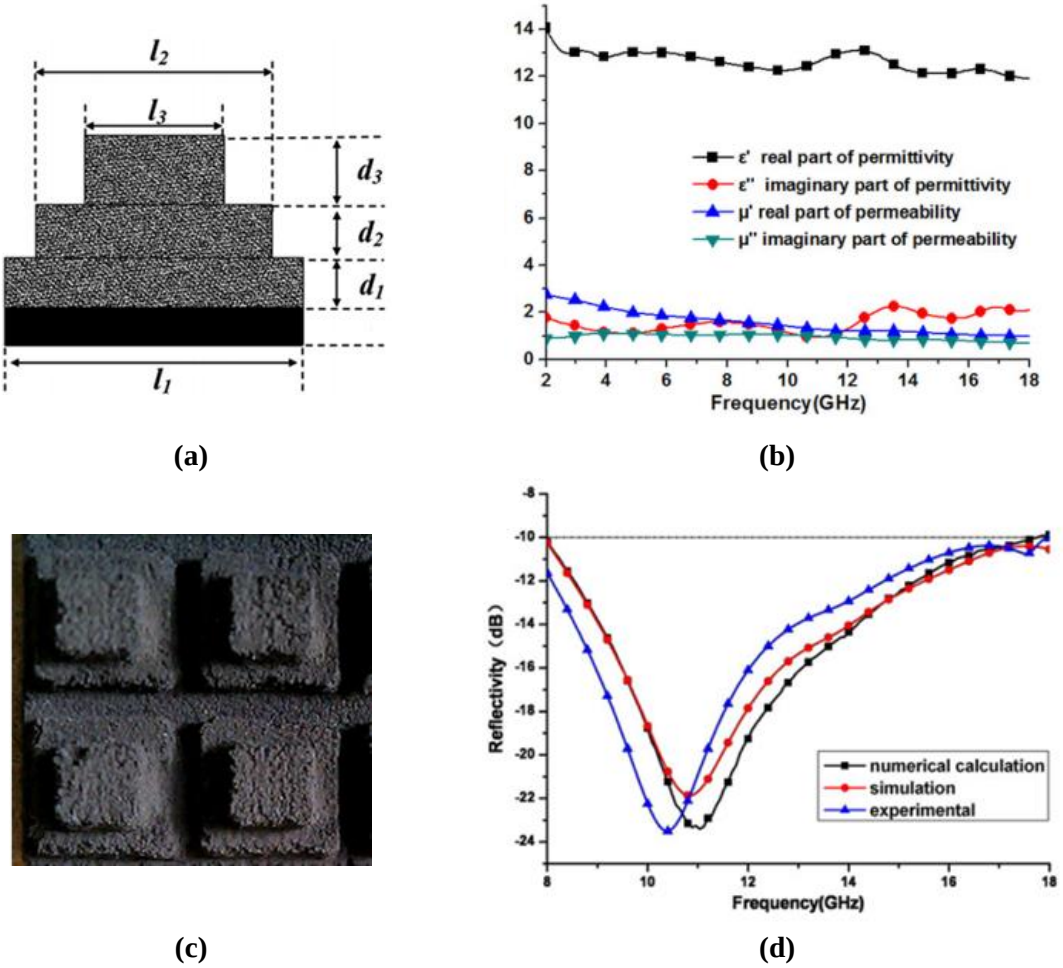

Figure 23. (a) Design of the multilayer structure printed with the Selective Laser Sintering (SLS) method, (b) constitutive parameters of the material, (c) fabricated structure and, (d) comparison between numerical calculation (in black), simulation (red), and measurement (blue) [74].

1.2.5.3 3D-printed honeycomb absorber

A structure composed of hexagonal honeycombs made of PLA (PolyActic Acid with ε'_r = 3.0 and tgδ = 0.01) illustrated in Figure 24(a) was published by Jiang et al. in 2018 [75]. This honeycomb-type absorber manufactured onto a ground plane combines resistive patches deposited on the hexagonal honeycomb walls, as seen in Figure 24(b), [75]. The structure was designed to operate in the 4-24 GHz frequency band for a total thickness of 16.1 mm. As seen from Figure 24(c), a reflectivity below -10 dB is observed in the wide frequency band of 3.5–24 GHz (FB = 1.49) under normal incidence that, however, show a high sensitivity to the polarization and to oblique incidences with degradation of the performance in terms of bandwidth for the TE mode.

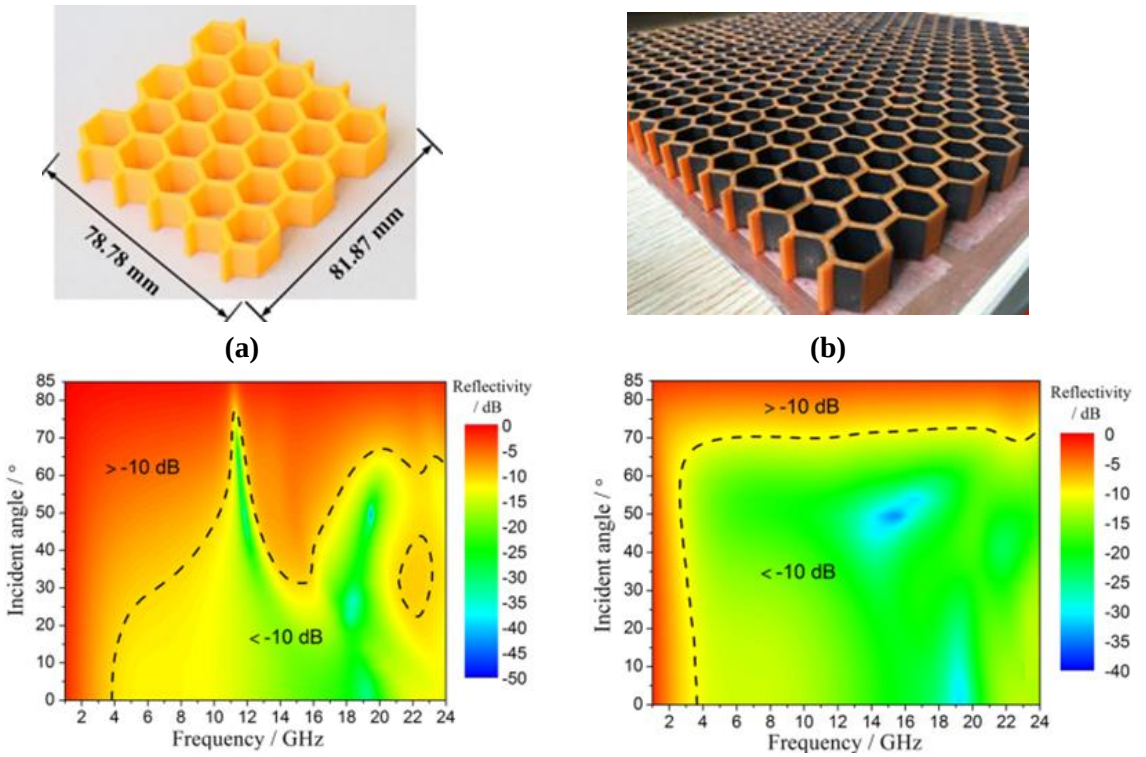

Figure 24. (a) Honeycomb 3D-printed structure made of PLA. (b) Complete structure with the addition of resistive sheets and (c) reflectivity for TE (left) and TM (right) modes for different incident angles [75].

To sum up, it can be concluded that the 3D-printed technology appears as a very promising route to implement unitary broadband absorbers, as demonstrated by these few examples. In the framework of this thesis, we exploit this innovative technology with particular attention to the achievement of ultra-broadband absorbers fabricated by using commercially available conductive and high permittivity filaments.

In conclusion, absorber characteristics in terms of compactness, operating frequency range, thickness and manufacturing process are shown in Table 1.

Table 1. Comparison between different works on metamaterial absorbers from 2010. The list is ordered by year of publication.

Reference	Bandwidth (GHz)	FB	Thickness (mm)	Technology	Year	Structure description
[25]	6.0 – 34.0	1.40	16.9 (1.12 λ_0)	PCB	2010	Layered capacitive absorber (5 dielectric layers)
[52]	5.4 – 18.0	1.08	9 (0.35 λ_0)	PCB Conductive paint	2011	1 FSS with resistive paints and 1 resistive layer (2 foam spacers)
[62]	7.8 – 14.7	0.61	5.05 (0.19 λ_0)	PCB	2012	20 pairs of tapered layers Cu-FR4
[41]	1.0 – 2.0	0.67	38.8 (0.19λ_0)	PCB and in house	2013	FR4 boards with 4 SRR-like metamaterials and 4 resistors
[63]	7.0 – 18.0	0.88	4.36 (0.18 λ_0)	PCB	2016	20 pairs of tapered layers Cu-FR4 with 2 different-sized pyramids in a unit cell
[65]	7.0 – 21.5	1.02	4.13 (0.20 λ_0)	PCB	2017	13 pairs of tapered layers Cu-FR4 with 4 different-sized pyramids in a unit cell
[57]	1.4 – 6.00	1.24	2.44 (0.03 λ_0)	PCB	2017	3 resistive sheets between 4 dielectric layers
[81]	2.64 – 40.0	1.75	5.5 (0.39 λ_0)	Milling	2017	Two-layer periodic stepped structure in conventional α Fe reinforced epoxy resin composite
[82]	2.8 – 16.8	1.43	15.0 (0.49 λ_0)	PCB	2018	Metallic fishbone structure inside distilled water substrate, assembled on a metal plane
[83]	3.7 – 17.5	1.30	11.5 (0.41 λ_0)	PCB	2018	Multilayer with dielectric layers, metasurfaces, and wide-angle impedance matching layers
[75]	3.5 – 24.0	1.49	16.0 (0.73 λ_0)	3D printing	2018	3D-printed hexagonal honeycomb in PLA with resistive patches attached on its walls, assembled on a copper plate
[76]	4.0 – 12.0	1.00	10.0 (0.27 λ_0)	3D printing	2018	Dielectric resonator in carbon-loaded ABS, assembled on a copper plate
[78]	5.6 – 24.2	1.25	6.00 (0.30 λ_0)	3D printing	2018	Cylindrical-water-based resonator, assembled on a copper plate
[84]	2.0 – 40.0	1.81	15.05 (1.05 λ_0)	In house	2019	Structural absorber by self-assembled reduced graphene oxide / polypropylene fabrics
[85]	7.74 – 23.56	1.01	12.08 (0.67 λ_0)	3D printing	2019	Water-based and ground-free resonator
[86]	2.20 – 9.50	1.25	4.00 (0.08 λ_0)	PCB and steel mold	2020	Multilayer absorber composed of metamaterial and magnetic coating
[87]	3.21 – 14.35	1.27	9.02 (0.26 λ_0)	In house	2021	Multilayer metamaterial with 2 dielectric and 3 resistive (conductive ink) layers

1.3 Conclusion

In this chapter, we presented the general principles that have to be satisfied to absorb totally an electromagnetic wave by emphasizing the importance of impedance matching. The underlying physical absorption mechanisms were firstly discussed based on the Poynting theorem by pointed out that the losses can be associated with the conductivity and/or to the dielectric and magnetic losses described by the imaginary parts of the complex-valued permittivity and permeability. The most common figure of merit that is used in this dissertation to qualify the performance of a given EM

absorber notably in terms of operation band was then presented. In a third stage, an overview of the literature on EM absorbers was presented by paying attention to the key papers related to the absorbing screen technology, in particular the so-called Dallenbach, Salisbury and Jauman. Such conventional technologies imply a dielectric thickness $d = \frac{\lambda}{4}$-condition that could be tricky to satisfy for low-profile absorbers operating in the low-frequency band of the microwave spectrum. To alleviate this problem, we then reported on the possibility of integrating Frequency Selective Surface (FSS) in the generic grounded dielectric scheme. It was shown that such FSS-based structures allow the cancellation of the reactive element of the surface impedance and the achievement of a resistive part equal to the free space characteristic impedance for a dielectric thickness lower than quarter-wavelength. At last, we considered the so-called metamaterial technology by reporting on the seminal papers published in the literature on Perfect Metamaterial Absorbers (PMAs) that operate with thickness much less than a wavelength. At the end of this chapter, we also introduced some key examples of full-absorbing structures reported in the literature that were manufactured by 3D-printed technology. Such additive fabrication techniques, particularly the Fused Deposition Modeling (FDM), were used in the framework of this thesis to fabricate the prototypes designed by full-wave simulation and constitute one of the originalities of the studies reported in the present work.

Chapter 2: 3D-printed multilayer metamaterial for wideband absorbers

This chapter provides an overview of the MIM absorber's operation, which serves as the basis for designing multilayer metamaterial absorbers. Following this, the complex reflection coefficient is defined in terms of the absorptive and radiative quality factors, allowing the introduction of the so-called critical coupling condition required for unitary absorption. When considering a stack of cavities, it is demonstrated how difficult it is to recover this condition. However, the significant advantage of a multilayer and multi-material absorber in terms of wideband absorption is demonstrated using a PCB absorber as an example. The advantages and disadvantages of the structure are discussed. These disadvantages can be overcome by utilizing 3D printing technology, which on the one hand simplifies significantly the fabrication of multilayer and multi-material pyramidal structures, and on the other hand allows using lossy materials (conductor with low conductivity in particular) leading to low quality factor and thus increasing the absorbed peak's bandwidth. Then, we present the characterization of a 3D-printed absorber operating in the X and Ku bands with an absorption level above 90%.

2.1 Design of a single MIM and theory of the complex reflection coefficient

Although the Metal-Insulator-Metal (MIM) absorber was briefly discussed in the first chapter, this paragraph provides a detailed analysis of its scattering properties with the goal of designing multilayered metamaterial absorbers. We begin with the simulation results of a metamaterial MIM structure composed of several periods, as shown in Figure 25(a), with the schematic cross-section of a single unit cell presented in Figure 25(b).

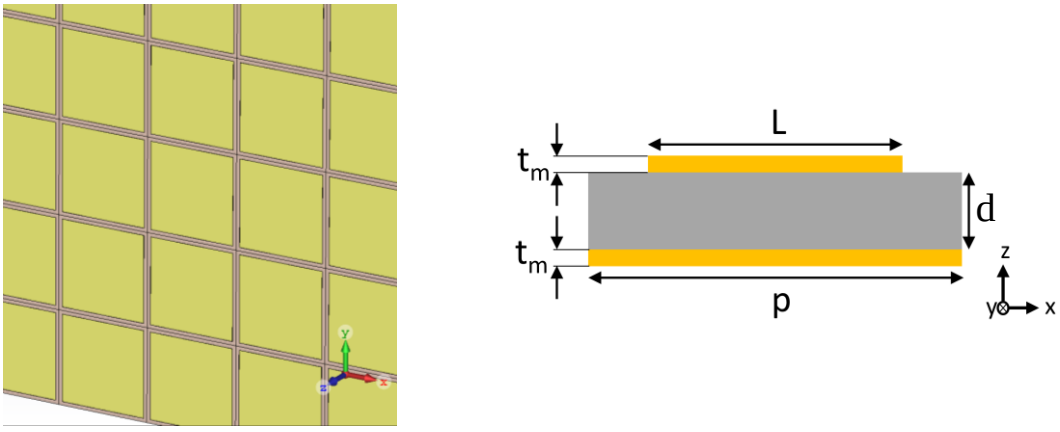

(a) **(b)**

Figure 25. (a) Metamaterial MIM absorber composed of several periods, and (b) schematic cross-section of a MIM unit cell composed of a copper (in yellow) ground plane, a dielectric (in grey) FR4 spacer, and a square copper patch on top.

The ground plane of dimension *p* corresponds to the period of the square-lattice array. A dielectric layer of the same size *p* is placed between the ground plane and a square metal patch with width *L* on top. Table 2 includes the list of the dimensions that are considered for a dense basic cell

array ($p \approx L$) that can be considered as a metasurface with $d << L$. The dielectric is FR4 ($\varepsilon_r = 4.4$; $tg\delta = 0.02$), whereas the metallic layers are made of copper ($\sigma = 5 \times 10^7$ S/m).

Table 2. Dimensions of the MIM metamaterial absorber in Figure 25.

	L	**p**	**d**	**t_m**
Dimension (mm)	15.0	16.3	0.3	0.02

The simulations are performed with CST Microwave Studio 2019 by considering the unit cell with periodic boundary conditions. Equation (1.3), described by the scattering parameter S_{11}, is used to compute the absorbance.

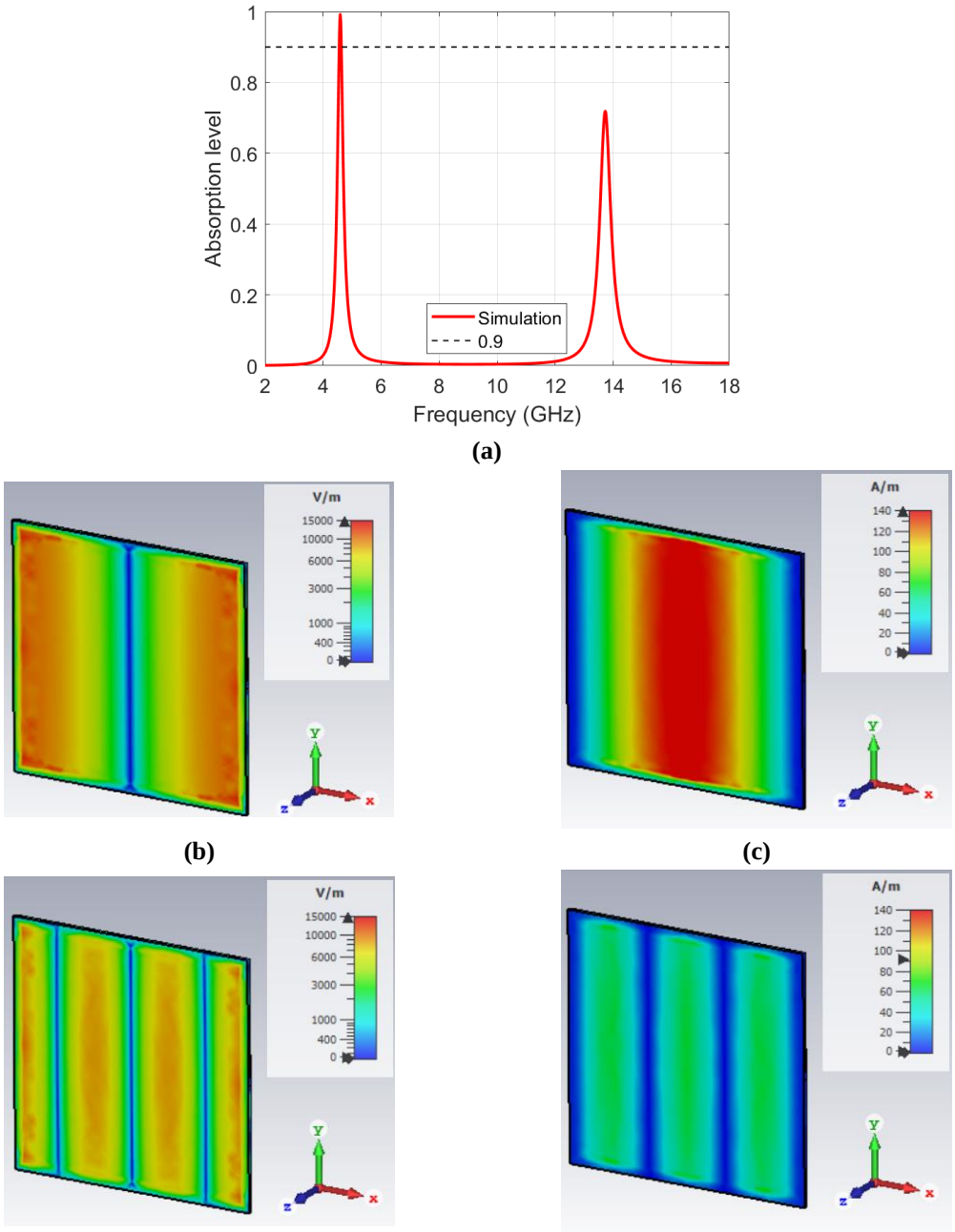

*Figure 26. (a) Frequency dependence of the absorbance under normal incidence. Electric field (**E**) and magnetic field (**H**) magnitudes. (b) **E** and (c) **H** at 4.62 GHz and (d) **E** and (e) **H** at 13.8 GHz. For all plots, the **E**-field is along the x-direction.*

Figure 26(a) shows the absorbance spectra with two peaks at 4.62 GHz and 13.8 GHz with 99% and 72% absorption. The impedance matching condition presented in Chapter 1 can be used to further interpret these simulation results in terms of characteristic impedance Z_c and scattering parameters as follows [88]:

$$Z_c = Z_0\sqrt{\frac{\mu_r}{\varepsilon_r}} = Z_0\sqrt{\frac{(1+S_{11})^2-(S_{21})^2}{(1-S_{11})^2-(S_{21})^2}} \tag{2.1}$$

due to the presence of the ground plane, S_{21} is 0, and thus from (2.1) Z_c is derived through (2.2):

$$Z_c = Z_0\frac{1+S_{11}}{1-S_{11}} \tag{2.2}$$

The characteristic impedance of the MIM structure is presented in Figure 27. The first peak at 4.62 GHz has a value of 316 Ω, close to 377 Ω (free space impedance), which satisfies the impedance matching condition with almost unitary absorptivity. The second peak at 13.8 GHz has a value of 117 Ω, which differs from the free space one reducing the absorptivity. The imaginary parts are zero at both resonant frequencies.

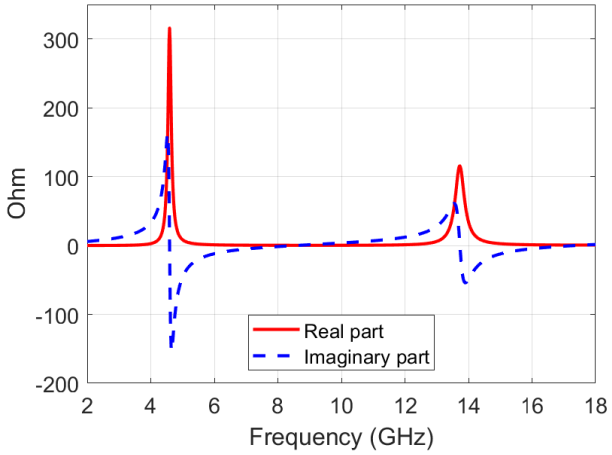

Figure 27. Characteristic impedance Z_c of the MIM structure computed with equation (2.2). The two peaks corresponds to the impedances at the two resonant frequencies. The first absorbed peak at 4.62 GHz almost matches free space, and quasi-unitary absorptivity is achieved. The second peak at 13.8 GHz has a reduced characteristic impedance that corresponds to a lower absorptivity.

After illustrating this initial example of a resonant metal-insulator-metal periodic array absorber, we now discuss the various approaches that can be used either from a physical point of view or with a resonant cavity antenna insight. For the first approach, we present a planar waveguide model stressing the standing wave mechanisms. The planar MIM absorber is composed of a square metallic patch with dimension *L* on the top layer, a ground metallic layer with period *p* on the bottom layer, and a dielectric spacer layer with thickness *d* and a relative permittivity ε_r, as depicted in Figure 28. Both metallic layers are thicker than their skin depth, preventing transmission of the EM field. Here we assume that the x, y, and z trihedron has its origin at the center of the rectangular patch.

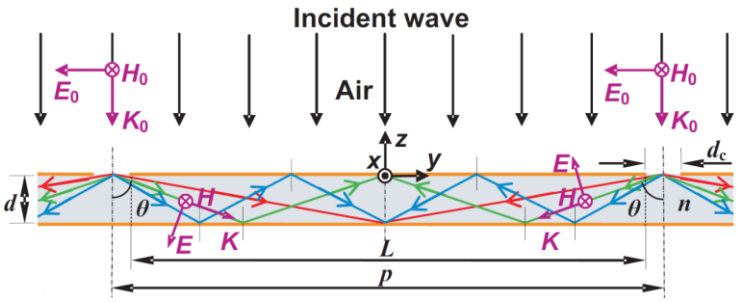

Figure 28. Ultrathin planar metamaterial absorber and the incident EM wave for a TM mode [89].

The incident **EM** plane wave travels in the air, with an electric field $\mathbf{E_0}$, oriented along the y-direction, a magnetic field $\mathbf{H_0}$ along the x-direction, and a wave vector $\mathbf{k_0}$ along the -z-direction is allowed entering into the spacer through the side holes [89]. The E-field is directed toward the absorber center with two waves traveling in opposite verses along y-direction that generate a standing wave. The waves bounce back and forth within the dielectric spacer layer with loss enhancement (absorption peaks) at the resonance frequencies. For how the trihedron is positioned, the node are always in the zero position, while the antinode are always at the patch edges. The equation of the standing wave formed by two opposing waves is given by (2.3)

$$E_{sw} = E_z^+ + E_z^- = -2\,jE\left(e^{-\alpha\left(\frac{L}{2}-|y|\right)-j\omega t}\right)\sin\left(\frac{2\pi\sqrt{\varepsilon_r}\,sin\theta}{\lambda_0}y\right) \qquad (2.3)$$

where E is the amplitude of the wave inside the cavity and α is the attenuation coefficient.

The nodes, with zero amplitude, are located at the points defined by equation (2.4a). The anti-nodes, which correspond to regions with the highest energy loss density, are found using (2.4b).

$$y = \pm m\frac{\lambda_0}{2\sqrt{\varepsilon_r}\,sin\theta} \qquad m = 0, 1, 2, \ldots \qquad (2.4a)$$

$$y = \pm(2m-1)\frac{\lambda_0}{4\sqrt{\varepsilon_r}\,sin\theta} \qquad m = 1, 2, 3, \ldots \qquad (2.4b)$$

Due to the symmetry of the geometry and the free boundaries conditions at the unit cell edges, the square patch center always has nodes, while the patch edges always have anti-nodes. As a result, when $y = L/2$, only the resonant standing wave modes listed below (2.5) exist:

$$f_{sw} = (2m-1)\frac{c}{2\sqrt{\varepsilon_r}\,L\,sin\theta} \qquad m = 1, 2, 3, \ldots \qquad (2.5a)$$

$$\lambda_{sw} = \frac{2\sqrt{\varepsilon_r}\,L\,sin\theta}{(2m-1)} \qquad m = 1, 2, 3, \ldots \qquad (2.5b)$$

Where f_{sw} is the frequency of the standing wave, λ_{sw} is the correspondent wavelength, and c is the speed of light.

In the metamaterial assumption ($\lambda >> d$), the higher-order metal-insulator-metal waveguide modes are evanescent, and only the fundamental waveguide mode is allowed to propagate along the waveguide; thus, we have $\sin\theta = 1$ ($\theta = 90°$), and (2.5) can be simplified in (2.6):

$$f_{sw} = (2m-1)\frac{c}{2\sqrt{\varepsilon_r}\,L} \qquad m = 1, 2, 3, \ldots \tag{2.6a}$$

$$\lambda_{sw} = \frac{2\sqrt{\varepsilon_r}\,L}{(2m-1)} \qquad m = 1, 2, 3, \ldots \tag{2.6b}$$

Equation (2.6) indicates that only the fundamental standing wave mode (m = 1) and its odd harmonic modes can exist, as depicted in Figure 29. The 1st and 3rd order modes correspond to the absorption peaks in the absorbance spectra reported in Figure 26(b, c) for the electric and magnetic field maps, for the fundamental mode at the frequency of 4.62 GHz, and in Figure 26(d, e) for the first odd mode m = 3, at the frequency of 13.8 GHz. One half-wavelength and three half-wavelengths are visible from these plots, in agreement with (2.6b).

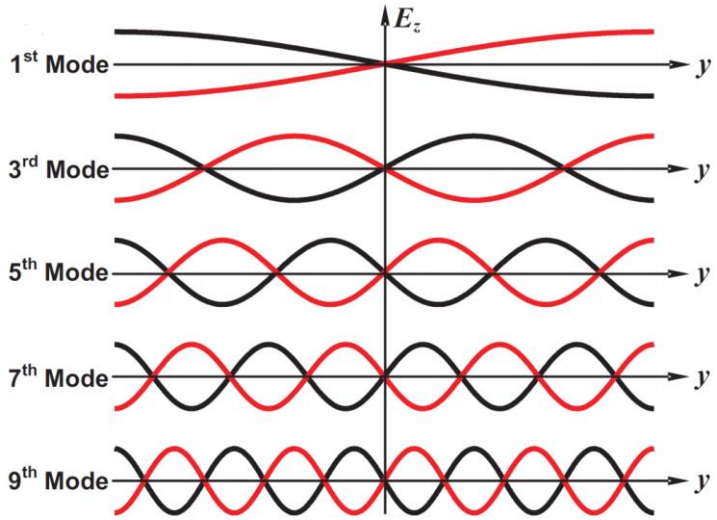

Figure 29. Normalized electric field of the fundamental mode and its odd harmonic modes at x = 0 and z = - d/2 in the case of strong diffraction effect calculated according to equation (2.3).

Targeting an absorption peak at the fundamental frequency f_1 and for a dielectric material permittivity ε_r, the dimension L of the top layer planar metallic structure can be determined using equation (2.7)

$$L = \frac{\lambda_1}{2\sqrt{\varepsilon_r}} = \frac{c}{2\,f_1\,\sqrt{\varepsilon_r}} \tag{2.7}$$

With λ_1 and f_1, the wavelength and the frequency of the first propagating and dominant mode TM_1.

This result is validated by cavity resonator theory as described in [2]. The resonant frequency of the cavity illustrated in Figure 30(a) is as follows:

$$f_{lmn} = \frac{c_0}{2\pi\sqrt{\varepsilon_r\mu_r}}\,k_{lmn}$$

with

$$k_{lmn} = \sqrt{\left(\frac{l\,\pi}{h}\right)^2 + \left(\frac{m\,\pi}{L}\right)^2 + \left(\frac{n\,\pi}{W}\right)^2} \tag{2.8}$$

Equation (2.8) can be written as (2.9) in terms of real part of the constitutive parameters

$$f_{lmn} = \frac{c_0}{2\sqrt{\varepsilon_r' \mu_r'}} \sqrt{\left(\frac{l}{h}\right)^2 + \left(\frac{m}{L}\right)^2 + \left(\frac{n}{W}\right)^2} \tag{2.9}$$

Where *l*, *m*, and *n* are the numbers of half-wavelengths along z, y, and x, respectively. In our case, the structure is a square, $W = L$, and we assume that the electric field of the incident wave is polarized in the y-direction. Under these assumptions, the dominant resonant frequency is denoted by (2.10)

$$f_{010} = \frac{c_0}{2\,L\sqrt{\varepsilon_r' \mu_r'}} \tag{2.10}$$

By inverting L in (2.10), the same relationship as in (2.7) can be found for a nonmagnetic material with μ_r equal to 1.

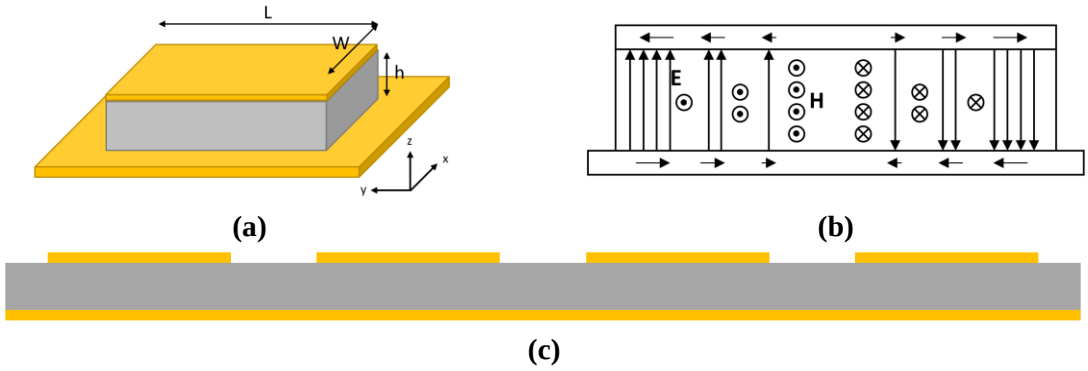

Figure 30. (a) Metal-Insulator-Metal rectangular cavity resonator. (b) E and H fields, and currents distribution inside the cavity resonator. (c) Schematic cross-section of an array composed of multiple patch unit cells. The yellow color corresponds to the metal, while the gray corresponds to the dielectric.

The last model to explain the electromagnetic behavior of a MIM metamaterial absorber is the antenna approach with a patch-like array, as depicted in Figure 30(c). It is demonstrated that such an array behaves like a subwavelength micro-resonators array, thereby justifying the term "metasurface". Considering the same operating conditions (plane wave impinging on the metasurface with normal incidence, and thus with the **k** vector normal to the metal layers), the incident **E** vector, polarized along the y-direction in this case, induces charges on the top metal plate, thereby acting like an elementary dipole antenna as depicted in Figure 30(b). Charges of opposite signs are also generated on the ground metal plate for ultra-thin dielectric substrates with h << L. In terms of equivalent circuit elements, the dielectric slab sandwiched between the two metal plates is analogous to a distributed capacitance in the transverse directions. The close coupling of the metallic layers, with locally opposite charges on the top and bottom plates, results in an electric quadrupole with charges at the edges of a parallel plate-type structure. The quadrupole moment explains the formation of a current loop with an antiparallel configuration of conduction currents on the metal plates and displacement currents within the dielectric layer. As a result, while the electric field is oriented out of the plane, the current loop induces an in-plane magnetic dipole. The coupling mechanism via magnetic and electric dipole interactions account for the electromagnetic field transition from a plane

wave propagating in free space in the normal direction to a surface wave propagating in the transverse directions.

After these various explanations of absorption mechanisms in MIM-type metasurface, we analyze hereafter the absorptivity following the energy conservation law in (1.3) in terms of the complex reflection coefficient Γ[5]. The complex reflection coefficient Γ can be expressed following the fundamental equation (2.11) as proposed in [90]:

$$\Gamma = \frac{{}^{2}/_{\tau_r}}{{}^{1}/_{\tau_a} + {}^{1}/_{\tau_r} - j\,(\omega - \omega_0)} - 1 \tag{2.11}$$

where τ_a and a τ_r are the lifetimes of the resonance due to the absorption inside the structure and to the radiation to the far-field, and ω and ω_0 are the angular frequency and the resonant angular frequency respectively. One can interpret τ_a as the characteristic time of the energy dissipation process strictly confined in a closed resonator and τ_r as the characteristic time of the radiative mechanisms that allow the EM wave to escape from the micro-resonator. If the resonant system is weakly coupled to its environment, the characteristic time τ_r is very long. In the limit $\tau_r \to \infty$ [6]and hence ${}^{1}/_{\tau_r} \to 0$ then $\Gamma = -1$. In that case, whatever the dissipation term and the operating frequency, one finds the characteristic unit modulus with a phase shift of π of the reflected wave on a uniform metalized plate.

Equation (2.11) can be written in terms of material properties by introducing the absorptive quality factor Q_a and the radiated quality factor Q_r, as expressed in (2.12). The quality factors are the ratio of the energy stored and the energy lost in the system. Q_a refers to the amount of energy lost owing to dissipation, while Q_r to the amount of energy exchanged with free space. For strict confinement in a closed dielectric resonator, this ratio does not depend on geometrical parameters (same volume for calculating the energy stored and dissipated). In that case, the Q factor is related to the material properties with $Q = (\tan\delta)^{-1}$.

$$Q_a = \frac{\omega_0\,\tau_a}{2} \tag{2.12a}$$

$$Q_r = \frac{\omega_0\,\tau_r}{2} \tag{2.12b}$$

We can then transform (2.11) into equation (2.13) as a function of the quality factors and the resonant angular frequency as in [91].

$$\Gamma = \frac{Q_a}{\frac{Q_a}{2} + \frac{Q_r}{2} - j\,Q_r Q_a \left(\frac{f}{f_0} - 1\right)} - 1 \tag{2.13}$$

At the resonance $f = f_0$.

[5] We remind that a ground plane bound the structure so zero transmission is assured.

[6] For instance, closing the slots between patches so that metasurface is equivalent to a uniform metal plate.

$$\Gamma = \frac{Q_a}{\frac{Q_a}{2} + \frac{Q_r}{2}} - 1 \tag{2.14}$$

To have unitary absorptivity from (1.3), we need Γ = 0 that is true when $Q_a = Q_r$. This is the so-called *critical coupling condition* that corresponds to a unitary absorptivity of the incident electromagnetic wave. As shown in (2.14), satisfying the resonance condition is a necessary but not sufficient condition for zero reflection at the resonance frequency. In contrast, the so-called critical coupling condition ($Q_a = Q_r = Q$) guarantees zero reflection and then total absorption of the electromagnetic energy, as in (2.15).

$$\Gamma = \frac{Q}{\frac{2Q}{2}} - 1 = 0 \tag{2.15}$$

Concerning the phase of the reflection coefficient, we can derive other considerations. From the previous analysis, we learned that Γ is real at the resonance frequency with the following expression as a function of the quality factor (2.14). An intuitive way to decrease the reflection loss at this resonant frequency is to minimize the intrinsic absorption loss. With the assumption of dominant dielectric loss with for instance, a quality factor around 1000 (based on a loss tangent in the 10^{-3} range and hence with $Q_a >> Q_r$) one finds the limit value (2.16)

$$\Gamma = \frac{Q_a}{\frac{Q_a}{2}} - 1 = +1 \tag{2.16}$$

Therefore, Γ = +1 with a zero-phase shift between the incident and reflected wave.

Let us now consider the asymptotic cases in the lossless case ($Q_a \to \infty$). Starting again from the general expression of Γ as in (2.13) can be written as:

$$\Gamma_{wol} = \frac{\frac{1}{2} + jQ_r\left(\frac{f}{f_0} - 1\right)}{\frac{1}{2} - jQ_r\left(\frac{f}{f_0} - 1\right)} \tag{2.17}$$

where Γ_{wol} is the complex reflection coefficient without loss. From (2.17), one obtains the ratio between two complex conjugate numbers with a modulus equal to unity whatever the operating frequency.

Away from the resonance, when f → 0, (2.18) is obtained

$$\underbrace{\Gamma_{wol}}_{f \to 0} = \frac{\frac{1}{2} + jQ_r}{\frac{1}{2} - jQ_r} \tag{2.18}$$

and since we can write $\Gamma = |\Gamma| e^{j\varphi}$ and the phase is expressed in (2.19)

$$\underbrace{\varphi}_{f\to 0} = 2\arctan 2Q_r \tag{2.19a}$$

with large Q_r

$$\underbrace{\varphi}_{f\to 0} = +2 \text{ x } \frac{\pi}{2} = +\pi \tag{2.19b}$$

Away from the resonance, when f → ∞, the obtained phase is described in (2.20).

$$\underbrace{\varphi}_{f\to \infty} = -2\arctan 2Q_r \tag{2.20a}$$

with large Q_r

$$\underbrace{\varphi}_{f\to \infty} = -2 \text{ x } \frac{\pi}{2} = -\pi \tag{2.20b}$$

This research demonstrates that by sweeping the frequency around the resonance frequency, the reflection coefficient phase may varied from +π to -π, or over 2π. The radiation quality factor Q_r dictates the steepness of this transition. In conclusion, the critical coupling condition is the point at which the quasi-constant dissipation quality factor determined by dielectric loss crosses the variable radiative quality factor determined by the dielectric thickness [92]. Additionally, this analytical analysis explains the parametric numerical results indicating that there is an optimal thickness for the dielectric layer aimed at perfect matching to free space and hence total absorption. This result enables the consideration of different thicknesses, as demonstrated in Chapter 3, where various thicknesses were used to increase the absorptivity of a metamaterial absorber

Despite the interesting approach of the quality factor, which is mandatory to study and to explain the absorptivity for structures less complex, we did not employ these quality factors to design our prototypes. Their relationships are straightforward to determine for a single MIM using either a circuit model, as in [93] or a parameter sweep as in [94] but are not trivial to find out for a stack of MIM. To our knowledge, there is no closed-form for this challenge in the literature.

For illustrating the difficulty associated with the extension of the design rules to multi-stacked layers, in Figure 31(a), we show the results of the absorption spectra calculated by full-wave analysis for stacked cavities in Figure 31(b). This study shows a quasi-unit absorbance level, which means that the critical coupling condition is satisfied, for ten resonant frequencies when ten cavities are stacked. However, when the number of cavities is reduced to one, the absorptivity reduces to 80%, which indicates that the critical coupling is no more fulfilled. The best option to calculate the absorptivity of a multilayer structure is then by full-wave simulations, which is what will be done from now on.

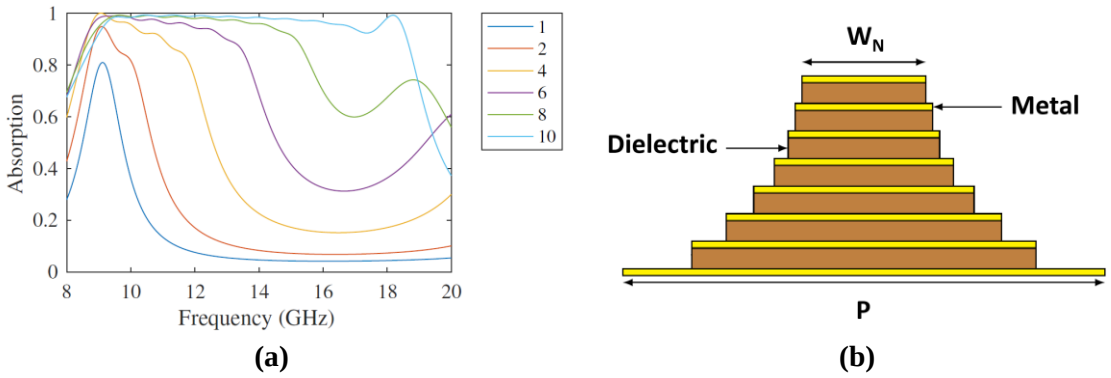

Figure 31. (a) Absorptivity results by increasing the number N of stacked cavities from bottom to top from 1. Widths are computed so that absorption peaks are at equidistant frequencies and cover 10 – 18 GHz when N = 10. (b) Simulated structure composed of N = 7 cavities.

2.2 From PCB to 3D printing metamaterial stair-like absorbers

As shown before single reflection-less Metal-Insulator-Metal (MIM) cavity traps the incident EM field within a thin lossy dielectric layer [95], but the structure is narrowband. Let us recall that one of the main goals of the present work is to design a broadband absorber. Planar and vertical integration of multi-resonator structures are the two strategies that can be used to increase the bandwidth of MIM structures, as discussed in the introduction chapter. The vertical integration employs a superposition of cavities with different resonance characteristics yielding multiple absorbance peaks. The dispersion characteristic of the EM wave that propagates within such a multilayered structure is hyperbolic, therefore, they are called hyperbolic metamaterials (HMM) [58]. In addition, the dielectric and metallic losses affect the resonance broadening and hence the overall absorbance window [96].

Let us remind that the HMM concept was firstly introduced in optics in 2012 using a sawtooth multilayered structure [60] whose fabrication was very challenging. The same year, Ding et al. applied the same idea to the RF domain by successfully manufacturing a quadrangular pyramidal-shaped absorber using Printed Circuit Board (PCB) technology. This structure exhibits an absorptivity above 0.9 throughout the frequency range 7.8 GHz – 14.7 GHz [62], trapping the incident energy in the stacked micro-resonators as a function of the dimension of the metal layer. In this publication, a physical interpretation of frequency selective dissipation is reported by considering the dispersion characteristic of multilayered metal-dielectric waveguides taking the transverse dimension as parameter. Such parametric study shows the possibility of modifying the fundamental propagating mode cut-off frequency with the transverse dimension variation. Below the cut-off frequencies, the EM wave dramatically slows down, explaining the EM wave localization effect and hence incident energy dissipation.

The structure for operating in the microwave range is depicted in Figure 21(a). The single unit element is composed of 20 pairs of metallic (copper, $\sigma = 5 \times 10^7$ S/m) and dielectric (FR4, $\varepsilon'_r = 4.4$; $tg\delta = 0.02$). Table 3 summarizes the geometrical parameters of this broadband structure manufactured by PCB technology published in [62].

Table 3. Parameters used for Ding structure [62].

Parameter	Values
Metallic thickness	t_m = 0.05 mm
Dielectric thickness	t_d = 0.15 mm
Period	P = 11 mm
Bottom width	w_l = 9 mm
Top width	w_t = 5 mm
Total thickness	T = 4.05 mm

Thales Research & Technology – France (TRT) investigated a similar structure in 2018 as part of an internship [97] with the important difference with respect to Ding et al. publication that the dielectric layers outside the pyramids were not etched. Another essential modification was also introduced in the metallization profile as shown in Figure 32(b) with the patch widths that are *not tapered linearly* from top to bottom with an illustration of the cross-section displayed in Figure 32(b). As for Ding structure, each unit cell consists of twenty pairs of metal and dielectric layers. The relevant dimensions are similar to those of the Ding et al. prototype with 0.035 mm-thick copper layer 0.2 mm-thick FR4 (assuming ε_r = 4.3, tanδ = 0.025) dielectric layers. The bottom and top patches have widths equal to 7.23 mm and 4 mm, respectively. The PCB-based structure has a total thickness of 4.7 mm. A photo of the fabricated 20 layers PCB-based absorber with overall dimensions 300 mm × 300 mm × 4.7 mm is shown in the inset of Figure 33.

Table 4. Parameters used for TRT structure.

Parameter	Values
Metallic thickness	t_m = 0.035 mm
Dielectric thickness	t_d = 0.2 mm
Bottom width	w_l = 7.23 mm
Top width	w_t = 4.7 mm
Total thickness	T = 4.7 mm

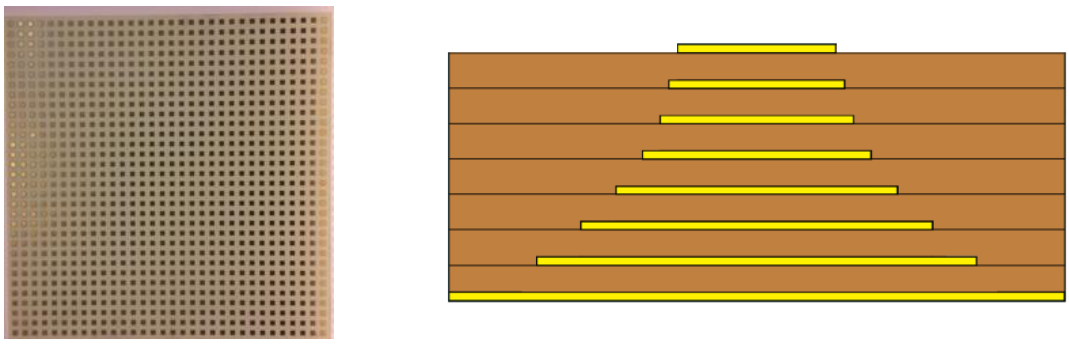

(a) **(b)**

Figure 32. (a) Front view of the 250 × 250 mm² MM absorber manufactured in PCB technology and (b) illustration of the metallization profile considering 8 copper layers (in yellow) and 7 FR4 layers (in brown) layers, for a total of 7 cavities.

One of the first step analyzed in the framework of the present work was the experimental assessment of the absorbance spectra under quasi-normal incidence carried out using a free space bistatic measurement setup, as illustrated in Figure 33(a). The Sample Under Test (SUT) was attached to a polystyrene slab. The reflectance spectra were measured for a bistatic test configuration

employing two high gain Satimo QR2000 antennas operating from 2 GHz to 18 GHz [98] at a distance of 125 cm from the prototype, which assures a Far Field (F. F.)[7] condition up to 12 GHz. It was estimated that the angle between the emission and detection directions for the S_{21} scattering parameter measurement was 4.5° and hence close to normal incidence conditions. Further details about bistatic measurements can be found in the chapter in the following sections devoted to measurements in non-anechoic (TRT setup) and anechoic chambers (IEMN setup).

A measurement of the S_{21} without sample ($S_{21}^{free\ space}$) and with a reference metal plate with the same transverse prototype dimensions (S_{21}^{metal}) were performed to extract the electromagnetic behavior of the sample free from the influence of the laboratory environment. It was observed that the difference between the reflection from free space and the metal plate is greater than 20 dB. This result confirms that the environment does not drastically affect the measurement. Therefore, the setup was considered a good approximation of free space conditions to carry out the characterization. Similar to equation (1.3), the absorbance of the metamaterial is calculated by (2.21a), where the reflection coefficient Γ^{SUT} is computed by (2.21b), as described in [99]:

$$A = 1 - |\Gamma^{SUT}|^2 \tag{2.21a}$$

with

$$\Gamma^{SUT} = \frac{S_{21}^{absorber} - S_{21}^{free\ space}}{S_{21}^{free\ space} - S_{21}^{metal}} \tag{2.21b}$$

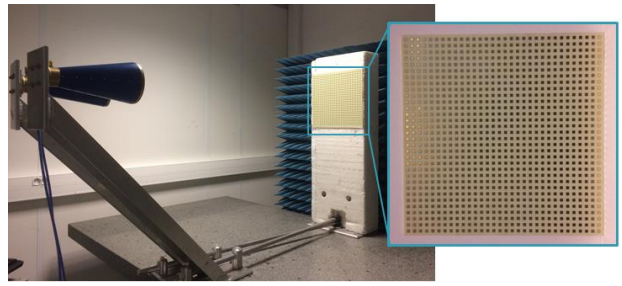

(a)

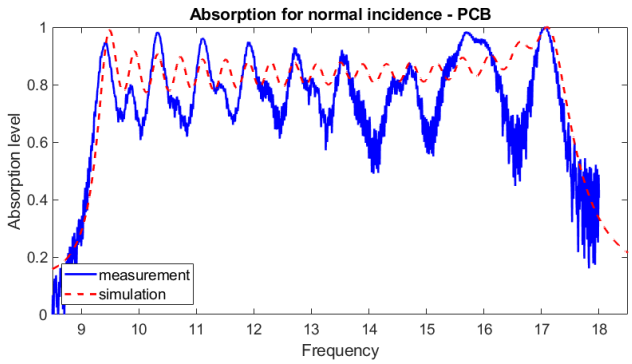

(b)

Figure 33. First characterization setup implemented during the thesis and (b) the absorptivity comparison for PCB-based absorber between the simulation (in red dashed line) and the characterization (in blue solid line), for normal incidence.

[7] The condition of F. F. is an approximation and we used the classical formula $R = 2D^2/\lambda$ [61] where R is the distance between the antenna and the sample under test, D is the aperture dimension of the antenna and λ is the free space wavelength.

The comparison between the simulation (performed in a previous TRT internship [97]) and the characterization of the TRT PCB-based absorber is presented in Figure 33(b), as presented in [100].

In agreement with the numerical assessment, the experimental spectra exhibit well-resolved multipeak feature equally spaced, particularly in the lower part of the absorption window. Concerning the peaks number, some discrepancies can be noted with some imbalance in the amplitude of various peaks. This discrepancy between measurement and simulation can be explained by applying the complex reflection coefficient theory outlined in a previous section, with in-phase and out-of-phase oscillators [101].

In conclusion, the results reported here devoted to metamaterial absorbers fabricated by PCB technology demonstrate the possibility of covering an ultra-broadband absorption window by overlapping a large number of *highly selective* resonance peaks. In addition, further improvement in the frequency distribution with equally spaced resonant frequencies can be foreseen by proper engineering of the tapered metal structure. Their manufacturing by PCB technology limits the degrees of freedom in their design due to technological constraints, notably the assembling by the adhesive of composite layers or milling in a top-down approach.

In the next section, the possibility of manufacturing these metamaterial structures using additive manufacturing is considered by stressing notably the differences that result from conductive filaments, with much lower conductivity with respect to copper layer values.

2.3 Square section metamaterial stair-like absorber for X-K_u bands

As introduced before, using a 2D-PCB technology could have some drawbacks, such as the difficulty of engineering the structure in the vertical axis, for instance, by changing the thickness of some cavities or fabricating a stair-like shaped structure defined by elemental planar surfaces. These drawbacks can be overcome with 3D printing technology by exploiting arbitrary geometries as well as tailor-made materials as presented in paragraph 1.2.5.

In this section, the stair-like (SL) pyramidal concept is further explained with the introduction of the losses of the conductive filament that increase the dissipated power, presenting the first demonstration of a RAM (Radar Absorbing Material) prototype fully fabricated in Fused Deposition Modeling (FDM) technology operating in the X and Ku-bands with 10 pairs of layers. The prototype was designed during a TRT internship [97]. The originality of the structure is to achieve high absorptivity by optimizing the patch width dimensions with equidistant absorbed frequencies as well as the manufacturing process.

For this model, the square-shaped unit cell of the periodic array, as described in Figure 34(a), aiming for a quasi-unitary absorption window between 10 GHz – 18 GHz, is exploited. The dielectric thickness was optimized by considering the printing technology constraints and the same dielectric thickness for all stacked micro-resonators. All the dielectric and metallic layers have the same thickness of 0.3 mm for an overall pyramid height of 6.3 mm considering the ground plane. The period of the unit cell size is 9.5 mm, the bottom and top layers measure 7.5 mm and 4.2 mm, respectively, as depicted in Figure 34(a).

Almost unitary absorptivity is obtained in simulation for normal incidence from 9.0 GHz to 18.7 GHz (FB = 0.70), as shown in Figure 34(c). Concerning estimating the bandwidth based on half-wavelength fit and of the micro-resonator side, some corrections resulting from fringing field effects have to be considered [61]. Moreover, the absorption bandwidth is calculated at 0.9, with the first peak around 9 GHz and the last around 18.2 GHz (around one octave).

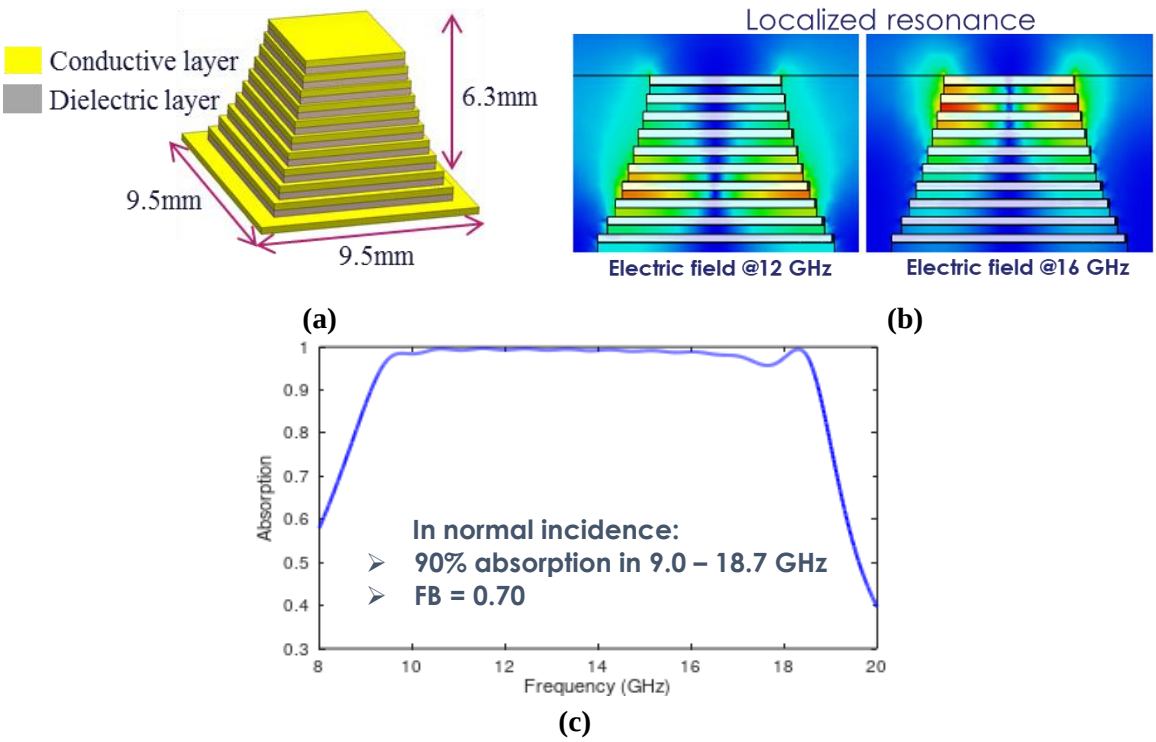

Figure 34. (a) unit cell design, (b) map of the electric field for 12 GHz and 16 GHz, and (c) the simulation of the absorptivity in normal incidence.

The design by numerical simulations has been performed using CST Microwave Studio 2018, with periodic boundary condition and Floquet modes as excitation ports. In Figure 34(b), the E-field maps at 12 GHz and 16 GHz were also reported in a vertical cross-section in the middle of the unit cell. From these E-field magnitude plots, we can deduce two fundamental points:

1. Fringing fields visible in yellow/green on the side wall of the structure are responsible for coupling the micro-resonator array to its environment and determining the so-called radiative quality factor.
2. For a distinct frequency, the resonance is not strictly localized in a single metal-dielectric-metal structure. One can note that EM energy is trapped mostly over two adjacent micro-resonators at 12 GHz and three at 16 GHz.

This short range delocalization effect, even though the metal thickness is 300 µm and hence much greater than the skin depth, explains in part the relatively flat absorption window pointed out in the simulation.

For the fabrication of the prototype, the FDM technique is used with commercially available filaments. For the dielectric layers, the filament Preperm DK400 with $\varepsilon_r = 4.0$ and $tg\delta = 0.004$ [69]. For the conductive layers, the filament is Electrifi [70] with $\sigma = 1.7 \times 10^4$ S/m measured with a 4-point probes measurement method [102].

The 250 mm × 250 mm structure with 26 × 26 pyramidal elements and a total thickness of 7.8 mm (6.3 mm for the printed structure and 1.5 mm for the support layer below the ground plane) is presented in Figure 35.

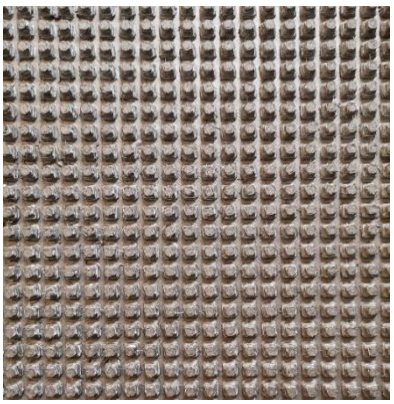

Figure 35. Picture of the 250 × 250 mm² prototype manufactured by additive manufacturing (FDM).

2.3.1 Characterization for normal incidence

The measurements were performed with the same setup displayed in Figure 33, and the absorbance is computed from equations (2.21a) and (2.21b). We remind that the spurious reflections due to the non-anechoic environment exhibit a difference over 20 dB between the response of the metallic reference plate (in blue) and without any sample (in orange) for normal incidence Figure 36(c) validating the experimental assessment in a non-anechoic chamber.

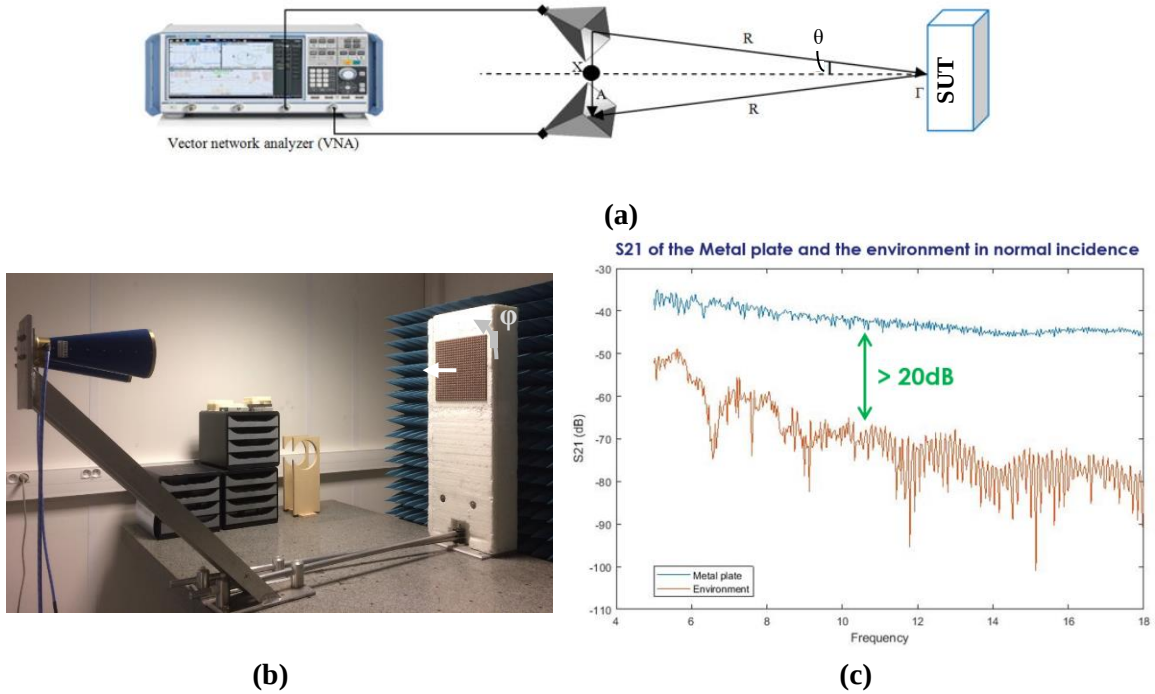

Figure 36. (a) Schematic of the characterization from [99], (b) the characterization setup with the angle φ, and (c) the S_{11} for a metallic plate (in blue) and the free space (in orange).

In Figure 37, the simulated absorption level versus frequency and measured performed at TRT for normal incidence are presented [103].

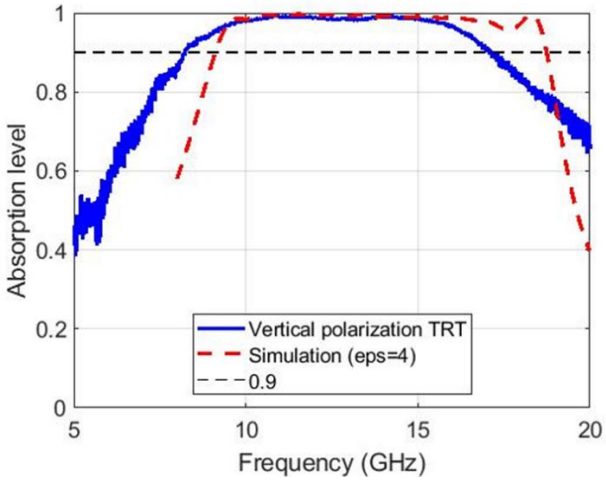

Figure 37. Comparison between simulation (in red dashed line) and measurement (in blue solid line).

A relatively flat band with an absorption level close to 100% can be noticed with a frequency shift toward high frequency. Three assumptions can be retained to account for this discrepancy:

1. Characterization errors
2. The difference in the layer widths between the fabricated and the designed structures
3. Different permittivity values of the dielectric layer

To check the measurement accuracy, a similar experiment was performed at Thales Defense Mission Systems (DMS)[8], this setup presented in Chapter 3 is compared with TRT results in Figure 38 for vertical polarization. This comparison shows a good agreement and thus validates the TRT characterization setup.

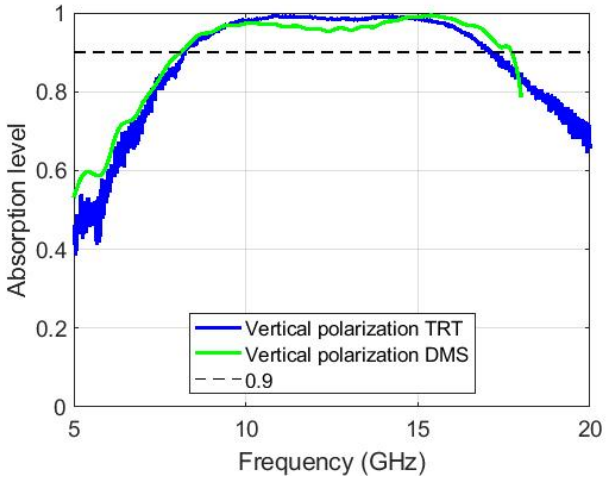

Figure 38. Comparison between measurement at TRT (in blue) and measurement at DMS (in green).

The second assumption concerns the difference in widths between the fabricated and the simulated multilayered structure. As shown in Figure 39, which displays the top and side views of six and one pyramid, respectively, many fabrication imperfections are presented. These imperfections are due to the different melting points between the two filaments, conductive and dielectric, composed of different bases. Electrifi is a PLA (Polyactic Acid) based polymer charged

[8] We would like to thank Isabelle Le Roy Naneix and Thierry Arreteau for these measurements at DMS.

with copper powders, while Preperm DK400 is an ABS (Acrylonitrile Butadiene Styrene) based thermoplastic charged with TiO_2 powders. For Electrifi, the melting point is 160°C, while for Preperm DK400 it is 230°C. This temperature variation impacts the quality of the printing notably by introducing some dispersion in the dimension of the staked micro-resonator and hence an additional distribution of the resonant frequencies for a nominal value.

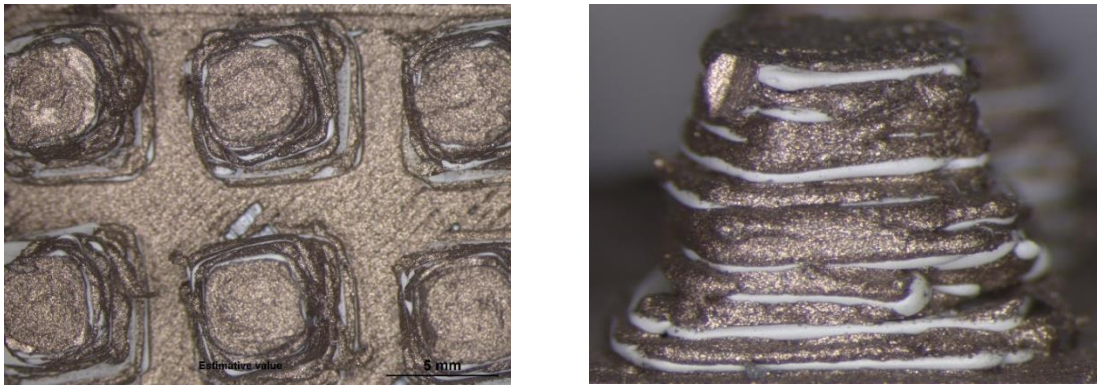

(a) **(b)**

Figure 39. (a) Top view for different pyramids and (b) front view of one of the pyramids.

To determine the layer widths, CT (Computed Tomography), described in A.1.3, was used to recreate a three-dimensional image of a small Sample Under Test (SUT) of 2 x 3 pyramids cut from a corner of the prototype as shown in Figure 40(a). Three orthogonal plane cuts of a single pyramid imaged by X-ray analysis are shown in Figure 40(b), where the top-left cut is for the second conductive layer, the bottom-left cut is for the right view and the top-right cut is for the front view. Holes are visible in the X-ray analysis, and the square geometrical shape is strongly degraded. Despite these manufacturing imperfections, which appear very important at the microscopic level, it is seen in the following that they do not have a critical impact on the macroscopic response of the periodic array absorber.

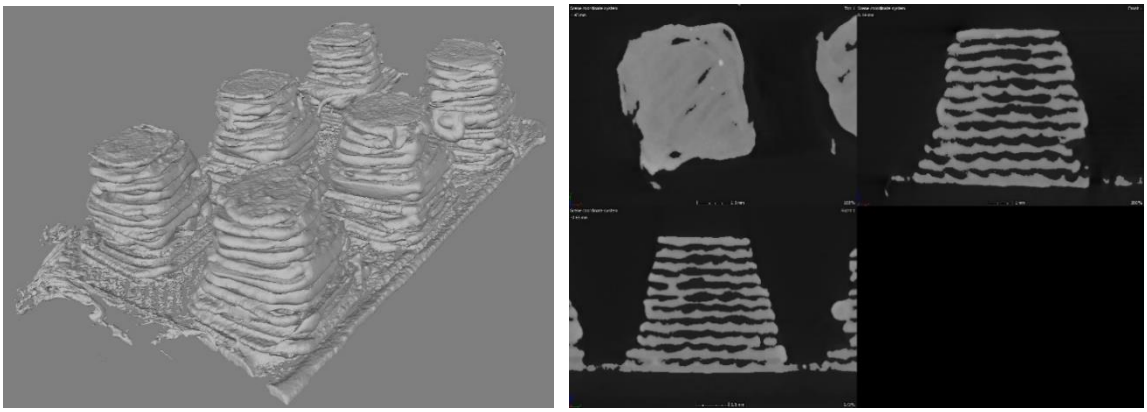

(a) **(b)**

Figure 40. (a) Reconstructed 3D image of the sample composed of six pyramids and (b) top view of the second conductive layer and two profiles (front and side) of two scans of one pyramid.

With the X-ray images, the exact dimensions of each layer can be determined. For our study, two pyramids were analyzed with multiple cutting planes for every single geometry. The dimensions reported in Table 5 are the average values of the collected data. In Figure 41, we compare the geometry of the designed unit cell pyramid through: (a) a schematic design, (b) an X-ray cross-section of the pyramid side, and (c) a 3D imaging by electron beam Microscopy.

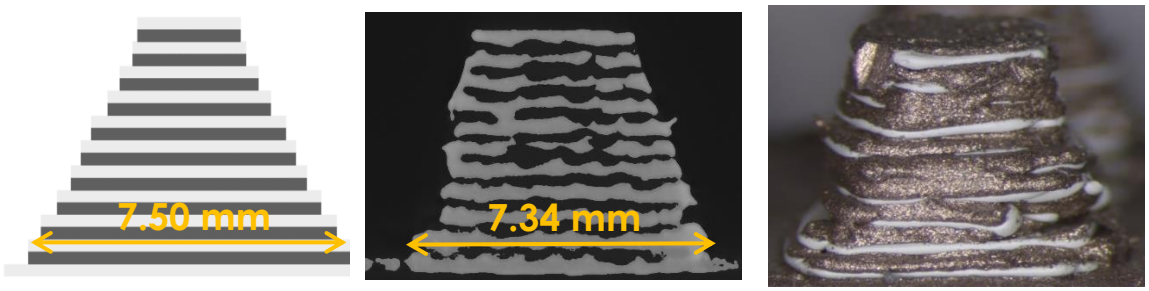

(a) **(b)** **(c)**

Figure 41. (a) ideal front view of the structure where light gray layers are conductive while dark gray layers are dielectrics, (b) right view from X-ray analysis, and (c) front view from electron microscopy.

The differences between the column 2 and column 3 is within a few percent, as shown in Table 5. Therefore, we can discard the second hypothesis.

Table 5. Comparison between the real width values of the prototype analyzed with X-ray, the designed width values exploited in the simulations and the standard deviation between the prototype average width and the design width.

Layer #	Prototype average width length (mm)	Design width length (mm)	Standard deviation (%)
1	7.34	7.50	2.13
2	6.53	6.88	5.09
3	6.37	6.36	-0.16[9]
4	5.89	5.92	0.51
5	5.82	5.53	-5.24
6	5.24	5.19	-0.96
7	4.51	4.89	7.77
8	4.40	4.62	4.76
9	4.45	4.38	-1.60
10	4.06	4.20	3.33

The third element that could lead to some uncertainty between the measurements and the simulations is the real part of the relative permittivity value. As seen from equation (2.10), the cavity resonant frequency is inversely proportional to the real part of the dielectric permittivity. At this stage it is essential to distinguish between the permittivity of the filament and that of a printed sample manufactured by FDM. Indeed, when using melted filament during 3D printing, one can expect a compression between printed layers leading to a lower porosity (or higher density) of the printed sample. This higher density provides higher permittivity on the printed sample than the one on the filament. This remark is only correct when the printing fill factor is sufficiently high.

In our case, the dielectric filament Preperm DK400 has a permittivity value of 4.0 that was characterized by using the perturbation method with a rectangular cavity whose frequency of resonance without a sample is 9.4 GHz. A transmission method using a coaxial line [104] has been used to characterize a printed sample. A permittivity value of 4.6 was obtained on a 2 mm-thickness printed torus, Figure 42(a), over the frequency band of 100 MHz - 18 GHz, as shown in Figure 42(b). The peak around 14 GHz is the higher-order mode that starts to propagate. This higher value of the printed sample permittivity with respect to the filament one (used in simulation) explains the frequency shift between simulation and experiment pointed out in Figure 37.

[9] The – sign is due to the prototype's average width being larger than the designed one.

Sample:
- External diameter = 7mm
- Internal diameter = 3.04mm

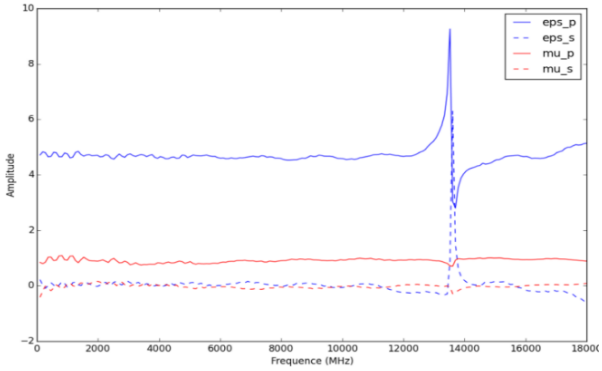

(a) **(b)**

Figure 42. (a) Printed torus sample and its dimensions. (b) Permittivity value of 4.6 measured with a transmission method in a coaxial line. In the legend: eps_p = ε'_r, eps_s = ε''_r, mu_p = μ'_r, mu_s = μ''_r.

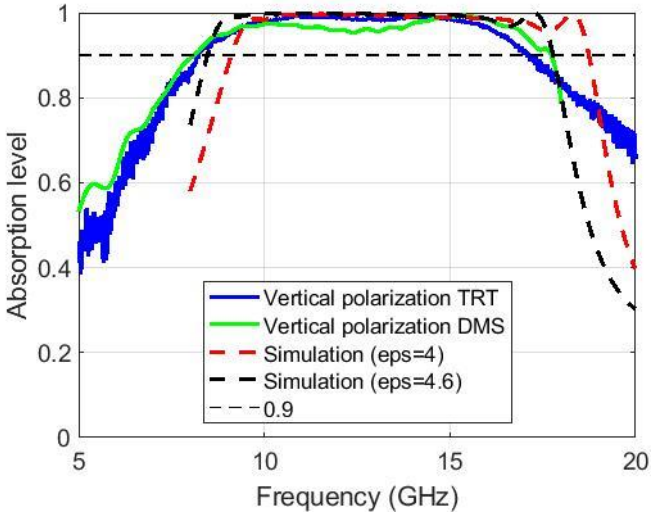

Figure 43. Comparison between the characterization at TRT (in blue solid line), DMS (in green solid line) Simulation with the initial permittivity of 4.0 (in red dashed line), and the simulation with the new permittivity of 4.6 (in black dashed line). All curves are for normal incidence.

In Figure 43, we present the comparison of the measurements made at TRT, the measurements performed at DMS, and the two simulations with the permittivity value of 4.0 and the corrected permittivity value of 4.6. From the figure, it can be noticed the agreement between the two characterizations and the corrected absorption plot obtained by retro-simulation. The frequency ranges that provide greater than 90% absorption (A > 0.9) are reported in Table 6.

Table 6. Frequency range for A > 0.9 for the square-sahped SL MMA.

	f_{min} (GHz)	f_{MAX} (GHz)	FB
Measurement at TRT	8.2	17.1	0.70
Measurement at DMS	8.1	17.7	0.74
Simulation (ε_r = 4.0)	9.0	18.7	0.70
Simulation (ε_r = 4.6)	8.5	17.8	0.71

So far, for the reported measurements, only the vertical polarization has been considered. The choice has been made with consciousness since the structure with a square section is polarization-insensitive. However, one can expect that the imperfections in manufacturing introduce

some sensitivity to polarization. To investigate this possibility, the structure was rotated along its normal axis by different φ angles, where the phi angle is presented in Figure 36(b). In Figure 44, the simulation curves (a), DMS measurement results (b), and TRT measurement results (c) are shown for the angles of 0°, 90°, and 180°.

Similar behaviors are noted in the measurements carried out at DMS in Figure 44(b), which confirms that the macroscopic response of the structure is globally very similar to what was expected with the simulations. In contrast, for the measurements performed at TRT in Figure 44(c), relatively variations depending on the rotation of the prototype are noticed.

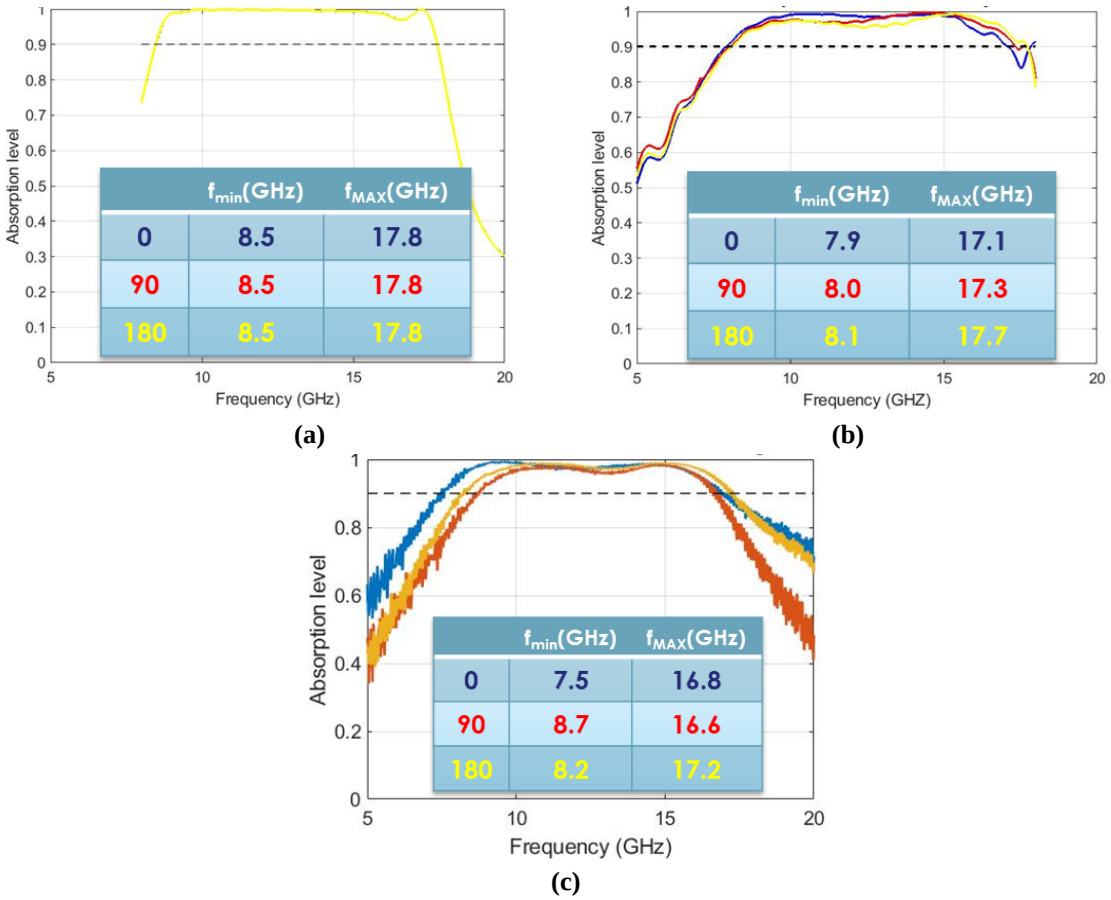

Figure 44. For normal incidence and φ rotations of 0°, 90° and 180°: (a) simulation result with the new value of permittivity, (b) characterization at DMS and (c) characterization at TRT.

For the high frequencies, the cut-off deviation between the three curves is about 0.6 GHz (0.5 GHz for DMS results), while for the low frequencies, it is about 1.2 GHz for TRT spectra (0.2 GHz for DMS data). This discrepancy can be explained based on the following constatations.

1. The prototype has to be removed and replaced on the sample holder for each phi rotation for each measurement. The re-positioning could lead to some uncertainty of the correct position.
2. For frequencies above 12 GHz, the F.F. (Far Field) condition is not fully satisfied and could be the source of measurement errors.
3. For low frequencies, the radiation pattern of the horn antenna used at TRT illuminates a large area (at 8 GHz around 60 cm x 60 cm compared to the 25 cm x 25 cm of the absorber) and could explain that the results are more sensitive to the measurement conditions between the three measurements with the metal plate, vacuum, and absorber.

Keeping in mind these limitations in the accuracy of the measurements performed at TRT, we consider hereafter the experiments under oblique incidences.

2.3.2 Characterization for oblique incidences

The characterization of the prototype under oblique incidence was performed at TRT and in the IEMN anechoic chamber[10].

The two setups are presented in Figure 45(a,b) where (a) corresponds to the TRT setup already described in the previous paragraph while (b) to IEMN setup using TRT horn antennas separated by a flat absorbing slab, in blue in Figure 45 (b).

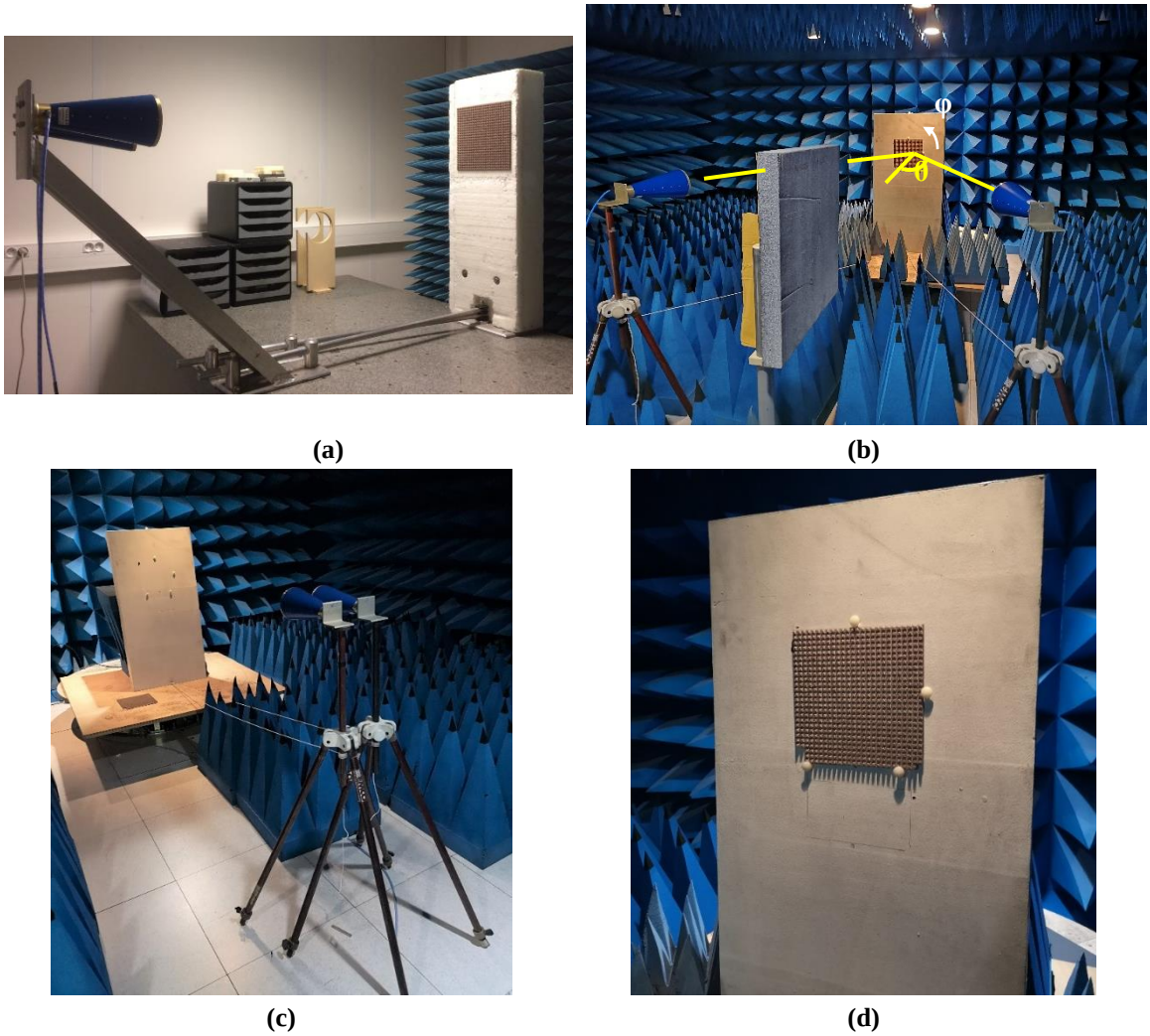

Figure 45. (a) TRT setup in the non-anechoic environment, (b) IEMN setup in the anechoic environment, (c) the two antennas mounted on the two three-foot movable mounts, and (d) the support for the absorber.

Before comparing the experimental spectra measured under oblique incidence at TRT and IEMN, it is important to detail further the experimental conditions that allow suppressing a large part of the spurious reflections of the multipath echoes in the anechoic chamber. The prototype under test

[10] We would like to thank Pierre Laly for his help in these measurements at IEMN.

was placed at 218 cm, at which the Far Field (F.F.)[11] condition is satisfied up to 18 GHz. For the incidence angle control, it is noticed from Figure 45(b) and Figure 45(c) that the angular position of the two horns is carried out manually, taking constant the distance between the horns and the prototype by using a string and a scale protector, on the center of the absorber support in Figure 45(d). Possible misalignments could occur because the system was not automated. Due to the anechoic chamber size, the maximum θ angle is limited to 40° for the horizontal polarization and 45° for the vertical one. Table 7 summarizes these information by comparing the two setups.

Table 7. Comparison between TRT and IEMN characterization setups.

TRT	**IEMN**
Non-anechoic chamber	Anechoic-chamber
Antenna – Sample distance: 125 cm	Antenna – Sample distance: 218.5 cm
Far Field (F.F.) up to 12 GHz	Far Field (F.F.) up to 18 GHz
Maximum incidence angle is 70° (until direct transmission between two antennas)	Maximum incident angle is 40° for H-pol. And 45° for V-pol. (limited by the chamber dimensions)
LoS (Line of Sight) assured	Manual control of LoS (Line of Sight)
4 ports VNA[12]	2 ports VNA

In Figure 48, the characterization results achieved at TRT (non-anechoic chamber) and at IEMN (anechoic chamber) are shown. The left-side of the figure corresponds to the measurements for vertical polarization, while the right side for horizontal polarization. A good agreement between the measurements in anechoic and non-anechoic chambers is found. More steepness variations around the low and high cut off frequencies can be noted for the measurements carried out at IEMN explained by the lower parasitic reflection background expected in an anechoic chamber.

[11] The condition of F. F. is an approximation and we used the classical formula $R = 2D^2/\lambda$ [61] where R is the distance between the antenna and the sample under test, D is the aperture dimension of the antenna and λ is the free space wavelength.

[12] A 4 ports VNA can reduce positioning errors and measure simultaneously both polarization thus reducing characterization time in half.

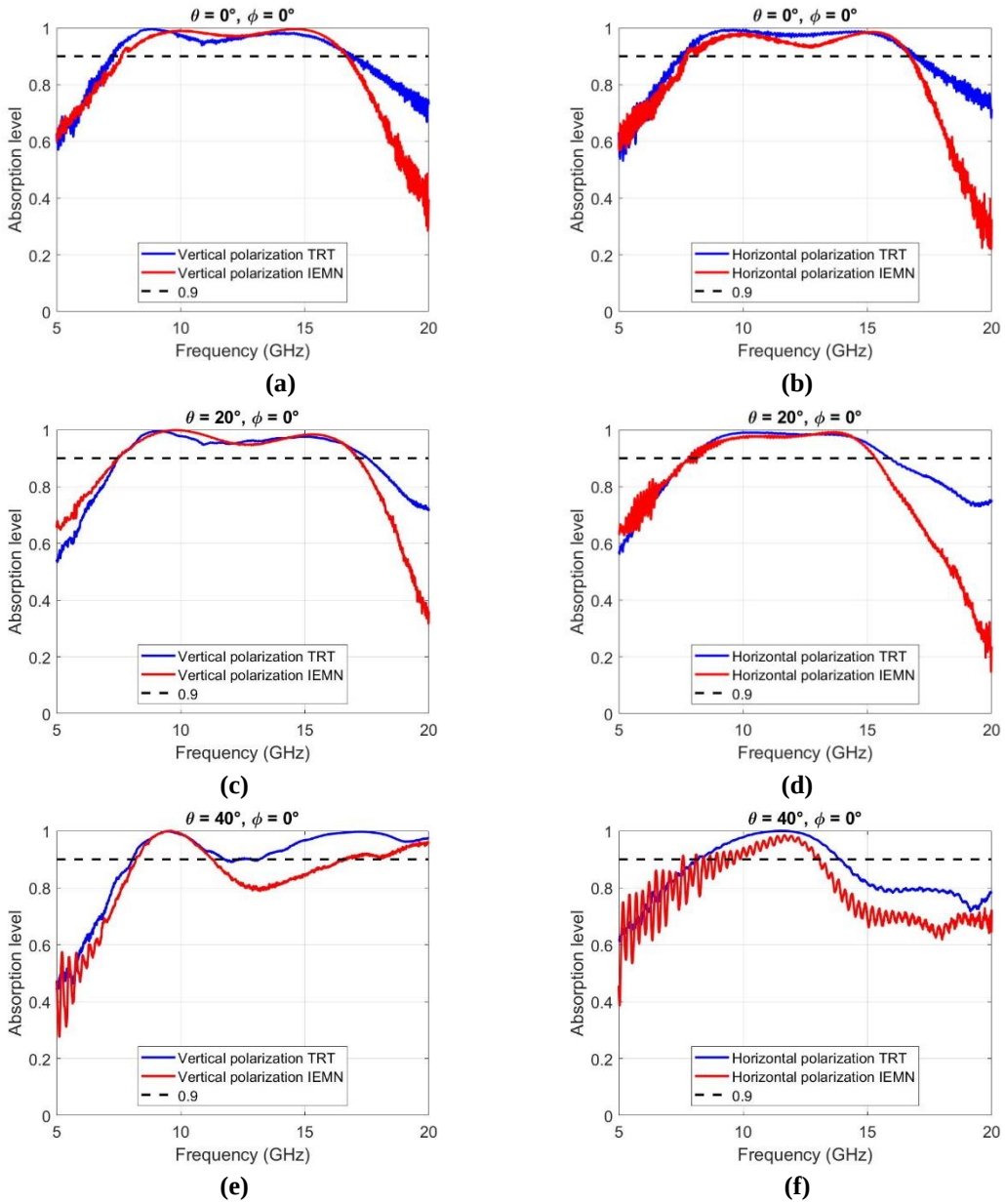

Figure 46. Comparison between the measurements made at TRT, IEMN and the simulations for oblique incident angles of 0°, 20° and 40° respectively (a), (c) and (e) for vertical polarization (TE in the simulation) and (b), (d) and (f) for horizontal polarization (TM in the simulation).

Further, considering these measurements, a difference between vertical polarization and horizontal polarization is obtained. From the physics point of view, this spectra dissimilarity could be interpreted by the excitations difference of the current flux densities in H- and V-polarizations. The current flux density is proportional to the magnitude of the parallel component of the electric field **E** to the absorber plane, which corresponds to the xy-plane in Figure 47. For the H-pol. (TM incidence), **E** can be decomposed into parallel component $\mathbf{E_x}$ and orthogonal component $\mathbf{E_z}$, as angle increases, the magnitude of the parallel component $\mathbf{E_x}$ decreases, and a lower current flux density is excited, resulting in an absorptivity degradation in H-pol.. For the V-pol. (TE incidence), the **E**-field is always parallel to the xy-plane, and its magnitude does not change with θ, resulting in higher absorptivity than in H-pol.. This difference in current excitation explains why the structure is more robust for vertically polarized waves.

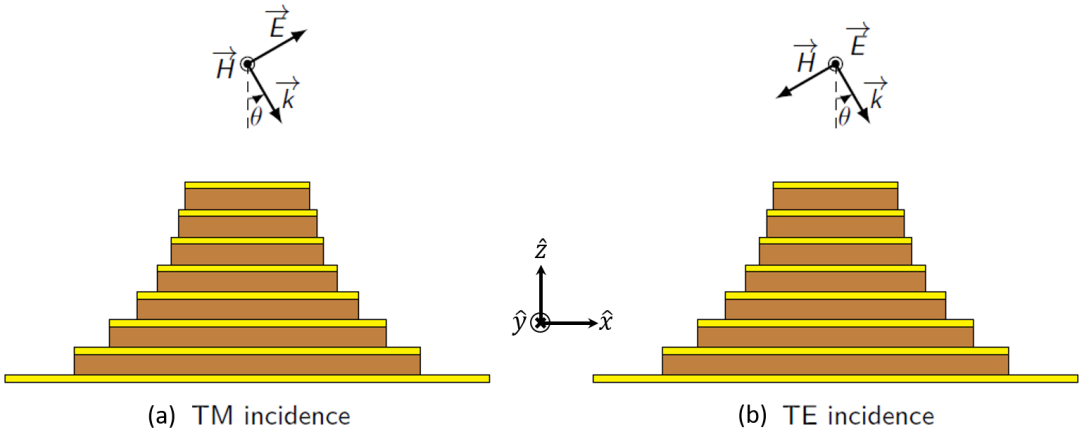

Figure 47. (a) Definition of TE mode (that corresponds to vertical polarization), and (b) of TM mode (that corresponds to horizontal polarization).

From the results displayed in Figure 48 with the plot of the absorption for different angles, a degradation of the absorption level in V polarization near the central frequency (approximately 13 GHz) that corresponds to the trapping and absorption in the central layers of the pyramid, can be noticed. So far, we do not have a clear interpretation of this feature in the absorption window.

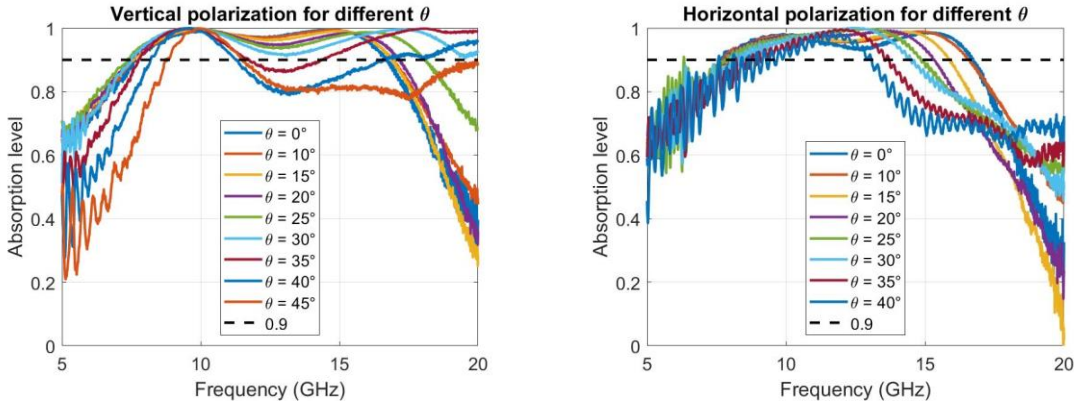

Figure 48. Measurements for different incident angles at IEMN (anechoic chamber) for (a) vertical polarization and (b) horizontal polarization and only for φ = 0°.

Due to the TRT and IEMN data similarity, and since the anechoic chamber arrangement precludes incidence angles greater than 45° for V-pol. and 40° for H-pol., only TRT absorption maps are reported in the following. In Figure 49, first, we compare the simulations (a and b) to the measurements (c and d) using the best performances obtained when φ = 180°. Second, we compare the data for the best with the worst case of φ = 30° (e and f).

A good agreement between simulations, in Figure 49(a,b), and measurements, Figure 49(c,d) is found. For vertical polarization, an absorptivity above 0.9 is measured between 8.2-17.2 GHz (FB = 0.71), from 0° to 10°. Between 10° and 40°, a shift toward higher frequencies is observed since the effective widths of the cavities are smaller than in the previous case, where the resonance requirement $\lambda_g/2$ is satisfied (with $\lambda_g = \lambda_i/\sqrt{\mu_r \varepsilon_r}$ and λ_i is the wavelength of the i-th layer). From 40° to 50°, the absorptivity is above 0.9 from 9.0 to 20.0 GHz (and beyond). This absorption is linked to the higher-order modes excited in the structure bottom half.

For the H-pol., an absorption level greater than 0.90 is found for the frequency range 8.2-17.3 GHz (FB = 0.71). The 0.9-absorption bandwidth continuously decreases as the incidence angle increases. A FB of 0.31 (9.7-13.3 GHz) is seen at an incidence angle of 50°.

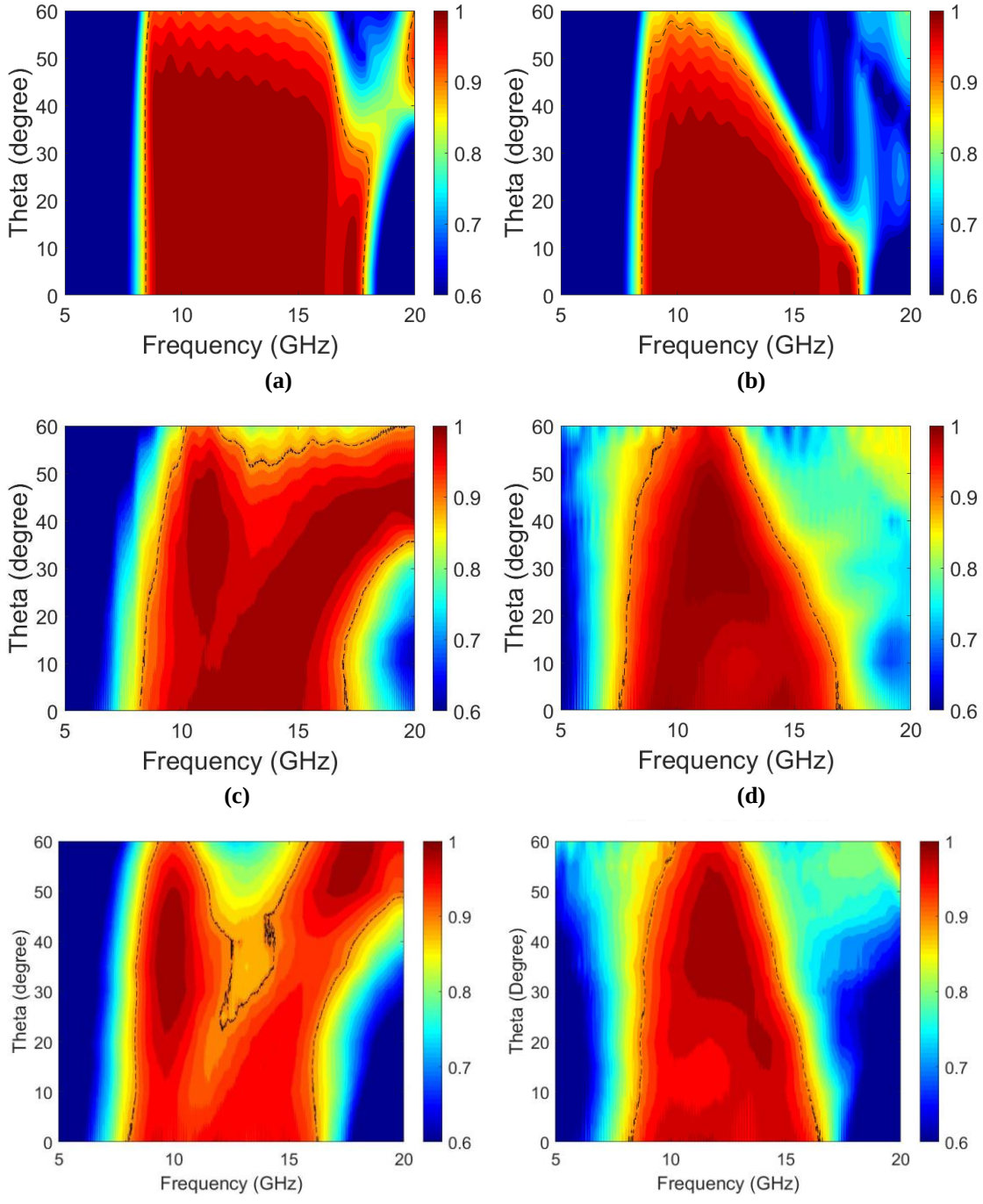

Figure 49. Measurements cartography in NAC (TRT) for different θ angles from 0° to 60°. (a), (c) and (e) represent simulation, characterization for φ = 180° and for φ = 30°, respectively, for vertical polarization. (b), (d) and (f) represent simulation, characterization for φ = 180° and for φ = 30°, respectively, for horizontal polarization.

For a φ rotation of 30°, in Figure 49(e, f), a slightly worst performance compared to the case for φ = 180° are observed. For the V-pol., an absorption level of more than 0.90 is achieved from normal incidence for the band 8.0 GHz – 16.3 GHz (FB = 0.68) and is maintained up to 25°. A narrower absorption window seems a result of an apparent narrowing of the cavity effective width for the incoming wave. Compared to the case at φ = 180°, an absorptivity above 0.90 is not achieved over the whole frequency band. Indeed a slightly lower absorption level of 0.85 is noticed in a sub-range between 12 GHz and 14 GHz for incidence angles ranging between 25 and 50 degrees. For the

H-pol, absorptivity greater than 0.90 is calculated for the frequency range 8.3-16.6 GHz (FB = 0.67), while it decreases to 50° for the band 9.3-13.8 GHz (FB = 0.39). The symmetry properties could explain the decreased performance in comparison to the first scenario. Due to its square shape, the absorber responds well to rotations of 90°, but its symmetry is lost at 30°. While this difficulty is alleviated at high frequencies by the higher-order modes of the cavities, on the contrary, towards the bottom side, there are no higher-order resonance modes at the mid-frequency of the absorption window resulting in a minor absorptivity reduction in the center frequency band. A metamaterial stair-like absorber with a circular shape can be utilized to circumvent these symmetry issues is presented in Chapter 3.

2.4 Conclusion

This chapter began by discussing the operation of a single MIM micro-resonator, which served as the basis for the tapered-multilayered perfect metamaterial absorbers considered in this work. By introducing the so-called critical coupling condition required for unitary absorption, the complex reflection coefficient was expressed in terms of absorptive and radiative quality factors. Extending this criterion to the case of a resonant cavity stack is not trivial, as there are no straightforward closed forms that allow for analytical optimization of the entire structure to our knowledge. As a result, the multilayered structure was designed numerically using the guidelines established by the single resonator geometry. This was particularly true for the transverse resonator dimension, which was optimized to produce equidistant resonant frequencies.

From the experimental side, the significant advantage of a multilayer and multi-material absorber in terms of wideband absorption was demonstrated using a PCB absorber as a first example. It was successfully evaluated experimentally in a non-anechoic environment by accounting for spurious reflection background when determining the absorbance spectra. The limitations of the conventional PCB technology were evaluated and compared with the potential advantages that a 3D printing technique can afford.

Therefore, in a second stage, we reported on the manufacturing of ultra-broadband total absorbers using the Fused Deposition Modeling technique and their free space characterization in the C, X and K_u bands carried out at TRT and DMS in a non-anechoic environment and IEMN in an anechoic chamber. To our knowledge, it is the first demonstration of a radar-absorbing material entirely manufactured using the Fused Deposition Modeling technique that constitutes one of the originalities of the present study [100]. A detailed physical analysis, notably by X-ray imaging, was conducted to assess the multi-stacked dielectric and metal layers morphology along with the measurement of their permittivity (cavity perturbation and transmission lines techniques) and conductivity properties.

A comprehensive electromagnetic characterization of the absorber under normal and oblique incidences was presented by comparing the best and worst performances in two scenarios for φ rotations of the absorber along its normal axis as presented in [103]. Two main problems, connected to the presented square-shape SL metamaterial absorber, were stressed: the first was that the structure is sensitive to polarization while the second was its angular robustness that varies greatly with polarization. To answer these problems, in the following chapter we present an SL structure with a circular cross-section, with different cavity thicknesses to satisfy the critical coupling and with different permittivity to make the structure less sensitive to oblique incidences.

Chapter 3: Enhancing polarization insensitivity and angular robustness with a circular section metamaterial stair-like absorbers for C-band

This chapter summarizes the best practices for designing multilayer, multi-material 3D-printed absorbers using Fused Deposition Modeling (FDM). Two 3D-printed metamaterial absorbers with stair-like cross-sections are designed and fabricated to operate in the C-band. Circular cavities are used to be polarization-independent and to simplify manufacturing. Also, the cavity thicknesses are optimized to increase the absorptivity. The absorbers are designed to operate similarly across the frequency spectrum but with varying dielectric materials. For the first structure, we utilize permittivity of 3.0, whereas, for the second structure, the permittivity value of 8.0 was used. Higher permittivity values by reducing the cavity radius show some improvements in the miniaturization of the basic cell and significantly affect angular robustness. The major fabrication issues are discussed, along with the solutions that have been developed. The two prototypes were manufactured and characterized using three setups for their free space measurements under normal and oblique incidences. These measurements confirm that the structures are polarization-insensitive and that using a dielectric layer with a permittivity higher of 58% with respect to a relative permittivity value of 3.0 increases the angular robustness by approximately 30%.

3.1 Choices in absorber construction and fabricated absorbers for C-band

When constructing an ultra-wideband 3D-printed absorber, the first requirement to set is the frequency band for total absorption (Perfect Metamaterial Absorber). The broader it is, the more layers are required so that the goal is to consider the tradeoff between absorption window and low-profile property. For our application, C-band (4 – 8 GHz) is required. The first step is to determine the number of layers required for an absorptivity greater than 90%. Considering the center frequency of 6 GHz, the fractional bandwidth at -3 dB of the pyramid center elemental cavity is approximately 4%[13], which corresponds to a relative bandwidth of 250 MHz. It means that for 4 GHz (from 4 to 8 GHz), 16 pairs of layers are required. We are interested in more than 90% absorption levels, and hence we used 15 pairs of layers in practice. Once the number of layers is determined, the layer widths of the cavities must be fixed. To be polarization-independent, cavities with a circular section are used. Additionally, the circular section was chosen due to the difficulty of printing square cavities and the 3D printing supplier preference for circular sections [105]. The diameter a is computed by using equation (3.1) [106]:

$$a_i = \frac{c\chi'_{11}}{2\pi f_i \sqrt{\varepsilon_r}} \tag{3.1}$$

where c denotes the speed of light in free space, χ'_{11} represents the first zero of the first-order Bessel function $J_1(x)$, a is the diameter of the layers, ε_r represents the relative permittivity of the

[13] The calculation is computed via full-wave simulation.

dielectric layer and f_i corresponds to the absorbed frequency. As for Chapter 2, layers widths are designed so that the frequencies are equidistant along with the target bandwidth. For Structure 1, the first cavity at the bottom has a width (metal layer diameter) of 23.4 mm ($a_{1,1}$) that decreases to 10.6 mm ($a_{1,15}$) for the 15th cavity at the top. For Structure 2, the bottom cavity width is 14.3 mm ($a_{2,1}$), and the top cavity width is 6.5 mm ($a_{2,15}$).

Our objective is to demonstrate that higher permittivity leads to higher angular robustness, so the dielectric filaments are Preperm DK300 (ε_r = 3.0, tgδ = 0.0046) and Preperm DK800 (ε_r = 8.0, tgδ = 0.0033) [69]. The conductive filament is Electrifi [70] with $\sigma = 1.7 \times 10^4$ S/m, as for the stair-like structure with square-section.

We now need to find the thickness of the stacked cavities and the period of the unit cell. For the first point, let us remind that no closed formula is reported in the literature to our knowledge. Therefore, the optimization of this relevant parameter was performed by numerical simulations by targeting to satisfy the critical coupling condition. To facilitate the comparison between the two structures, each pair of layers has the same height, as described in Table 8 for both absorbers. For the conductive layers, the thickness of 0.3 mm is chosen as trade-off between Electrifi skin depth[14] and printing constraints for homogeneous layers (sufficiently thick to be printable).

Table 8. Dielectric thicknesses of each cavity for Structure 1 and Structure 2.

Cavity #	**Structure 1 and Structure 2 dielectric thickness (mm)**
1 - 4	0.7
5 - 9	0.5
10 - 12	0.4
13 - 15	0.3

The dielectric layer thickness reduction guidelines are based on the technological constraints and the optimization rules for the radiative quality factor or equivalently the resonant state lifetime to satisfy the critical coupling condition. For a single resonator configuration, the period and the dielectric layer thickness are the degrees of freedom for coupling the cavity to its environment. These rules allow the optimization of the low-frequency resonators, with a dielectric thickness of 0.7 mm chosen for the first four bilayers. Doubling the operating frequency from 4 GHz to 8 GHz for the C-band, one can expect to reduce the dielectric thickness approximately with the same ratio. Consequently, a value of 0.3 mm was chosen for the three top-resonators and 0.5 and 0.4 mm for the intermediate resonating structures.

To address the second point, the optimal method for determining the period size of the unit cell is through iterative simulations, aiming at an absorptivity over 90% for normal incidence. For Structure 1 and Structure 2, a period p_1 of 25.4 mm and p_2 of 16.3 mm, hence 1 mm for each side, were found. These period dimensions can be compared with the free space wavelength at 6 GHz (λ_0 = 50 mm). For Structure 1, we obtain a ratio $\frac{p_1}{\lambda_0} = 0.5$, and for Structure 2 $\frac{p_1}{\lambda_0} = 0.3$. Therefore, increasing the permittivity is more favorable to operate in the long-wavelength regime by shifting at a higher frequency high order diffraction effects. In the following, however, we only address specular reflection, which means that grating effects are not considered ($p < \lambda_0$). One can also compare the period and the largest diameter of the tapered metal layer $a_{1,1}, a_{2,1}$. For Structure 1, we obtain: $\frac{a_{1,1}}{p} =$

[14] Electrifi skin depth at 6 GHz is 0.050 mm. More details are given in Table 2.

0.92. and for Structure 2 $\frac{a_{2,1}}{p} = 0.87$. Both metasurfaces have approximately the same filling factor with an increase of basic resonator number per unit area due to the resonator width reduction for a permittivity of 8. By reminding that we did not vary the dielectric thickness tapering for a better comparison between Structure 1 and Structure 2, the total thickness *h* is 12 mm and hence a little bit above the targeted limit around 10 mm for both structures.

To summarize, the methodology for designing such stair-like metamaterial absorbers is shown in Figure 50.

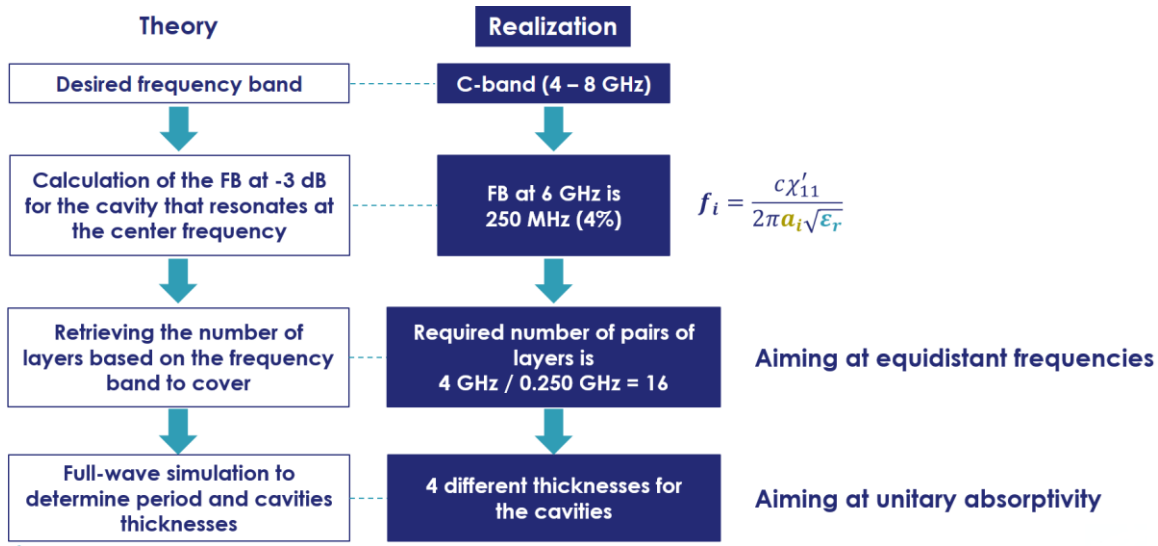

Figure 50. Methodology to follow to design SL absorbers. On the left, the theory while on the right the practical example followed to design the structures of this chapter.

The 3D schematics of Structure 1 and Structure 2 are reported in Figure 51(a) and Figure 51(b), respectively, and the illustration of Structure 1 considering several periods is shown in Figure 51(c).

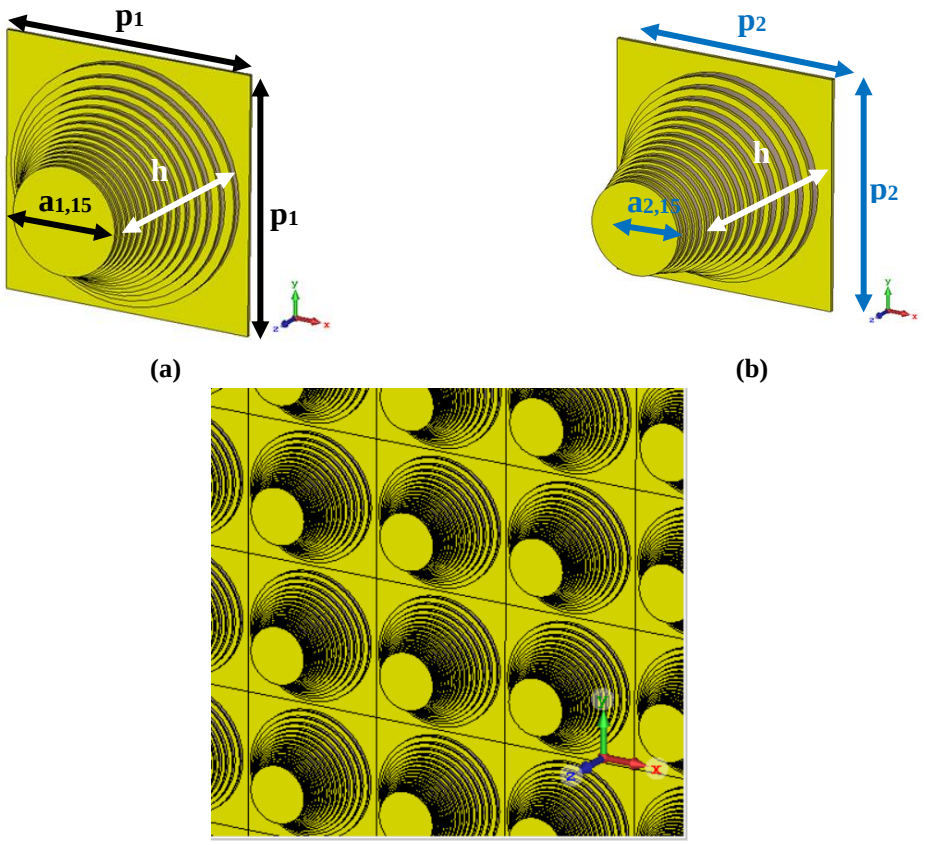

Figure 51. 3D Schematics of stair-like circular shaped multilayered absorbers. (a) Structure 1 with a relative permittivity value of 3.0 and a period p_1, the top pairs of layers is $a_{1,15}$. (b) Structure 2 with a relative permittivity of 8.0 and a period p_2, the top pairs of layers is $a_{2,15}$. Both structures have the same thickness h. (c) Structure 1 metamaterial SL absorber with several periods.

To illustrate the optimization stages simulated with CST Microwave Studio 2019 by considering the basic cell with periodic boundary condition, we first consider the E-field magnitudes maps in a vertical cross-section at the center of the circular pattern. Assuming an electromagnetic wave that impinges on the array with normal incidence and thus propagates normally to the metal-dielectric layers, the E-field maps for Structure 1 are plotted in Figure 52(a), at the resonant frequency of 5.5 GHz, and in Figure 52(b), at 8.5 GHz. The figure shows the localization of the EM wave in different regions across the multi-stack layers, close to the top of the basic cell for the upper frequency and close to the pyramid center that resonates at 5.5 GHz, which was chosen a little bit lower than the central frequency (6 GHz). In addition, the electric field enhanced by resonance effects is not strictly confined in one cavity but involves several adjacent cavities, around 3 for 5.5 GHz with a maximum for the $a_{1,5}$ bilayer and 4 cavities for 8.5 GHz with electric field values that are equally shared between the bilayers $a_{1,13}$ and $a_{1,14}$.

Turning now to the magnetic field maps, Figure 52(c) and Figure 52 (d) show the magnitude for 5.5 and 8.5 GHz, respectively. In contrast to the E–field maps with out-of-plane components in the dielectric layers, these maps show in-plane H-fields components with maxima in the center of the bilayer.

At last, for a deeper understanding of the way the impinging EM wave is coupled to the opened resonators, the Poynting vector maps were plotted in Figure 52(e) in a vertical cross-section at the center of the multilayered structure and in a horizontal cross-section corresponding to the $a_{1,5}$ bilayer for which a maximum of the E- and H -field magnitudes were detected for 5.5 GHz.

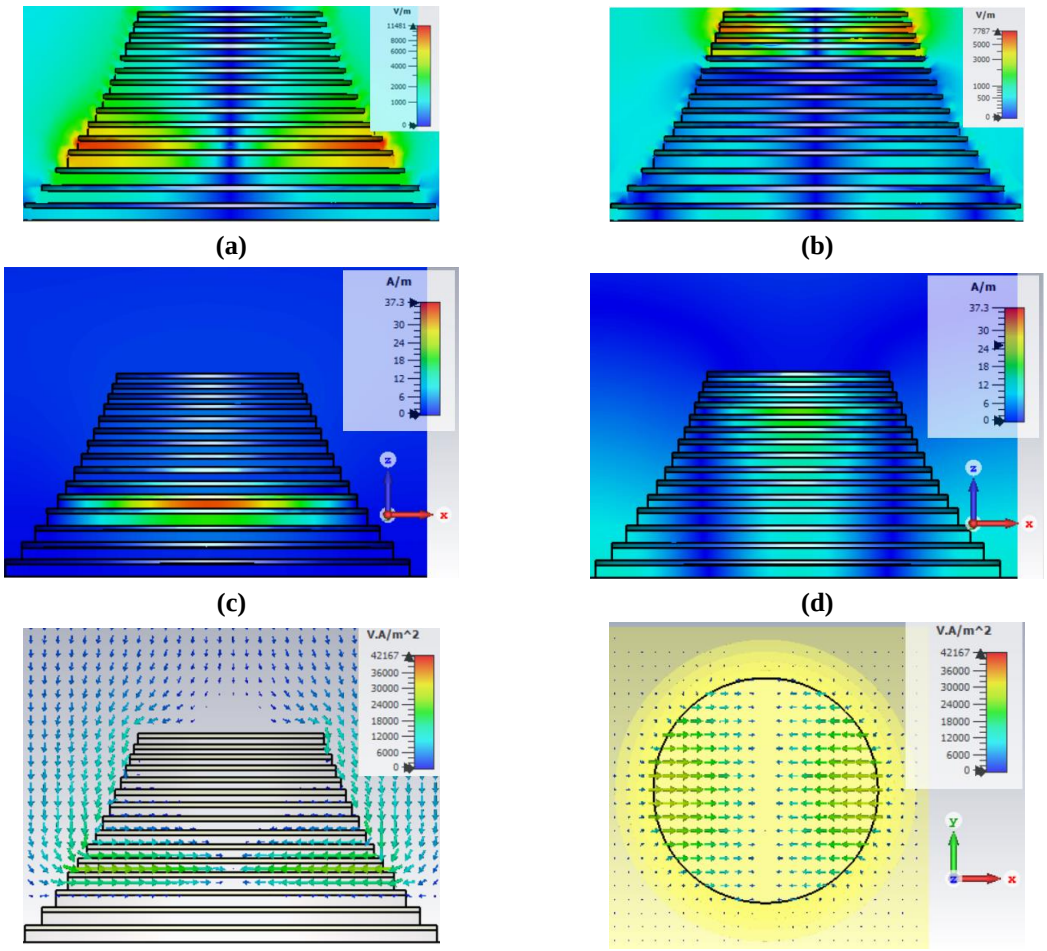

*Figure 52. Designs of the two stair-like Structure 1 with a circular shape. Electric field (**E**) magnitude at (a) 5.5 GHz and (b) 8.5 GHz. Magnetic field (**H**) magnitude at (c) 5.5 GHz and (d) 8.5 GHz. Poynting vector (S) at 5.5 GHz for (e) vertical cross-section, and (f) horizontal cross-section corresponding to the 5th bilayer center ($a_{1,5}$).*

Considering now the same configuration of an electromagnetic wave impinging normally to the structure, the S vector (power flux) orientation normal with respect to the top of the pyramid is split into two fluxes that propagate at the interfaces between the pyramid side walls and the air-filled etched regions. When the wavelength of the incident EM wave, which corresponds to an EM propagation in a MIM-type waveguiding structure, matches its transverse dimension according to the resonance criterion, the incident energy is trapped in the corresponding resonator. The strong S vector bending in the vicinity of the cavities, where the EM energy is trapped, demonstrates this.

As explained before, the trapped EM field bounces back and forth in the corresponding transverse open cavity with a resonant state lifetime that depends on the coupling of the cavity to its environment. As aforementioned, matching this resonance lifetime, described by the radiative quality factor in paragraph 2.1, to the characteristic time for dissipation is equivalent to the critical coupling condition.

Considering now the snapshot of the S-vector plot in the horizontal plane, a vortex-like pattern can be noticed, further illustrating the ***k*** vector orientation of the traveling wave from normal to transverse directions along with the localization of the impinging energy.

As a last comment concerning the trapping mechanism, the dispersion approach involving the engineering of the cut-off frequency of the HMM waveguides, as proposed in the original paper of Ding et al., seems difficult to apply for the multilayered structure studied here. Indeed, from the S vector plot, coupling effects dominate the structure feeding via the side walls, whereas Ding et al.

interpretation was mainly based on dispersion characteristics of the HMM (Hyperbolic MetaMaterial) waveguides.

In practice, this means that the outer regions of the multilayer stack play a major role in the trapping and dissipation mechanisms. This predominance of coupling phenomena from the side walls could explain in part the fact that, for the non-etched dielectric layer PCB technology presented in Chapter 2, the resonance peaks show higher frequency selectivity. The other reason was the use of a copper metal layer with high conductivity (5 x 10^7 S/m), while for the 3D printing metasurface, the conductivity of the Electrifi filament was 1.7 x 10^4 S/m. It is interesting to compare the skin depth between copper and electrifi layers, as reported in Table 9.

Table 9. Skin depth comparison between copper (with a conductivity of 5 x 10^7 S/m) and Electrifi (with a conductivity of 1.7 x 10^4 S/m)

Frequency (GHz)	Copper skin depth (mm)	Electrifi skin depth (mm)
1	0.021[15]	0.122
4	0.001	0.061
6	0.0009	0.050
8	0.0007	0.043
10	0.0006	0.038

The skin depth varies between one and two orders of magnitude, indicating that the E-field can easily penetrate the conductive filaments, increasing dissipated power and thus absorptivity.

In the next section, we consider the absorption spectra calculated with equation (1.3) in terms of scattering parameters (S_{11}), for the incident angles of θ = 0° (normal incidence) and θ = 50°, and for V-pol., as depicted in Figure 53. These spectra calculations prove the enhancement of the angular robustness by increasing the dielectric permittivity. As seen in this Figure 53, the 'merging' of multiple resonances allows the ultra-wideband behavior over the C-band (one octave) with quasi-unit absorption peaks at normal incidence.

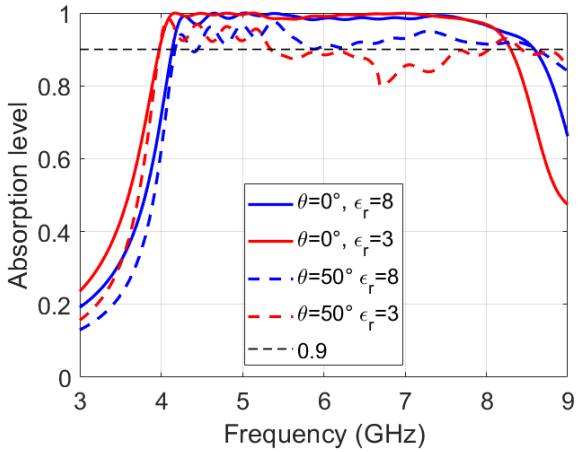

Figure 53. (a) Frequency dependence of absorbance for vertical polarization for both Structure 1 (in red), with εr = 3.0, and Structure 2 (in blue), with εr = 8.0, under normal incidence (in solid lines) and at the incident angle of 50° (in dashed lines).

[15] Skin depth is usually measures in µm but here mm is considered to compare skin depth to the electrifi layer thickness

Thanks to the higher permittivity value, for oblique incident angles, Structure 2 ($\varepsilon_r = 8.0$) has a better response than Structure 1 ($\varepsilon_r = 3.0$). As described in [2], higher dielectric permittivity enables better confinement of an EM field, which means that the wave stays inside the cavity for a longer time, thereby ensuring the critical coupling condition in terms of lifetime.

The power loss densities at 8.5 GHz are shown for normal incidence for Structure 1, in Figure 54(a), and Structure 2, in Figure 54(b). The highest dissipation is seen at the resonant cavities edges. These points correspond to the zones where the energy is dissipated, the anti-node (lateral sides) rather than the node points (center), where the energy dissipation is null. Figure 54(d and e) shows the magnitude of the surface power density that describes the losses at the metal-dielectric interfaces. From Figure 54(d), higher dissipation losses can be seen close to these interfaces and hence in the two evanescent E-field tails characteristic of surface modes in MIM-type structures. One can interpret this enhancement for high permittivity as a result of the augmented absorptivity due to the conductive losses. The power loss densities at 8.5 GHz, for $\theta = 50°$, are also reported for Structure 1, in Figure 54(f) and Structure 2, in Figure 54(g).

From Figure 54(g) and Figure 54(f), it can be noticed a significant change concerning the results reported for $\theta = 0°$ with some energy trapped in the top layers, as expected, but also in the bottom resonator ($a_{1,1}$, $a_{2,1}$). This trapping effect at the pyramid bottom seems more efficient for the high permittivity structure ($a_{2,1}$), and dissipation occurs in the central regions instead of the edge ones. It is believed that such extra dissipation mode in the bottom resonator is related to the excitation of the higher cavity mode. The operating frequency chosen for the energy dissipation plot is 8.5 GHz and hence higher than the expected frequency cut-off of higher-order modes of the bottom cavity designed for operating in the dominant mode at 4 GHz.

From an electromagnetic point of view, this higher-order mode excitation could explain why the absorption is further increasing in the upper part of the frequency window for oblique incidence angle with $\theta = 50°$.

As last point, the color variations of the power is due to the unit of measure that is W/m^3, for the power loss density, and W/m^2 for the surface power density. Since Structure 1 has a bigger volume, the color of its map is less intense compared to Structure 2.

As a last comment about the volume and surface power energy loss commented before, it has to be emphasized that the normalization of the power density implies the basic cell cross-section area and the active regions filled with matter. Consequently, it seems challenging to deduce further quantitative information based solely on the color intensity owing to the difference in material volume.

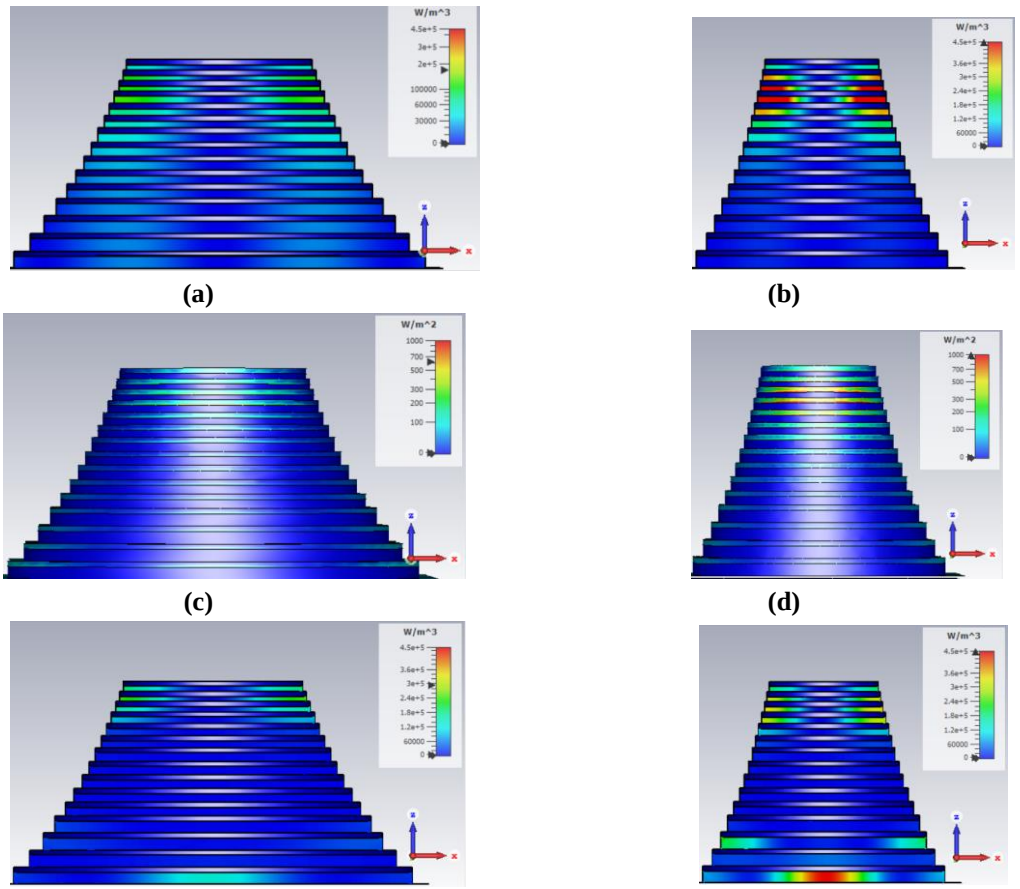

Figure 54. At 8.5 GHz for normal incidence: the magnitude of the power loss density for (a) Structure 1 and (b) Structure 2, and the magnitude of the surface power density for (c) Structure 1 and (d) Structure 2. At 8.5 GHz for an oblique incident angle θ of 50°: the power loss density magnitude for (e) Structure 1 and (f) Structure 2.

The simulated frequency dependence of the absorptivity of both absorbers for incident angles θ ranging from 0° to 60° is hereafter presented.

As presented in Figure 55(a), for Structure 1 in vertical polarization (V-Pol.), the 0.9-absorptivity requirement is met up to 28° for the whole C-band. It is satisfied up to 45° for the frequency range from 4 GHz to 6.5 GHz. For horizontal polarization (H-Pol), illustrated in Figure 55(c), as a general comment, the angle robustness is weaker than in vertical polarization one, and one can interpret this difference in the current density excitation as described in Chapter 2.

On the right side of Figure 55, the absorbance spectra for Structure 2 ($\varepsilon_r = 8.0$) for V-pol. (b) and H-pol. (d) modes are presented. The result for V-pol. meets the 0.9-absorptivity requirement for the C-band up to 50°, increasing the angular robustness by 79% over Structure 1. For TM mode, the angle robustness of Structure 2 increases by 140% with respect to Structure 1 with an absorptivity above 0.9 up to 24°instead of 10°.

In conclusion, exploiting dielectrics with higher permittivity allows increasing the angular robustness significantly, as demonstrated here, in the absorption window greater than 90% over the C-band. The same conclusion can be drawn with less stringent requirements such as a limit fixed to 80%, as often chosen in the literature.

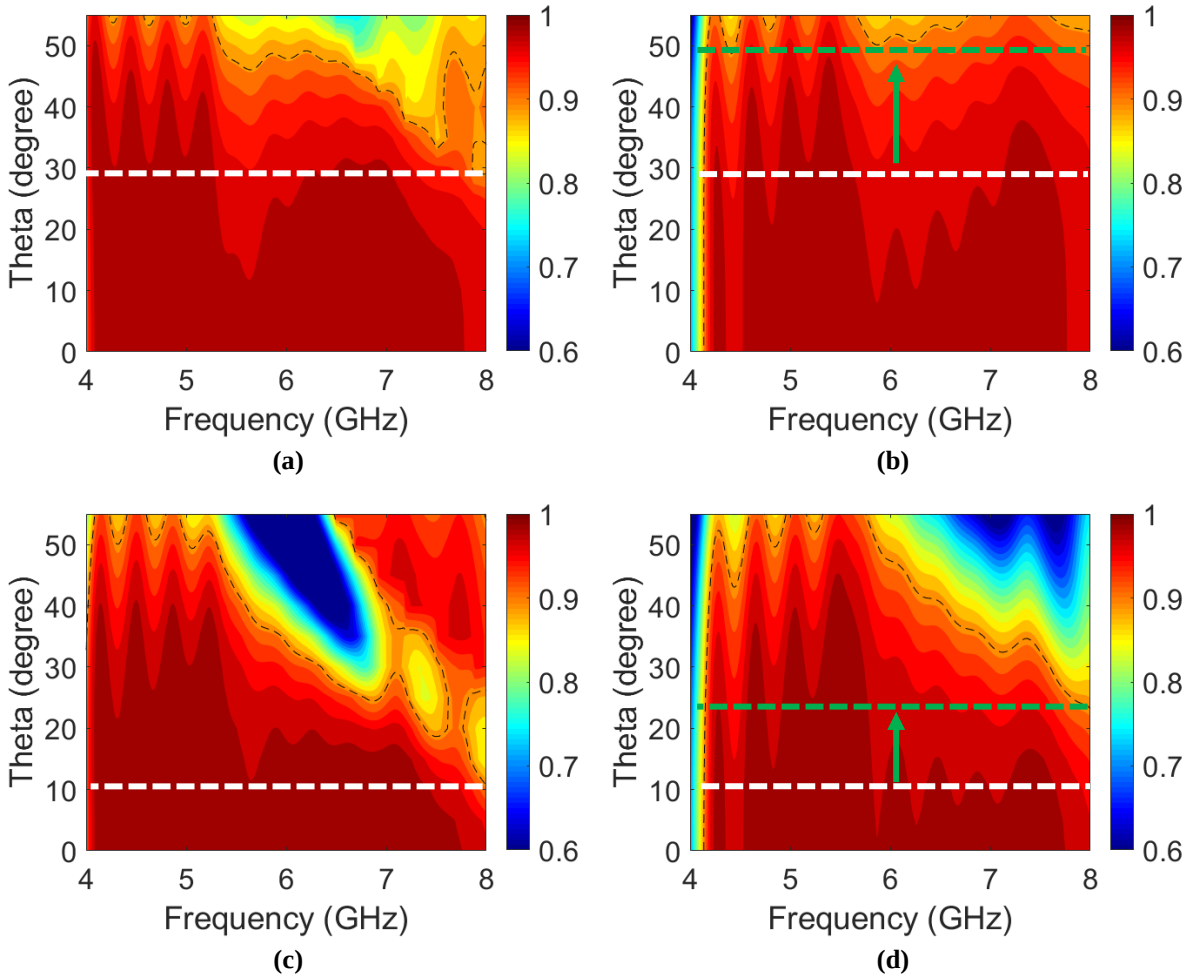

Figure 55. Simulations of frequency and theta dependences of the absorbance for vertical polarization (V-pol.) for (a) Structure 1 (ε_r = 3.0) and (b) Structure 2 (ε_r = 8.0), and for horizontal polarization (H-pol.) for (c) Structure 1 (ε_r = 3.0) and for (d) Structure 2 (ε_r = 8.0). The dashed horizontal lines correspond to the maximum angle at which the absorptivity is greater than 90% for Structure 1 (in white) and Structure 2 (in green).

3.2 3D-printed manufactured absorbers

In this paragraph, we shortly present the 3D-printed absorbers that were manufactured by Plastic2Print [105] exploiting, as for the square-shaped pyramidal structures reported in Chapter 2, FDM technology but by changing the process to stack to the multilayered array aiming to increase the pyramid array quality.

Also, with respect to the first part of the Ph.D. work in Chapter 2, the quality of printed devices was dramatically improved, notably benefiting from the circular-shaped pattern that facilitates the printing stages. However, owing to rigidity issue, the prototypes were printed on mirror-like rectangular supports of larger dimensions (29 cm x 26 cm) compared to the absorbing metasurface area (25 cm x 25 cm), raising some problems in their experimental assessment resulting due to spurious reflections of the mirror-like frame. In the characterization section, the solution to this problem is presented.

Structure 1 was manufactured with the dielectric filament (Preperm DK300) with ε_r = 3.0 while Structure 2 with ε_r = 8.0 (Preperm DK800). The photos of the two prototypes are shown in Figure 56(a) and Figure 56(b), respectively, for Structure 1 and Structure 2. Both printed metasurfaces have the dimension of 25 cm x 25 cm with a total thickness *h* of 1.2 cm without support. 81 stair-like pyramids were assembled for Structure 1 and 225 with a smaller diameter due to higher

permittivity for Structure 2. To improve resolution and printing accuracy compared to the structure presented in Chapter 2, the manufacturer printed the dielectric and conductive disks individually and then formed M-I cavities by heating the conductive layers and gluing them to the dielectric one[16]. One of the main problems in array printing is the difference between filament temperatures introduced in Chapter 2. So far, this problem was not been entirely overcome.

This two-stage manufacturing process ensured a better structuring of the pyramids, as shown in Figure 56(a) and Figure 56(b), where single pyramids for Structure 1 and Structure 2 are shown.

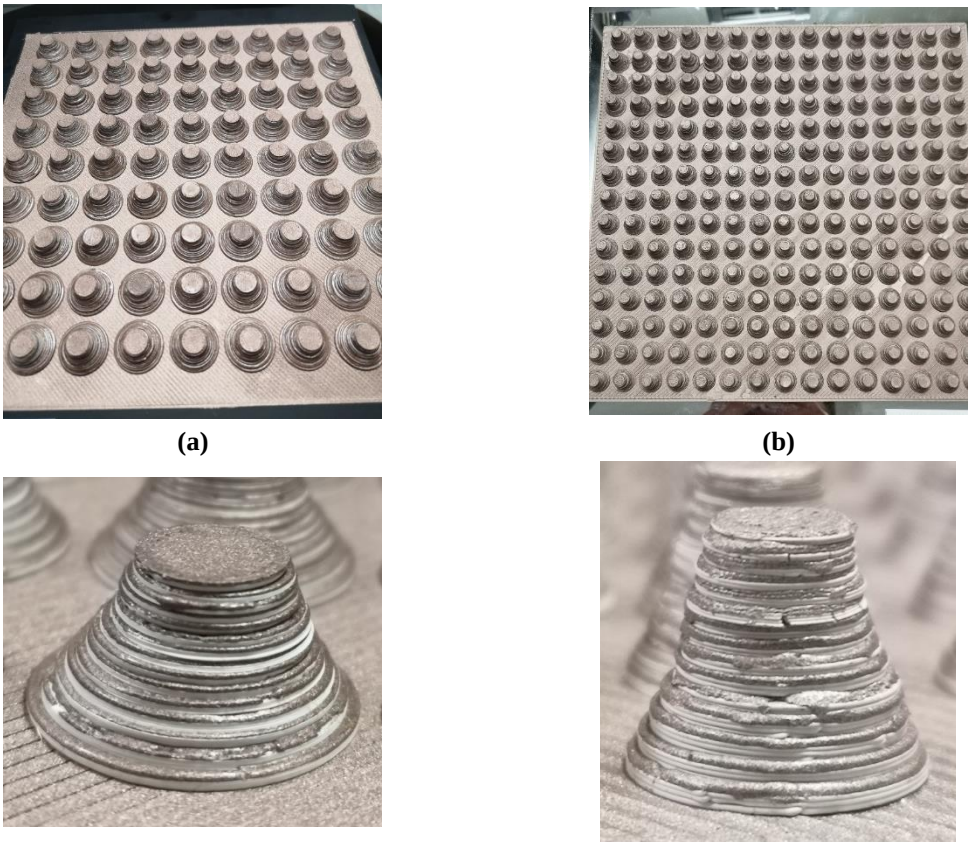

(a) **(b)**

(c) **(d)**

Figure 56. Fabricated 3D-printed absorbers: (a) Front view of Structure 1 with a dielectric filament with ε_r = 3.0, (b) front view of Structure 2 with a dielectric filament with ε_r = 8.0, (c) side view of one pyramid of Structure 1 and (d) one of Structure 2.

The electromagnetic properties of these 3D-printed absorbers are analyzed for normal incidence in paragraph 3.2.1 and oblique incidence in paragraph 3.2.2.

3.2.1 Characterization for normal incidence

For the characterization under normal incidence, three setups were used to improve data accuracy. The first is the same as in Figure13(b) in Chapter 2, and equations (2.21a) and (2.21b) are used to deduce the complex reflection coefficients. The simulated plots of the absorbance under normal incidence are presented in Figure 57(a), for Structure 1 and Figure 57(b), for Structure 2. The characterization results, measured using the setup illustrated in Chapter 2, are presented in Figure 57(b), for Structure 1 and Figure 57(d), for Structure 2. The simulations that do not consider the mirror-like support (see the previous manufacturing section) show almost unitary absorptivity across

[16] No addition glue was used.

the 4 – 8 GHz band of interest. Additionally, only one polarization is shown due to the prototype pattern symmetry. In contrast, V-pol and H-pol. polarizations are considered for the experimental assessment with array symmetry breaking.

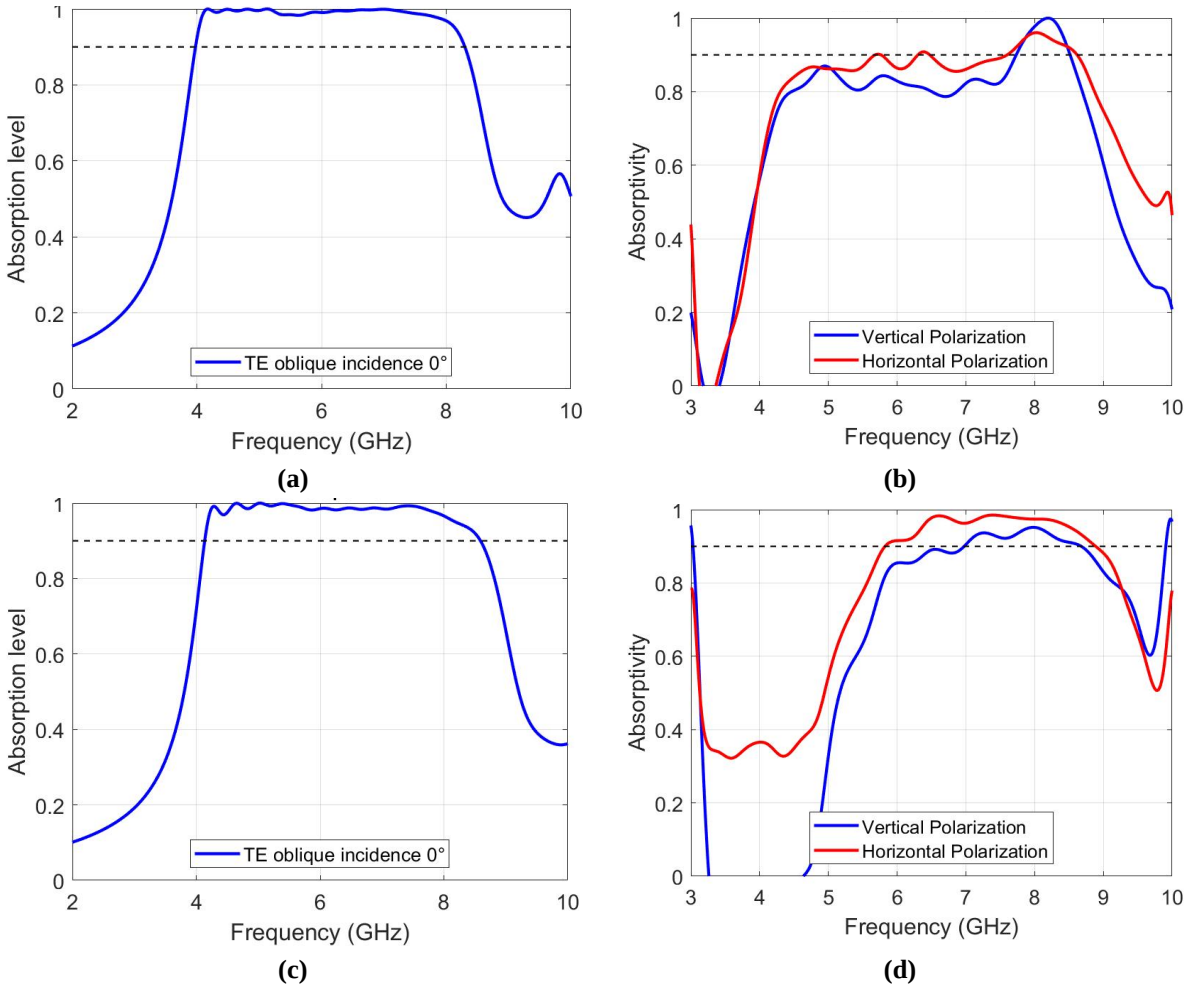

Figure 57. Frequency dependence of the absorbance under normal incidence for the simulations of (a) Structure 1 (ε_r = 3.0) and (c) Structure 2 (ε_r = 8.0) considering only V-pol. due to the pattern symmetry. Characterizations measured with the setup presented in Chapter 2 of (b) Structure 1 and (d) Structure 2 for V-pol. (in blue) and H-pol. (in red). The black dashed line corresponds to an absorptivity value of 0.9. For the characterizations, a time-gating is applied to the signals in post-processing.

Significant discrepancies between simulation and experiment can be noticed. While the numerical results show almost perfect absorption in the frequency band of interest, lower absorption levels and band reductions are pointed out experimentally, with significant differences between vertical and horizontal polarizations despite the normal incidence condition. The main reasons for these discrepancies between simulation and experiment seem to be the rectangular mirror-like outer frame on which the prototypes are printed and the illuminated area of the wideband antenna of around 77 cm x 77 cm at 6 GHz[17]. The metasurface support is covered by a thin aluminum layer that reflects the part of the radiation beam that illuminates this rectangular frame, with dimensions of 29 cm long for the direction corresponding to the vertical polarization and around 26 cm for the horizontal one. This difference in dimensions explains the discrepancy between V-pol and H-pol experimental results by pointing out the impact of this frame on the overall metasurface reflectivity.

For Structure 2, a frequency shift toward high frequency is observed, and it could be due to:

[17] Very similar problem to the one discussed in Chapter 2 for the characterization of the SLMMA at 8 GHz.

1. A discrepancy in the widths of the designed and constructed structures
2. The disk permittivity that could be different from the filament one.

First, the discrepancy in the absorption level of the two structures between simulations and characterizations is investigated, and then the frequency deviation analysis on Structure 2 is conducted.

Because the aperture diameter of the ultra wideband Satimo QR2000 antenna is 77 cm^2, at a distance of 1.25 m from the Sample Under Test (SUT), this illuminated area does not assure a proper focus of the incident wave on the prototypes to be measured [98]. Therefore, to check the absorptivity, we performed other measurements to Thales DMS[18]. In Figure 58(a), the schematic of the DMS characterization setup is shown. It is composed of a paraboloid reflector, as in Figure 58(b), placed at 1.5 m from the top surface of the absorber fixed on the prototype support. The ultra-wideband sinuous antenna, shown in Figure 58(c), was used as EM wave emitting and receiving element in front of the paraboloid reflector. The antenna operates from 2 GHz to 18 GHz for vertical and horizontal polarizations, which can be changed using a switch. It is worth mentioning that the illumination of the outer frame due to the mirror support can be avoided thanks to the collimated beam adequately aligned on the SUT center.

As the first result, Figure 58(d) shows the S_{11} parameter in dB for a 25 cm x 25 cm copper plate, as a Perfect Electric Conductor (PEC), in red, in place of the absorber and for empty support, in green. The difference between the two scattering S_{11} parameters is more than 30 dB. This difference in dB scale corresponds in linear scale to a reflected signal at the one-port of the Vector Network Analyzer 1000 times less than when using a metal plate. It can be concluded that the spurious reflecting contribution can be negligible. Thus, the calculation of the reflectivity reduces to (3.2).

$$\Gamma^{SUT} = \frac{S_{11}^{absorber}}{-S_{11}^{metal}} \tag{3.2}$$

[18] We would like to thank Grégoire Pillet and Stefan Varault for their availability and their advices during the measurement session.

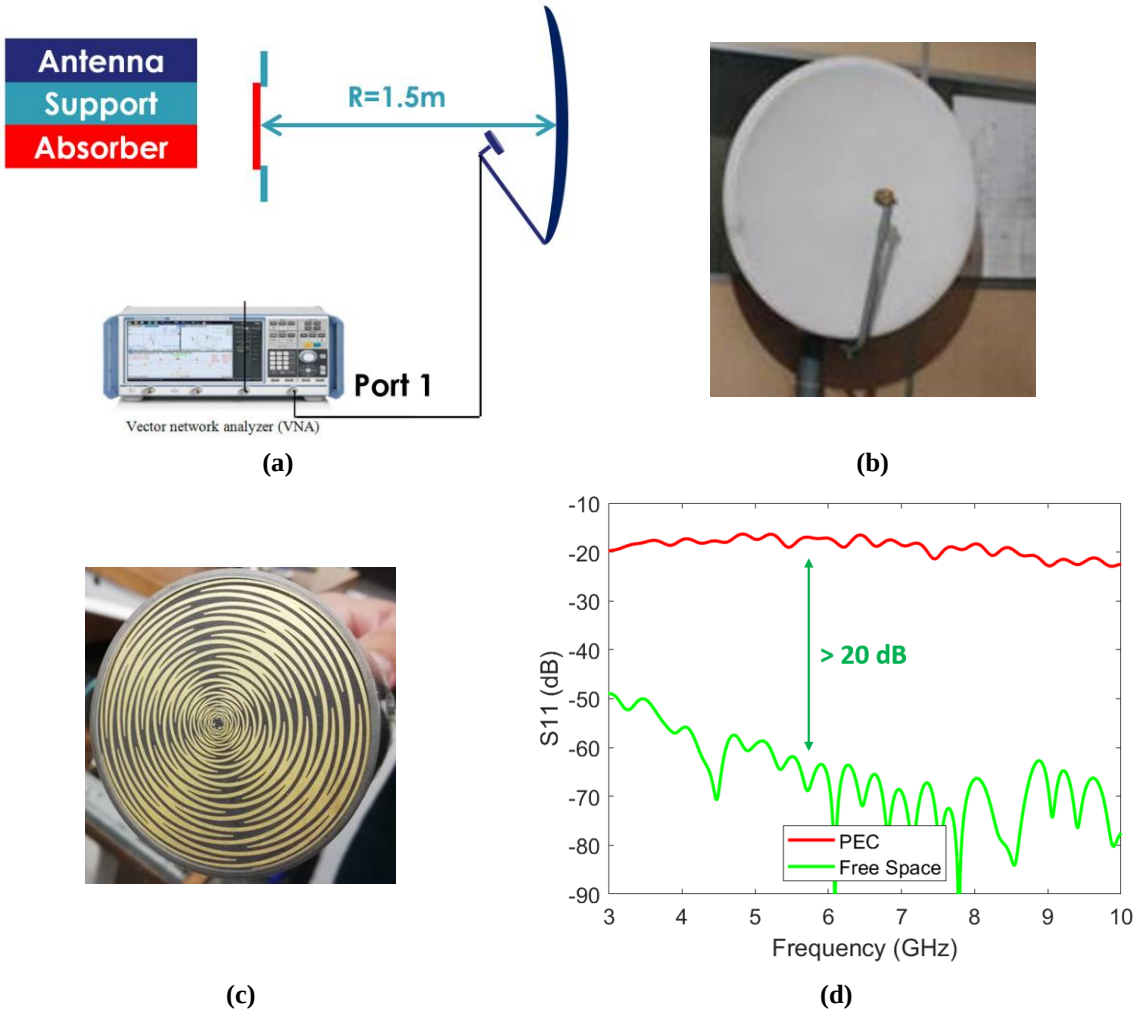

Figure 58. (a) Schematic of the setup at DMS. Photos of the paraboloid (b) and radiating element (c) antenna. (d) Frequency dependence of the S_{11} parameter for a copper plate (PEC, in red) and without a sample (Free Space, in green).

A Matlab time-gating code was developed to reduce the spurious deterministic fluctuations caused by undesired multipath signals reflected from the environment [108]. The code converts the data from the frequency domain to the time domain using an IFFT (Inverse Fast Fourier Transform). The Hanning (or Hann) window is then used to gate the time-domain data, thanks to its high performance and ease of implementation. The span and center of the Hanning function are adjusted so that only the signal of interest is preserved while filtering multipath reflections. The time-domain data is then transformed using an FFT, resulting in the time-gated frequency domain data presented below. This procedure is carried out during the post-processing stage.

In Figure 59, the time-domain S_{11} signals are presented when the copper plate is positioned on the support (in red) and when the support is empty (in green), Hann window is in blue, and the filtered signal is in black. For both Free space and PEC signals, the first peak at 43 ns is the reflected wave from the paraboloid. The second peak at 56.8 ns corresponds to the reflection of the metal plate. This peak is not present with free space. Hann filter center is then positioned at 58 ns with a span of 7 ns to include most of the useful signal. Hann window function $\omega[n]$[19] is written in (3.3).

$$\omega[n] = 0.5\left[1 - cos\left(\frac{2\pi\, n}{N}\right)\right] \tag{3.3}$$

[19] [n] denotes discrete values.

In (3.3), *N* is the filter span, and *n* is the number of points of the filter window, with $0 \leq n \leq N$. The number of points *n* depends on the frequency sampling of the VNA. In our case, the VNA was set from 2 GHz to 18 GHz with 1901 points, which means a sampling rate of 62.5 ps (each point in Figure 59 is taken each 62.5 ps).

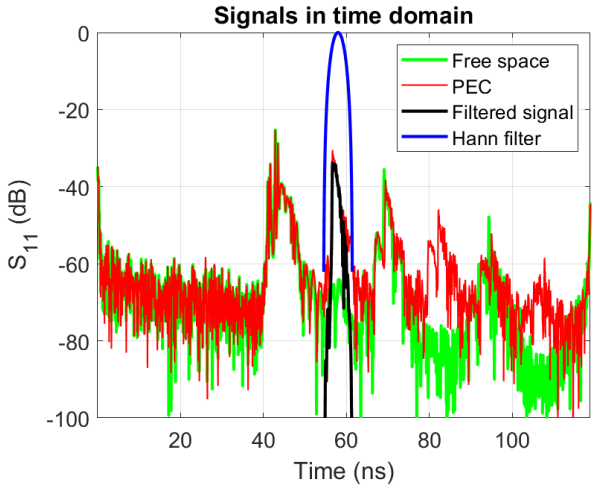

Figure 59. Reflection coefficient in terms of the scattering parameter S_{11} in the time domain when on the support is posed a copper plate (PEC, in red), when the support is empty (free space, in green), Hann window centered at 58 ns with a span of 7 ns (in blue) and the filtered signal (in black).

Figure 60(a) illustrates the comparison between simulation and characterization for Structure 1 (ε_r = 3.0). The characterization is carried out for various 90° φ-rotations of the absorber along its axis. The measurements show an excellent agreement with the simulation results, with unitary absorptivity for the frequencies ranging from 4.4 GHz to 7.7 GHz (FB = 0.55) and absorptivity above 0.9 for the entire C-band of the range 4 GHz – 8 GHz (FB = 0.67). In addition, the absorber is polarization independent.

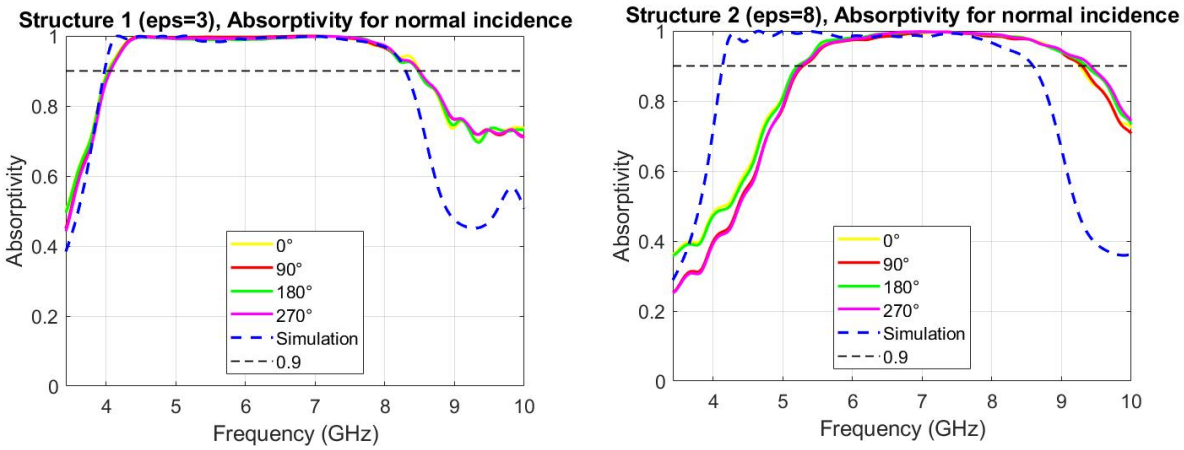

(a) **(b)**

Figure 60. Comparison between simulations and characterizations at DMS for (a) Structure 1, where 0° to 270° are φ-rotations of the absorber along its normal, and for (b) Structure 2 with the same φ-rotations of the absorber along its normal.

Figure 60(b) illustrates the comparison between simulation and characterization for Structure 2 (ε_r = 8.0). The frequency band for unit absorption from 6.5 GHz to 8 GHz (FB = 0.21) is reduced compared to Structure 1. An absorptivity above 0.9 is shown for 5.2 GHz – 9.3 GHz (FB = 0.57). As

for Structure 1, this absorber is polarization independent. The shift of the absorption band towards higher frequencies already pointed out at TRT can also be noticed. In Table 10, the comparison between DMS measurements and Simulation for Structure 1 (ε_r = 3.0) and Structure 2 (ε_r = 8.0) for an absorption level above 90% is presented.

Table 10. Absorptivity comparison for normal incidence between DMS measurements and Simulation for Structure 1 (ε_r = 3.0) and Structure 2 (ε_r = 8.0).

A > 90%	**Structure 1**	**Structure 2**
Measurement at DMS	4.0 GHz - 8.5 GHz, FB = 0.72	5.2 GHz - 9.3 GHz, FB = 0.57
Simulation	4.0 GHz – 8.3 GHz, FB = 0.70	4.1 GHz – 8.6 GHz, FB = 0.71

We now investigate hereafter the frequency shift of Structure 2. The first assumption that could explain this deviation is that manufactured disks diameters are not the same as the designed one. In practice, to check the disk diameter values, a caliper was employed to measure the width of the bottom cavities, as in Figure 11(a), and of the upper cavities, as in Figure 61(b).

(a) **(b)**

Figure 61. Disk diameter measurements for Structure 2. (a) Width of the bottom cavity ($a_{2,1}$) and (b) width of the top cavity ($a_{2,15}$).

In Table 11, the diameter dimensions used for the full-wave simulation and the measured cavities diameters are compared.

Table 11. Comparison between the ideal diameter dimensions used for the simulation and the real diameter dimensions of the pyramids. The values of the pyramids are taken considering a cluster of around 10 various stair-like pyramids.

Layer #	Ideal diameter (mm)	Real diameter (mm)
1	14.3	14.1 ± 0.2
2	13.2	13.5 ± 0.3
3	12.2	12.2 ± 0.2
4	11.4	N.A.
5	10.6	N.A.
6	10.0	N.A.
7	9.4	N.A.
8	8.9	N.A.
9	8.5	N.A.
10	8.0	N.A.
11	7.7	N.A.
12	7.3	N.A.
13	7.0	N.A.
14	6.7	N.A.
15	6.5	6.3 ± 0.3

N.A. = Not Available since the measurements were too tricky or not precise. ± is usually minus.

The reported results ensure that the deviation in frequency of 1.1 GHz (between simulation and characterization) is not due to the size of the disks. Therefore, the second and most likely hypothesis is that the frequency shift is due to the different dielectric permittivity values between filament and disks.

To obtain the real permittivity value of the printed disks, a square sample printed with Preperm DK800 filament and the same printing parameters of the 3D-printed was characterized using a cylindrical cavity method. Figure 62(a) illustrates the cavity with a diameter of 25.05 mm and a resonance frequency of 15.72 GHz connected to the VNA[20]. Two photos of the DK800 sample corresponding to the front and back sides are presented in Figure 62(b) and (c), respectively. The top side appears to be less uniform in appearance than the back side. The reason is that high permittivity filaments are made by incorporating TiO_2 particles into the polymer matrix, which alters the dielectric constant and mechanical properties of the filaments. As a result, the disks are stiff and fragile and can break when detached from the printing support. To avoid such breakages, the manufacturer printed one side of each disk with a lower fill factor. Due to the lower density of the printed disks, their effective permittivity is lower than that of the filament [109].

[20] More details of the characterization setup are given in the Annex A.1.1.

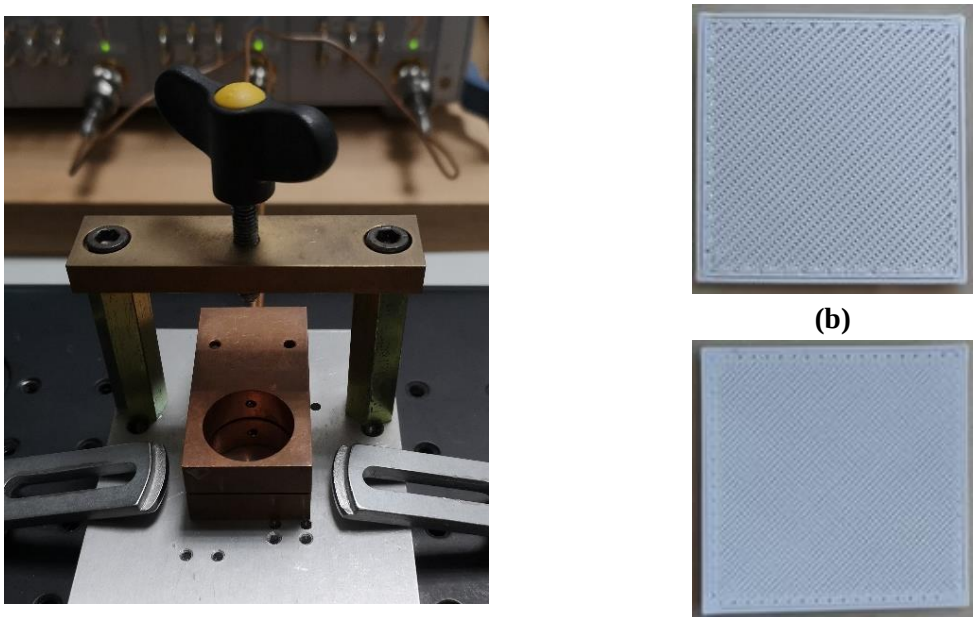

(a) **(b)** **(c)**

Figure 62. (a) Cylindrical cavity used to measure the permittivity, and (b) front and (c) back sides of the square 25 x 25 mm² Preperm DK800 sample.

The characterization result is reported in Table 12.

Table 12. Comparison between the expected permittivity value and the measured values of the Preperm DK800 rectangular sample.

Expected permittivity value	**Real permittivity value**
$\varepsilon_r = 8.0$; $tg\delta = 0.0033$	$\varepsilon_r = 5.1$; $tg\delta = 0.0031$

The effective permittivity of the disks gives a reduced value of about 20% from $\varepsilon_r = 8.0$ to $\varepsilon_r = 5.1$. Retro-simulations of Structure 2 were carried out using this new permittivity value. The comparison between simulation and characterization is depicted in Figure 63. It is worth mentioning that from now on, all simulations consider a permittivity value ε_r of 5.1 instead of 8.

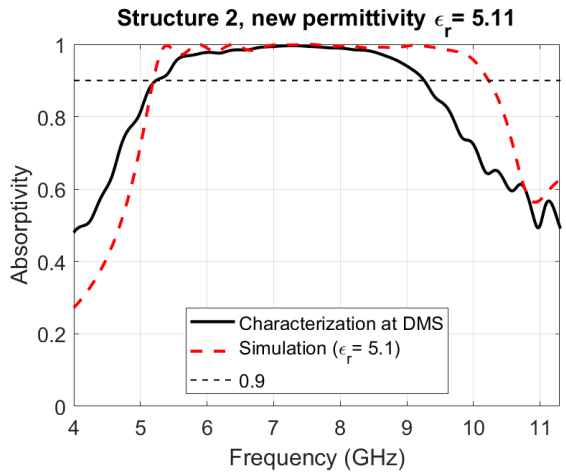

(a)

Figure 63. Retro-simulation for Structure 2 with the new permittivity value of the dielectric disks of 5.1 (in red dashed line) and the characterization at DMS (in black solid line) from normal incidence.

An absorption level above 90% is seen for the characterization from 5.2 GHz to 9.3 GHz (FB = 0.57) while for the simulation the range is 5.2 GHz – 10.2 GHz (FB = 0.65). A relatively good agreement is found out for the low-frequency part. In contrast, for high frequencies, the maximum frequency with an absorptivity of 90% is about 9.3 GHz for the measurements and 10.2 GHz for simulation, showing an absorption band reduction around 1 GHz.

The first hypothesis to explain this band reduction is that top cavities are not resonating. Considering this assumption, new retro-simulations were performed considering the Electrifi filaments of the upper layers as simple PLA (Electrifi base polymer). In the retro-simulations, we increased the cavities with PLA polymer instead of Electrifi, starting from the top cavities and going downwards. The retro-simulated results are displayed in Figure 64, assuming 5 PLA-layers (in dark green) and 4 Preperm DK800 layers on top of the pyramid (in rose). Under such an assumption, a better agreement is achieved between simulation (in red dashed line) and characterization (in black solid line) can be noticed in Figure 64(c).

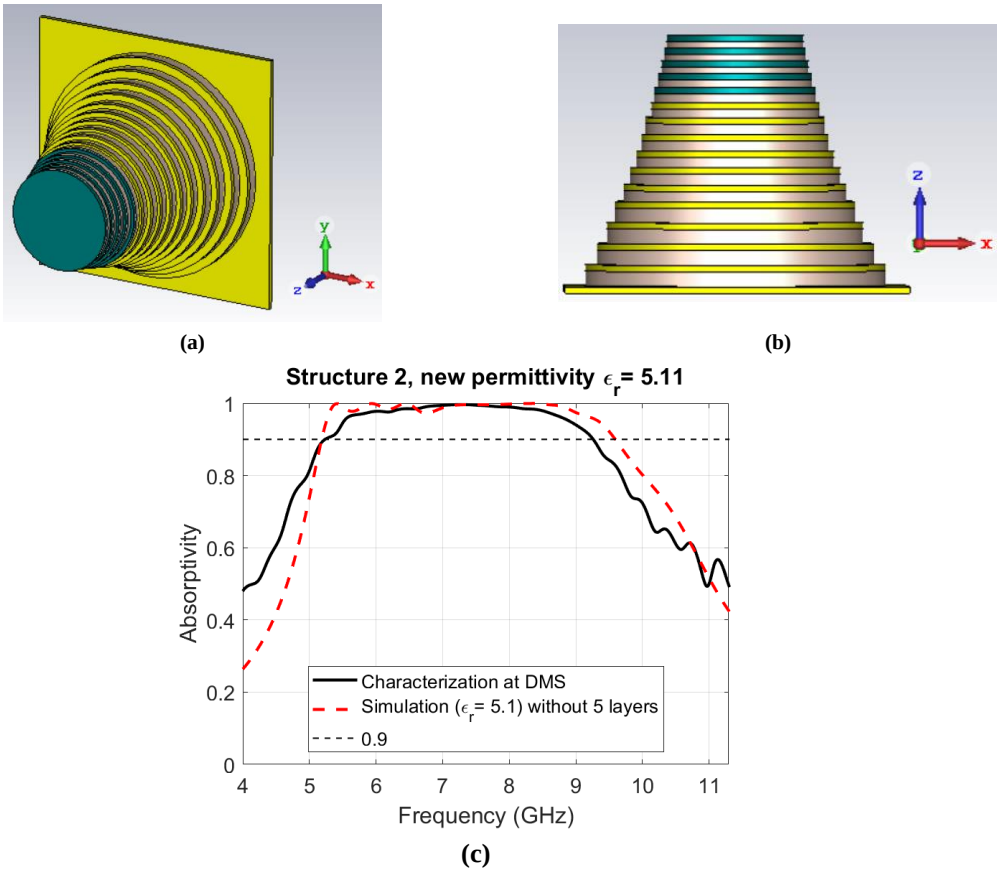

Figure 64. Design of the retro-simulated structure (a) 3D view and (b) front view with 5 layers in green made of PLA (base polymer of Electrifi) instead of the conductive filament Electrifi. (c) Comparison of the frequency dependence of the absorbance between the characterization at DMS (in black solid line) and the simulation considering the new design and the new permittivity value of 5.1 (in red dashed line).

Other structural modifications as melted conductive layers could also explain this frequency shift. However, it was impossible to analyze the multilayered structure with X-ray analysis and conclude further.

After the study for normal incidence, the response of two absorbers for oblique incident angles is presented in the next paragraph. The characterization was performed at TRT since the setup at DMS did not allow an oblique incidence experiment.

3.2.2 Characterization for oblique incidences

The schematic of the new bistatic measurement setup used at TRT for the characterization under oblique incidence is illustrated in Figure 65(a). It is composed of one arm fixed to a rigid sample holder that supports the absorbing metasurface and a second arm that can rotate. As in Chapter 2, two Satimo QR2000 horn antennae are used as emitting and receiving radiating elements fixed at the end of measurements arms. More important, unlike Chapter 2, two lenses[21] (one for each arm) are used to provide an additional directivity gain of 5-10 dB in the 4.5 GHz -10 GHz frequency range and a more focused beam on the SUT as it was possible with DMS setup. The distances for an optimized lens positioning close to the focal point are listed in Table 13. The photo of the bistatic setup is shown in Figure 65(b).

Table 13. Distances for TRT bistatic setup with horn antennas and lenses.

R	65.5 cm	Antenna to SUT distance
R_1	30.0 cm	Antenna to lens distance
R_2	34.0 cm	Lens to SUT distance
T_L	1.5 cm	Lens thickness

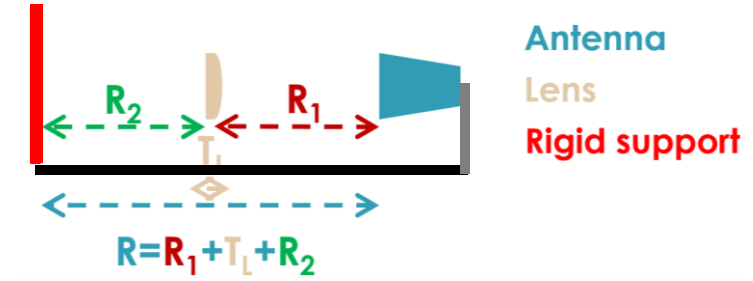

(a)

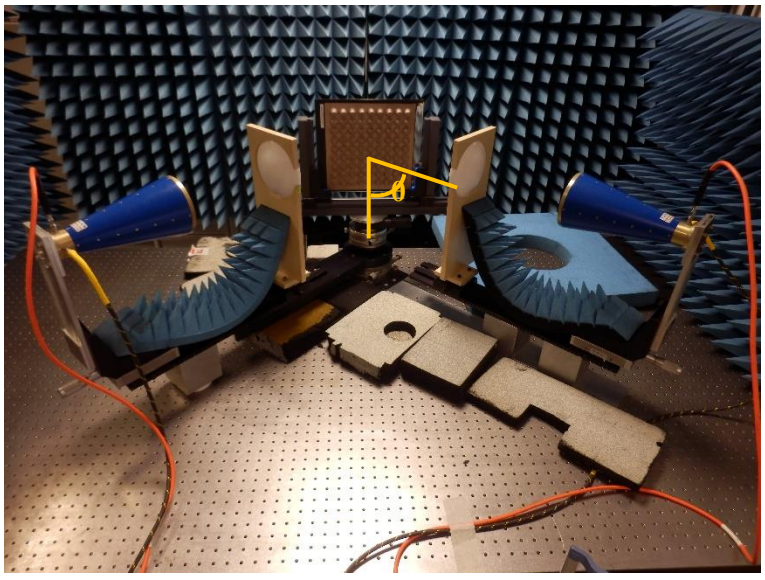

(b)

Figure 65. (a) Schematic of the new measurement setup considering one single antenna for simplicity and the labels for the distances reported in Table 6. (b) Bistatic setup picture with two Satimo QR2000 horn antennas and two lenses. Theta θ definition is reported for clarity.

[21] The lens were designed in internal TRT many years ago. No documentation exists on these lenses.

For the measurement under strict normal incidence, only one arm is used, and the reflection coefficient Γ^{SUT} is computed following (3.4)

$$\Gamma^{SUT} = \frac{S_{11}^{absorber} - S_{11}^{free\ space}}{S_{11}^{free\ space} - S_{11}^{metal}} \tag{3.4}$$

Notice that in (3.4), the scattering parameter is S_{11} instead of S_{21} since only one antenna is used as transmitter and receiver. The first step is to validate this new setup by comparing the measurements performed at TRT to those at DMS under normal incidence, as depicted in Figure 66(a) for Structure 1, and in Figure 66(b) for Structure 2.

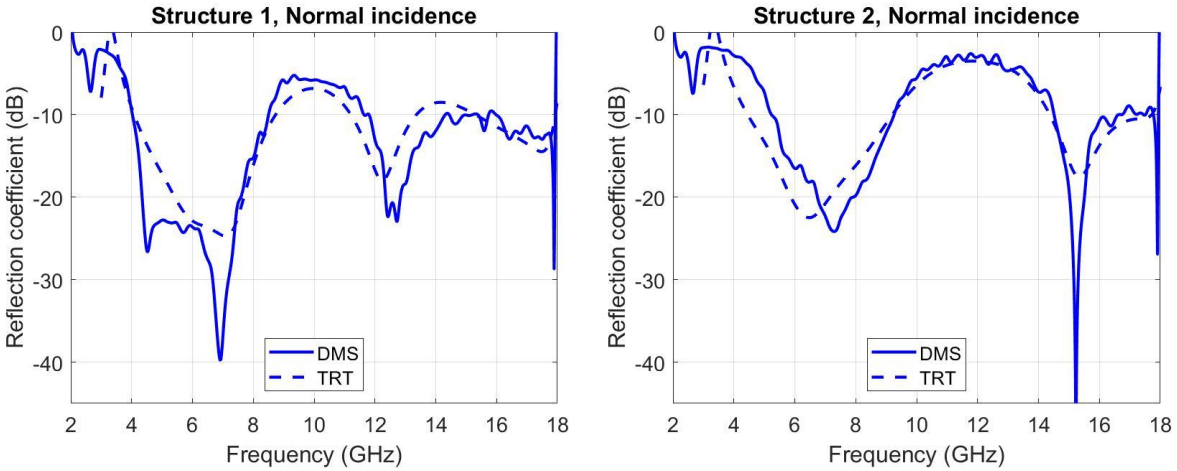

Figure 66. Comparison of the reflection coefficient Γ^{SUT} between (a) the measurements at DMS (in solid line) and TRT with the new setup (in dashed line) of Structure 1 (ε_r = 3.0), and (b) Structure 2 (ε_r = 5.1).

The data are obtained by applying the time-gating technique previously described in post-processing with a window span of 2 ns. The reflection coefficient plots show similar trends confirming the TRT setup validity. One can note, however, some discrepancies near the resonance peaks. For instance, for Structure 1, we could not record the anti-resonant peak at 4.2 GHz with the TRT setup. One can expect that such a discrepancy is due to the lower performances of the lenses at low frequencies, unable to focus the beam at the SUT center.

In addition to the reflectivity spectra, we report the absorptivity spectra for Structure 1, in Figure 67(a) and Structure 2, in Figure 67(b), both for the characterizations at DMS (in black solid line) and TRT (in blue solid line) and for simulation (in red dashed line). For Structure 1, a good agreement between the curves is noticed whereas, the absorption at TRT is reduced and shifted by 0.3 GHz at low frequencies. This problem is not present for Structure 2, for which a better agreement is found between characterizations.

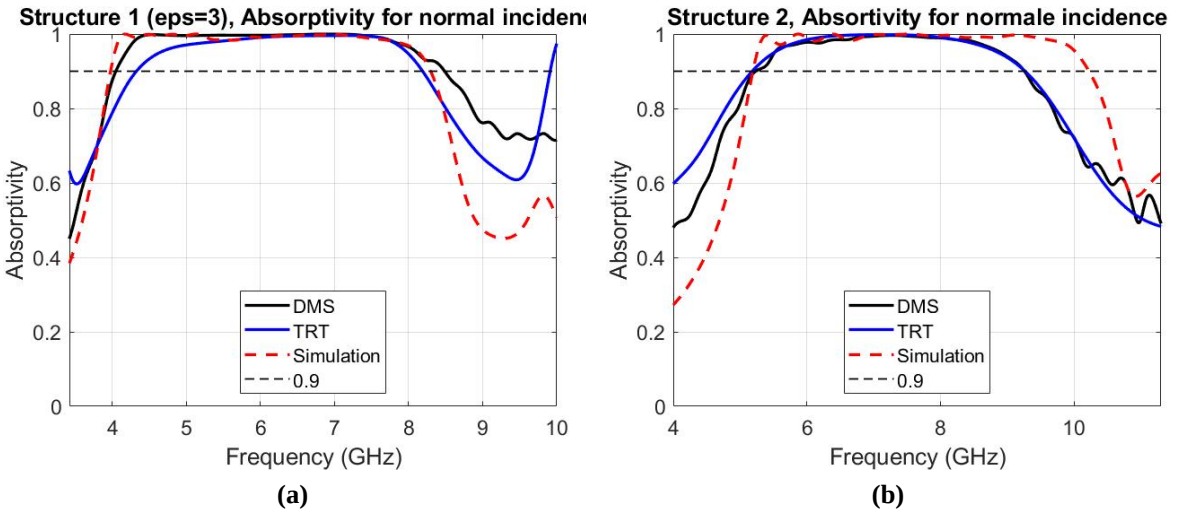

Figure 67. Comparison of the frequency dependence of the absorbance between the characterization at DMS (in black solid line), the characterization with the new setup at TRT (in blue solid line), and the simulation (in red dashed line) for (a) Structure 1 (ε_r =3.0), and (b) for Structure 2 (ε_r = 5.1).

Table 14 summarizes the fractional bandwidths (FB) of the two structures under study achieved in simulation and experiments.

Table 14. Comparison between Structure 1 and Structure 2 for the measurements at DMS, TRT, and the simulations for an absorption level greater than 90%.

A > 90%	**Structure 1 (ε_r = 3.0)**	**Structure 2 (ε_r = 5.1)**
Measurement at DMS	4.0 - 8.5 GHz, FB = 0.72	5.2 - 9.3 GHz, FB = 0.57
Measurement at TRT	4.3 - 8.2 GHz, FB = 0.63	5.3 - 9.3 GHz, FB = 0.57
Simulation	4.0 - 8.3 GHz, FB = 0.70	5.2 - 10.2 GHz, FB = 0.65

Turning now to the oblique incidences, both setup arms are used in these measurements, with the emitting arm fixed (on the right side) and the receiving arm (left side), which is possible to move. When the two arms are close together, the lenses touch each other, limiting the minimum theta angle to 15°. When they are apart, we can achieve incidence angles of 70°. Nevertheless, at these large angles, the antennas are nearly in the line of sight; and it is difficult to discriminate the signal reflected by the metasurface and the signal transmitted directly between the two antennas, which arrive at approximately the same time.

The S_{21} spectra for PEC and Free space conditions are depicted in Figure 68 for an incident angle θ of 15° and vertical (a) and horizontal (b) polarizations, respectively. Both polarizations show a dynamic above 20 dB so that the measurements are meaningful. On the other hand, for θ angles of 65°, the differences are less than 20 dB for vertical (c) and horizontal (d) polarizations. Thus, setup is inappropriate for such a large incidence angle, and the time-gating becomes ineffective. The characterization results are unreliable. Consequently, to calculate the absorbance, equation (3.4) is exploited with S_{21} instead of S_{11} for oblique incidences from 15° to 60°.

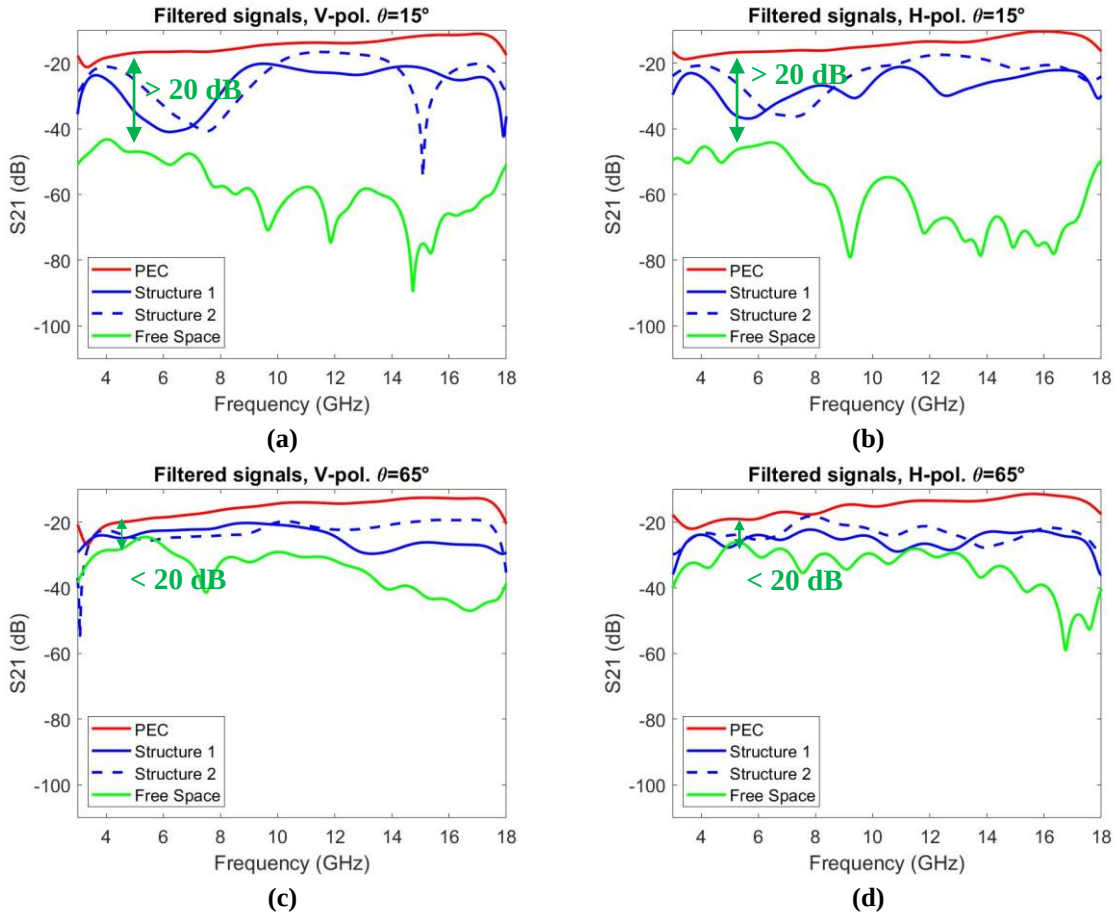

Figure 68. Comparison of the scattering parameter S_{21} for Structure 1 (in blues solid line) and Structure 2 (in blues dashed line) with PEC (in red solid line) and free space (in green solid line) for an incident angle of 15° for: (a) vertical polarization (V-pol.) and (b) horizontal polarization (H-pol.) and for an incident angle of 65° for (c) V-pol. and (d) H-pol..

We now present the mapping of simulations and characterization results for both Structure 1 and Structure 2 by reminding that for the simulation data, we consider Structure 2 composed of cavities of Preperm DK800 (with the disk permittivity value of 5.1) and Electrifi.

In Figure 49, the results for Structure 1 with $\varepsilon_r = 3.0$ are presented for simulations in vertical polarization (a) and horizontal polarization (b) and characterizations in vertical polarization (c) and horizontal polarization (d).

For V-pol., the characterization is in agreement with the simulation. At low frequencies, the shift of 0.3 GHz is due to the lenses, as commented before. The well-defined peaks at high theta are not present, probably due to the imperfect geometries of the cavities at the bottom. Despite this, the higher-order modes increase the absorptivity for high frequency in 7 GHz – 8.5 GHz. Consequently, the fabrication inaccuracy can be seen as an advantage from the absorbance point of view. A 90% absorption level is constant up to 48°. Above, the absorbance decreases linearly from 8.5 GHz to 4.2 GHz.

For H. pol., the absorptivity is less than simulations at low frequencies but similar at high frequencies. For low frequencies, a 90% absorption level is seen for incident angles from 0° to around 20°. Above 20° and above 6.5 GHz, higher-order modes do not resonate, decreasing the absorptivity compared to the simulation. The absorptivity is still greater than 90% between 20° and 42°, but the fractional bandwidth of 0.66 at 20° decreases linearly. Above this angle, the absorbance is less than 90%.

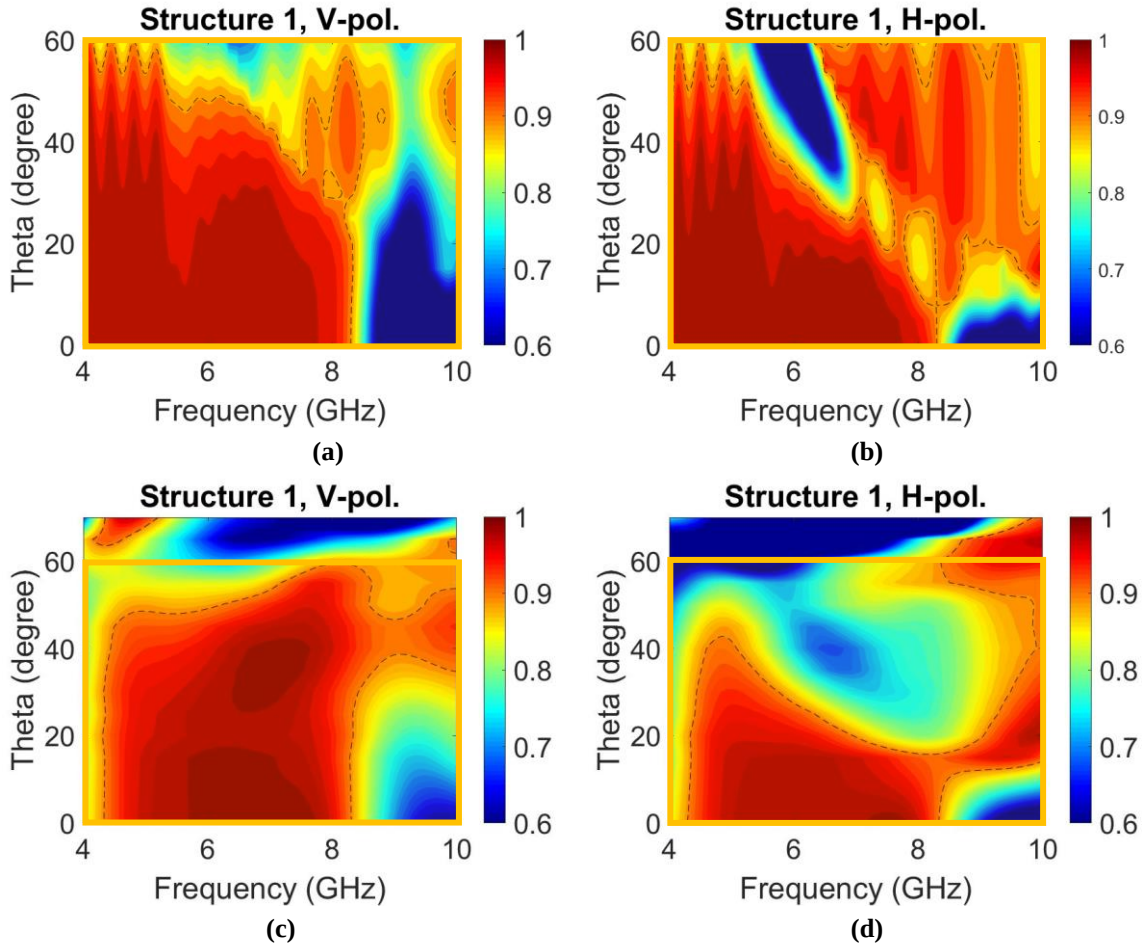

Figure 69. Measurements (with the new setup at TRT) and simulations of frequency and theta dependences of the absorbance for Structure 1. For vertical polarization, the left side, (a) and (c), corresponding to simulation and characterization, respectively. For horizontal polarization, the right side, (b) and (d), corresponding to simulation and characterization, respectively. The black dashed line corresponds to an absorptivity value of 0.9.

In Figure 70, the results for Structure 2 with $\varepsilon_r = 5.11$ (differently from Figure 55 where the permittivity is 8.0) are reported for the simulations in vertical polarization (a) and horizontal polarization (b) and characterizations in vertical polarization (c) and horizontal polarization (d). For V-pol., the characterization is in agreement with the simulation. For low frequencies, an absorptivity above 90% is reached up to up to 60°. For high frequencies, the combination of higher dielectric and higher-order modes allows an absorptivity above 90% up to 60°. The FB of 0.57 remains stable along with the operating band from normal incidence to 58°, where a slight reduction occurs at 6 GHz. For H-pol., the 3D-printed absorber behaves similarly to the simulations, with an FB of 0.55 up to incident angles of 20°. Above, it reduces up to 60°.

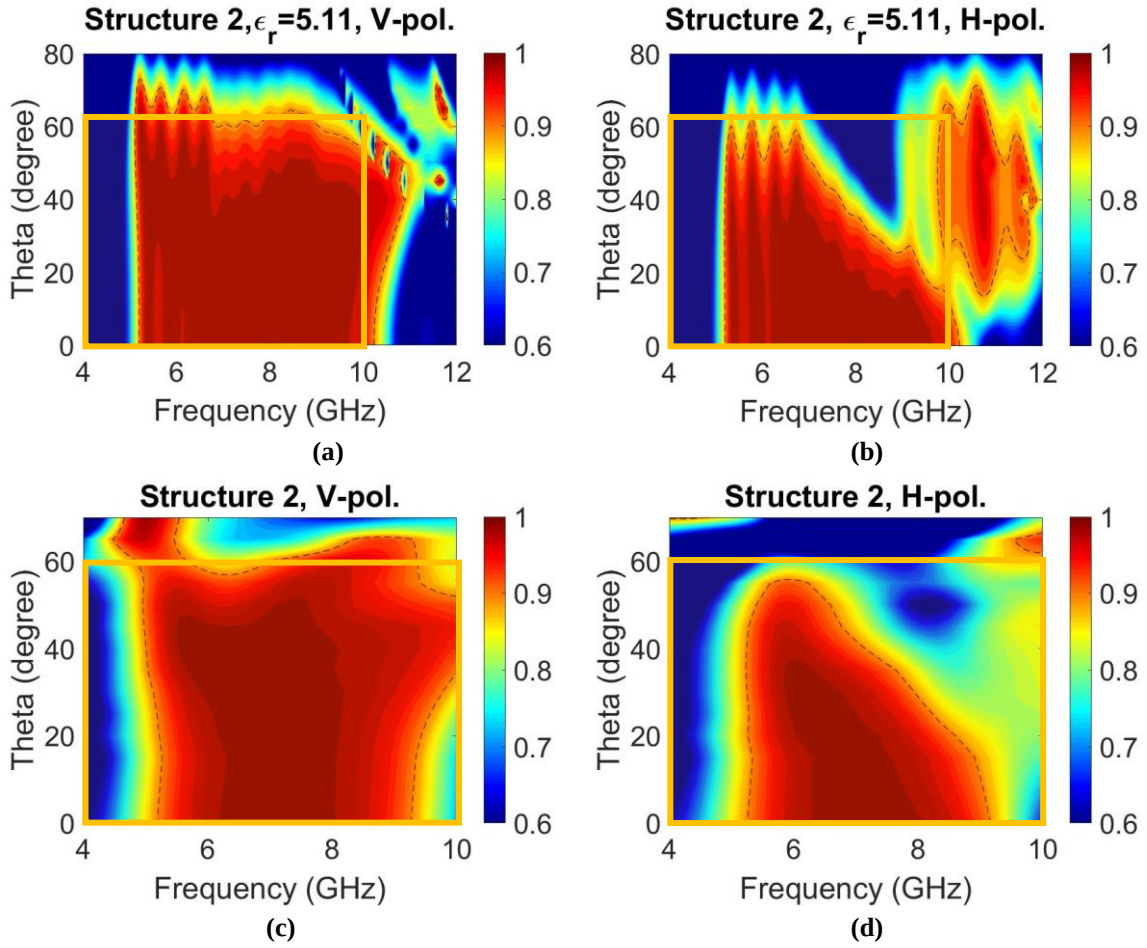

Figure 70. Measurements (with the new setup at TRT) and simulations of frequency and theta dependences of the absorbance for Structure 2. For vertical polarization, the left side, (a) and (c) correspond to simulation and characterization, respectively. For horizontal polarization, the right side, (b) and (d) correspond to simulation and characterization, respectively. The black dashed line corresponds to an absorptivity value of 0.9.

Finally, Figure 71 shows the direct comparison between characterizations in V-pol. for Structure 1 (a) and Structure 2 (b) and in H-pol. for Structure 1 (c) and Structure 2 (d). The angular robustness increases by around 30% for V-pol. when the permittivity of the dielectric layers with initially ε_r = 3.0 is increased of 58%. For H-pol., an overall increase in performances is observed with an enhancement of the angular robustness of around 40%.

These results are in agreement with the increase of angular robustness exploiting dielectrics with high permittivity as stated at the beginning of the chapter.

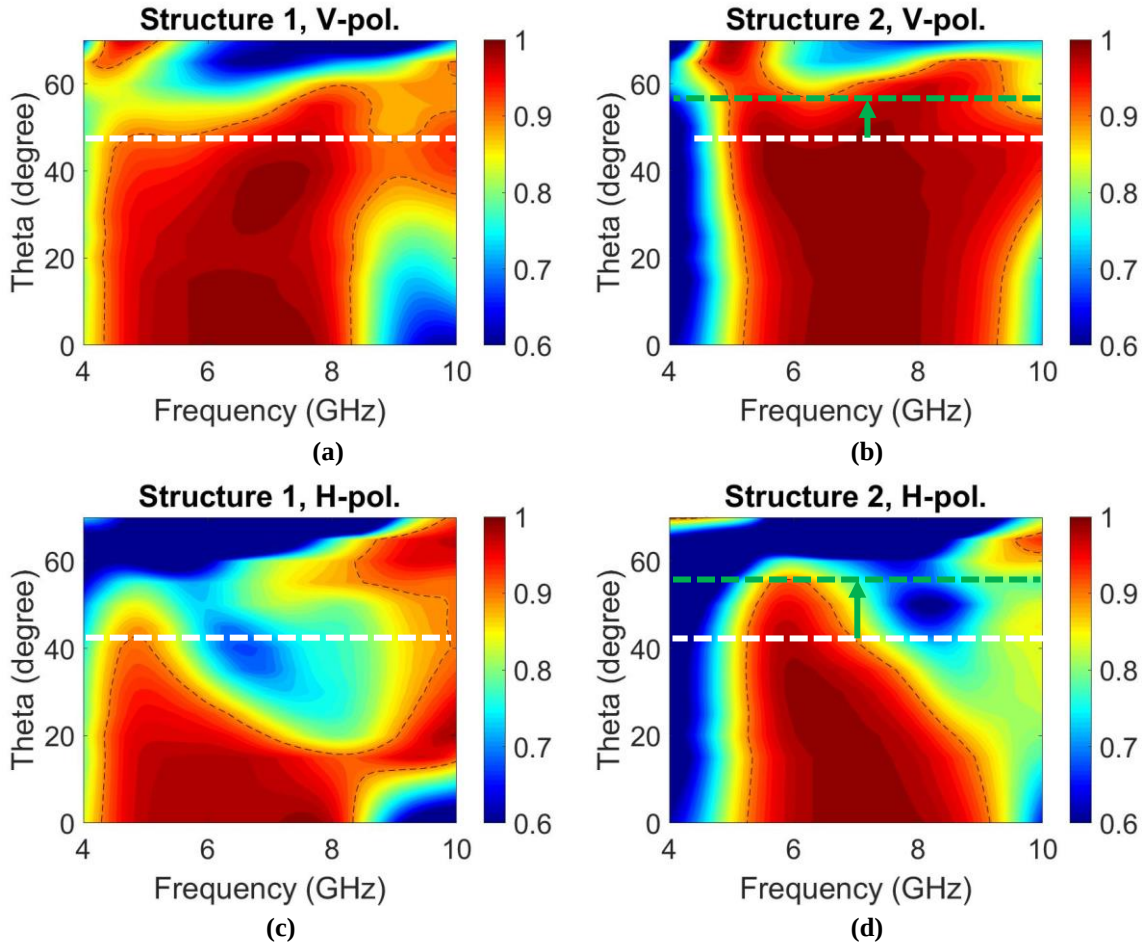

Figure 71. Measurements (with the new setup at TRT) comparison of frequency and theta dependences of the absorbance for Structure 1 for (a) vertical polarization (V-pol.) and (c) horizontal polarization (H-pol) and for Structure 2 for (b) V-pol. and (d) H-pol.. For V-pol., Structure 2 has a 1.7 stronger dielectric, which is 30% more robust than Structure 1. For horizontal polarization, the overall response of Structure 2 is more robust than for Structure 1. The black dashed line corresponds to an absorptivity value of 0.9. The dashed horizontal lines correspond to the maximum angle at which the absorptivity is greater than 90% for Structure 1 (in white) and Structure 2 (in green).

3.3 Comparison with the state of the art

In this section, the comparison between the proposed SL absorbers of the chapter and some of the absorbers presented in Table 1 is presented. The normalized thickness (to the wavelength of the center frequency) over FB, as well as the angular robustness over FB, are considered in this comparison and are depicted in Figure 72 and in Figure 73, respectively. For both pictures, green color represents the desired zone, red color the undesired zone, and orange color the zone with at least a good behavior in terms of either FB, normalized thickness, or angular robustness.

For the first case in Figure 72, the proposed SL structure satisfies the condition of wideband absorptivity above 0.67[22] with a FB of 0.72 corresponding to a larger zone than the interested C-band. Other structures have a better response in terms of FB but higher normalized thickness compared to our absorber. Furthermore, the ability of SL structures to have wide angular robustness, while maintaining a wideband behavior, in terms of FB, is their most notable feature.

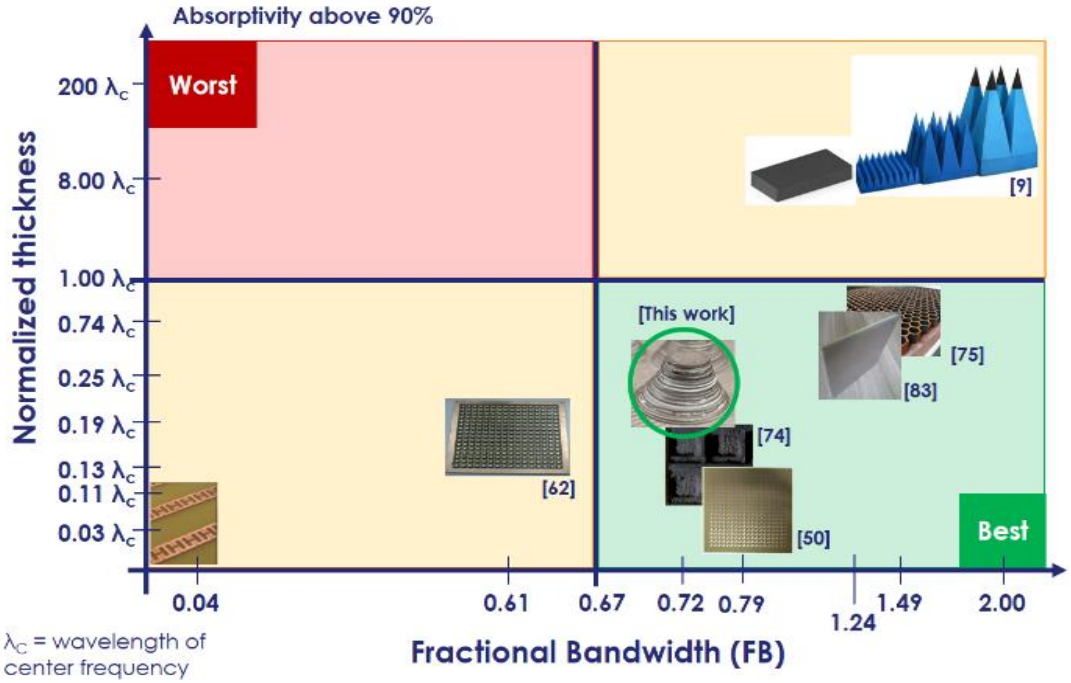

Figure 72. Comparison between the proposed work and the state of the art considering the normalized thickness over the fractional bandwidth. [This work] refers to the prototypes presented in this chapter.

In Figure 73, in which only characterizations for vertical polarization are considered, the comparison between the same structures in Figure 72 ([74] has been changed with [57] since no information on oblique incidence is given in the paper) and our work reflects the high angular robustness SL absorbers. Considering the strict criterion of angular robustness above 45°, classic bottlenecks limit of metamaterial absorbers, in between all the considered structures, only [57] has angular robustness of around 50° while maintaining a low profile. Nevertheless, our SL absorber with a relative permittivity value of around 5.1, achieves higher angular robustness of 58° as well as a low profile. It is worth noting that this achieved result, for an absorptivity above 90%, is extremely rare in the literature and only classic pyramidal foam absorbers are better in terms of angular robustness but with the significant disadvantage in terms of a thick structure with a normalized thickness of the order of many wavelengths.

[22] We remind that an absorber is considered wideband when its FB exceeds 0.67. (one octave).

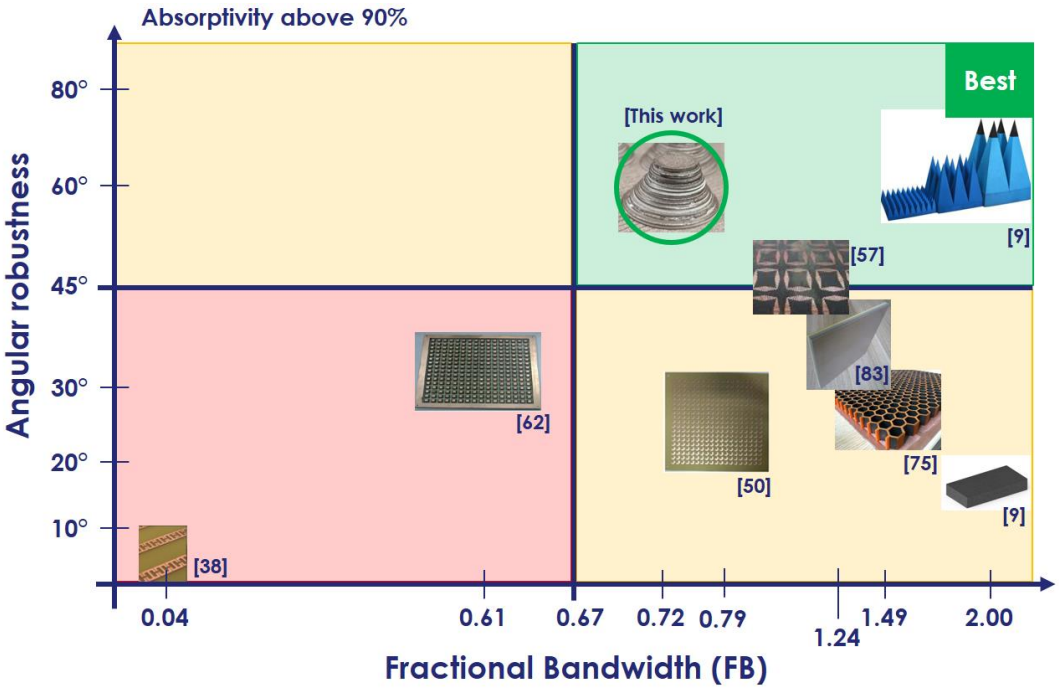

Figure 73. Comparison between the proposed work and the state of the art considering the the angular robustness over the fractional bandwidth. [This work] refers to the prototypes presented in this chapter.

By analyzing the two previous pictures, one can notice that a possible limitation of SL metamaterials is the fractional bandwidth in relation to the normalized thickness (we remind that to increase FB, more cavities need to be added by increasing the total thickness). Nonetheless, the outstanding behavior of SL structures under oblique incidence allows us to consider these absorbers to be the best solution nowadays present in the literature in terms of angular robustness when considering an absorptivity greater than 90%, a FB greater than one octave, and a very thin total thickness.

3.4 Conclusion

Two 3D-printed metamaterial absorbers with stair-like geometry operating in the C-band were presented in this chapter. Manufacturing was carried out using a single conductive filament with a conductivity of 17000 S/m and two different dielectric filaments with a relative permittivity of 3.0 for Structure 1 and 8.0 for Structure 2, both with a tgδ of around 0.004. We demonstrated that high permittivity multilayered structures exhibit better angular robustness compared to low permittivity arrays. In addition, a circular section was chosen to be polarization independent.

To explain these improvements, the power dissipation in both the dielectric and the conductive layers was first illustrated for normal incidence and an incident angle of 50°, pointing out stronger confinement, as expected, for high permittivity structures. Quantitatively simulations for normal and oblique incidences for Structure 2 showed a gain in angular robustness, over Structure 1, from 28° to 50° for vertical polarization (V-pol.) and from 10° to 24° for horizontal polarization (H-pol.).

Then, we discussed the technological options chosen to increase the quality of the fabricated arrays by additive fabrication technique, notably the difference in the printing conditions between the dielectric and conductive layers.

From the experimental assessment side, the preliminary measurements at TRT with the same setup used in Chapter 2 with a larger illuminated area than the absorbing regions have pointed out spurious reflections resulting from a highly reflective frame used as a substrate. To solve this problem, a second measurement session was performed using DMS setup that accurately defines the regions where the reflectivity is probed under normal incidence. Under these measurement conditions and post-processing the measured data through time-gating techniques, a satisfactory agreement was found in terms of absorbance level and frequency windows for Structure 1. In contrast, for Structure 2, a shift towards high frequencies of the absorption band with respect to the simulation result was pointed out. The cause of the shift was found in the different permittivity values between the filaments and the printed disks, and such an assumption was corroborated by retro-simulations using a lower permittivity value ($\varepsilon_r = 5.1$) than the value initially assumed for the simulation ($\varepsilon_r = 8.0$). Additional retro-simulations were also performed to analyze the reduction of the absorption window in the upper part of the reflectivity spectra with presumably 4 top cavities that are not resonating correctly. Finally, the results of the experimental assessment carried out at TRT for oblique incidences were presented with the development of a new bi-static setup using dielectric lenses to better focus the probing beams onto the samples. It was shown experimentally that a 58% permittivity increase with respect $\varepsilon_r = 3.0$ improves the incidence angle robustness by 30% for V-pol. and an overall better response for H-pol.

Chapter 4: Several concepts for low frequency absorbers

The importance of absorbers operating at low microwave frequencies can be identified by numerous businesses and research organizations. The primary challenge is the design of ultra-thin structures that resonate at long wavelengths. Various solutions to this challenge are examined in this chapter. We begin by considering the possibility of employing vertical integration by stacking cavities of different sizes as in the previous two chapters. Then, we consider the planar integration of resonant structures usually exploited for dual or triple bands absorbers with the originality of using FDM commercial dielectric and conductive filaments to increase the resonant peak's bandwidth. In the third stage, we investigate the interest of using ad-hoc materials for elemental structures such as a dielectric slab. Magnetic losses are added, targeting total absorption at a lower frequency for non-magnetic materials solutions. Finally, two utilizations of magnetic materials as bases for full-dielectric cylinder resonators are discussed. Both structures are called Chess-Based metamaterial absorbers (CBMMA). The first operates at low frequencies (L-S bands), while the second is wideband, with an absorption spectrum extending over a decade between 2.4 and 26 GHz (S to K bands).

4.1 From vertical to horizontal resonances

The first step of our study for the absorbers operating at low frequency, targeting unitary absorbance for L-S bands (1 GHz – 2 GHz for L-band and 2 GHz – 4 GHz for S-band), concerns the design of a multilayered stair-like (SL) structure, as proposed in Chapter 2 and Chapter 3 by using however higher dielectric permittivity values $\varepsilon_r = 12$. In this first section, we consider an SL absorber with a circular section as in chapter 3. We further explore the limitations of the vertical integration and the fabrication issues by pointing out the difficulty of implementing such SL in the current mastery of printing technology processes.

The guidelines for designing a 3D-printed SL absorber were discussed in detail in Chapter 3. We concentrate on the frequency range of 1 GHz to 4 GHz by designing a structure with 20 pairs of conductive (in yellow) and dielectric (in rose) layers, as depicted in Figure 74(a). The conductive filament is Electrifi [70], with a conductivity σ of 17000 S/m, while the dielectric filament is Preperm DK1200, with relative permittivity of the filament of ε'_r of 12 and tgδ of 0.0029 [69]. The choice of a high permittivity for the dielectric filament is favorable to operate in the long-wavelength regime since the layer dimensions are inversely proportional to the permittivity. In fact, according to equation (3.1) in Chapter 3, achieving a resonance at approximately 1 GHz (λ_0 of 300 mm) with a high permittivity appears a welcome feature for reducing the diameter with respect to the operating wavelength. With this permittivity value, the cavity diameter at the bottom is 48.1 mm and decreases down to 11.4 mm for the cavity at the top. The period is 50.1 mm, with thus an additional 1 mm on both sides of the bottom cavity. We assumed a constant thickness of 2.3 mm for all the dielectric layers, which was found by full-wave simulations. All conductive layers have the same thicknesses of 0.3 mm. The overall structure is 92.3 mm thick.

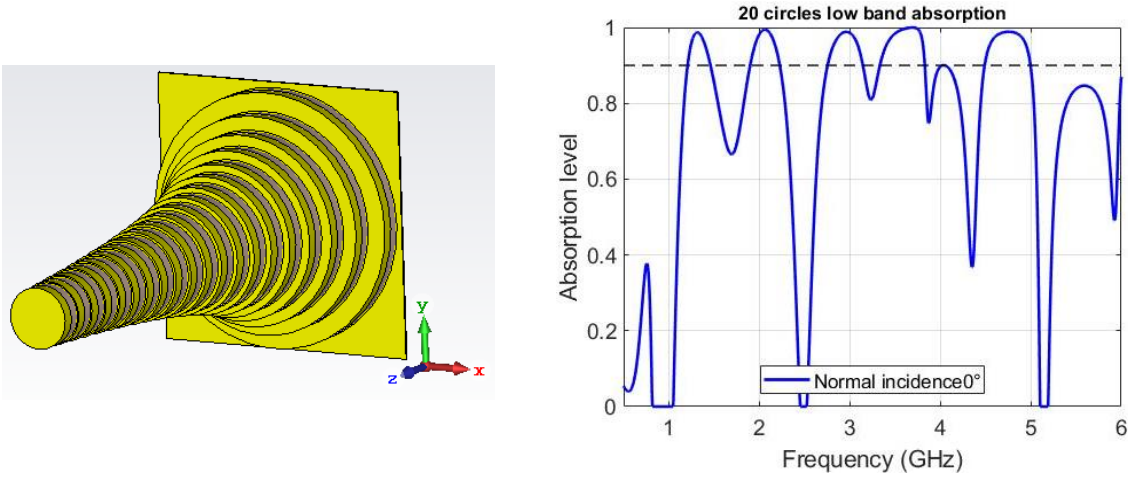

(a) **(b)**

Figure 74. (a) Design of the stair-like (SL) structure for L and S bands with circular section constituted of 20 pairs of conductive (Electrifi, with a conductivity σ = 17000 S/m, (in yellow) and dielectric (Preperm DK1200, with permittivity of ε'_r = 12 and tgδ = 0.0029, (in rose) filaments. (b) The absorbance across the frequency range from 0.5 to 6 GHz, aiming for an absorptivity greater than 90%. The black dashed line indicates an absorption level of 0.9. (90%).

The absorbance as a function of frequency was calculated as in the previous chapters using CST Microwave Studio with periodic boundary conditions and Floquet ports as excitations. Unless otherwise specified, the simulations throughout the chapter are conducted under the same conditions. In Figure 52(b), the simulation results indicate that the structure exhibit four unitary absorption peaks across L and S bands but with pronounced anti-resonance dips. Numerous other simulations involving removing or adding layers have been performed to avoid the anti-resonances in the 1-4 GHz frequency band, notably at 2.5 GHz. None has resulted in an ultra-wideband response over the frequency bands of interest (1 - 4 GHz). More important, the 3D printing technology envisaged here for manufacturing such a metamaterial absorber would face considerable difficulties. Besides the difference in melting temperatures of dielectric and conductive filaments as discussed in Chapter 2, increasing the permittivity of a dielectric filament means increasing the charge rate of ceramic powders (for example, TiO_2 powders) into the polymer matrix, which yields to very stiff and brittle filaments and makes the printing very challenging, as described in Chapter 3. In the current technological state of the art, these issues lead us to conclude that SL metamaterial absorbers are not yet a feasible option for absorbers operating in L and C bands.

We will now investigate whether the in-plane structuring of the metal layer layout could represent a more suitable solution to use in place of the vertical structuring. As a preliminary remark to this new study, let us remind that in the literature, several groups have presented FSS-type pattern with multiple resonances in a single unit cell as in [110], [111]. Numerous attempts were made to design miniaturized MMA [53]-[54]. In particular, several authors have proposed structures similar to a spiral antenna that are intrinsically wideband [113], such as the one proposed in [93], where a rectangular spiral absorber has been exploited to have different resonances in the horizontal plane.

Hereafter, we exploit a similar idea of structuring the metallization of the top patch to have more resonances within the horizontal spatial axis. In addition, it is believed that commercial conductivity filaments, with lower conductivity compared to classic metallic materials as copper, could increase the bandwidth of the absorption band with FDM as a fabrication process. To this aim, we report the comparison between a single uniformly metalized patch and a slotted top metal layer. This structure is called recursive slice absorber (RSA) and comprises 3 inversed L-shaped strips and one square-shaped metal layer. The goal of the design is to increase the bandwidth as in [114], with

three rectangular cavities that resonate at three different frequencies and one square cavity that resonates at another frequency. By this means, the RSA should exhibit 4 different broad resonant peaks.

Single patch and L-shaped strips are made of Electrifi as conductor material for the ground plane and the patterns printed on top of a Preperm DK1200 dielectric layer. As a first stage, let us consider Figure 75, which illustrates patch antenna edge effects [61]. The formula to calculate the effective length L_{eff} of the resonant rectangular patch side is described by (4.1)[23].

$$L_{eff} = L + 2\Delta L \tag{4.1a}$$

$$\Delta L = 0.412 \frac{\left(\varepsilon_{reff} + 0.3\right)\left(\frac{W}{h} + 0.264\right)}{\left(\varepsilon_{reff} - 0.258\right)\left(\frac{W}{h} + 0.8\right)} h \tag{4.1b}$$

Where L is the physical length of the resonating side found with equation (2.7), in Chapter 2, L_{eff} and ΔL are the effective length of the patch and the additional length due to fringing fields, respectively, W is the non-resonating side of the rectangular patch described by (4.2), ε_{reff} is the effective dielectric constant written as (4.3) and h is the patch thickness.

$$W = \frac{c_0}{2 f_r} \sqrt{\frac{2}{\varepsilon_r + 1}} \tag{4.2}$$

$$\varepsilon_{reff} = \frac{\varepsilon_r + 1}{2} + \frac{\varepsilon_r - 1}{2} \sqrt{1 + 22 \frac{h}{W}} \tag{4.3}$$

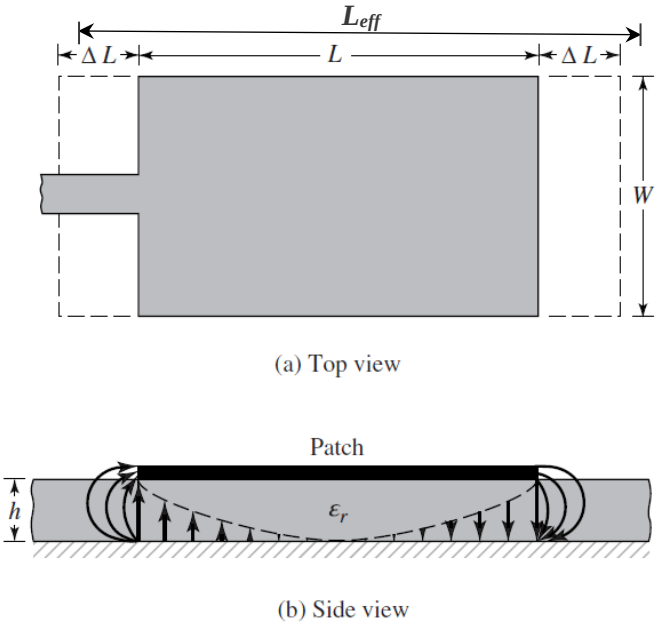

Figure 75. (a) Top view of a patch antenna illustrating the physical length L of the resonating side and the effective length L_{eff} = L + 2ΔL caused by the fringing fields on both sides of L. W denotes the patch non-resonant side. (b) Side view of the patch antenna with h denoting the thickness and ε_r representing the relative permittivity of the dielectric substrate. Round arrows indicate the fringing fields that result in the additional lengths ΔL. The picture is from [61].

[23] In contrast to Chapter 2, where the fringing fields for a square multilayer structure are complex and ΔL is difficult to define, the structure in this section is composed of a single layer, and equation (4.1) is used.

The corrections to consider the fringing field were first applied to the single patch radiating element in Figure 76(a). We exploited (4.1) to find the effective length L_{eff} value of 51.4 mm assuming a thickness h of 3.8 mm found through a parameter sweep in full-wave simulation. The value of 51 mm, which assures to have the same dimension of the RSA, was used in the simulation. The period has been determined to have unitary absorptivity of the structure and avoid grating lobes for normal incidence at 4 GHz. From [115], one can find the condition $p < \lambda_0$, for normal incidence, so the period must be less than 75 mm, in our case, a period of 60 mm optimizes the absorptivity of the patch absorber.

For the RSA in Figure 76(b), the ground plane dimension corresponding to the unit cell dimension has the same 60 mm period. The lengths of the resonating sides of the L-shaped patterns were obtained following (4.1) and considering a thickness of 15.5 mm found with a parameter sweep in full-wave simulations. We imposed W to 8 mm to limit the total width to 51 mm and reduce mutual coupling between the strip lines. Additionally, for the L-shaped geometries, the choice of a width of 8 mm is motivated by the increase of the bandwidth around 3.3 GHz as visible in Table 15 in which the real lengths L used for the simulation, and the effective theoretical lengths L_{eff} are listed for absorption frequencies ranging from 0.9 GHz up to 3.3 GHz. The effective lengths in relation with the frequency are calculated by using equation (2.9) with L_{eff} instead of L.

Table 15. For five frequencies, the lengths of the RSA are compared between the real length (used in simulation), the physical length (L) and the effective length from (4.1).

Absorbed frequency (GHz)	**L for the design (mm)**	**L_{eff} theoretical from (4.1) (mm)**
0.9	51.0[24]	60.4
1.3	39.0	41.8
1.8	27.0	30.2
3.0	15.0	18.1
3.3	8.00	17.0

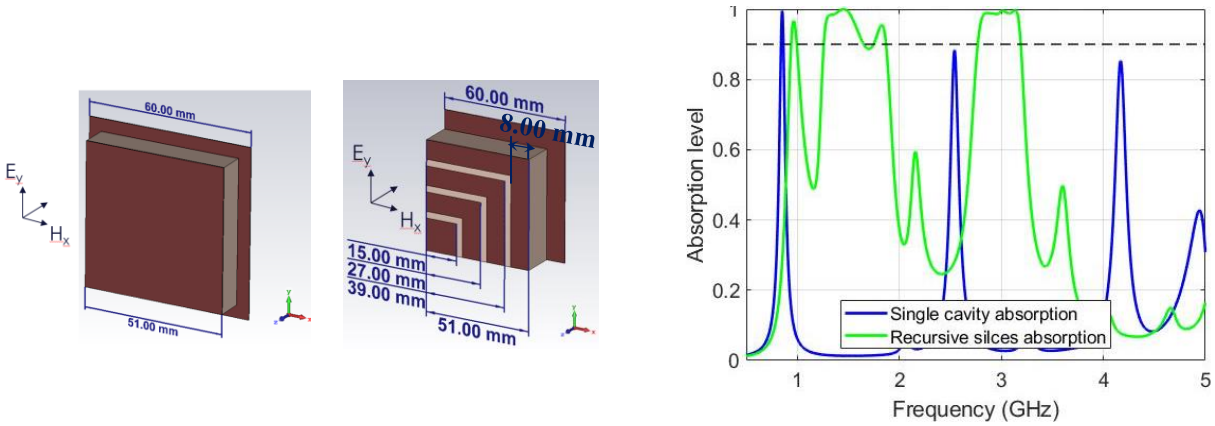

(a) **(b)** **(c)**

Figure 76. (a) MIM (Metal-Insulator-Metal) absorber with a period of 60 mm (ground plane of 60 x 60 x 0.3 mm^3) a square dielectric layer of 51 x 51 x 3.8 mm^3 with a conductive screen of the same dimensions. (b) RSA (Recursive Slice Absorber) has the same unit cell and ground plane dimensions and a dielectric thickness of 15.5 mm. The top conductive layer pattern is constituted of 3 L-shaped strips and a square patch whose dimensions are listed in Table 15. For both (a) and (b) brown color is the conductive filament Electrifi with σ = 17000 S/m and rose color is the dielectric filament Preperm DK1200, with ε'_r = 12 and tgδ = 0.0029. (c)Comparison for the frequency dependence of the absorbance between the single cavity (MIM) in blue, with three peaks corresponding to fundamental mode and odd higher modes, and the RSA operating as a triple band absorber.

[24] The value of 51 mm was chosen to have an appropriate comparison with the square patch dimensions.

Figure 76(c) shows the frequency dependence of the absorbance for the single patch in blue, and for the RSA in green. For the patch absorber, the first absorption peak is at 0.84 GHz rather than 0.9 GHz because the actual design length of 51 mm is slightly greater than the theoretical physical length of 48.6 mm calculated from equation (2.9). The two subsequent peaks correspond to higher-order odd modes resonating at 2.52 GHz (third) and 4.2 GHz (fifth), respectively.

For the RSA, with three L-shaped structures and one square patch, several distinct absorption bands with nearly unitary absorptivity can be noticed. However, their interpretation, notably in terms of the dimension of the various resonating elements, is not straightforward. Overlaps occur between higher-order modes in large resonant rectangular cavities and fundamental modes in small ones.

Furthermore, the first absorption peak is at 0.94 GHz with a maximum of around 0.95, while unit absorption was achieved at 0.84 GHz for the uniformly metalized layer. These slight differences can be explained by the real length of the largest L pattern (51 mm)[25], slightly smaller than the theoretical physical length (52.2 mm), and the thickness of the dielectric substrate that was adjusted to achieve maximum absorbance across the entire band of interest and not just for this peak. We find a second absorption band at higher frequencies with a first peak at 1.3 GHz attributed to the intermediate L pattern whose length is 39 mm. This absorption band with levels above 90% starts from 1.25 GHz up to 1.8 GHz that corresponds to the response of the third L shape strip whose length is 27 mm. The fact to link the relevant dimensions (here, the length of the strip lines matching the half-wavelength) to absorption spectra features gives some indication about the resonant modes that are involved in the electromagnetic response. However, it is worth noting from the layout that the various planar resonators are nearby and that they can be coupled via the narrow slots between them.

At last, we find a third quasi-flat band can be noted centered around 3 GHz. This absorption window starts from 2.75 GHz due to the third-order resonant mode of the longest L-shaped cavity that resonates at 2.82 GHz. The central frequency of 3 GHz corresponds to the resonance of the square patch size. The upper frequency around 3.3 GHz seems to correspond to resonance effects that occur for lengths of 8 mm equal to the value W of the width of the L sides.

In conclusion, using the recursive slice absorber concept could be a good alternative for designing a perfect absorber in the low frequency part of the microwave spectrum. With respect to the vertical integration for which there is no direct interaction between the stacked MIM type micro-resonator, it appears, however, that the scattering of the impinging electromagnetic wave with the various planar resonant structures is complex and involves not solely the dominant modes but higher-order modes and edge coupling effect via the slots. As for the vertical integration, the use of relatively low conductivity and high dielectric filaments also affects the broadening of the elemental resonance bands. The counterpart with respect to these potential advantages is the complexity in the design rules with the goal in the present work to cover the whole L and S bands by keeping an insensitivity to polarization by implementing L-type resonators. In addition, intrinsically, the multi-dimension of patterns yields a multiband operating well separated over the 1-4 GHz band of interest. For all these reasons, in the next stage, we investigate the possibility of using a magneto-dielectric material, which combines dielectric and magnetic losses.

[25] We remind that for this numerical calculation W is set to 8.

4.2 Increase of the absorptivity at low frequency with magnetic losses

As previously mentioned, it is challenging to engineer either multi-stacked cavities or planar structured metal patterns printed onto a grounded dielectric slab to achieve quasi-unitary absorption over the L and S bands even when conductive and dielectric losses are considered. Consequently, in the following section, attention will be paid to the use of magneto-dielectric layers [116], [117].

Hereafter, we consider for simplicity a single slab composed of a lossy material of thickness d above a PEC (Perfect Electric Conductor) metal plate as ground plane as in Figure 77(a). The lossy material has $\mu = \mu_0 \mu_r$ ($\mu_r = \mu'_r - j\,\mu''_r$ with $\mu'_r > 1$), and with $\varepsilon = \varepsilon_0 \varepsilon_r$ ($\varepsilon_r = \varepsilon'_r - j\,\varepsilon''_r$).

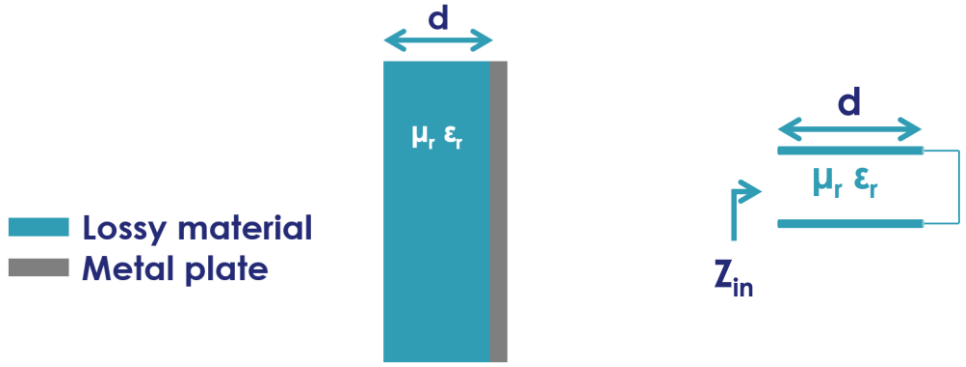

(a) **(b)**

Figure 77. (a) Schematic of the absorber composed of a lossy material of thickness d (in blue), with $\varepsilon_r = \varepsilon'_r - j\,\varepsilon''_r$ and $\mu_r = \mu'_r - j\,\mu''_r$, and a PEC (Perfect Electric Conductor) (in gray), and (b) the corresponding transmission line with input impedance Z_{in}, the substrate with its characteristic impedance ($\eta = (\mu_0\mu_r/\varepsilon_0\varepsilon_r)^{1/2}$) loaded by a short circuit that corresponds to the metal plate.

The reflection coefficient Γ was introduced in equation (1.4). Hereafter, it expressed in the transmission line terms by emphasizing the normalized input impedance z_{in} expressed by (4.4) [14]:

$$\Gamma = S_{11} = \frac{Z_{in} - \eta_0}{Z_{in} + \eta_0} = \frac{z_{in} - 1}{z_{in} + 1} \tag{4.4}$$

where η_0 is the free space impedance, Z_{in} corresponds to the input impedance, as in Figure 77(b), and z_{in} is the normalized impedance to free space Z_{in}/η_0. The expression for the input impedance for a lossy material with magnetic behavior is written as (1.8b) that divided by the free space impedance η_0 leads to (4.5)

$$z_{in} = \sqrt{\frac{\mu'_r - j\,\mu''_r}{\varepsilon'_r - j\,\varepsilon''_r}}\, tanh\left(j\frac{2\pi}{\lambda_0}\sqrt{(\mu'_r - j\,\mu''_r)(\varepsilon'_r - j\,\varepsilon''_r)}\,d\right) \tag{4.5}$$

To have zero reflectivity, we need (4.5) to be equal to 1. Five parameters could allow this:

- Thickness *d* of the lossy material
- Real part of permittivity ε'_r
- Imaginary part of permittivity ε''_r
- Real part of permeability μ'_r
- Imaginary part of permeability μ''_r

Various papers discuss optimizing these five factors to achieve zero reflection [118], [119]. Beyond the optimization of these geometrical and parameters, it also appears necessary to consider the material issues and, notably, the material parameters chosen for the absorber design are realistic. Let us remind one of the Pd.D. goals, the development of a new printable material for absorbing a low frequency band. To this aim, we discussed with TRT chemical experts[26] to know the value range that could be reached for 3D-printed magneto-dielectric material properties. Considering the frequency of 2 GHz, a thickness d of 5 mm to reduce the overall dimension, and a value of μ'_r and μ''_r equal to 2.50 was chose. As a result, the best combination of ε'_r and ε''_r values was obtained using Matlab, with 7 and 0.84 for the real and imaginary parts of the relative permittivity, respectively. Thus, the five parameters required to achieve quasi-zero reflectivity at 2 GHz are listed in Table 16.

Table 16. Values of the 5 parameters (thickness d, real and imaginary permittivity, ε'_r and ε''_r, real and imaginary permeability, μ'_r and μ''_r) that were used to achieve almost zero reflectivity at 2 GHz.

Parameter	Value
d	5 mm
ε'_r	7.00
ε''_r	0.84
μ'_r	2.50
μ''_r	2.50

Once the most suitable combination of values is found, an automatic fit is used to generate the material curve as in Figure 78(a) [120].

For the simulations, two approaches are used. The first is the full-wave simulation, while the second is a Transmission Line method (TL) developed with MATLAB expanding equation (4.4) in equation (4.6), which is expressed in terms of real and imaginary parts of the input impedance [121].

$$|\Gamma| = \sqrt{\frac{(Re\{z_{in}\}-1)^2 + (Im\{z_{in}\})^2}{(Re\{z_{in}\}+1)^2 + (Im\{z_{in}\})^2}} \tag{4.6}$$

[26] We would like to thank Lilia Qassym for her useful advices in material domain.

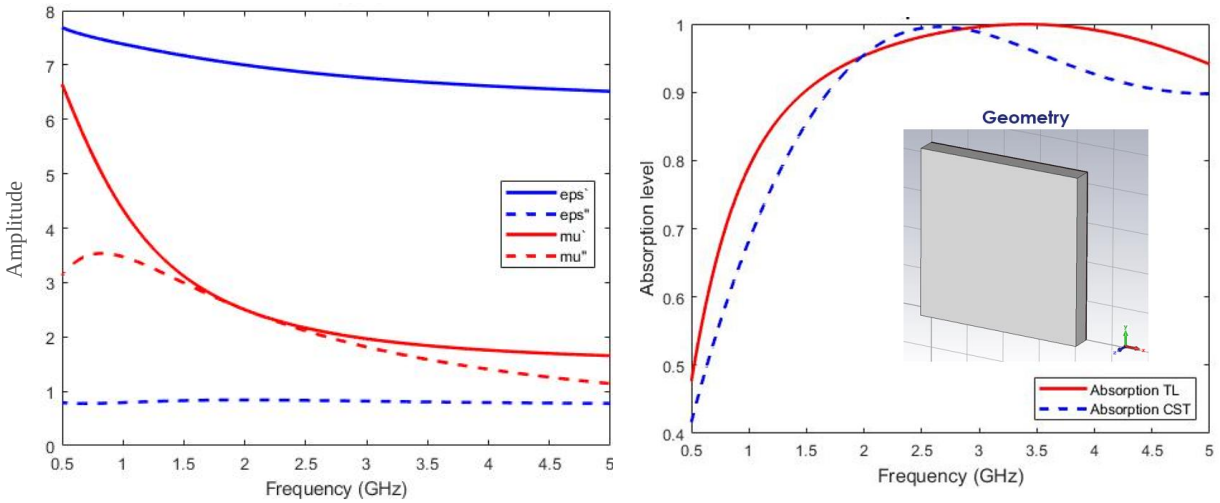

(a) **(b)**

Figure 78. Dispersion characteristics (a) permittivity real (in blue solid line) and imaginary (in blue dashed line) parts, permeability real (in red solid line) and imaginary (in red dashed line)parts, (b) Comparison of the absorption level in normal incidence between the transmission line (TL) model (in red solid line) from (4.6) and (4.4) and the full-wave simulation (in blue dashed line). In the inset a 5 mm-thick magneto-electric material (in gray) onto a PEC.

The absorbance versus frequency is plotted in Figure 78(b) (TL model in red and full-wave simulation in blue lines) for the structure presented in the inset. The bilayer material geometry consists of a 5 mm-thick slab using the magneto-dielectric filament and a PEC plate at the bottom. An absorption level over 0.9 is found for the frequency range 1.6 GHz - 4.5 GHz (FB = 0.95) in normal incidence for the simulation in full-wave. The difference between full-wave simulation and TL results stems from the difference in the E-field configurations close to the metal plane considered here as a PEC.

To sum up, to improve the absorptivity in the low frequencies band, the following constitutive material properties of the thin layer with $\varepsilon_r = 7.0 - j\ 0.84$ and $\mu_r = 2.5 - j\ 2.5$ at 2.5 GHz, can absorb more than 90% of the incident energy between L and S bands. Moreover, the thickness of the magneto-dielectric layer of 5 mm is relatively small with respect to the wavelength ($\lambda/35$, with lambda of 1.6 GHz).

4.3 Practical examples for wideband (L to C bands) and ultra-wideband (S to k bands) metamaterial absorbers exploiting magnetic losses

The results presented in this section are an initial study on full-dielectric structures whose absorbance is enhanced with magnetic materials. This study was interrupted since the interest on this Ph.D. project focused in a different direction. Thus, for the simulations in this section, we consider an absorption level above 90% and 80%.

Hereafter, we evaluate full-dielectric cylindrical metamaterial absorbers, which are widely used in the literature to achieve wideband absorptivity [76]. To this purpose, we consider full-dielectric resonators by reminding us that magnetic materials help improve the performances of an absorber, as described in [122].

Let us remind that we aim to design a metamaterial absorber operating at low frequencies (1 – 4 GHz). To do so, a cylindrical resonator absorber fully made of carbon-loaded ABS (CLABS) filament, TW-CON175BK of the Torwell Technologies [123], whose properties obtained from [76] are depicted in Figure 79, and a PEC layer at the bottom of a square base is used for the full-wave simulations.

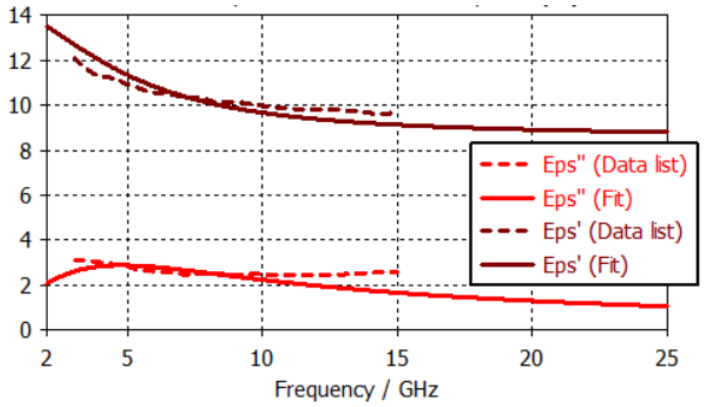

Figure 79. Dispersion characteristics of the complex permittivity of TW-CON175BK filament. The plot corresponds to the used filaments for the full-wave simulations that follow in CTS Microwave Studio 2019.

Equation (4.7) is exploited, as described in [61], to approximate the resonant frequency of the pillar array. Then, the absorption level at this resonant frequency is optimized by full-wave simulations.

$$(f_r)_{mn0} = \frac{1}{2\pi\sqrt{\varepsilon}}\left(\frac{\chi'_{mn}}{d_e}\right) \tag{4.7a}$$

with

$$d_e = \frac{d_r}{2}\left\{1 + \frac{2h_r}{\pi d_r\, \varepsilon_r}\left[ln\left(\frac{\pi d_r}{4h_r}\right) + 1.7726\right]\right\}^{\frac{1}{2}} \tag{4.7b}$$

where d_e is an effective radius that considers the fringing field similarly to equation (4.1).

The above equations show that the absorbed frequency depends on the material properties and to both radius (d_r) and thickness (h_r) presented in the schematic draw in Figure 80(a).

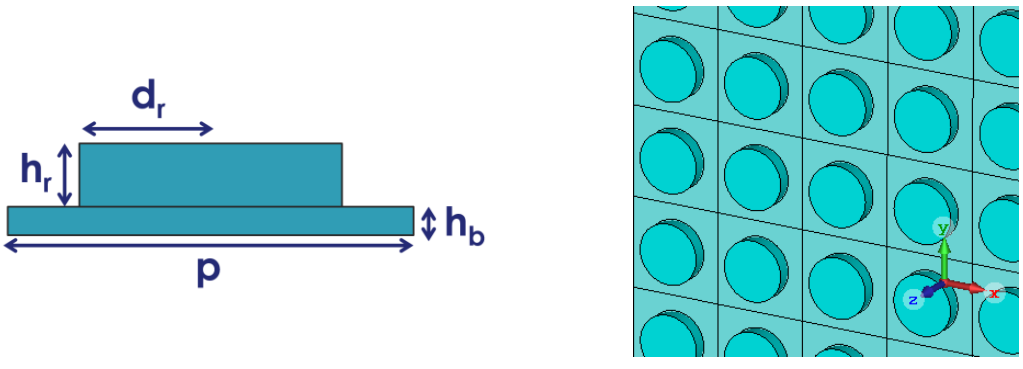

(a) **(b)**

Figure 80. (a) Schematic front view of the unit cell cylindrical resonator with a thickness h_r and radius d_r above a square dielectric base of thickness h_b. A PEC layer is at the bottom of the base. In blue, carbon loaded ABS TW-CON175BK filament. (b) Design of the simulated MMA with CST Microwave Studio for several periods. Each 45 mm unit cell comprises a 3.25 mm-thick dielectric base and a 7 mm-thick cylinder resonator with a 15 mm radius.

Since equation (4.7) does not allow retrieving the resonant frequency of the MMA, but only of a cylindrical resonator, our goal is to find the best combination of thickness (h_r) and radius (d_r) of the resonator and the thickness of the square base (h_b) to obtain a wideband absorptivity at low frequency. For the simulated structure, in Figure 80(b), several periods of the simulated unit cell are

presented, we fixed the thickness base (h_b) at 3.25 mm[27] and iterative changed both the cylinder thickness h_r and cylinder radius d_r by parameter sweep.

In Figure 81, we present the results of a parametric study targeting a wide absorption window in the frequency range of 1 GHz - 4 GHz. The parameters for the different simulations are described in Table 17 with simulations 1, 2 and 3 that differs from 4, 5 and 6, respectively, for the resonator thickness. The thickness of 7 mm has been chosen to satisfy the 10 mm-thickness condition while 15 mm was chosen to decrease the resonance frequency[28].

Table 17. Description of the three parameters that change in the simulations; radius (d_r), period (p), resonator thickness (h_r), to obtain the frequency dependence of the absorption, as in Figure 81. The last column is referred to as the resonant frequency (f_r) when a dielectric cylinder is considered alone obtained from equation (4.7).

Simulation #	d_r (mm)	p (mm)	h_r (mm)	f_r (GHz) from equation (4.7)
1	15	45	7	1.85
2	20	50	7	2.32
3	25	55	7	3.10
4	15	45	15	1.87
5	20	50	15	2.35
6	25	55	15	3.15

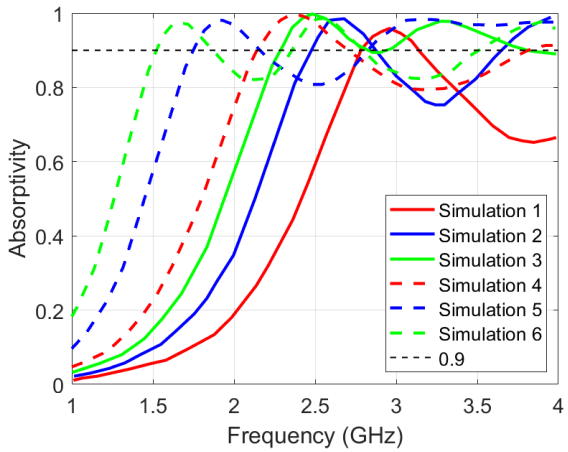

Figure 81. Plots of absorptivity over the frequency range 1 GHz to 4 GHz for various simulations with a parameter sweep. The various parameters are defined in Table 17.

From these simulated results by means of a parameter sweep over the frequency range 1 - 4 GHz, five conclusions can be derived:

1. The absorption level is almost unitary for all the different geometries
2. Equation (4.7) works correctly when the cylinder is much thicker than the dielectric plate (more than 5 times)
3. High thickness decreases the absorbed frequency considering the same radius
4. High diameter decreases the absorbed frequency considering the same cylindrical thickness
5. The thickness of the cylinder has a negligible effect on the amount of absorption

[27] The same value as in [76] is exploited for simplicity.

[28] The 10 mm-thickness specification is less stringent than for high frequencies since, decreasing the absorbed frequency band, typically requires increasing the absorber thickness.

Based on this preliminary study, we now continue our analysis at low frequencies by designing two identical geometries with different material slabs between the pillar array and the ground plane but with a different material for the square base. The dielectric material is always the CLABS, as the structure depicted in Figure 82(a). In contrast, a Magnetic Material (MM1) is assumed for the structure displayed in Figure 82(b). We will notably see in the following that the dispersion characteristic of the MM1 slab with relative permittivity close to 50 at 1 GHz is particularly favorable for low frequency successful operation.

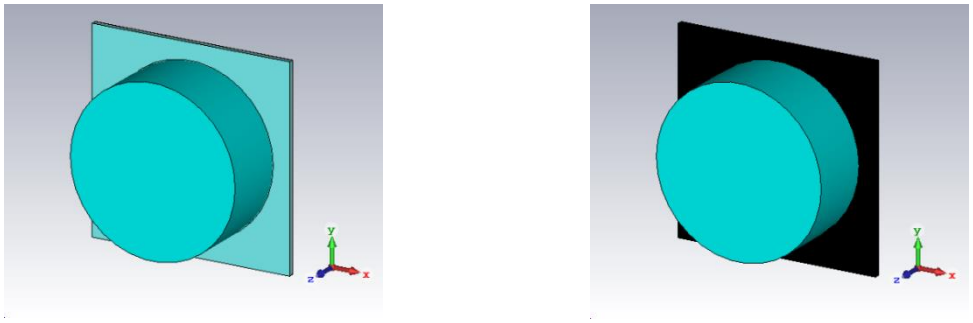

(a) **(b)**

Figure 82. Identical geometries of the low frequency absorbers, both of which are composed of a cylindrical dielectric CLABS resonator and a PEC at the bottom of the structure, as well as (a) a dielectric CLABS slab and (b) a magnetic material (MM1) slab in black, whose properties are given in Figure 83.

The frequency dependence of the complex permittivity and permeability of MM1 material over 0.8 GHz – 12 GHz range is reported in Figure 83. The real and imaginary parts of the permittivity are relatively constant over this frequency band, with a very high value of around 45 and a loss tangent of the order of 10%. For the complex measured permeability, the real and imaginary parts are equal ($\mu' = \mu'' = 2.5$) at frequencies of the order of 4 GHz. Concerning the dispersion characteristics of the magneto-dielectric filament afore reported in Figure 78(a), it can be seen a significant increase of the permittivity constant ($\varepsilon'_r = 7.5$ to $\varepsilon'_r = 49$ at 1 GHz). This enhancement is a welcome feature to design perfect absorbers in the low frequency part of the spectrum, as described in Section 4.1.

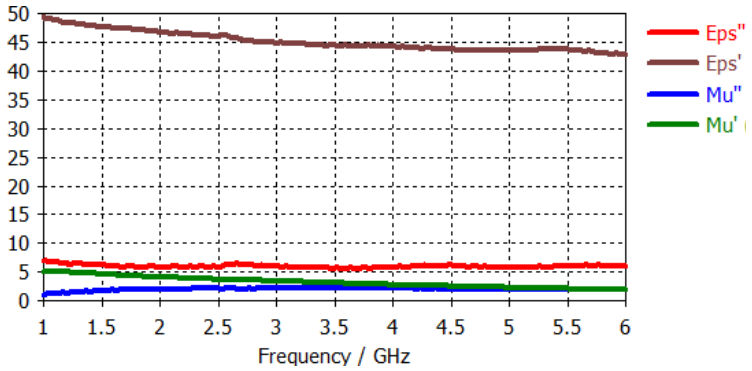

Figure 83. Measured material properties of the Magnetic material 1 (MM1) with the real part of the permittivity ε'_r (in brown), the imaginary part of the permittivity ε''_r (in red), the real part of the permeability μ'_r (in green) and the imaginary part of the permeability μ''_r (in blue).

From the guideline rules, we know that the large radius (d_r) and high height (h_r) of the cylinder resonator shift the resonant frequency towards low frequencies and that h_r does not affect the absorption level. The geometrical parameters that were finally determined by simulation are listed in Table 18, and the results of the spectra are presented in Figure 84.

Table 18. Parameter of the two identical absorbers geometries in Figure 82. The unit cell period is *p*, the slab thickness is h_b, the PEC thickness is h_m, the cylinder radius is d_r, and the cylindrical resonator height is h_r.

Parameter	Value (mm)
p	60
h_b	1.5
h_m	0.1
d_r	25
h_r	20

In Figure 84, the absorptivity over the frequency is presented. The dashed lines correspond to the cylinder with a CLABS base, as in Figure 82(a), with two visible resonant peaks at 1.55 GHz and 2.4 GHz. The two peaks do not allow absorbing a wideband, and the absorptivity below 90% is observed at 2 GHz. Complementary results to the previous ones in the frequency range 1 – 2.5 GHz are observed in solid line for the structure in Figure 82(b). The introduction of a magnetic base allows increasing the absorption around the frequency of 1 GHz. At this frequency (for which the corresponding wavelength is 300 mm), the ratio of wavelength to cylinder height is $\lambda_0/15$. Thus, it is reasonable to think that the incident signal does not see the dielectric cylinder and envisage the structure as a single magnetic slab with consequent absorption due to magnetic losses only. Increasing the frequency, the cylinder starts to resonate, and the magnetic material allows enlarging its absorption band from 2 GHz to over 4 GHz. Two critical issues now arise: the first is that magnetic materials are heavy, and thus the less of them used, the better. The second reason is that the magnetic base with its dielectric cylindrical resonator precludes an absorption coefficient greater than 90% in the L-S bands. To resolve these two issues, a solution is proposed in the following section by combining the structures depicted in Figure 82.

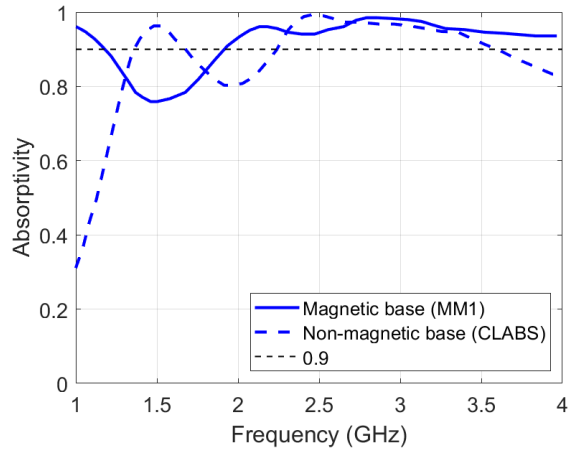

Figure 84. Simulation of the frequency dependence of absorptivity under normal incidence for the metamaterial absorber with a resonator thickness h_r of and 20 mm and a radius d_r is 25 mm. The solid line indicates the design using the MM1 base, while the dashed line the design using the CLABS base.

By combining the two 20 mm-height basic cells studied, the supercell configuration called Chess-Based metamaterial absorber (CBMMA) is proposed as depicted in the inset of Figure 85, with h_r of 20 mm, h_b of 1.5 mm, and a 60 mm x 60 mm x 0.1 mm PEC ground plane for a total thickness of 21.5 mm.

A critical point to underline is that the unit cell period of 60 mm corresponds to the wavelength of a 5 GHz signal. When the period is greater than the wavelength, grating lobes appear. Therefore, above 5 GHz, the equation to determine the absorption level must be changed to take into

account all diffracted modes. Indeed, not only the reflection of the principal mode is subtracted but also the diffraction of the higher modes [124] as given in the following:

$$Absorptivity = A = 1 - \sum_{i=1}^{N} \left|S_{N,1}\right|^2 \tag{4.8}$$

where $S_{N,1}$ is the scattering parameter related to the N^{th} diffracted mode, and *1* is referred to the incident electromagnetic wave.

The frequency dependence of the absorbance obtained with (4.8), considering 10 diffracted modes in normal incidence (N = 10) is presented in Figure 85. To quickly evaluate the value of N, one can take the number of modes with a phase constant (β) different from zero in the "Sort evaluation point" in the Floquet boundaries settings of CST Microwave Studio.

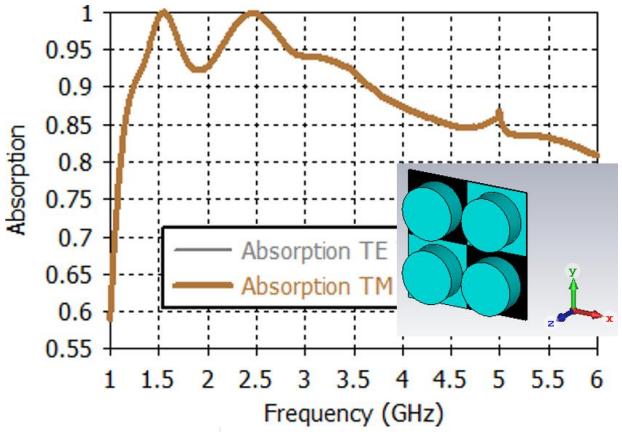

Figure 85. Total absorptivity with A > 0.9 in the frequency range of 1.2 to 3.7 GHz and A > 0.8 in the frequency range of 1.11 to 6 GHz for the Chess-Based Metamaterial Absorber (in the inset) that combines the responses of Figure 84. TE and TM modes are depicted and have the same behavior under normal incidence.

An absorptivity greater than 0.9 is observed in the frequency range of 1.20 GHz – 3.70 GHz with a FB of 1.02. A broader absorption band is obtained for A > 0.8 in the frequency range 1.11 GHz – 6.00 GHz with a FB of 1.38. The peaks at 1.5 GHz and 2.5 GHz of the non-magnetic base (CLABS) are enhanced with the magnetic material reaching almost unitary absorptivity. In addition, magnetic bases increase the fractional bandwidth by shifting the low frequencies of around 200 MHz for A > 0.9 and 300 MHz for A > 0.8 compared to the case where only CLABS bases are used.

The obtained results were very encouraging, showing that introducing the magnetic material layer improves the absorption response in the low frequency band. In addition, by using ultra-thin magnetic material layers in a chess-based configuration, we limit the overall mass of the prototype since it is well known that magnetic materials are heavy.

Based on the successful operation of a CBMMA in a wideband, we decided to exploit the same concept to design an ultra-wideband absorber operating over a decade in the next and last section. It was necessary to use a second type of magnetic screen called MM2 and introduce different heights for the dielectric CLABS cylinders.

As previously described, by changing the cylinder thickness, we modify the absorbed frequency. This rule is used to design a 2 x 2 metamaterial absorber with two diagonal elements with a cylindrical height of 12 mm and two diagonal elements with a cylindrical height of 7 mm.

As aforementioned for these new simulations, we consider another magnetic material, Magnetic Materials 2 (MM2), whose properties are described in Figure 86. The MM2 material is

engineered to operate starting from 4 GHz to very high frequency, and it exhibits a permittivity constant as high as 27 up to 26 GHz.

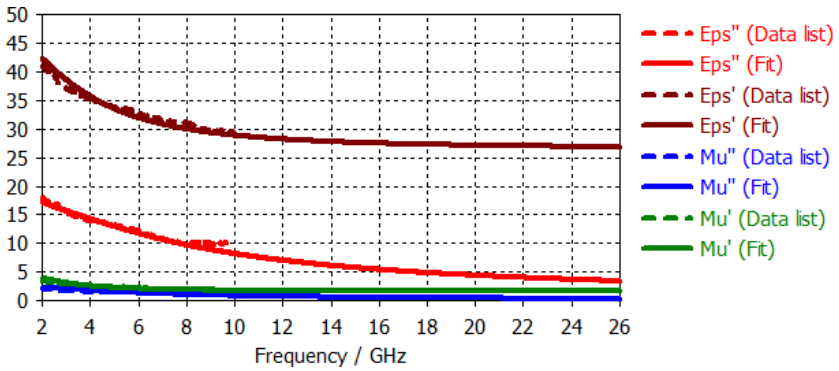

Figure 86. Material properties of the Magnetic material 2 (MM2) with the real part of the permittivity ε'_r (in brown), the imaginary part of the permittivity ε''_r (in red), the real part of the permeability μ'_r (in green) and the imaginary part of the permeability μ''_r (in blue). The dashed line represents the values obtained during the sample characterization, while the solid line represents the fit obtained using the CST Microwave Studio assuming a single frequency Debye relaxation model.

In Figure 87(a), the geometry of this new structure is depicted.

Table 19 describes the parameters used for the simulations with h_{r1} that corresponds to the cylinder thickness above the MM2 base and h_{r2} that is the cylinder thickness above the CLABS. The total thickness, considering the highest cylinder, is 15.35 mm.

Table 19. Parameter of the design in Figure 87(a). The period of the design is denoted by *p*, the slab thickness is denoted by h_b, the PEC thickness is denoted by h_m, the cylindrical resonator thickness is denoted by h_{r1} for cylinders above the MM2 slab and h_{r2} for cylinders above the CLABS slab, and dr denotes the radius of the cylinder.

Parameter	Value (mm)
p	29.5
h_b	3.25
h_m	0.1
h_{r1}	12
h_{r2}	7
d_r	10

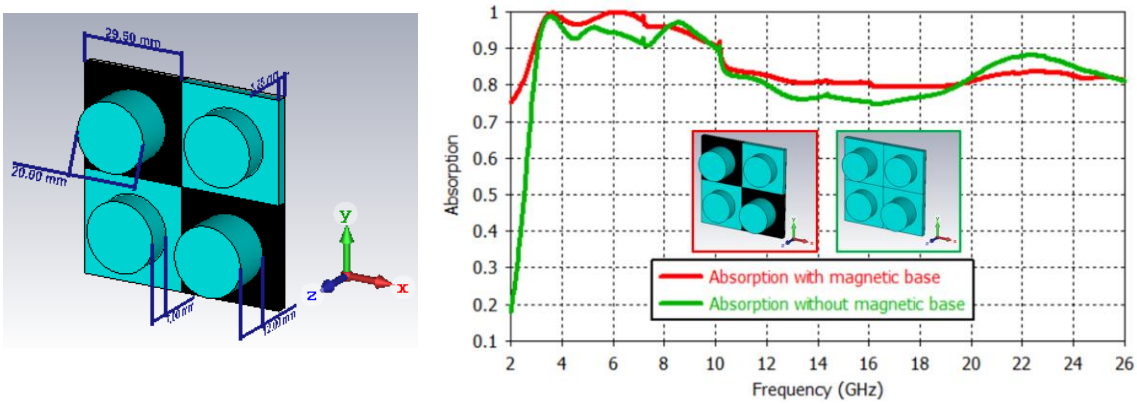

(a) **(b)**

Figure 87. (a) The design of the CBMMA for wideband absorptivity, and (b) the comparison of frequency dependence of the absorptivity between the CBMMA (in the red inset) described by the red solid line and the MMA without the chess-based geometry in green solid line. The additional introduction of magnetic losses with MM2 allows increasing the absorptivity of the structure.

In Figure 87(b), the absorptivity of the chess-based absorber is compared to that of the absorber without a magnetic layer. The absorbance is calculated with equation (4.8) with N=42 diffraction modes for normal incidence. CBMMA (in red solid line) has an absorptivity above 90% for the frequency range from 2.91 GHz to 10.02 GHz with a FB of 1.10 and an absorptivity above 80% over more than one decade for the from 2.43 GHz to 26 GHz. In contrast, for the structure without a magnetic base (in green solid line), the absorption drops in the same frequency range for A > 0.9 and also for absorption for A > 0.8. The results are in agreement with what we would expect. Indeed, at low frequency, the absorption can be related to the cylinder array since MM2 was designed for a noticeable contribution above 4 GHz. Therefore, the MM2 impact is seen at high frequency above 80% that increases around 14 GHz when magnetic losses are exploited.

In conclusion, two full-dielectric chess-based MMA absorbers were presented in this section to demonstrate that the addition of magnetic properties is one of the methods to address lower frequency range for RF absorbers and at the same time improve their absorptivity over ultra-wide frequency band from 2 GHz up to 26 GHz.

4.4 Conclusion

In this chapter, different solutions to design wideband metamaterial absorbers operating at low frequencies (1 GHz to 4 GHz) were presented. Various techniques were exploited: the first two solutions are related to the use of moderate conductivity and high permittivity dielectric filaments lowering the resonance selectivity while preserving unit absorption level.

The first approach used the so-called Stair-Like structure presented in the previous two chapters 2 and 3. However, it was shown that this solution was not compatible for two reasons; the first is that many layers (~20) are required with a thickness greater than 90 mm, which is not acceptable for low-profile absorber applications. The second reason is that to have small resonant cavities for long wavelengths, a high value of the real part of the relative permittivity is required. In the present FDM technologies using high permittivity filaments, this requirement seems challenging to satisfy. As explained in Chapter 3, high permittivity filaments give fragile disks that are difficult to stack.

Since this solution of stacking metal-dielectric bilayer in the vertical direction is not suitable, in a second stage, we investigated the possibility of structuring the top conductive layer of a single MIM quadri-layered structure by seeking planar multi resonance effects and by continuing to exploit

conductive and dielectric lossy filaments. This planar structure is called Recursive Slices Absorber (RSA) and it was compared with a single patch (MIM) absorber. It was concluded that such an absorber works appropriately as a dual-triple band absorber at low frequency, but it does not satisfy an absorptivity above 90% for the whole band of interest, namely 1-4 GHz.

For this reason, we investigate in a third study the possibilities of improvement afforded by magnetic material layers. Towards this goal, we first reported the absorption properties of a grounded magneto-electric slab with advanced properties that are not commercially available, and that our TRT expert chemists estimate to be technologically affordable. The numerical study carried out based on the complex value permittivity and permeability showed that a quite low thickness of 5 mm for the magnetic layer could offer an absorptivity greater than 90% for the frequency range 1.6 GHz to 4.5 GHz, with thus a fractional bandwidth of 0.95.

In conjunction with the use of magnetic materials, the performance of a broadband Meta-Material Absorber (MMA) based on a full-dielectric approach was demonstrated, as well as the additional losses associated with materials with magnetic properties used as bases. Apart from demonstrating that these materials have high permittivity values (close to 45 for MM1 and 27 for MM2) and permeability of around 2.5, it was demonstrated that using these material properties, a chessboard configuration (CBMMA) of a cylinder resonator array with magnetic or dielectric slabs underneath enables the design of a low-profile absorber with a total height of 21.6 mm and an absorptivity greater than 90% for the frequency range 1.2 to 3.7 GHz and 80% in the frequency range of 1.11 to 6 GHz. A second CBMMA study using a second magnetic material MM2 and varying the dielectric pillar heights demonstrated an overall global response of greater than 80% over a decade of operation between 2.4 and 26 GHz with an FB of 1.66.

Chapter 5: RF absorbers with controlled absorption levels

Different from the previous chapters, in which the main interest is achieving more than 90% absorption over a given frequency band, in this chapter, our study focuses on achieving the ability to control the absorption level from a few percent to 100% over a frequency range of interest. This will enable us to obtain a surface with gradual absorptivity along the transverse directions of space, which allows for the possibility of reducing the Radar Cross Section.

To analyze the results reported in the present chapter, we first introduce the concept of Radar Cross Section (RCS) and edge diffraction, which is a particular case of RCS. A brief introduction of the problematic and some solutions proposed in the literature are also reported. In order to obtain the controlled absorption levels, single resistive screen absorbers are proposed, operating for both normal and oblique incidences. An equivalent transmission line approach is utilized to retrieve the resistive value, aiming at achieving a target absorption level. The scalability in frequency of this concept is then analyzed for different frequency bands. It was concluded that the surface resistance concept allows obtaining the same target absorption level for different frequency bands if the fractional bandwidths (FB) are similar. In addition, to increase the fractional bandwidth, a configuration with two resistive screens is investigated on the basis of the transmission line theory.

The advantage in RCS reduction by using a surface with gradual absorptivity along the transverse directions of space instead of a homogeneous absorber is demonstrated by studying an absorber with three different sheet resistances.

Finally, three resistive screen absorbers were fabricated by using cannon beam technique are presented and the experimental assessment of these structures under normal and oblique incidences is presented.

5.1 Introduction to the problematics

When an electromagnetic wave interacts with an object such as an aircraft, the incident wave is scattered in all directions. The back-scattering energy in the direction of the source corresponds to the radar echo. As a result, it is essential to describe an echo in terms of target parameters such as its size, shape, and orientation. On this basis it is convenient to define a target with its effective area referred to as the Radar Cross Section (RCS), which is expressed in m² and is a measure of how detectable this object is by radar. The RCS is the projected area of a metal sphere that would generate the same echo signal as the target if the sphere were used in place of the target [125]. For further information, a detailed overview of the RCS and different types of scattering can be found in [8].

The technical term for the Radar Cross Section is expressed by (5.1):

$$RCS = \sigma = \lim_{R\to\infty} 4\pi R^2 \frac{|E_S|^2}{|E_0|^2} \tag{5.1}$$

where E_0 denotes the electric field strength of the incident wave impinging on the target, E_S is the electric field strength of the scattered wave arriving at the radar, and R denotes the distance between the radar and the target. The above equation is derived assuming that a target radiates the

energy of the source uniformly in all directions. Although real targets do not scatter energy uniformly in all directions, the definition assumes that they do.

RCS reduction is particularly important in stealth technology because with small RCS, these vehicles would be able to evade radar detection. Different methods have been proposed in the literature to reduce RCS. Many articles exploit checkerboard configurations in which the basic principle is a modulation of the reflection phase properties of a structure to modify the directions of the scattered fields. In [126], a checkerboard alternating two Electromagnetic Band Gap (EBG) structures with square and circular patterns, as depicted in Figure 88(a) and Figure 88(c), respectively, is proposed. The square and circular shapes introduce the frequency dependence of the phase reflection displayed in Figure 88(b) and Figure 88(c), respectively. The complete structure is shown in Figure 88(e) and a good agreement between the simulation and the measurement can be noticed in Figure 88(f) showing a reduction of -10 dB with a FB of 0.60. Instead of using EBG, other solutions are presented in the literature using Artificial Magnetic Conductors (AMG) [127] or the combination of EBG and magnetic material [128].

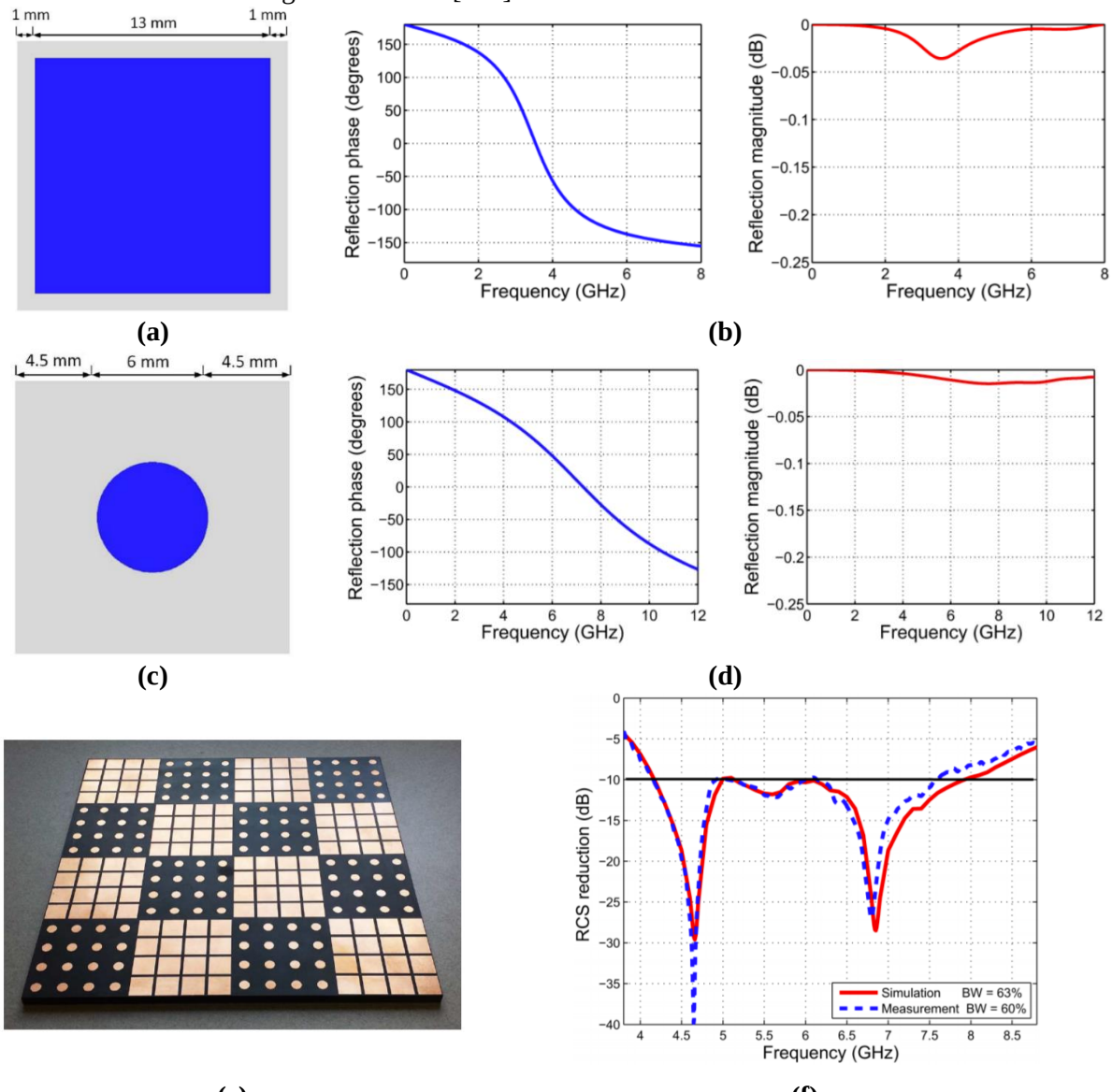

Figure 88. Unit cell of the EBG structures with its (a) square patch of 13.0 mm-width and 2.0 mm-gap with (b) the corresponding reflection phase (in blue) and the reflection magnitude (in red). (c) Circular patch of 3.0 mm-radius and 9.0 mm-gap (EBG2) with (d) the corresponding reflection phase (in blue) and the reflection magnitude (in red). (e) The fabricated square checkerboard surface and (f) normal incidence RCS reduction versus frequency. A 10-dB RCS reduction bandwidth for the checkerboard surface is 63%. The measured RCS reduction, with a bandwidth of 60%.

Many other articles focus on reducing the RCS with metamaterial designed with conventional checkerboard patterns. A destructive reflection phase difference is obtained by combining Artificial Magnetic Conductor (AMC) to Perfect Magnetic Conductor (PEC) [129] or exploiting Polarization Conversion Metasurfaces (PCM) [130], [131] that convert the incident waves to its cross-polarized wave yielding scattered waves cancellation. Nowadays, an engineered phase gradient modulation can be implemented to increase the operational bandwidth [132].

These techniques allow reducing the scattering, consequently the RCS, but they do not reduce the diffraction effects at the edge that is our goal and that is outlined in the following section.

When complex structures like an airplane are illuminated by an electromagnetic wave, different types of diffraction can occur, as depicted in Figure 89(a)[29], and significantly contribute to the RCS of the structures. These phenomena are linked to two aspects: geometry discontinuity and impedance discontinuity.

The first point relates to corners, cylindrical geometries, bending edges between two or more metallic surfaces. A classical technique to reduce the RCS due to the geometry discontinuity is to shape the design to redirect the incident wave in the specular direction. As an example, in Figure 89(b), planar metallic geometries are exploited by Northrop Grumman with the B-2 Spirit, allowing for the reduction of the RCS for monostatic radars. However, it does not prevent being visible to bistatic radars.

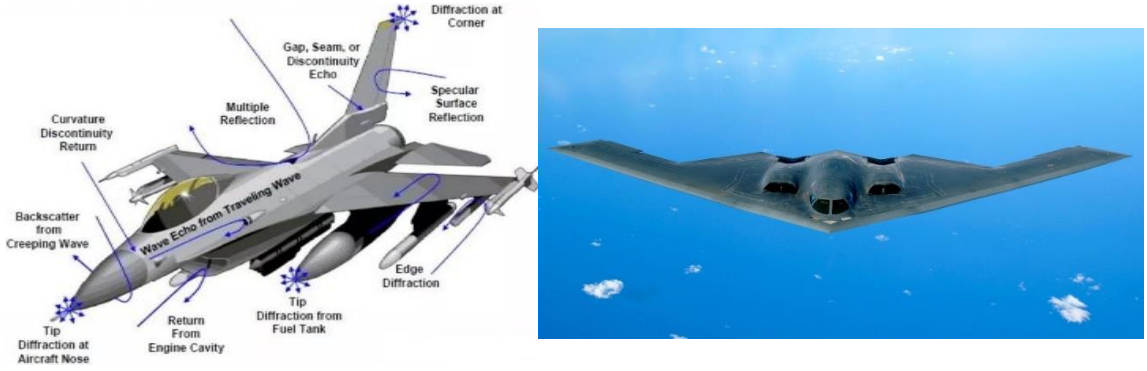

(a) **(b)**

Figure 89. (a) Various types of diffractions from an airplane, (b) stealth-bomber Northrop B-2 Spirit able to reflect the energy of an incoming wave toward the specular direction with its flat surfaces.

The second point is linked to the impedance discontinuity that occurs between different parts of the aircraft (metallic parts and antennas location) or between the metallic parts of the aircraft and the free space. Due to the classification of the RCSR, it is not easy to find relevant papers on the reduction of edge diffraction. For grazing angles, the so-called R-cards (resistive cards) [133] was proposed to obtain the gradual and progressive increase of the surface resistance to match free space impedance, thus absorbing progressively the electromagnetic energy.

In this context, the present chapter aims to present a possibility to create a surface with gradual absorptivity along the transverse directions of space, which would lead to the reduction of the Radar Cross Section due to edge diffraction. We start, in the following section, the concept of controlling absorption levels in order to be able to generate any value of absorptivity of interest from few percent to 100%. At industry level, target objectives are listed below:

- Modulation of the absorptivity from 10% to 100%, forming a gradient.
- Low-profile structure with a maximum thickness of 10 mm.

[29] All the images of the chapter that do not come from articles are available online.

- Absorbance ripple less than 5% for a given absorption level over the frequency of interest.

5.2 Controlling the absorption level

This section proposes RF absorbers with a controlled absorptivity over a frequency range of interest. By arranging these individual absorbers with controlled absorption levels next to each other, an absorbing structure with a transverse absorptivity gradient can be realized, thus obtaining a gradual impedance matching and leading to an RCS reduction.

We will focus our study on the absorbers operating at X-band (8 to 12 GHz). Moreover, an attention will be paid on the stability of absorption levels over the entire frequency of interest. Indeed, a variation of less than 5% is fixed as objective.

As seen above, the structures presented in the literature exploit complex geometries for RCS reduction, with EBG, AMC, or PCM. The operation of such artificial structures is based on resonant elements that introduce a phase shift able to cancel the backscattering and to redirect the incident wave toward other directions.

In comparison with the aforementioned structures, in the present work we aim to design an absorber (i) that is not resonant, (ii) that does not require periodicity (iii), that does not use complex EBG, AMC, or PCM structures simplifying the design and manufacturing for different frequency bands, and (iv) assuring the same absorption levels and ripple. Towards this goal we are now consider single resistive screens with different absorptions level

5.2.1 Single resistive screen for different absorption levels

The resistive screen absorbers proposed in this chapter are inspired from the well-known Salisbury absorber, which operates with a resistive screen whose surface resistance equals to the free space impedance. In Chapter 1, it was pointed out that such an absorber does not require complicated geometry with an operation based on a resistive screen at $\lambda_g/4$ from the ground plane, and dissipation within the conductive losses. Based on this principle, by adjusting the surface resistance of the resistive screen, one can modulate the absorption level between a few percent and 100%.

Let us first consider the basic structure with a schematic drawing In Figure 90 (top), from the right, a metal plate (dark blue), a dielectric spacer (green), and a resistive foil (red). The equivalent circuit in a TLM approach corresponds to a transmission line loaded by a short circuit so that the incoming wave forms a standing wave with the reflected one. For this configuration, the voltage[30] is maximum at $\lambda_g/4$, as depicted in Figure 90 (bottom) [2], and if a resistive layer is placed at this distance, the conductive losses dissipate the electromagnetic energy converting it into heat. The result is a unitary absorption of the frequency f related to the wavelength λ_g for optimizing the thickness.

[30] Voltage and electric field can be seen as equivalent since $\nabla V = -\int \boldsymbol{E} \cdot d\boldsymbol{l}$.

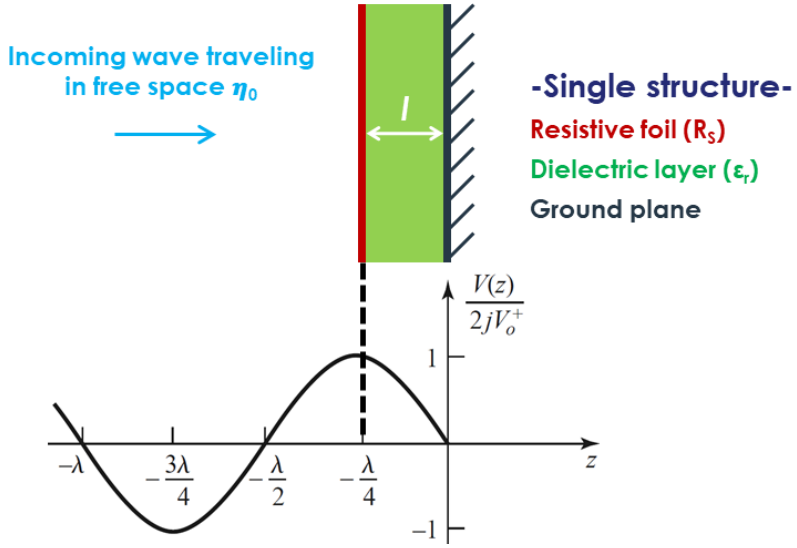

Figure 90. (top) Single resistive screen absorber with a resistive sheet (in red), a dielectric layer with thickness l (in green), and a ground plane (in dark blue). (bottom) the voltage of the equivalent transmission line closed on a short circuit with twice the input voltage at λ/4 (where λ of the picture corresponds to λ_g in the material).

Figure 5 shows the transmission line equivalent circuit involving the air and dielectric media for a single resistive screen absorber. From the left, the transmission line of the free space η_0 = 377 Ω (in light blue), followed by the surface resistance R_S (in red), and the transmission line of the dielectric spacer (in green) loaded by a short circuit (in dark blue) are shown. The input impedance at the dielectric substrate Z_{in} (in violet in Figure 91) is calculated with (5.2) that can be deduced for a lossless dielectric pacer (tangent function instead of hyperbolic tangent function for a short circuit as loading impedance).

$$Z_{in} = j\sqrt{\frac{\mu_0\mu_R}{\varepsilon_0\varepsilon_R}}\tan(\beta l) \tag{5.2}$$

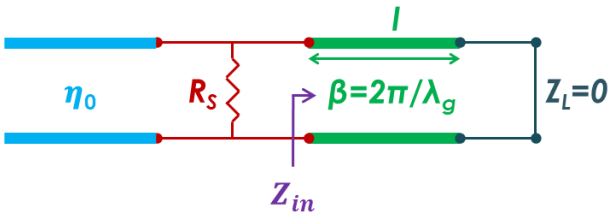

Figure 91. (a) Equivalent transmission line for a single element composed of the air intrinsic impedance η_0 (in blue), the surface resistance R_S (in red), the equivalent transmission line of the dielectric (in green), and the short circuit of the ground plane (in dark blue).

When the dielectric thickness is equal to $\lambda_g/4$, where λ_g is the wavelength in the medium at the frequency for maximum absorption, the argument of the tangent function is $\beta l = \frac{2\pi}{\lambda} \times \frac{\lambda}{4}$, the value of the tangent goes to infinity and Z_{in} goes towards infinite. The impedance Z_{eq}, depicted in blue in Figure 92, is the equivalent impedance of the surface resistance R_S in parallel with the input impedance Z_{in}. Since Z_{in} is infinite, Z_{eq} reduces to R_S (5.3),

$$Z_{eq} = R_S // Z_{in} = R_S \tag{5.3}$$

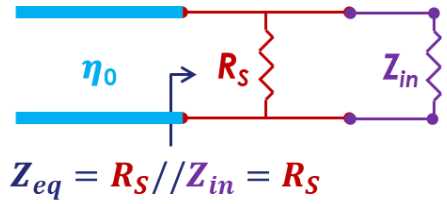

Figure 92. Equivalent transmission line corresponding to two parallel impedances, one of discrete value R_S of the surface resistance, and one with the infinite value of Z_{in}, which reduces to R_s.

In Figure 93, the equivalent circuit reduces to a simple transmission line closed on the surface resistance load R_s, and the reflection coefficient Γ is computed with (5.4)

$$\Gamma = \frac{Z_{eq} - \eta_0}{Z_{eq} + \eta_0} = \frac{R_S - \eta_0}{R_S + \eta_0} \tag{5.4}$$

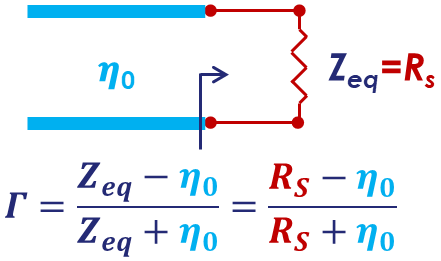

Figure 93. Equivalent transmission line composed of the equivalent impedance Z_{eq} of the resistive screen absorber corresponding to its surface resistance at the center frequency and the reflection coefficient Γ.

We now establish the equations to calculate the resistance Rs required for a targeted absorptivity. As shown in equation (1.1), the absorption level is determined from the reflection coefficient as expressed again in the following:

$$A = 1 - |\Gamma|^2 \tag{5.5}$$

Once A is set, we can find the value of Γ by inverting (5.5) and then R_S by using (5.6)

$$R_S = \eta_0 \frac{1 + \Gamma}{1 - \Gamma} = \eta_0 \frac{1 + \sqrt{1 - A}}{1 - \sqrt{1 - A}} \tag{5.6}$$

Table 20 shows the target absorption level, reflectivity, reflection coefficient, and surface resistance. For instance, to have an absorption level of 0.4 (40%), the required surface resistance is 48 Ω/m². By combining equations (5.5) and (5.6), one can calculate the resistance value required to obtain any absorption level between 0.0 and 1.0.

Table 20. Target discrete absorptivity values ranging from 0.1 (corresponding to 10% absorptivity) to 1.0 (corresponding to 100% absorptivity) and the corresponding reflectivity, reflection coefficient and required surface resistance values.

Target absorptivity	**Reflectivity (Γ^2)**	**Reflection coefficient (Γ)**	**Surface resistance R_s (Ω/□)[31]**
0.1	0.9	0.95	10
0.2	0.8	0.90	21
0.3	0.7	0.83	34
0.4	0.6	0.77	48
0.5	0.5	0.71	64
0.6	0.4	0.63	85
0.7	0.3	0.55	110
0.8	0.2	0.44	145
0.9	0.1	0.31	200
1.0	0.0	0.03	358

Notably, the surface resistance value for a unitary absorption is 358 Ω/□, which is less than the Salisbury perfect matching value of 377 Ω/□. The reason for this is related to the ripple over the X-band. At 8 GHz and 12 GHz, a perfect Salisbury screen introduces more absorptivity variations than a slightly mismatched resistive screen.

Now that the resistive screen values corresponding to the various absorptivity levels are calculated, we can validate the absorptivity using full-wave simulations in CST Microwave Studio 2019 using the unit cell as simulation box with periodic boundary condition. Unless otherwise stated, this condition is set for all the simulations in this chapter. We begin by assuming normal incidence and illustrating the absorption levels at X-band for various resistances. We then analyze the performance under oblique incidences and conclude by comparing the–resistive screens for two different frequency bands, C and K_a bands.

5.2.1.1 Performance under normal incidence for X-band

In Figure 94(a), the design of the structure defined in xy-plane is presented. The incident wave propagates toward the z-direction with a vertical electric field polarization along the y-axis. The basic cell is composed of a PEC (Perfect Electric Conductor) at the bottom, a vacuum layer in the middle (in blue), and the resistive screen (in brown) simulated as an ohmic sheet with R_s = 358 Ω and a reactance[32] of 0.1 Ω, as depicted in Figure 94(b). Since the center frequency of the X-band is 10 GHz (λ_0 = 30 mm), the vacuum dielectric layer (ε_r = 1.0), whose thickness must be $\lambda_g/4$, is 7.5 mm-thick.

[31] To notice that in this chapter, the unit of measure is either Ω/m² or Ω. The first (Ω/m²) refers to the physical surface resistance (it corresponds to the unit of the resistive screens in the simulations). The second (Ω) refers to the equivalent transmission line model (where the only physical dimension of interest is the thickness of the dielectric slab).

[32] CST requires a non-zero reactance value for the simulation.

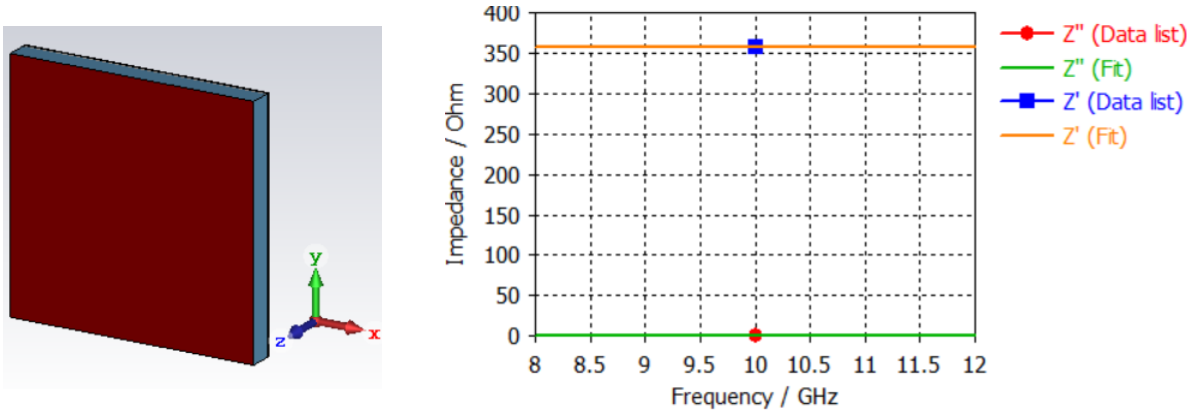

(a) **(b)**

Figure 94. (a) The geometry of the simulated structure with a metal plate at the bottom, air substrate (in blue) in the middle and a resistive screen (in brown) on top of it. (b) Properties of the resistive screen over the frequency with the real part of the impedance Z' (in orange), corresponding to the resistance of 358 Ω, and the imaginary part Z'' (in green), corresponding to the reactance of 0.1 Ω.

In Figure 95, we show the absorption levels considering the parameters in Table 20. One of the most critical requirement of the stability of the absorption level over the entire X-band from 8 to 12 GHz is satisfied with a tiny ripple of less than 5%. The absorptivity is perfectly flat up to 0.8, and minor variations are visible between 0.8 and 1. The most significant variation of 2.5% is observed at 8 GHz and 12 GHz edge frequencies, where absorptivity is 97.5% rather than 100%.

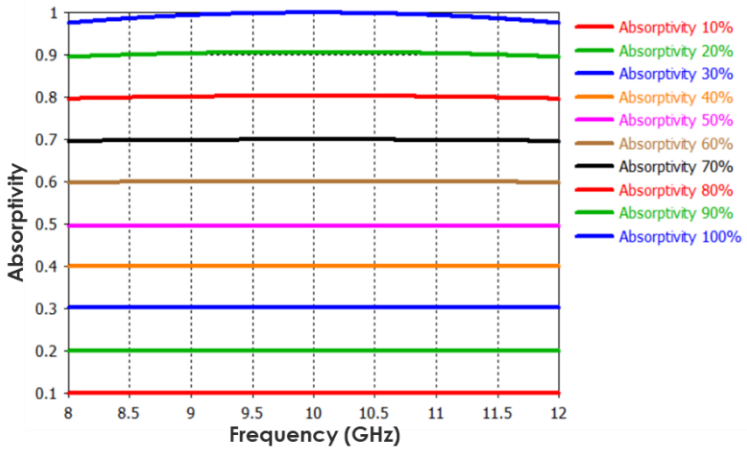

Figure 95. Absorptivity of different elementary structures each simulated with the appropriate surface resistance for absorption levels from 10% to 100% each 10%.

To understand this variation in frequency of the absorption level, we analyze equation (5.3), where the impedance Z_{eq} is equivalent to the surface resistance R_S in parallel with the input impedance Z_{in}. Let us remind that this input impedance becomes infinite when the dielectric slab has a physical thickness of a quarter-wavelength. This condition is satisfied at only one given frequency, which is the center frequency f_c of 10 GHz. At the frequency edges, the quarter-wavelength condition is not satisfied anymore, the equivalent impedance Z_{eq} is no longer equivalent to R_S, explaining the variations of reflection coefficient expressed by equation (5.4).

Always speaking about the ripple, considering the input impedance Z_{in} in equation (5.2), one can notice that the intrinsic impedance of the substrate $\eta = \sqrt{\mu_0\mu_r/\varepsilon_0\varepsilon_r}$ modifies the reflection coefficient, thereby increasing the absorptivity variation in frequency. When changing the substrate, ε_r varies, and two different cases can be analyzed:

- The center frequency for which the dielectric thickness is optimized to be quarter-wavelength.
- The other frequencies for which the thickness is not adapted.

Equation (5.3) is always satisfied at the center frequency since $tan\beta l$ is infinite regardless of the permittivity value. The structure thus absorbs according to the exact targeted level.

For the other frequencies, the input impedance variation is more significant for higher permittivity values resulting in less absorption and more ripple. This variation is more pronounced at the frequency edges and for high absorption levels, as visible in Figure 96 where three different resistances for the absorptivity of 10%, 60% and 100%, red, green and blue, respectively, are illustrated. The geometry is the same as Figure 8(a), with different substrates, the solid lines correspond to an air spacer (permittivity of 1) while the dashed lines correspond to a dielectric with permittivity of 9.

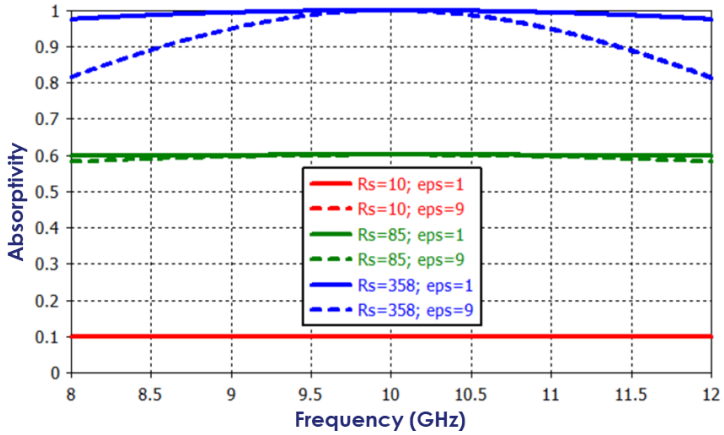

Figure 96. Frequency dependence of the absorbance for three different surface resistances, of 10 Ω (in red), 85 Ω (in green) and 358 Ω (in blues). The solid lines correspond to a permittivity value of 1 (air), while dashed lines correspond to a permittivity value of 9. Increased permittivity enables thinner structure but more frequency selective.

Table 21 summarizes the absorptivity variations between the edge frequency of 8 GHz and the center frequency of 10 GHz for two different dielectrics of permittivity of 1 and 9.

Table 21. Variation between the center frequency (10 GHz) and the edge frequency (8 GHz)[33] of the absorption levels at 10%, 60%, and 100% considering two different dielectrics with ε_r=1.0 and ε_r=9.0.

	Variation at 10%	**Variation at 60%**	**Variation at 100%**
ε_r = 1.0	0%	0%	2.5%
ε_r = 9.0	0%	3%	19%

It is observed that significant variations occur for greater absorptivity. The reason is related to the surface resistance R_s and the input impedance Z_{in}. For small absorption levels, R_s is small, the equivalent input Z_{eq} is a parallel between a quasi-zero impedance (short circuit) and a high input impedance. The equivalent impedance Z_{eq} always sees the quasi-short impedance R_s regardless the permittivity value of 1 or 9. If we now increase both R_s and dielectric permittivity, we change Z_{eq} leading to greater mismatching with free space, which is more critical when ε'_r is bigger since η reduces.

[33] The response of the structure is symmetric, which means that the variation at 12 GHz is the same as at 8 GHz.

While increasing the dielectric permittivity value (ε'_r) may appear to be a disadvantage concerning the frequency selectivity, it allows for a structure with thin thickness in relation with $\lambda_0 / 4\sqrt{\varepsilon'_r}$. If frequency selectivity is required, this technique enables to reduce the overall thickness.

In the section above, we presented the simulations under normal incidence for resistive absorbers that can change the absorption levels with the modulation of the surface resistance. In the next section, we analyze the same structures for oblique incidences.

5.2.1.2 Performance under oblique incidences

We investigate hereafter the behavior of the previous design, depicted in Figure 94(a), for oblique incidences from 0° to 50°. In Figure 97, considering a vertical polarization excitation, six structures with different resistances of 10 Ω, 48 Ω, 85 Ω, 145 Ω, 220 Ω and 358 Ω corresponding to absorption levels of 10%, 40% 60%, 80% 90% and 100%, respectively, are depicted. The dashed lines correspond to the target absorption levels minus a ripple of 3%. For instance, for the target absorption level of 40% we have a good behavior up to 26° with an absorptivity that decreases by 3%.

Symmetric behavior is observed up to an absorptivity of 80%, for the same reason of the small ripple for low surface resistances when using different permittivity discussed in the previous section. For absorption level above 80% an asymmetric behavior is visible with the enhancement of the absorption level toward high frequency.

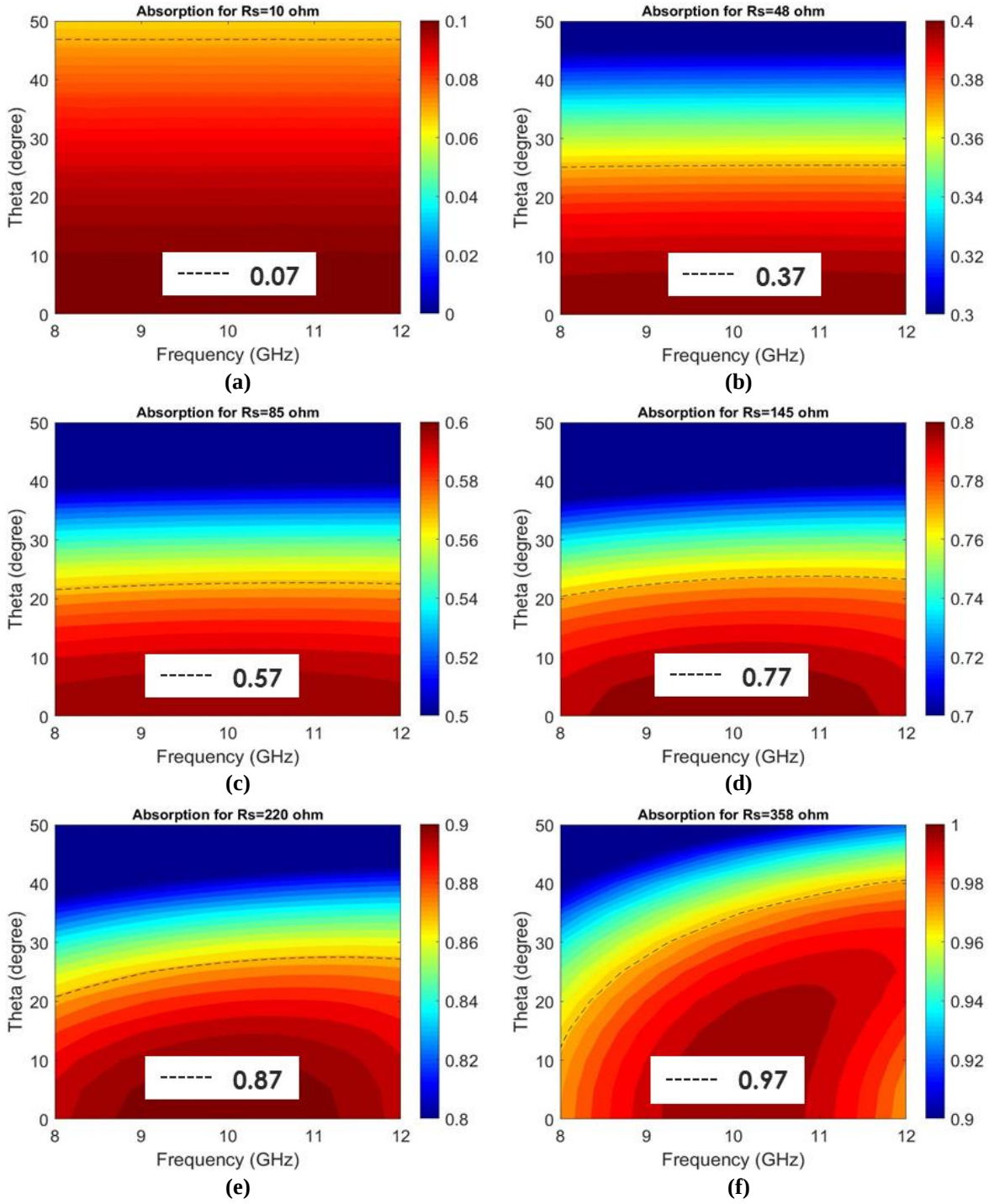

Figure 97. Absorption levels for vertical polarization for different incident angles from 0° to 50° of 10%, 40%, 60%, 80%, 90% and 100% corresponding respectively to (a), (b), (c), (d), (e) and (f). The dashed lines correspond to the ripple of 3% below the desired absorptivity.

The angular robustness can be improved by adjusting the surface resistance *Rs*, thus modifying the input impedance at an incident angle of interest. Consequently, we can have different absorption levels at precise incident angles. For instance, Figure 98 shows the input impedance values as a function of the incident angle required for unitary absorptivity for V-pol. (TE, in blue), and H-pol. (TM, in red).

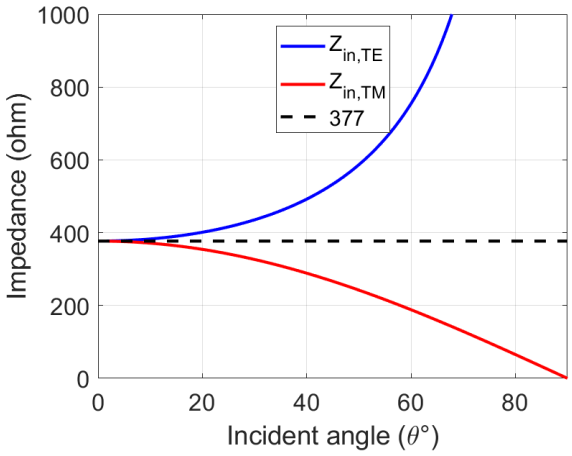

Figure 98. Incident angle dependence of the input impedance for TE-mode (V-pol.) in blue and TM-mode (H-pol.).

To plot these curves, equation (5.7a) for V-pol. and (5.7b) for H-pol. [134], which describe the reflection coefficient for different incident angles, are used:

$$\Gamma(V) = \frac{Z_{in} - {\eta_0}/{cos\theta}}{Z_{in} + {\eta_0}/{cos\theta}} \tag{5.7a}$$

$$\Gamma(H) = \frac{Z_{in} - \eta_0\, cos\theta}{Z_{in} + \eta_0\, cos\theta} \tag{5.7b}$$

Once Γ(V) and Γ(H) are fixed for a target absorptivity, the input impedance can be calculated by inverting (5.7a) or (5.7b) to exact absorber the desired energy level. It is worth notice that for normal incidence, Z_{in} of both polarizations has the same free space impedance. At the same time, for θ angles close to 90°, the absorber behaves as a PEC for TM mode, introducing a 180°-phase shift of the electric field, while for TE mode, the absorber behaves like an HIS with a 0°-phase shift of the electric field.

5.2.2 Scalability in frequency: Application in C-band and K_a-bands

The great advantage of exploiting such resistive screens is that one could use the same values of surface resistances, or the same resistive screen, for any frequency band absorbing the same amount of energy. The only one parameter needs to be paid attention on is the dielectric spacer in order to satisfy the quarter-wavelength condition and thus operating in others frequency ranges. To confirm this assertion, we consider hereafter two different frequency bands, C and K_a bands.

The simulated structures are the same as depicted in Figure 94(a) but with $\lambda_g/4$-thickness that changes in relation to the target center frequency. For C-band, 4GHz – 8GHz (FB = 0.67) with the center frequency at 6GHz corresponding to a wavelength in free space λ_0 of 50 mm, the thickness of the air spacer is 12.5 mm. We used the same resistances in Table 20, obtaining the results depicted in Figure 99.

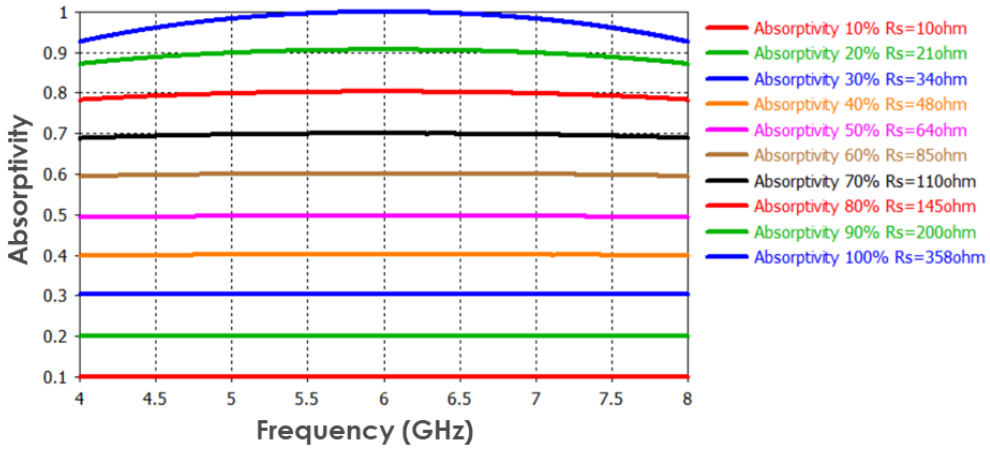

Figure 99. Absorption levels for C-band) considering the same surface resistances but different thickness of the simulated structure

For the K_a-band, 27GHz – 40GHz (FB = 0.39) with the center frequency at 33.5GHz corresponding to a wavelength λ_0 of 9 mm, the thickness of the structure is 2.25 mm corresponding to $\lambda_0/4$, considering air as dielectric. We used the same resistances in Table 20 obtaining the results in Figure 100.

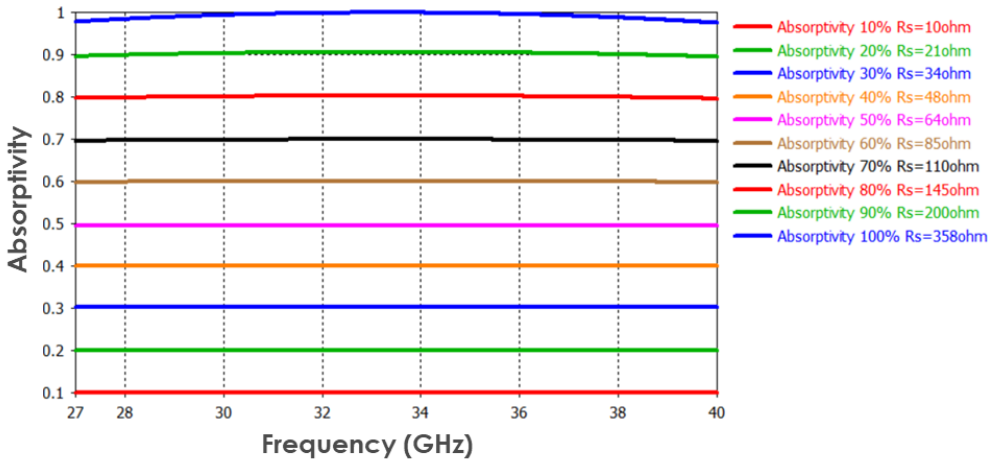

Figure 100. Absorption levels for K_a-band considering the same surface resistances but different thickness of the simulated structure.

For the two bands, at the center frequency the absorption levels correspond to the target absorptivity as notice from Table 22 where the variation of the absorptivity between the center frequency and the edge frequencies is given for C-band (FB = 0.67), for K-band of 0.39 (FB = 0.39) and for X-band (FB = 0.4). If we change the bandwidth while maintaining the same FB, for instance, passing from X-band to K_a-band, we expect the variations of absorptivity in frequency to be similar. These results confirm that by exploiting resistive screen absorbers, one can predict the behavior for different frequency bands while maintaining the same surface resistances.

Table 22. Variation between the center frequency and the edge frequency for different frequency bands (different fractional bandwidths).

Absorptivity (%)	Variation of absorptivity FB=0.67 (C-band) (%)	Variation of absorptivity FB=0.39 (K_a-band) (%)	Variation of absorptivity FB=0.4 (X-band) (%)
100	7.0	2.2	2.5
90	3.0	0.4	0.6
80	2.0	0.3	0.4
70	1.0	0.4	0.5
60	1.0	0.1	0.2
50	1.0	0.0	0.5
40	0.0	0.0	0.0

In conclusion, the presented section shows how resistive absorbers can be used for different frequency bands while maintaining the same surface resistances with a limit FB of 0.57 at which the ripple is less than 5%. If broader bandwidth is required, the easiest solution is to increase the number of layers, as it is shown in the next section.

5.2.3 Widen operating bandwidth by using multilayer structures

A conventional method to increase the bandwidth of an absorber is to add additional layers by considering the trade-off between fractional bandwidth and the overall thickness of the structure [135], [136]. In this section, we consider simple resistive screens composed of real surface impedances. We aim to double the FB of the X-band presented in Paragraph 4.1 corresponding to a value of 0.8. Different techniques can be exploited for the calculation of the surface resistances as using ABCD matrix [137], but, as for the single screen case, the transmission line theory is adopted. To simplify the calculation, two screens are considered. If more layers are required, the same process can be applied iteratively. The designed structure is shown in Figure 101 with a gray ground plane, two green air dielectric spacers with the same thickness $l_1 = l_2$, and two resistive layers with different surface resistances in brown for the first layer, in blue for the second. Our goal is to find the combination of the values of the two resistive surfaces that increases the fractional bandwidth and ensures a ripple of less than 5%.

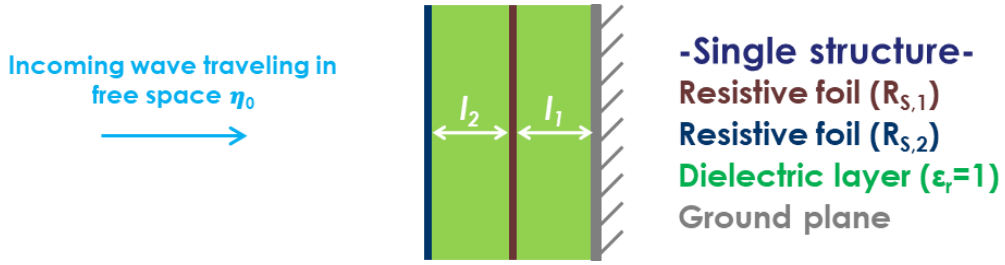

Figure 101. Schematic for the two-layer resistive absorber composed of a ground plane, two identical air spacer, and two resistive screens with surface resistances noted $R_{S,1}$ and $R_{S,2}$

The equivalent transmission line depends on:

- The two values of the surface resistances (or sheet resistances)
- The values of ε'_r for the two dielectric layers
- The thickness of the dielectric layers

Here, we analyze a simple case to show how adding one layer to increase the FB and to reduce the frequency variations of the absorptivity simultaneously.

The two air dielectric layers (ε_r = 1.0) have the same thicknesses of 7.5 mm. The resistances have two different values that are related. Let us begin considering the equivalent transmission line depicted in Figure 102.

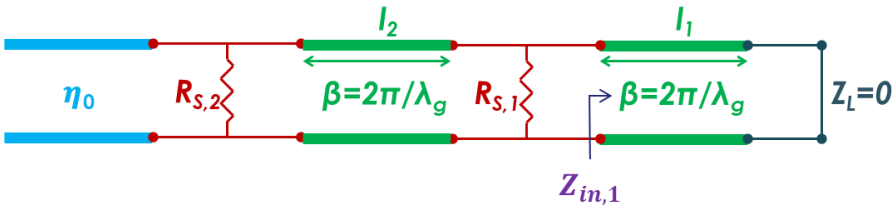

Figure 102. Equivalent transmission line for a structure composed of two resistive screens composed of the air intrinsic impedance η_0 (in blue), the surface resistance $R_{S,2}$ and $R_{S,1}$ (in red), the equivalent transmission lines of the two dielectrics (in green), and the short circuit of the ground plane (in dark blue).

The first step is to calculate the input impedance $Z_{in,1}$ as for the single screen absorber. Following equation (5.2) and considering l_1 equal to $\lambda_g/4$ $tan\beta l_1 \rightarrow \infty$ and so does $Z_{in,1}$, as depicted in Figure 103.

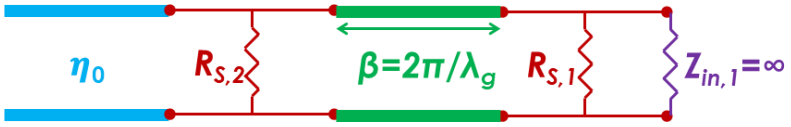

Figure 103. Equivalent transmission line for a structure composed of two resistive screens composed of the air intrinsic impedance η_0 (in blue), the surface resistance $R_{S,2}$ and $R_{S,1}$ (in red), the equivalent transmission lines of the second dielectric (in green), and the input impedance seen at 10GHz when the tangent value is infinite (in violet).

The value of the parallel configuration between the $R_{S,1}$ and $Z_{in,1}$ is equivalent to the resistance $R_{S,1}$, and the input impedance seen in Figure 104 is found with the equation of the input impedance $Z_{in,2}$of a transmission line loaded here by $R_{S,1}$ as in (5.8a).

$$Z_{in,2} = Z_{sub,2}\frac{R_{S,1} + jZ_{sub,2}tan(\beta l_2)}{Z_{sub,2} + jR_{S,1}tan(\beta l_2)} \tag{5.8a}$$

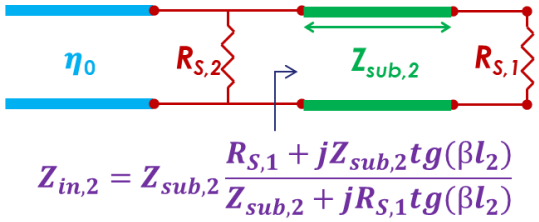

Figure 104. Equivalent transmission line for a structure composed of two resistive screens composed of the air intrinsic impedance η0 (in blue), the surface resistance RS,2 (in red), the new input impedance of a dielectric closed on the load RS,1 (in violet).

When l_2 is equal to λ/4, tan $\beta l_2 \rightarrow \infty$, giving the right term of (5.8b).

$$Z_{in,2} = \frac{Z_{sub,2}^2}{R_{S,1}} \tag{5.8b}$$

From Figure 105, the resulting transmission line comprises the free space impedance, the resistive screen $R_{S,2}$, and the input impedance $Z_{in,2}$.

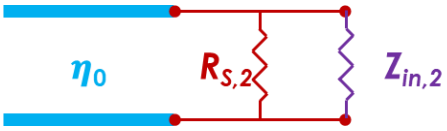

Figure 105. Equivalent transmission line for a structure composed of two resistive screens.

The equivalent impedance Z_{eq}, which is presented in Figure 106, is deduced from the parallel configuration between R_{S2} and $Z_{in,2}$ $(R_{s,2}//Z_{in,2})$calculated with (5.9)

$$Z_{eq} = R_{s,2}//Z_{in,2} = \frac{R_{S,2}\left(Z_{sub,2}\right)^2}{R_{S,2}R_{S,1} + \left(Z_{sub,2}\right)^2} \tag{5.9}$$

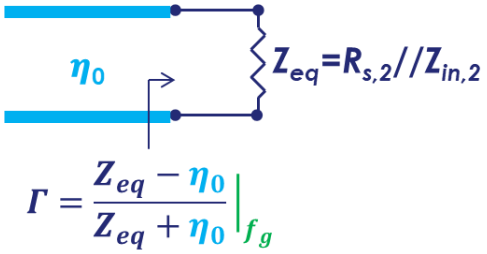

Figure 106. Calculation of the reflection coefficient gamma for the equivalent transmission line for a structure composed of two resistive screens.

The desired absorptivity can be found from (5.4), (5.5) and (5.6) but changing R_S in (5.5) with $Z_{required}$ as in (5.10)

$$Z_{required} = Z_{eq} = \frac{R_{S,2}\left(Z_{sub,2}\right)^2}{R_{S,2}R_{S,1} + \left(Z_{sub,2}\right)^2} = \eta_0 \frac{1-\Gamma}{1+\Gamma} \tag{5.10}$$

Once $Z_{required}$ value to achieve at certain level of absorptivity is set, the relation between the first resistive screen and the second can be retrieved with (5.11) considering $Z_{sub,2}$ of 377 Ω since the dielectric is air, it follows:

$$R_{S,2} = \frac{Z_{required}\,(377)^2}{(377)^2 - R_{S,1}Z_{required}} \tag{5.11}$$

The values of the $Z_{required}$ are the same as R_s in Table 20 and in Table 23, the target absorptivity as well as the resistive layer values $R_{S,1}$ and $R_{S,2}$ are depicted by fixing $R_{S,1}$ to 266 Ω[34] and $R_{S,2}$ retrieved from (5.11).

[34] This value has been chosen arbitrarily to be similar to [19].

Table 23. Target discrete absorptivity values ranging from 0.1 (corresponding to 10% absorptivity) to 1.0. (corresponding to 100% absorptivity) and the corresponding required impedance. By setting $R_{S,1}$ equal to 266 Ω, $R_{S,2}$ is derived from (5.11).

Target absorptivity	$Z_{required}(\Omega)$	$R_{S,1}(\Omega)$	$R_{S,2}(\Omega)$
0.1	10	266	10
0.2	21	266	22
0.3	34	266	36
0.4	48	266	53
0.5	64	266	73
0.6	85	266	101
0.7	110	266	139
0.8	145	266	199
0.9	200	266	319
1.0	377	266	1288

In Figure 107(a), the geometry of the simulated structure composed of two resistive layers is shown. Aiming at unitary absorptivity, the frequency dependence of the absorbance is presented in Figure 107(b) in blue, with R_{S1} of 266 Ω and R_{S2} of 1288 Ω corresponding to the resistance values of the first and second layers, respectively that give an equivalent input impedance of 377 Ω. In the same plot, the absorptivity variation over the frequency is shown in red for a structure composed of a single screen with 377 Ω-sheet resistance at a distance of 7.5 mm from a metal plate. Considering X-band, the absorption level for the double screen is unitary compared to the single screen structure where a variation of the 2.5% occurs at 8 GHz and 12 GHz.

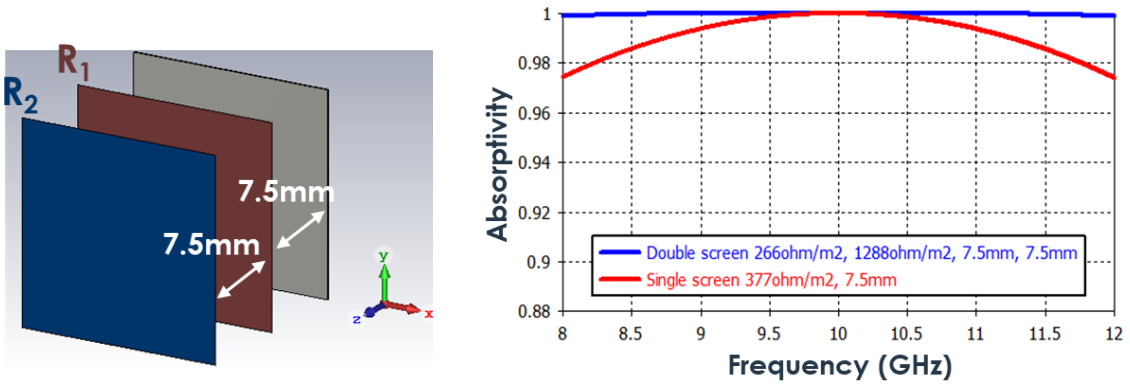

(a) **(b)**

Figure 107. (a) the geometry of the double screen used for the simulation and (b) comparison of the frequency dependence of the absorbance between a single screen of 377 Ω/m² and two screens with R_1 = 266 Ω/m² and R_2 = 1288 Ω/m², which corresponds to an equivalent impedance of 377 Ω/m², over the frequency range 8 – 12 GHz corresponding to a FB of 0.4.

Since we are interested in a FB of 0.8, the frequency of interest was chosen between 6 GHz and 14 GHz (FB = 0.8) to make the comparison between the double and single screens illustrated in Figure 108. The blue rectangle in the picture corresponds to the X-band frequencies.

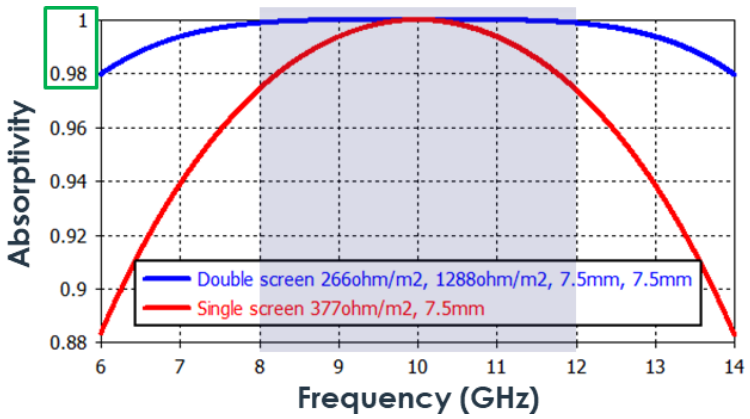

Figure 108. Comparison of the frequency dependence of the absorbance between a single screen of 377 Ω/m² and two screens with R_1=266 Ω/m² and R_2=1288 Ω/m², which corresponds to an equivalent impedance of 377 Ω/m², over the increased frequency range 6 – 14 GHz corresponding to a FB of 0.8.

Doubling the layers increases the robustness to absorptivity variations with an six-folding improvement, passing from a difference between the center frequency and edge frequency of 2% for a double screen to a variation of 12% for a single screen.

We can now present the results for different absorption levels as depicted in Figure 109. The curves are plotted for ten target levels from 10% to 100% considering the sheet resistance values of Table 23. A flat behavior is observed for the absorption levels up to 0.6, while a slight enhancement of the absorptivity is observed at the edges frequency of 6 GHz and 14 GHz for the absorptivity from 0.7 to 1.0. Regardless of this enhancement, the structure fully satisfies the requirement of a ripple variation of less than 5%.

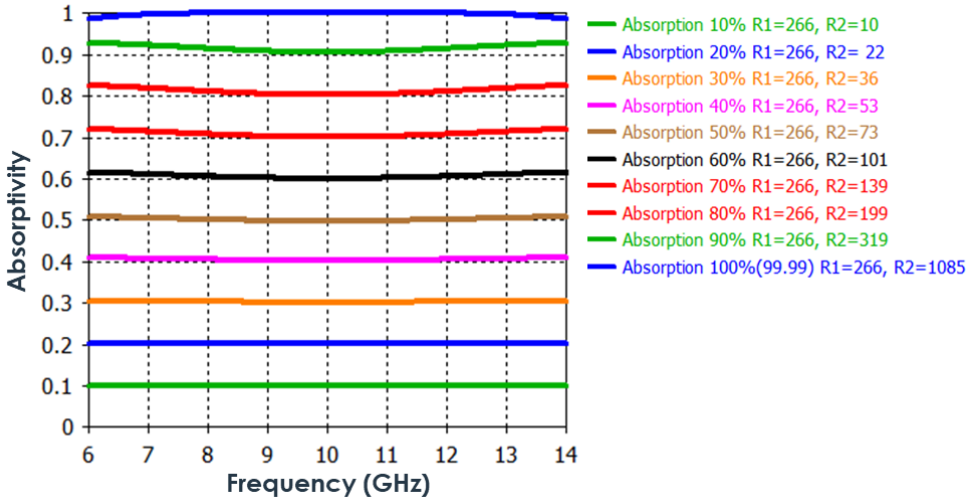

Figure 109. Different levels of absorptivity from 10% to 100% for a FB of 0.8.

Considering unitary absorptivity target, the comparison between one layer and two layers structures is summarized in Table 24, where the yellow background corresponds to a FB of 0.4 while the blue background corresponds to a FB of 0.8.

Table 24. Parameters comparison between the structure composed of one resistive layer of 377 Ω and the structure composed of two resistive layers with an equivalent input impedance of 377 Ω.

	One layer	Two layers
Frequency	8GHz-12GHz	8GHz-12GHz
FB	0.4	0.4
Max ripple	2.5%	0.2%
Frequency	6GHz-14GHz	6GHz-14GHz
FB	0.8	0.8
Max ripple	12%	2%
Thickness (ε_r=1.0)	7.5 mm	15 mm

To sum up, the two screens absorber shows better performance than a single screen at the detriment however of a higher thickness. Nevertheless, thanks to the possibility to optimize many parameters such as the sheet resistances, the addition of reactive elements, the material properties (permittivity and permeability), and the spacer thicknesses, one can develop optimization codes to find the best combination in terms of the broadest frequency band for the lowest profile.

5.3 Towards the structure with a transverse absorptivity gradient

5.3.1 Transverse assembly of multiple resistive screens

The analysis of a single screen has been presented in the previous three sections and their results are applied in this paragraph for the complete structure.

In Figure 110, an RF absorber structure with a transverse absorptivity gradient is presented. It consist in implementing 10 individual resistive screen absorbers at positions x_i (where $i = 1,\ldots,10$ from position *1* to position *10*), one next to each other. Each element has a distinct surface resistance that increases from 10 Ω for an absorption level of 10% to 358 Ω for an absorption level of 100%.

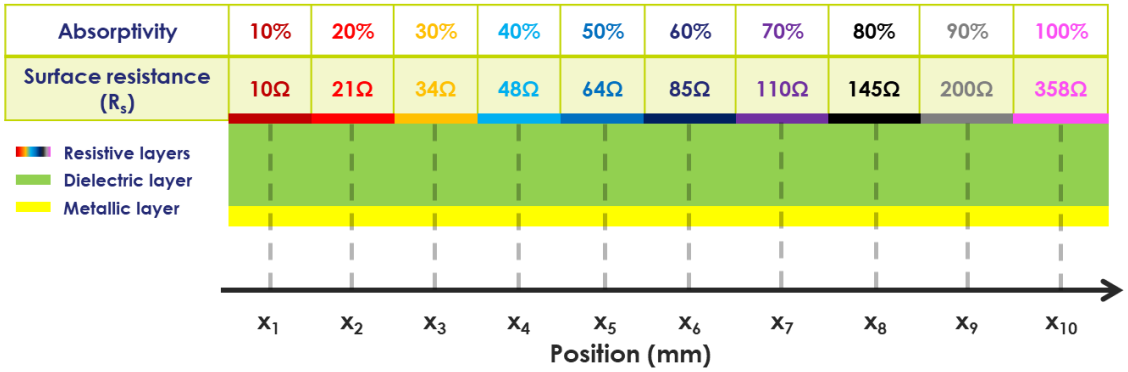

Figure 110. RF absorber with a transverse absorptivity gradient composed of 10 elements with 10 different surface resistances to absorb the levels from 10% to 100%.

Quasi zero variation between the center frequency (at 10 GHz) and the edge frequencies (at 8 GHz and 12 GHz) was observed below 0.8-absorptivity. A maximum variation of 6.1% was found for an incidence angle θ = 60° at the position of 100 mm (not presented here). Considering these slight variations we report in Figure 111, the absorptivity response at each positions of the RF absorber considering only the frequency of 10 GHz. The black curve corresponds to the ideal case of a linear dependence from 10 % to 100%. A very similar behavior with respect to this reference is observed up to incidence angles of 20° with a maximum relative drop of 2.5% around 50 mm. From

20° to 45° the maximum of reduction is 10%, also around 50 mm. Higher variations with respect to a linear behavior of the absorptivity are seen from 45° to 80°.

It is important to note that the curves presented in Figure 111 is an assembly of results separately obtained from 10 resistive screen absorbers, in which each individual resistive screen provides a given absorptivity, instead of one obtained from a complete structure. The transverse spacing of 10 mm between two resistive screens is only chosen for plotting purpose without any physical implication.

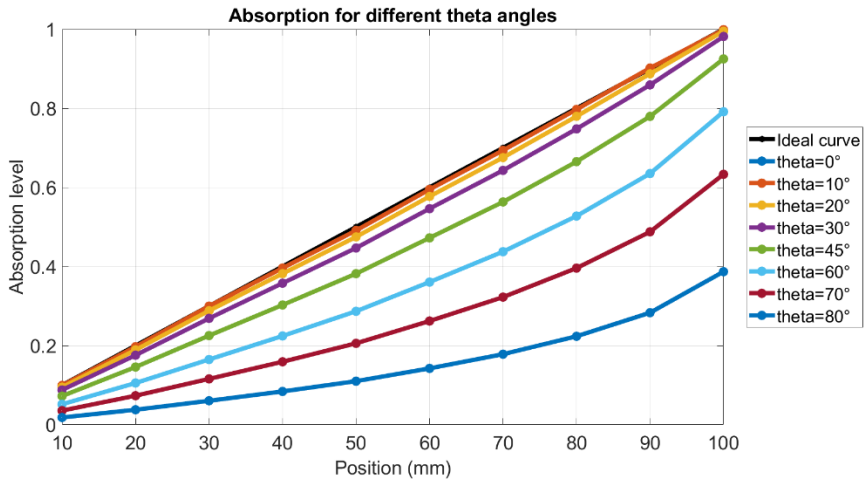

Figure 111. Gradient profile for the RFAG always maintained for any incident angle considering the center frequency of 10 GHz.

It is worth noting that the ripple is not to be considered as a problem since we can change the resistance to increase the absorptivity at one incident angle. Instead, the conservation of the gradient profile, which is satisfied for any incident angle.

In the following section, a numerical proof of concept of a RF absorber with gradient absorptivity gradient is presented. It will be seen that the absorber yields a reduction of the RCS of around 10 dB compared to uniform metal plates. In the last section of the chapter, the absorption properties of three manufactured structures will be experimentally characterized. Two of these structures correspond to single screen absorbers for absorption levels of 20% and 50%. The third structure is a combination of two adjacent resistive screens.

5.3.2 Application for RCS reduction

In this section a numerical proof of concept in the RCSR context is proposed by reducing the edge diffraction effects. Let us remind that the edge diffraction issue can be related to the different impedances that are involved when an electromagnetic waves is scattered at a metal free-space interface. To evaluate the validity of our proposition, three different cases are analyzed:

- Design of a double metallic plate
- Design of a homogeneous absorber with unitary absorptivity
- Design of an absorber with absorptivity gradient (for the sake of simplicity, “gradient absorber” is the name used in the rest of the section)

The first case is considered as the reference, the second quantifies the reduction of the RCS when implementing a homogeneous absorber with unitary absorptivity while the third one illustrates the advantage of using a gradient absorber in RCS reduction instead of a homogeneous absorber.

The simulations of the RCS are performed with the asymptotic solver in CST Microwave Studio 2019. To validate the solver, the RCS calculated by the full-wave simulation of a 240 x 240 mm² metal plate was compared to the one obtained from equation (5.12) [8], where both *a* and *b* dimensions are of 240 mm, as in Figure 112(a)

$$\sigma = \frac{4\pi}{\lambda^2} a^2 b^2 \qquad (5.12)$$

One can notice that (5.12) depends on the wavelength λ. As a consequence different frequencies were analyzed in the bands from C to K_u. A zoom of the simulation results is presented in Figure 112(b) for different incident angles from 80° to 100°[35]. The RCS value σ deduced from the analytic formula and the full-wave simulation at the frequency of 10 GHz and for normal incidence are described in Table 25.

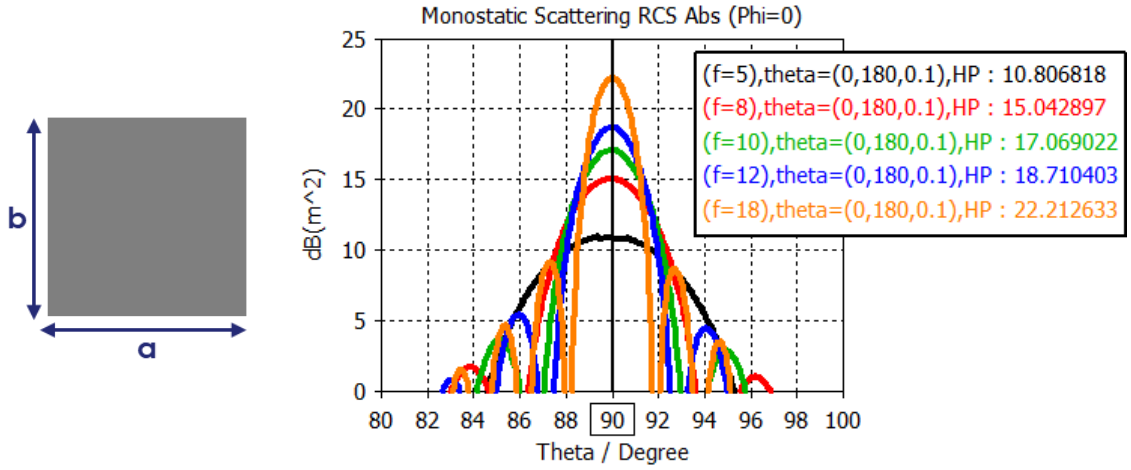

(a) **(b)**

Figure 112. (a) Metal plate of dimensions a and b and (b) the simulations for the same structure with a = b = 240 mm using the asymptotic solver in CST with a zoom at the incident angles 80° to 100°. Normal incidence for this design is at 90°

Table 25. Comparison between the RCS (σ) of a metal plate for normal incidence between the analytical formula and the simulations in CST Microwave Studio 2019 using the asymptotic solver.

Frequency (GHz)	σ analytic (dBm²)	σ asymptotic solver (dBm²)
5	10.6	10.8
8	14.7	15.0
10	16.7	17.1
12	18.2	18.7
18	21.8	22.2

The good agreement between analytic calculation and full-wave simulation allows concluding that the asymptotic solver can be used to determine the RCS of our structures.

We present hereafter the numerical results for the three study cases: a double metallic plate, a homogeneous absorber, and a gradient absorber.

For all structures with vacuum as dielectric layer, the absorbers are located in the yz-plane. For normal incidence a plane wave is impinging, with φ = 0°, and an incidence angle (θ) of 90°, as illustrated in Figure 113(a). In that case the EM wave propagation is along the direction –x. At θ =

[35] We remind that normal incidence corresponds to an incident angle θ of 90°.

0° corresponding to a grazing incidence, the k vector of the plane wave is parallel to the structure with propagation toward the direction -z. At θ = 90° as explained before, the incident wave is normal to the structure propagating toward –x. At θ = 180°, the wave propagates toward +z. The simulations were reported for both horizontal polarization (HP) and vertical polarization (VP) for plane waves that impinge the structure for incident angles from θ = 0° to θ = 180° each 1°. Within this paragraph, all RCS simulations are performed at 10 GHz except explicitly stated.

The reference structure is composed of two 240 x 270 mm² metallic plates with a spacing of 7.5 mm. The RCS of this first structure is presented in Figure 113(b), and when normally illuminated, the RCS is 17dBm², corresponding to an effective area of 50 m². It is thought that the difference between the two polarizations is linked to the reflections within the two metallic plates that alter the backscattering.

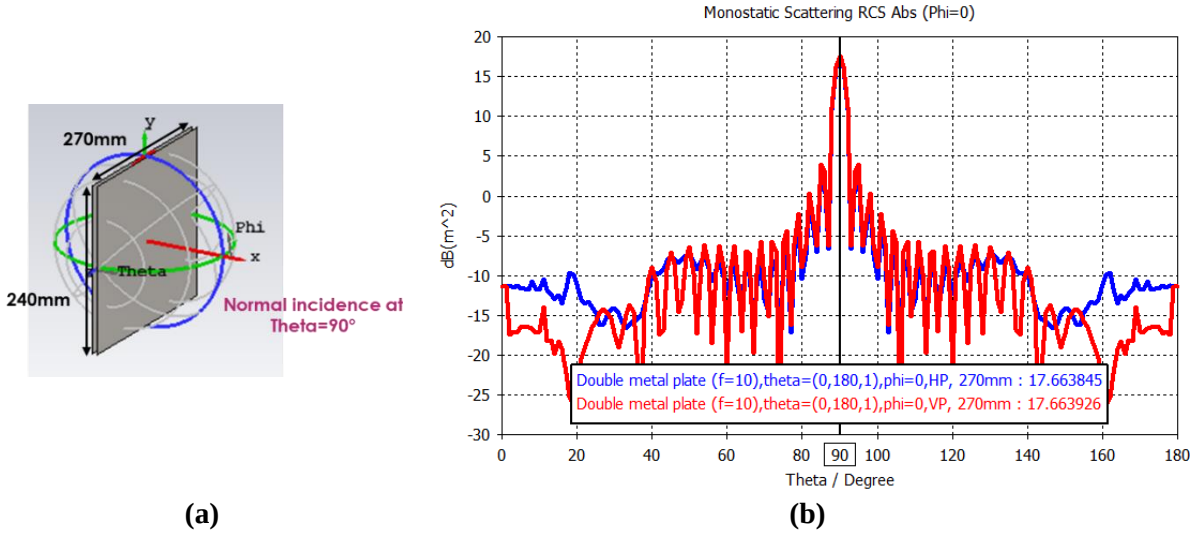

(a) **(b)**

Figure 113. (a) Reference structure composed of two metallic plates of 240 x 270 mm² and spaced of 7.5 mm and description of the incident angles θ and φ. (b) simulations of the RCS over the incident angles for vertical polarization (VP) in red, and horizontal polarization (HP) in blues for the reference structure.

The second structure, which corresponds to the homogeneous absorber in Figure 114(a), and the third structure, which corresponds to the gradient absorber in Figure 114(b), are presented. Both geometries are designed from starting from the reference structure and replacing a tiny metal strip of 30 mm on its right extremity with either a homogeneous absorber or a gradient one. The purple color represents a resistive screen of 358 Ω/m², the blue of 64 Ω/m², and the red of 21 Ω/m², corresponding to an absorptivity of 100%, 50%, and 20% respectively.

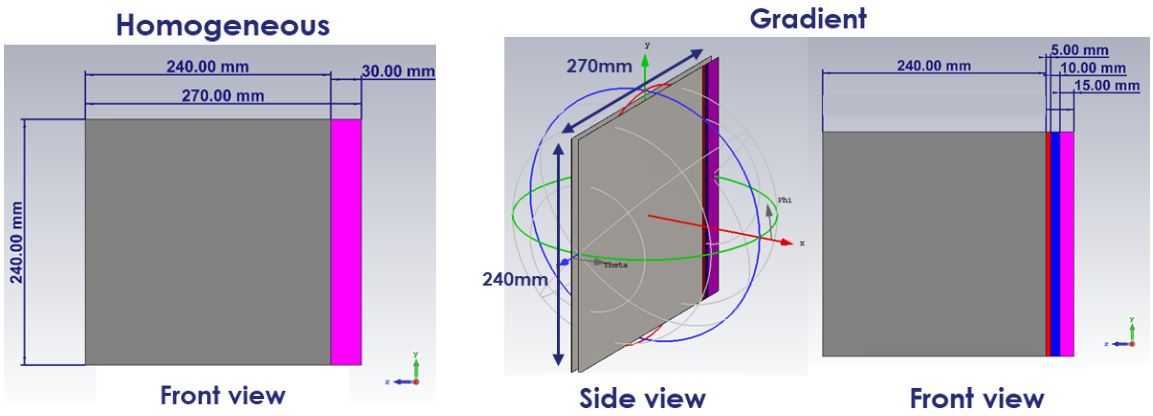

(a) **(b)**

Figure 114. Geometries of the structures adding (a) the homogeneous absorber and (b) the gradient absorber. The purple color is a resistive screen of 358 Ω/m², the blue of 64 Ω/m², and the red of 21 Ω/m² corresponding to absorptivity of 100%, 50% and 20%, respectively.

The comparison of the RCS simulations between the double metal plate (in blue), the homogeneous absorber (in green), and the gradient absorber (in red) are presented in Figure 115(a), for vertical polarization, and in Figure 115(b), for horizontal polarization. Considering vertical polarization, the same behavior is observed between incident angles from 0° to 110° with three nearly equal maximum values for normal incidence (θ = 90°) since the dimensions of the top metal plate are similar for the three cases. For the range 110° - 140°, slightly better performance is visible for the gradient absorber reducing the RCS of 1 – 2 dB compared to the reference and the homogeneous absorber (in the dark blue circle). The contribution of the gradient absorber, as well as of the homogenous absorber, is not significant. The reason of this minor modifications seems related the electric field direction as depicted in the inset of Figure 115(a), with excitation of surface current along a direction parallel to the partially or totally reflecting layers. For horizontal polarization with a cross E-field orientation, a significant contribution of the gradient absorber layers is visible in Figure 115(b), for the incident angles range of 110° - 140°, with a Radar Cross Section reduction of 5 - 10 dB compared to the reference and of 2.5 - 5 dB with respect to the homogenous absorber (in the light blue circle). It is worth noting that the reduction of the RCS is effective on a specific range of incident angles by pointing out that the resistive screens operate at those incident angles.

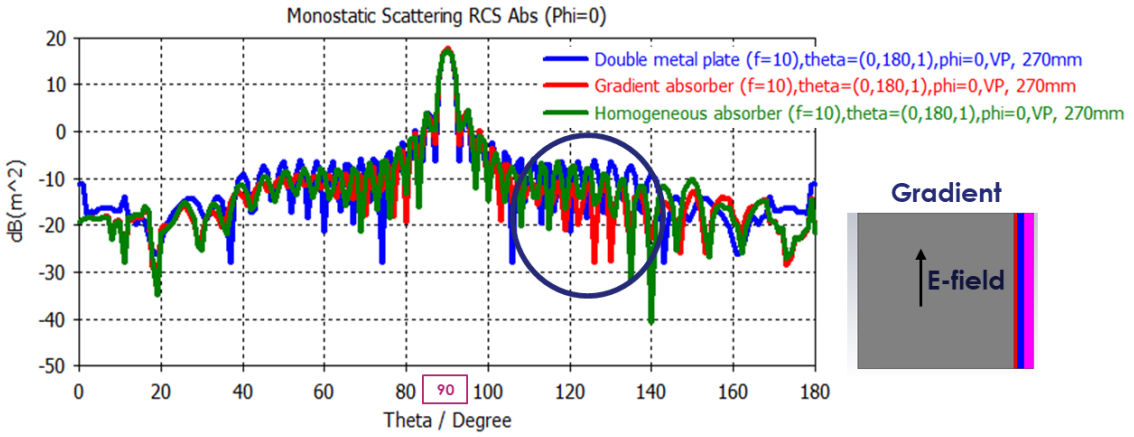

(a)

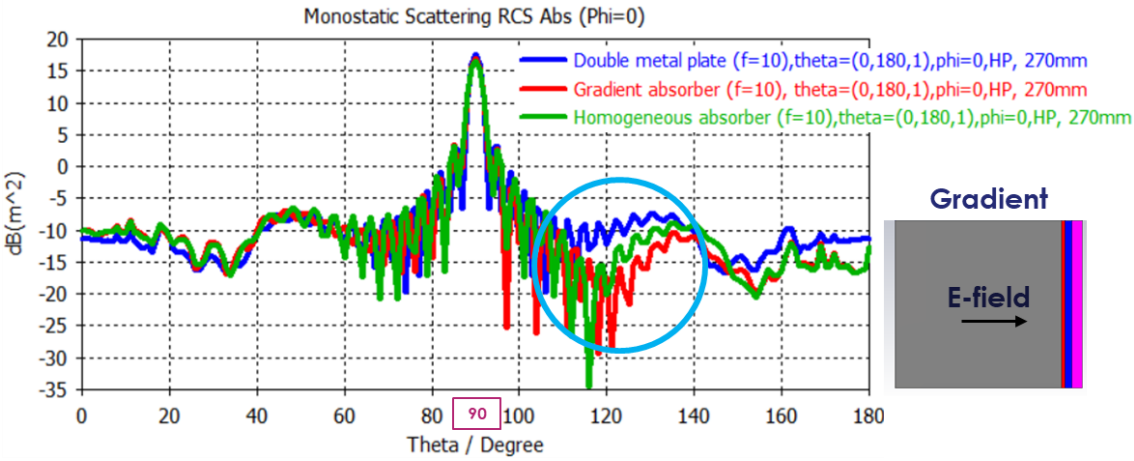

(b)

Figure 115. Comparison of the RCS over the incident angles theta at 10 GHz between the reference structure (in blue), the homogeneous absorber (in green), and the gradient absorber (in red) for (a) vertical polarization (E-field as in its inset) and (b) horizontal polarization (E-field as in its inset). In the circle, the zone interested by the reduction of the Radar Cross Section.

To conclude this analysis, the comparison of the RCS for the gradient absorber between the frequencies of 8 GHz, 10 GHz, and 12 GHz is presented in Figure 116. Higher RCS can be noted for higher frequency since the metal plate RCS is inversely proportional to the wavelength λ but a similar behavior is observed in the range 110° - 140°. Moreover, it is interesting to notice that for low frequencies, the resistive screens to operate more efficiently for near grazing angles.

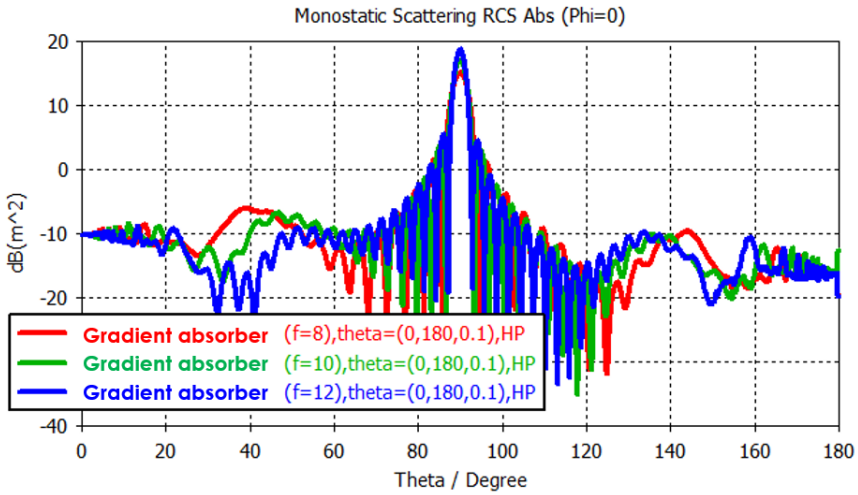

Figure 116. Comparison of the RCS between three X-band frequencies of 8 GHz (in red), 10 GHz (in green), and 12 GHz (in blue).

To briefly conclude on these preliminary calculations a relatively narrow (3cm to be compared to the overall dimensions of 24 cm) absorbing layer could yield significant reduction of the RCS at large incidence angle with respect to the normal one. However, a deeper analysis of the underlying scattering mechanisms should be conducted before concluding about the potential interest of such gradient edge layers applied notably to stealth applications.

5.4 Experimental validation

In order to validate experimentally the concept of controlling the absorption level by using inspired-Salisbury-resistive-screen structures, two prototypes have been fabricated: one with 64 Ω/□ to obtain 50% absorptivity and the other with 21 Ω/□ to obtain 20% absorptivity. The third prototype is manufactured and composed of two areas of two different resistance values. The objective of this last prototype is, on one hand, to demonstrate the technological ability to manufacture a quite large structure (25cm x 25cm) with two areas of controlled values of resistance, and on the other hand, to evaluate the diffraction effect which could be observed at the frontier between two resistance areas.

We introduce hereafter both the simulations and characterizations of absorption level of three prototypes, which use PolyEtherKetoneKetone (PEKK) as material for dielectric layer and which were designed to operate at X-band, for different incident angles and different polarizations.

The three structures 25cm x 25cm consist in a 2µm-thickness copper plate at the bottom (in red), a 4.2 mm-thick PEKK dielectric spacer (in rose), and a Nikel Chrome (NiCr) coating resistive screen (in grey) as depicted in Figure 117(a) with an overall weight of 0.36 Kg. The results of the simulation of the absorbance spectra of these structures are presented in Figure 117(b) with: in blue the curve for an absorptivity of 50% that corresponds to a surface resistance of 64 Ω/□. In red, the plot for an absorptivity of 20%, which is obtained for a sheet resistance of 21 Ω/□, and in green, the last composite structure. For this last structure, it appears that the incident wave ‘sees’ an average value of the two resistive layers with a mean absorbance value around 35 % while the separate samples shows values close to 20% and 50 % respectively. In addition, for this two resistance sample it can be noted a slightly higher variations at the frequency edge of the absorption window.

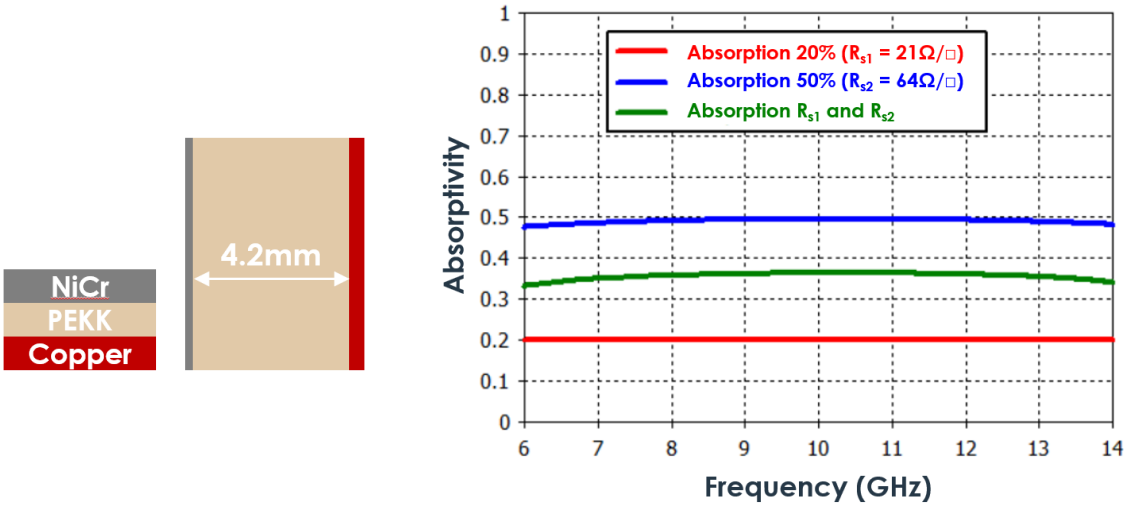

(a) **(b)**

Figure 117.Schematic design of a single resistive screen absorber and (b) simulations of the frequency dependence of the absorbance for the three structures fabricated. In red, Structure 1 with an absorptivity at 10 GHz of 20% with a surface resistance of 21 Ω/□, in blue, Structure 2 with an absorptivity at 10 GHz of 50% with a surface resistance of 64 Ω/□, and in green, Structure 3 with equally area two sheet resistances.

For the manufacturing of these structures, PEKK thermoplastic polymer substrates of 250 x 250 x 4.2 mm^3 were manufactured by thermal compressing with temperatures of around 320-380°C, by the platform Canoe[36] [138] starting from the KEPSTAN 6003PF resin produced by ARKEMA [139]. A photo of a realized substrate is shown in Figure 118, with visible black traces presumably due to pollution during the manufacturing process. Indeed the stainless steel sheets are cleaned with ethanol, it is believed that the pollution should rise from granules during the molding process, made in the press at 300°C (fiber of the anti-heat gloves, paper residues used for cleaning, or similar).

Figure 118. Single 25 x 25 x 0.42 cm PEKK layer after the molding process.

The frequency dependence of the complex permittivity between 1 and 12 GHz of the PEKK dielectric layer are given by the supplier ARKEMA and are plotted in CST Microwave Studio as shown in Figure 119. The real part of the relative permittivity in Figure 119(a), shows a value close to 3.3, while the losses expressed in terms of loss tangent indicate values lower than 5 x 10^{-3} up to 11 GHz in Figure 119(b).These dielectrics characteristics substrate have motivated the choice of this substrate material with low dielectric losses and quasi –constant relatively low permittivity in the X-band. In fact, considering a center frequency of 10 GHz and a real dielectric permittivity of 3.3, the

[36] Centre Technologique Nouvelle Aquitaine composites et nouveaux matériaux www.plateforme-canoe.com

structure should have a thickness of 4.1 mm (thickness = $\frac{\lambda_0}{4\sqrt{\varepsilon_r}} = \frac{30}{4\sqrt{3.3}}$ = 4.13 mm). With respect to this targeted thickness, the dielectric PEKK layers that were fabricated exhibit very close values around 4.2 mm measured with a caliper. The second reason this substrate has been chosen is that it can be heated to high temperatures that allow the manufacturing process to be applied for the resistive layers and ground plane.

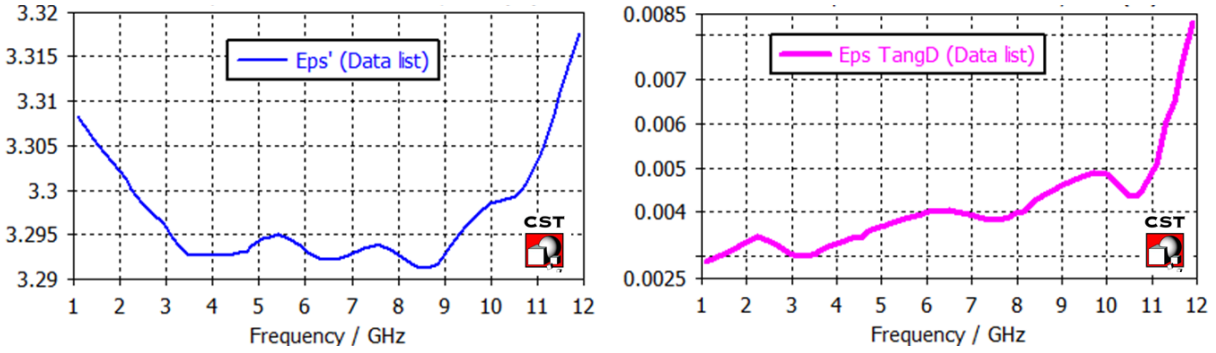

(a) **(b)**

Figure 119. For the PEKK material (a) real relative permittivity and (b) losses in terms of loss tangent. Both are exploited in the full-wave simulations.

Resistive screens and copper ground plane were fabricated by electron beam evaporation technique (in clean room)[37], as described in the annex A.2.2, to both PEKK sides, by Neyco company [140]. For the ground plate, a thin copper layer of 2 μm[38] was deposited. Nikel Chrome (NiCr) was used for the resistive screens by controlling their thicknesses that determine the sheet resistance values. The thicknesses are of 67 nm and 25 nm, with an error of ±5%, for a the surface resistances of 21 Ω/□ for the structure in Figure 120(a) and 64 Ω/□ for the structure in Figure 120(b).

From the technological side, it is worth mentioning that the two areas of the Structure 3, in Figure 120(c), are not adjacent and superposed as demanded. Due to lack of time, it was not possible to request a new prototype with tightly joined regions 1 and 2. Therefore, we studied the structure as it was provided.

[37] We would like to thank Paolo Martins for his technical help and support.
[38] We remind that copper skin depth is 0.65 μm at 10 GHz.

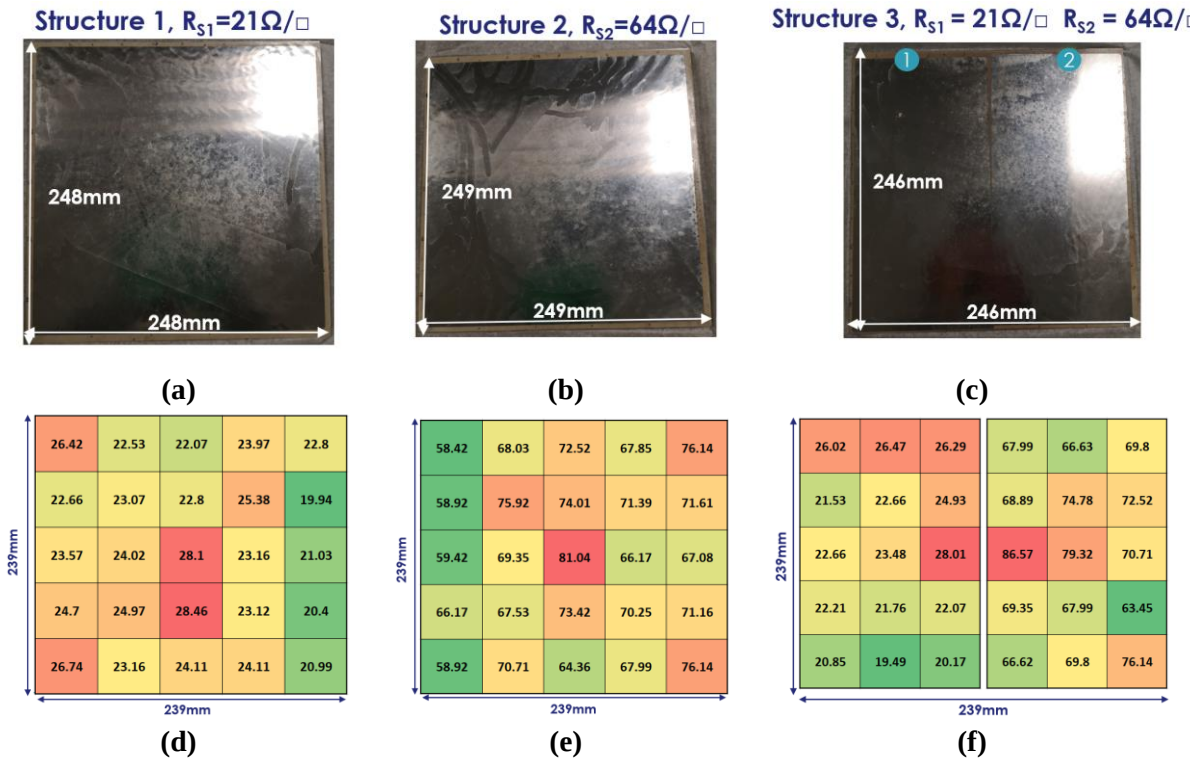

Figure 120. Prototypes fabricated with the electron beam evaporation process. (a) corresponds to Structure 1 with a surface resistance of 21 Ω/□, (b) to Structure 2 with a surface resistance of 64 Ω/□, (c) to Structure 3 with side 1 and side 2 having the same resistances of Structure 1 and Structure 2, respectively. Cartography of the cells surfaces resistance values. For each structure, the green color corresponds to the minimum resistive value characterized while the red corresponds to the maximum resistive value.

As the first step, the cartographies of the surface resistances for the three samples, were performed characterized with a 4-point probes method [102] as presented in the annex. Structure 1 and Structure 2 have been divided into 25 cells (5 for each side), while for Structure 3, each of the two sides has been divided into 15 cells (30 in total). For each cell, a mean resistance value was determined by averaging three different measurements in regions close to the cell center. The cartographies for Structure 1, Structure 2 and Structure 3 are shown in Figure 120(d), Figure 120(e) and Figure 120(f), respectively. The green color depicts the minimum resistance value for each figure, while the red color represents the maximum one. All the three structures exhibit similar resistance dispersion characteristics, with the highest resistances values in the center vicinity and the lowest one close to the edges.

For all structures, the average sheet resistance is comparable to the value of the manufacturer as summarized in Table 26, as well as the minimum and maximum resistance that were experimentally determined.

In it is worth noting that for Structure 2, in Figure 120(b), the average value of the first column is 60.37 Ω/□ (the greenest part) and 72.42 Ω/□ for the last column. This gradual change along the horizontal axis could affect the absorption level with an enhancement of the absorptivity for horizontal polarization rather than for vertical polarization, for which the first (top) and last (bottom) lines have similar resistive values of 67.62 Ω/□ and 68.59 Ω/□, respectively.

The minimum and maximum values, as well as the averaged data, are listed in Table 26.

Table 26. Summary of the characterized surface resistances for the three structures and the one provided by the supplier.

Surface resistance	Structure 1	Structure 2	Structure 3 (side 1)	Structure 3 (side 2)
$R_{s,min}$ (Ω/□)	19.94	58.42	19.49	63.45
$R_{s,max}$ (Ω/□)	28.46	81.04	28.01	86.57
$R_{s,average}$[39] (Ω/□)	23.69	68.98	23.24	71.37
$R_{s,supplier}$ (Ω/□)	21.00	64.00	21.00	64.00

From this table, one can expect that the fluctuations of the sheet resistance influence the absorption level.

The RF setup that was used for the measurement of the reflectivity under oblique incidence is the same as the one presented in Chapter 3. It is again depicted in Figure 121 with a photo of the set up that allows measurements for an oblique incident angle θ of 45°, using two horn antennas at the distance of 57.5 cm from the center support and two lenses. For both vertical and horizontal polarizations, the characterizations were performed in the frequency range of 5 - 16 GHz, comparable to 6 – 14 GHz frequency band of the simulations. To calculate the absorptivity, equation (2.21) and a time-gating are applied to the measured signal in post-processing.

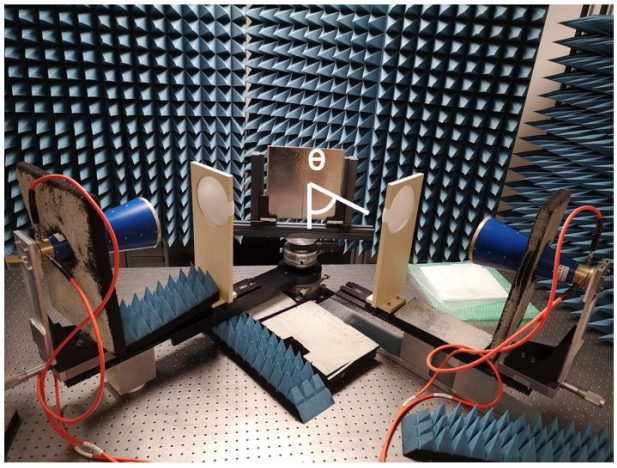

Figure 121. RF characterization setup at TRT for oblique incidences. Two horn Satimo QR2000 antennas are used as well as two lenses. Various absorbers are located close to critical reflection surfaces to avoid spurious reflected signals.

The comparison between the simulations for: minimum surface resistance value (in violet), maximum resistance value (black solid line) and average value (black dashed line), and the characterization results for vertical polarization (in blue) and horizontal polarization (in red) are depicted in Figure 122(a) for Structure 1 and in Figure 122(b) for Structure 2. For Structure 3, only the characterization for oblique incidences is proposed since the structure has no homogeneous value.

As noticed in the simulations, the frequency responses of the resistive screen absorbers are flat over the X-band. A quasi flat response is found for the experimental results for Structure 1, in Figure 122(a), in normal incidence, for both polarizations. In addition the results are comparable to those deduced by simulation with $R_{s,average}$ confirming the homogeneity of the structure around the value of 23.7 Ω/□.

[39] To remind that the average value is not the mean value between the minimum and maximum values of the table but it considers all the cells.

In contrast considering Structure 2, in Figure 122(a), a significant increase (for instance from 0.55 up to 0.6 for Horizontal polarization) of the absorptivity at increasing frequencies can be noticed. Moreover, one can note that the characterization for vertical polarization has an absorptivity of around 55%, while horizontal absorptivity has a value of 60%. This difference is related to the different resistance levels that the incident electromagnetic wave probes during the scattering: for V-pol., the bottom and top sides of the structure have similar average values of 67.62Ω/□ and 68.59 Ω/□, while for H-pol., the average values from left to the right side are 60.37 Ω/□ and 72.42Ω/□.

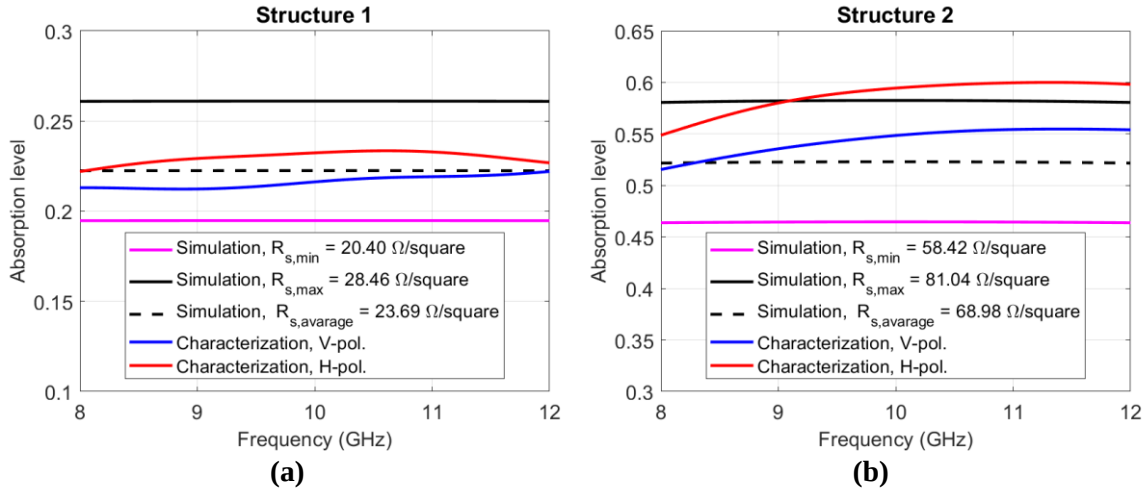

Figure 122.Comparison of the absorption levels over the frequency for the simulations and characterizations of (a) Structure 1 and (b) Structure 2.

As previously discussed, the 5%-ripple constraint over an extended frequency band is considered as critical. As a consequence, we present the characterizations of Structure 1 in Figure 123(a), Structure 2 in Figure 123(b), and Structure 3 in Figure 123(c), in the range 6 – 15 GHz.

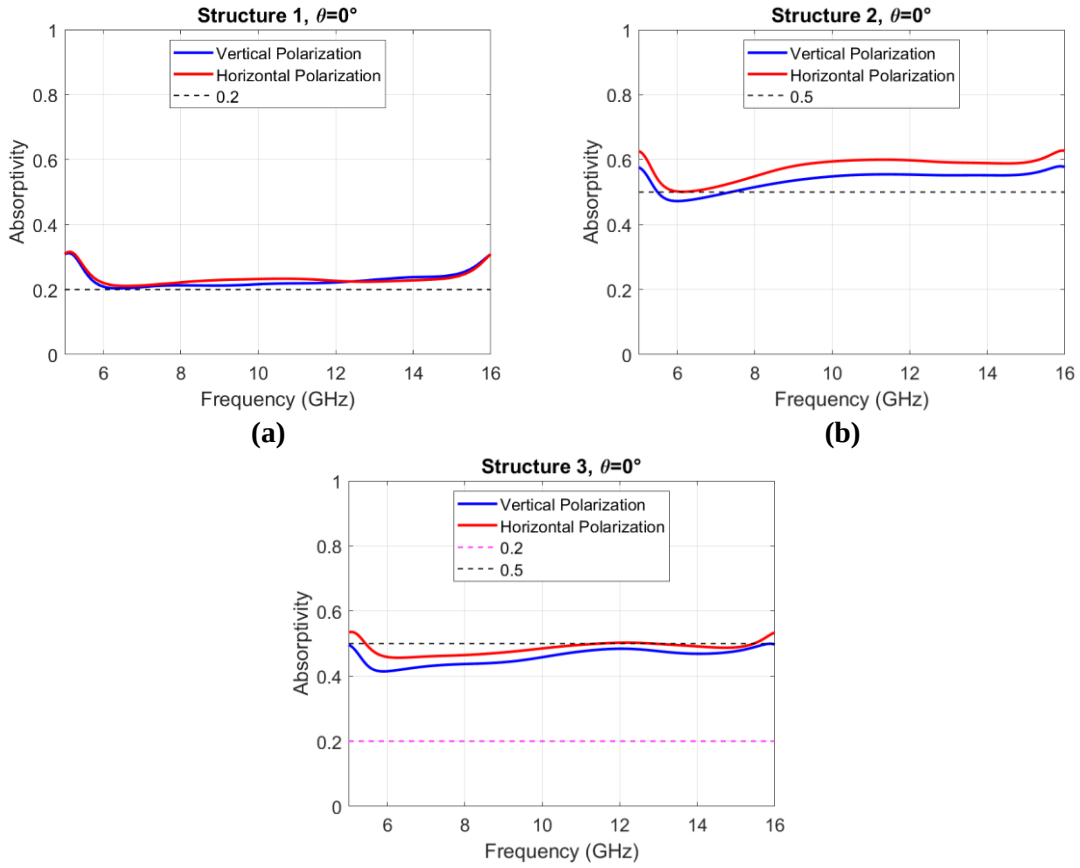

Figure 123. Flatness assessment of the absorbance over the frequency 5-16 GHz for (a) Structure 1, (b) Structure 2, and (c) Structure 3. For all, V-pol. is depicted in blue while H-pol. is depicted in red. The characterization confirms relatively good polarization insensitivity.

With respect to this 5% criterion a quasi-flat absorptivity plateau is shown over the X-band frequency with a ripple of 1.0% in H-pol. for Structure 1, as outlined in Table 27, of 4.9% in H-pol. for Structure 2, as outlined in Table 28, and of 4.7% for V-pol. for Structure 3, as outlined in Table 29. The constraint is then satisfied.

Considering now the extended frequency range from 6 GHz to 15 GHz, this requirement about the relative variations (< 5%) is not satisfied for Structure 2 and Structure 3 with a variation of 9% and 6.9% in V-pol. for Structure 3.

Table 27. Absorptivity for vertical and horizontal polarizations for 5 different frequencies for Structure 1.

Frequency	Absorptivity (V-pol.)	Absorptivity (H-pol.)
8 GHz	21.3%	22.2%
10 GHz	21.6%	23.2%
12 GHz	22.2%	22.7%
6 GHz	20.9%	22.3%
15 GHz	24.5%	23.7%

Table 28. Absorptivity for vertical and horizontal polarizations for 5 different frequencies for Structure 2.

Frequency	Absorptivity (V-pol.)	Absorptivity (H-pol.)
8 GHz	51.5%	54.9%
10 GHz	54.9%	59.5%
12 GHz	55.4%	59.8%
6 GHz	47.2%	50.2%
15 GHz	55.5%	59.2%

Table 29. Absorptivity for vertical and horizontal polarizations for 5 different frequencies for Structure 3.

Frequency	Absorptivity (V-pol.)	Absorptivity (H-pol.)
8 GHz	43.7%	46.5%
10 GHz	45.8%	48.5%
12 GHz	48.4%	50.3%
6 GHz	41.5%	45.8%
15 GHz	47.7%	48.9%

Turning now to the measurements for oblique incidences it is worth-mentioning that while the setup could operate up to 65° two "rules" about the signal dynamic were set to choose the maximum incident angle in the frequency and time domains with a variation in excess of 25 dB between a PEC and free space (set up environment):

In Figure 124(a), PEC (in red) and free space (in green) signals in the time domain at θ = 50°, as well as the applied time-gating windows (in blue), are presented with a dynamic of about 30 dB. In Figure 124(b), the same signals in the frequency domain are plotted, and the dynamic between the metal plate and the free space of more than 25 dB is observed. When increasing θ angle to 55° or more, the dynamic criterion is no longer satisfied.

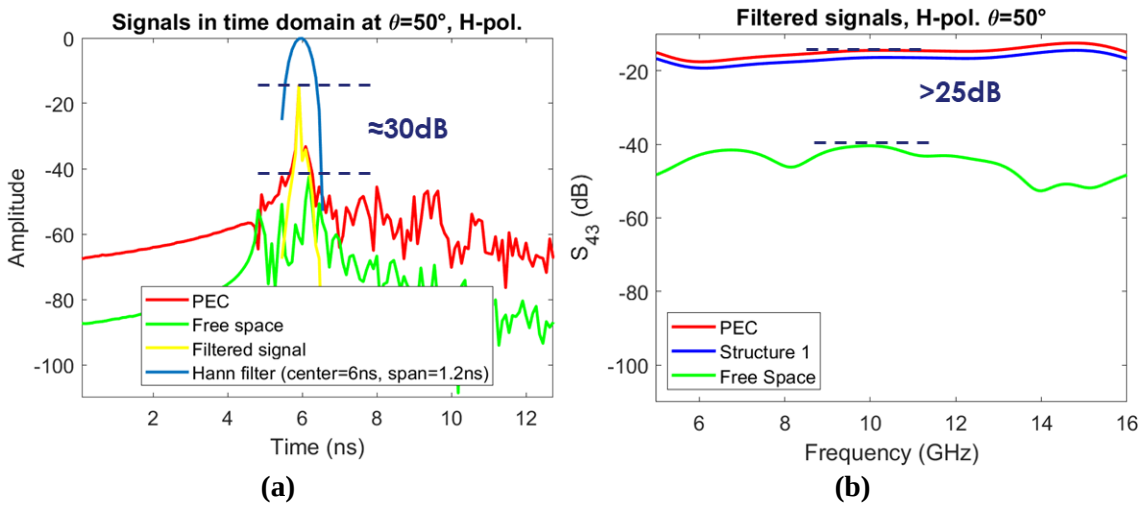

Figure 124. Reflection coefficient of PEC and free space with:(a) signals in the time domain and (b) signals in the frequency domain at the incident angle of 50°. Both have a dynamics of more than 25dB satisfying the criteria of maximum incident angle.

All cartographies in the following are labeled with the same figure notation: (a) and (b) correspond to vertical polarization simulation and characterization, respectively, and (c) and (d) correspond to horizontal polarization simulation and characterization, respectively.

For Structure 1, Figure 125 shows that simulations and characterizations exhibit similar behavior for both V-pol. and H-pol., with a singular behavior for V-pol. around 7 GHz that is difficult to clearly explain owing to the possibility of measurement inaccuracy of fabrication imperfections. For V-pol., angular robustness is maintained up to 30° for a target absorptivity of 20%, as demonstrated by the flat X-band behavior, whereas for H-pol., a different behavior is observed, with the absorption level increasing with incident angle. To illustrate these results, we consider the reflection coefficient formulas, which take incident angles into account and are also used in the simulations below[40].

Because $cos\theta$ is a positive number between 0 and 1, the reflection coefficient Γ(V) increases as the incidence increases, while the reflection coefficient Γ(H) decreases. As a direct result, absorptivity decreases in the first case and increases in the second, as demonstrated by simulations and characterizations.

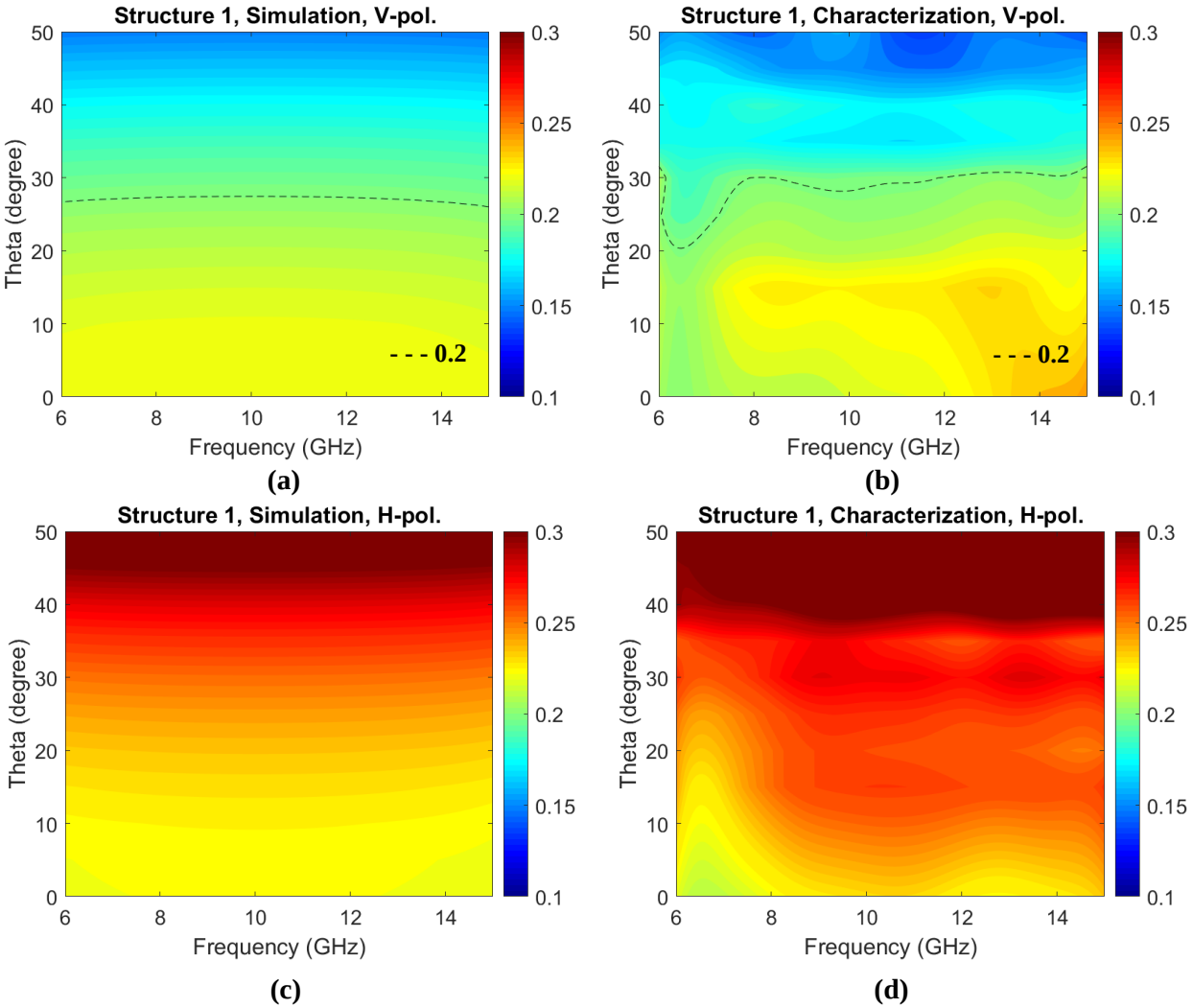

Figure 125. Cartography of the absorptivity for the frequency range of 6 – 15 GHz and for incident angles from 0° to 50° for Structure 1. (a) and (b) correspond to the simulation and characterization for V-pol., respectively. (c) and (d) correspond to the simulation and characterization for H-pol., respectively.

We now consider the simulation and characterization results of Structure 2 as depicted in Figure 126. The characterization and simulation plots for H-pol. are comparable with high absorptivity for high incident angles that decreases following equation (5.7b). For V-pol., simulation

[40] All the simulations from now on are performed in Matlab.

and characterization, two main points can be pointed out. The first point concerns the center frequency in the characterization, in Figure 126(b) that exhibits a shift toward high frequency to around 13 GHz. The second is frequency behavior at a low frequency between 6 and 8 GHz that does not correspond to simulation.

For the first issue, the explanation is that the PEKK dielectric layer has not a permittivity value of 3.3 but a little bit lower. Unfortunately, it was not possible to retrieve this value from a characterization stage. For the second issue, a physically-based explanation was not found so far. However, it is believed that measurements errors could occur during samples characterization since Structure 1 has a similar problem in the same frequency range. Nevertheless, the response over the frequency band in X-band is flat up to incident angles of 28° for an absorptivity of 50%.

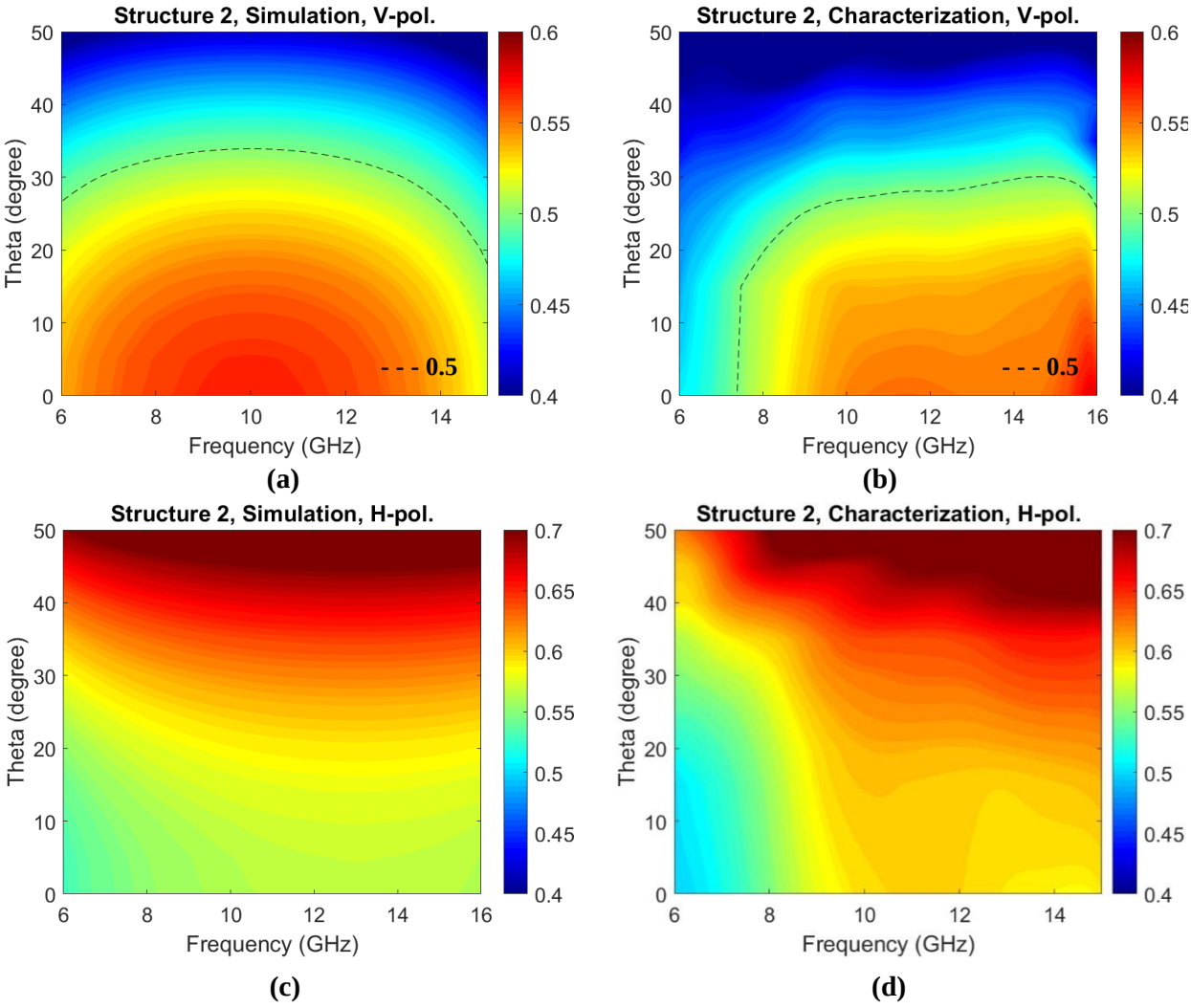

Figure 126. Cartography of the absorptivity for the frequency range of 6 – 15 GHz and for incident angles from 0° to 50° for Structure 1. (a) and (b) correspond to the simulation and characterization for V-pol., respectively. (c) and (d) correspond to the simulation and characterization for H-pol., respectively.

In conclusion, both single resistive layer structures satisfy the specifications with flat absorptivity levels of 20% up to $\theta = 30°$ for Structure 1 and of 50% up to $\theta = 28°$ for Structure 2, for vertical polarization.

The results on absorption performance achieved with the third structure are presented in Figure 127. The evaluation of the diffraction effect, which could be observed at the frontier between two resistance areas on the structure, will be characterized with the ISAR technique. This

measurement campaign is scheduled for Mid-October, the results have not been available to present in this dissertation.

For Structure 3, similar conclusions can be drawn with respect to those deduced from the study on Structure 1 and 2 notably with the fact more absorption is observed for H-pol compared with V-pol results for high incident angles. The unusual behavior between 0° and 15° in Figure 127(b) can be related to the limitations of the characterization setup since no measurement is performed in between these two values due to the lens proximity.

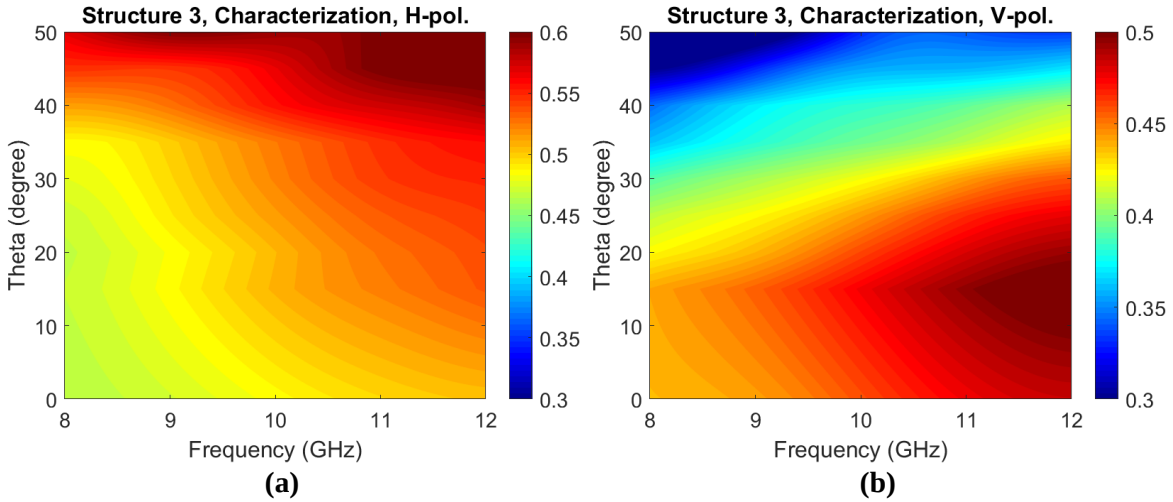

Figure 127. Cartography of the absorptivity for the frequency range of 6 – 15 GHz and for incident angles from 0° to 50° for Structure 3. (a) and (b) correspond to the characterizations for H-pol. and V-pol., respectively.

We can conclude the experimental part of this chapter by presenting Figure 128, which shows the ideal curve (in blackline) of a perfect RF absorber with a linear absorptivity gradient as presented in paragraph 4.1.2. The simulation results (symbols labelled S,$S_{1,2}$) along with the characterization results (symbols noted C,$S_{1,2}$) at the center frequency of the X –band (10 GHz) are also reported. It was found that a quasi-linear gradual variation in the absorption profile was respected for incident angle ranging from 0° to 50° (the results for the latter angle being not plotted for the sake of clarity).

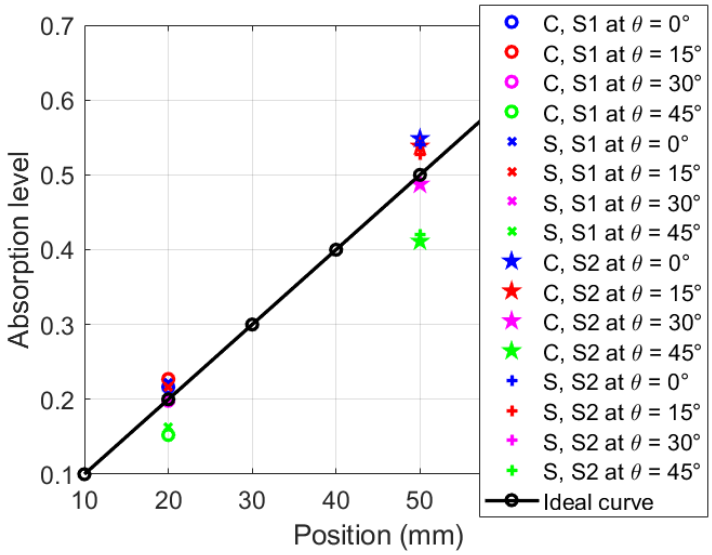

Figure 128. Comparison between ideal RF absorber with absorptivity gradient and the characterization (C) and simulation (S) of Structure 1 (S1), of Structure 2 (S2) for the incident angles of 0° (in blue), 15° (in red), 30° (in rose) and 45° (in green).

The RF characterization results confirm the ability to obtain controlled absorption levels over a given frequency of interest by using inspired-Salisbury-resistive-screen structures with associated values of resistance. Furthermore, from the technological point of view, these results demonstrate the ability to manufacture a quite large and homogeneous resistive surface with controlled values of resistance on a thermoplastic polymer substrate like PEKK.

5.5 Conclusion

The design of a transverse gradient absorber aiming at reducing the Radar Cross Section (RCS) of metallic plates over a broad frequency band was presented in this chapter. Toward this goal, the underlying principle is to introduce a gradual change of the reflectivity of ground metal- λ/4 dielectric spacer - top resistive layers by controlling the sheet resistance through their thickness. By the choice of a λ/4 condition for the dielectric layer, as in a conventional Salisbury screen, it was possible to suppress the imaginary part of the surface impedance resulting from the grounded metal plate and to control the reflectivity level via the value of the sheet resistance that has to be compared the free space real impedance.

Besides the simplicity of this solution from the technological point of view, avoiding complex topologies such as those involved in FSS-based absorbers, it was shown numerically that such structure present some potential advantages. Notably in terms of scalability afforded by the invariance of the sheet resistance gradient that does not depends of the operation frequency. The λ/4 condition that is satisfied at the center frequency of the targeted bands (in the present work from C- to Ku- band with however special attention to the X-band) could however limit the bandwidth. As for the so-called Jauman Screen, a solution to this limitation can be found, as demonstrated numerically in the present work, by stacking two λ/4 -spaced elementary resistive layers at the detriment however of the overall thickness. As a consequence, some tradeoffs have to be found in the context of low-profile transverse gradient absorbers.

The concept of transverse gradient absorber was then applied to the calculation of the Radar Cross Section of uniform metal plates that are compared to the RCS of a prototype with the same overall dimension structures but by replacing a border line by full absorbing strip-shaped layers or whose absorbance is varied gradually from 10 % to 100%. Intuitively it is believed such a gradual absorptivity profile at the boundaries between air and a perfect reflector could modify the edge diffraction effects.

A numerical study of the impact of these gradual absorbance characteristics in the vicinity of the metallic sample boundary shows lower RCS values. They are depending on the EM wave polarization condition with respect to the direction and asymmetry for implementing a single partially absorbing strip layer. The RCS modifications were found essentially at large incidence angles towards grazing incidence. No significant impact was noticed for normal incidence with comparable RCS value with or without absorbers. The scattering mechanisms between an electromagnetic plane wave in the vicinity of the interface between the uniform metal layer and the gradient absorbing layers appear complex. Indeed it seems difficult to have a deep understanding of these scattering mechanisms, that involves surface waves propagating modes, on the sole background of a surface impedance concept. It is thus believed that more rigorous electromagnetic analysis would be necessary for a deeper understanding and better parameter optimization.

From the experimental side, three samples of single NiCr resistive layer / PEKK dielectric slabs /copper ground plate were manufactured by molding and evaporation techniques for an operation in X-band. Their free space characterization confirms the possibility to modulate the

absorbance via the control of the sheet resistance of the NiCr layer opening the way for an engineering of the RCS of metal structures via the engineering of their transition from total to zero reflection.

General conclusion and perspectives

RF metamaterial absorbers with transverse gradients were the focus of my doctoral research, and three different subjects were agreed upon over the three years of work, resulting in this dissertation. To summarize, the first is the development and characterization of thin metamaterial absorbers that operate over a wide frequency range (from 2 to 18 GHz), are polarization-insensitive, and robust to oblique incidences. The second goal is to find new printable filaments for low frequency absorbers (1–4 GHz). The final topic is the design and characterization of thin RF absorbers with an absorptivity gradient that operate in the X-band (8–12 GHz) and can absorb from 0% to 100% along with the structure.

Toward the first goal, a stair-like metasurface absorber was studied by stacking multiple pairs of layers made of alternating metal and dielectric square patches. As shown in chapters 2 and 3, these multilayer and multi-material structures were fabricated by additive manufacturing (Fused Deposition Modeling printing technology), which constitutes one of the main originalities of the present work. Full-wave scattering analysis of an impinging EM wave on such vertically integrated multilayered structures shows frequency-selective trapping modes with the transverse dimensions as resonance relevant parameters. A non-linear variation of this dimension in a stair-like pyramidal pattern has shown equally-spaced resonant frequencies, improving the nearly perfect flat absorption window with a maximum deviation of 2% with respect to the unit absorptivity. From the technological side, it was found that the conductive filament used in the Fused Deposition Modeling technique, whose conductivity of 17000 S/m is much lower than the copper one generally employed in the PCB technology, is another improvement factor to satisfy the critical coupling condition.

In Chapter 2, the experimental results of a successfully 3D-printed stair-like prototype with a square section were presented. The absorber operates in X and Ku bands, 8.2 – 17.2 GHz (FB = 0.71), with a stable absorptivity above 90% up to incident angles of 30° in vertical polarization. Above 30°, the characterized absorbed frequency range is shifted from around 8.5 GHz to above 20 GHz, up to 50°. Due to its square geometry, the structure is not polarization-insensitive for azimuth rotations of the absorber along its normal axis. For instance, for 30° azimuth, the FB is reduced to 0.68 for incidence angles from 0° to 25°. Above this angle, a slightly lower absorption level of 0.85 is noticed in a sub-range between 12 GHz and 14 GHz for incidence angles ranging between 25° and 50° reducing the angular robustness of the structure.

In Chapter 3, two stair-like absorbers with a circular shape and different dielectric thicknesses were presented for C-band to address polarization insensitivity and angular robustness issues. Tuning the dielectric thickness was a practical way to satisfy the critical coupling condition to increase the absorptivity for normal incidence. The circular shape was chosen for two reasons: the first was to keep the structure symmetric for all polarizations, and the second was to make the fabrication process more accessible than the previous structure. The characterization of both structures confirmed the answer to the first issue regarding polarization insensitivity. The two absorbers were made with two different dielectrics to validate using high permittivity material to increase the angular robustness. It was experimentally demonstrated that increasing the real value of the permittivity by 58% resulted in a 30% enhancement in angular robustness for vertical polarization and a generally better response for horizontal polarization of around 40%.

Chapter 4 was devoted to studying design and technological solutions to satisfy the specifications of absorbers operating at low frequencies (L – S bands) and the development of new printable materials. Due to the high thickness of the geometry, the first approach of exploiting stair-like structures with a high permittivity value was not an optimal solution. Furthermore, the challenges of printing such a structure are currently too difficult to overcome. New solutions were proposed, including planar structuring techniques and full-dielectric approaches using novel magneto-dielectric materials to introduce an intrinsic magnetic response. The real and imaginary parts of permittivity and permeability, and the material thickness brought numerous degrees of freedom for optimizing a planar structure. Optimizing a magneto-dielectric material for quasi-unitary absorptivity at 2 GHz, with a structure of 5 mm-thickness, offered a simulated absorption level above 90% over the frequency range of 1.6 – 4.5 GHz. Nevertheless, magnetic materials have a significant disadvantage in terms of weight. In a preliminary investigation, full-dielectric resonators with transversely alternating magnetic and thin dielectric bases were designed to build a chess-based metamaterial absorber, reducing the volume of magnetic material used. With this technique, two absorbers were designed: the first one operates in the frequency range 1.11 – 6 GHz (FB = 1.38) while the second one from 2.43 GHz to 26.0 GHz (FB = 1.66) with an absorptivity value above 80%. Despite these promising results, a solution based on magnetic materials was found unoriginal for doctoral research. The Ph.D. program's research axis shifted to a more scientifically attractive topic that addressed the third point of the dissertation.

In Chapter 5, a study about the impact on the Radar Cross Section of variable sheet resistance absorbing screens with lateral reflectivity gradient was reported to answer the last problematics of the Ph.D.. The simulated Radar Cross Section over the incidence angle showed significant improvement, between 5 dB and 10 dB in X-band compared to a reference structure, a double metal plate, for angles between 20° and 50°. This improvement was possible by implementing a surface with gradual absorptivity along the transverse directions of space, which can be realized by changing the surface resistances. The calculated surface resistances are frequency-independent, suggesting that the concept of such partial absorbing structures is scalable in different frequency bands (C and Ku bands were investigated as well). It was also shown that the Radar Cross Section reduction depends on the EM wave polarization and the symmetry in implementing the gradients in the vicinity of the metal plates. To go further in this direction, it is believed that an in-depth full-wave scattering analysis will be essential. Three different sheet resistance absorbers were successfully fabricated on the experimental side by evaporating NiCr resistive layers on molded PEKK thermoplastic substrates. The preliminary characterization of their absorption levels in a free space measurement set-up has confirmed the validity of this sheet resistance approach. The variation of the absorptivity between the simulations and the characterizations of two prototypes was 3% for a structure with an absorptivity of 0.23 and 1.7% for the structure with an absorptivity of 0.58, both for horizontal polarization. For vertical polarization, the variation was 2.7% and 5.4%, respectively. Other measurements will be performed to determine the Radar Cross Section of the prototypes within a measurement session that could not be performed before the redaction of the manuscript.

What could be the perspectives of development of the next absorbers?

To begin with, it is expected that rapid advancements in additive fabrication technology, particularly in the structuring of multiple materials (conductor, (magneto)-dielectrics, etc.), will enable the fabrication of more complex structures that would be more resistant to oblique incidences and easier to fabricate.

Planar geometry was primarily evaluated in this study, although non-planar multilayered structures could potentially benefit from future enhancement, particularly in terms of incidence angle robustness.

Combining multi-scale resonators in multiple axes could improve overall performance by optimizing the trade-off between absorption bandwidth and low-profile structure. For instance, the optimal combination between the number of layers, dielectric thicknesses, EM properties of materials, and surface resistances, as demonstrated by M. Lobet et al. form Harvard University, can be determinate.

Frequency agility could also be introduced so that the performance of the absorbing screen, notably in terms of reflectivity, could be dynamically controlled. One can find in the literature already a successful demonstration of PMA frequency agility through Liquid Crystals infiltrated in between the conductive layers that could be generalized to multilayered structures, as described by W. Padilla et al. from Boston College.

Concluding these future research axes with the resistive screens discussed in Chapter 5, one could envision increasing the layers number and EM material properties to increase the fractional bandwidth as well as the angular robustness of these Salisbury-inspired absorbers. In addition, low observability could be achieved in various frequency bands. Indeed, industrial research on resistive screens enables the fabrication of meters of these layers, for example, via R2R (Roll to Roll) machining, which produces an absorber with a gradient of absorptivity that can be attached to a variety of substrates with varying thicknesses to change easily the operating frequency band.

Annex

A.1 Analysis and characterization techniques

In this section, we present three techniques that were exploited during the Ph.D. work to characterize and analyze the samples:

- Dielectric characterization using a cylindrical cavity to determine dielectric permittivity,
- Resistivity characterization using a 4-point probes technique,
- Computed Tomography (CT) technology using X-ray to analyze the internal part of one of the proposed structures.

A.1.1 Permittivity characterization

A cavity perturbation method is a technique that allows retrieving the complex permittivity exploiting a resonant cavity. An empty cavity has a specific resonance frequency. By inserting a dielectric sample, this resonance is shifted and the quality factor is reduces, allowing for the determination of the dielectric properties [141].

For our measurements, the cylindrical cavity has a diameter of 25.05 mm resonating at 15.72 GHz with a quality factor without any sample inserted Q_0 of 17200, the cavity is presented in Figure 129(a). The complete setup for the characterization is shown in Figure 129(b).

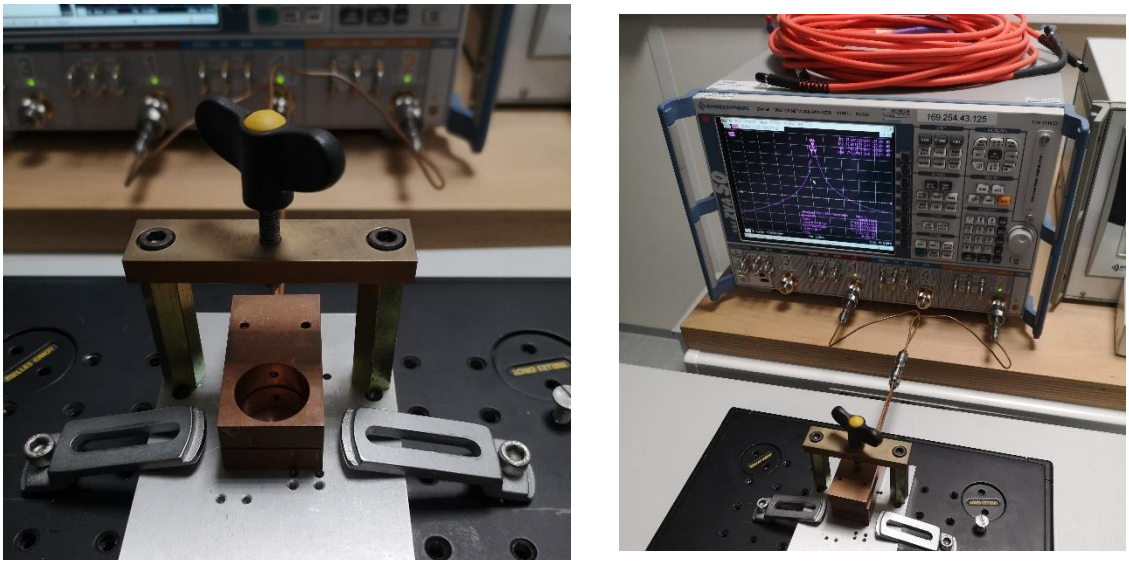

(a) **(b)**

Figure 129. (a) Picture of the open cylindrical cavity with a diameter of 25.05 mm and resonating at 15.72 GHz. (b) Complete measurement setup with the cylindrical cavity that is close and attached to the VNA through two coaxial cables and the resonant peak being visible in the VNA display.

A.1.2 Resistivity characterization

The four-probe method is the most often used approach for determining sheet resistance. Electrical contact with the material is made by employing four equidistant, co-linear probes as

illustrated in Figure 130(a). The measurement consists of passing a current through the resistive screen and measuring the corresponding voltage drop.

The method allows calculating the sheet resistance ($R_{\square}$ in Ω/□) with (1.16a) and the resistivity (ρ) with (1.16b)

$$R_{\square} = C\ R_{4-point} \tag{1.16a}$$

$$\rho = R_{\square}\ t \tag{1.16b}$$

Where C is a geometrical factor of the sample to measure [102], $R_{4\text{-}point}$ is the calculated resistance from an ohmmeter and t is the thickness of the resistive sheet. The exploited setup is presented in Figure 130(b).

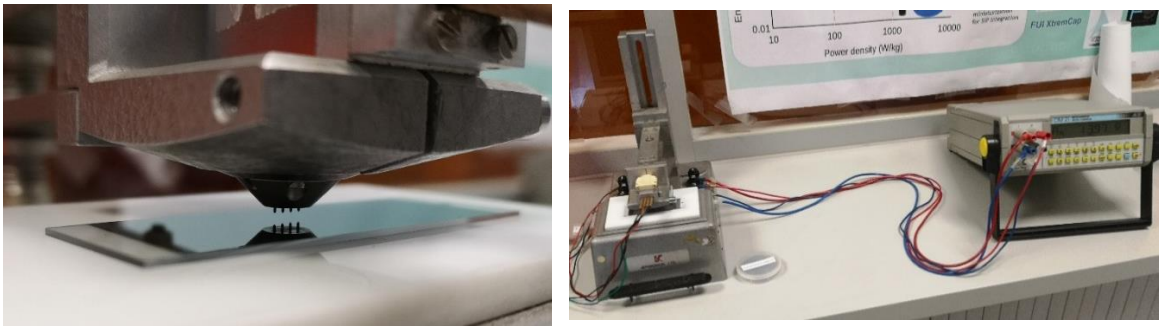

(a) **(b)**

Figure 130. (a) Picture of the 4-point probes setup available at TRT with an AOIP OM 21 benchtop on the right and the rigid support for the four points on the left. (b) a zoom of the 4 points exploited with a sample of 2.5 cm x 6.45 cm.

A.1.3 Computed Tomography technique

CT scanning is a non-destructive technique that utilizes X-rays to visualize interior features within solid objects and realize cross-sectional scans of their 3D geometries. Cross-sections images are reconstructed using measurements of the attenuation in intensity of X-ray beams within the volume of the objects under investigation [142].

An example of CT scanning result is shown in Figure 131, in which a 3D reconstruction of a portion of the structure presented in Chapter 2 is presented.

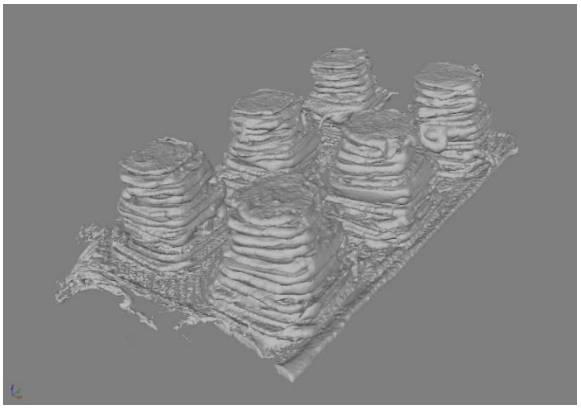

Figure 131. 3D reconstruction of a 3D-printed structure exploiting CT technique. The X-ray analysis of the presented structure is detailed in Chapter 2.

A.2 Manufacturing technology within the thesis

This section presents two manufacturing techniques we exploited to fabricate the 5 prototypes in the 3 years-Ph.D.. Fused Depositing Modelling (FDM) that is exploited in Chapter 3 and Chapter 4 and E-beam technology that is exploited Chapter 5.

A.2.1 FDM technique

Fused deposition modeling (FDM) is an additive manufacturing (AM) technology, which uses continuous filaments of thermoplastic materials. Typically, the filament is heated to the melting point before being extruded via a 3D printer nozzle. The nozzle goes back and forth defined in the original CAD model file according to the spatial coordinates in x, y-axis and in the z-axis with a power screw. The polymer can be deposited using multiple extrusion nozzles and the resolution and efficacy of extrusion are typically heavily dependent on the thermoplastic filament qualities. Figure 132 shows the FDM process conceptually, with the material filament being supplied continuously into the heater and the machine nozzle by two opposing driving pulleys. The fused material is deposited on the machine bed layer by layer modeling the structure. As a result, special 3D printers for certain filament materials have been developed while the majority of low-cost FDM 3D printers can only print with a single type of thermoplastic. The most common are PolyLactic Acid (PLA) or Acrylonitrile Butadiene Styrene (ABS) and most of the filaments have one between these two polymers as base.

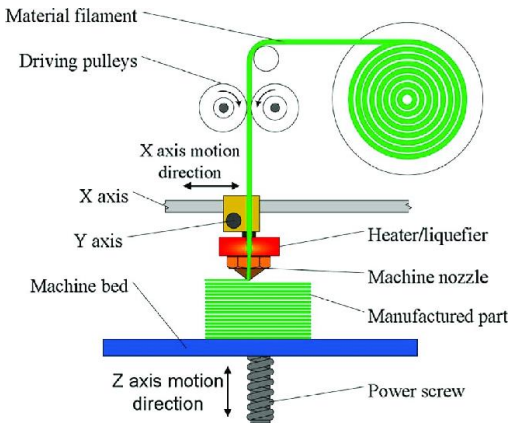

Figure 132. Model of a 3D-printed for Fused Deposition Technology (FDM) technology.

A.2.2 Electron beam evaporation

The electron beam (E-beam) evaporation process is a physical vapor deposition technique that produces high deposition rates from 0.1 μm/min to 100 μm/min. The E-beam technique allows manufacturing thin film [143]. The pressure in the deposition chamber is set to 10^{-5} Torr or less. Materials in the form of ingots or compacted solids are used to be evaporated. The electron beam is focused on the coating material that is after accelerated to a high kinetic energy. The electrons kinetic energy is transformed into thermal energy, which raises the surface temperature of the materials, causing evaporation and deposition on the substrate. As a result, a coated dielectric is obtained as presented in Chapter 5.

References

[1] K. Y. Bliokh, Y. P. Bliokh, V. Freilikher, S. Savel'ev and F. Nori, "Colloquium: Unusual resonators: Plasmonic, metamaterials, and random media," Rev. MOD. Phys, vol. 80, no. 4, pp. 1201-1213, Oct., 1, 2008. DOI: 10.1103/RevModPhys.80.1201.

[2] D. M. Pozar, *Microwave Engineering*, 4th ed., USA: Wiley, 2011.

[3] C. A. Balanis, *Advanced Engineering Electromagnetics*, 2nd ed., USA: Wiley, 2012.

[4] W. Emerson, "Electromagnetic wave absorbers and anechoic chambers through the years," *IEEE Transactions on Antennas and Propagation*, vol. 21, no. 4, pp. 484-490, July 1973.

[5] Naamlooze Vennootschap Machmerieen, French Patent 802 728, Feb., 19, 1936.

[6] L. J. Du Toit, "The design of Jauman absorbers," *IEEE Antennas and Propagation Magazine*, vol. 36, no. 6, pp. 17-25, Dec. 1994.

[7] W.W. Salisbury, "Absorbent Body for Electromagnetic Waves," U.S. patent 2 599 944, Jun., 10, 1952.

[8] E. F. Knott, J. F. Schaeffer and M. T. Tuley, *Radar Cross Section*, 2nd ed., Raleigh, NC, USA: SciTech Publishing, 2004.

[9] X. C. Tong, *Advanced Materials and Design for Electromagnetic Interference Shielding*, USA: CRC Press, 2009.

[10] H. A. Tanner, "Fibrous microwave absorber," U.S. Patent 2 977 591, Mar., 28, 1961.

[11] M.J. Park, J. Choi and S.S. Kim, "Wide bandwidth pyramidal absorbers of granular ferrite and carbonyl iron powders," *IEEE Transactions on Magnetics*, vol. 36, no. 5, pp. 3272-3274, Sep., 2000. DOI: 10.1109/20.908766.

[12] J. J. Gau, W. D. Burnside and M. Gilreath, "Chebyshev multilevel absorber design concept," *IEEE Transactions on Antennas and Propagation*, vol. 45, no. 8, pp. 1286-1293, Aug. 1997. DOI: 10.1109/8.611249.

[13] B. A. Munk, *Frequency Selective Surface: Theory and Design*, USA: Wiley, 2000.

[14] E. Knott, "The thickness criterion for single-layer radar absorbents," *in IEEE Transactions on Antennas and Propagation*, vol. 27, no. 5, pp. 698-701, September 1979. DOI: 10.1109/TAP.1979.1142149.

[15] W. Li, T. Wu, W. Wang, P. Zhai, and J. Guan, "Broadband patterned magnetic microwave absorber," *Journal of Applied Physics*, vol. 116, pp. 044110, Jul., 30, 2010. [DOI: https://doi.org/10.1063/1.4891475].

[16] M.-J. Park, J. Choi and S-S. Kim, "Wide bandwidth pyramidal absorbers of granular ferrite and carbonyl iron powders," *IEEE Transactions on Magnetics*, vol. 36, no. 5, pp. 3272-3274, Sep. 2000. DOI: 10.1109/20.908766.

[17] R. L. Fante and M. T. McCormack, "Reflection properties of the Salisbury screen," *IEEE Transactions on Antennas and Propagation*, vol. 36, no. 10, pp. 1443-1454, Oct. 1988, DOI: 10.1109/8.8632.

[18] T. Beeharry, "Study of the electromagnetic interactions between radar equipment under integrated and compact mature: design and validation," Thèse de doctorat Electronique, Optronique et Systèmes Paris 10, 2019. http://www.theses.fr/2019PA100011/document.

[19] H. Singh, E. J. Duraisingh Daniel, H. Singh Rawat, R. George, *Fundamentals of EM Design of Radar Absorbing Structures (RAS)*, Singapore, Springer, 2018.

[20] E. Michielssen, J. -. Sajer, S. Ranjithan and R. Mittra, "Design of lightweight, broad-band microwave absorbers using genetic algorithms," *IEEE Transactions on Microwave Theory and Techniques*, vol. 41, no. 6, pp. 1024-1031, 1993. DOI: 10.1109/22.238519.

[21] B. Chambers and A. Tennant, "Optimised design of Jaumann radar absorbing materials using a genetic algorithm," *IEE Proceedings - Radar, Sonar and Navigation*, vol. 143, no. 1, pp. 23-30, Feb. 1996. DOI: 10.1049/ip-rsn:19960316.

[22] A. Ghadimi, V. Nayyeri, M. Khanjarian, M Soleimani, and O. M. Ramahi, "Design and simulation of a wideband, wide-angle and polarization-insensitive microwave absorber based on pattern optimization of resistive films," *Journal of Physics D: Applied Physics*, vol. 54, no. 5, pp. 055102, Nov., 9, 2020. DOI: 10.1088/1361-6463/abbb46.

[23] Y. Han and W. Che, "Low-Profile Broadband Absorbers Based on Capacitive Surfaces," *IEEE Antennas and Wireless Propagation Letters*, vol. 16, pp. 74-78, Apr., 26, 2017, DOI: 10.1109/LAWP.2016.2556753.

[24] B. A. Munk, P. Munk and J. Pryor, "On Designing Jaumann and Circuit Analog Absorbers (CA Absorbers) for Oblique Angle of Incidence," *IEEE Transactions on Antennas and Propagation*, vol. 55, no. 1, pp. 186-193, Jan. 2007. DOI: 10.1109/TAP.2006.888395.

[25] A. Kazem Zadeh and A. Karlsson, "Multilayered wideband absorbers for oblique angle of incidence," *IEEE Transactions on Antennas and Propagation*, vol. 58, no. 11, pp. 3637–3646, Nov., 2010. DOI: 10.1109/TAP.2010.2071366.

[26] A. Kazem Zadeh and A. Karlsson, "Capacitive Circuit Method for Fast and Efficient Design of Wideband Radar Absorbers," *IEEE Transactions on Antennas and Propagation*, vol. 57, no. 8, pp. 2307-2314, Aug. 2009. DOI: 10.1109/TAP.2009.2024490.

[27] F. Bilotti and L. Sevgi, "Metamaterials: definitions, properties, applications, and FDTD-based modeling and simulation," *International Journal of RF and Microwave Computer-Aided Engineering*, vol. 22, no. 4, pp. 422-438, July, 2012. DOI: 10.1002/mmce.20634.

[28] V. G. Veselago, "The Electrodynamics of Substances with simultaneously negative Values of ε and μ," *Soviet Physics Uspekhi*, vol. 10, no. 4, Apr., 30, 1968.

[29] J. B. Pendry, "Negative Refraction Makes a Perfect Lens," Phys. Rev. Lett. vo. 85, no. 18, pp. 3966, Oct., 30, 2000. DOI: 10.1103/PhysRevLett.85.3966.

[30] N. Engheta and R. W. Ziolkowski, *Metamaterials: Physics and Engineering Explorations*, Piscataway, NJ, USA, Wiley-IEEE press, 2006.

[31] D. R. Smith and J. B. Pendry, "Homogenization of Metamaterial by Field Averaging," *J. Opt. Soc. Am. B*, vo. 23, no. 3, pp. 391-403, Mar. 2006. [DOI: https://doi.org/10.1364/JOSAB.23.000391].

[32] C. Pfeiffer and A. Grbic, "Metamaterial Huygens' Surfaces: Tailoring Wave Fronts with Reflectionless Sheets," *Phys. Rev. Lett.*, vol. 110, no. 19, 197401, [DOI: https://link.aps.org/doi/10.1103/PhysRevLett.110.197401].

[33] J. B. Pendry, A. J. Holden, D. J. Robbins and W. J. Stewart, "Magnetism from conductors and enhanced nonlinear phenomena," *in IEEE Transactions on Microwave Theory and Techniques*, vol. 47, no. 11, pp. 2075-2084, Nov. 1999. DOI: 10.1109/22.798002.

[34] N. Engheta, "Thin absorbing screens using metamaterial surfaces," *IEEE Antennas and Propagation Society International Symposium (IEEE Cat. No.02CH37313)*, San Antonio, TX, USA, 2002, pp. 392-395 vol.2. DOI: 10.1109/APS.2002.1016106.

[35] F. Costa, A. Monorchio and G. Manara, "Analysis and Design of Ultra Thin Electromagnetic Absorbers Comprising Resistively Loaded High Impedance Surfaces," *IEEE Transactions on Antennas and Propagation*, vol. 58, no. 5, pp. 1551-1558, May 2010. DOI: 10.1109/TAP.2010.2044329.

[36] K. N. Rozanov, "Ultimate thickness to bandwidth ratio of radar absorbers," *IEEE Transactions on Antennas and Propagation*, vol. 48, no. 8, pp. 1230-1234, Aug., 2000. DOI: 10.1109/8.884491.

[37] F. Bilotti, A. Toscano, K. B. Alici, E. Ozbay and L. Vegni, "Design of Miniaturized Narrowband Absorbers Based on Resonant-Magnetic Inclusions," *IEEE Transactions on Electromagnetic Compatibility*, vol. 53, no. 1, pp. 63-72, Feb., 2011. DOI: 10.1109/TEMC.2010.2051229.

[38] N. I. Landy, S. Sajuyigbe, J. J. Mock, D. R. Smith, and W. J. Padilla, "Perfect Metamaterial Absorber," Phys. Rev. Lett., vo. 100, no. 20, pp. 207402-1-4, May, 18, 2008. DOI: 10.1103/PhysRevLett.100.207402.

[39] D. R. Smith, S. Schultz, P. Markoš and C. M. Soukoulis, "Determination of effective permittivity and permeability of metamaterials from reflection and transmission coefficients," *Phys. Rev. B*, vol. 65, no. 19, pp. 195104, Apr., 19, 2002, DOI: 10.1103/PhysRevB.65.195104.

[40] J. Hao, J. Wang, X. Liu, W. J. Padilla, L. Zhou and M. Qiu, "High performance optical absorber based on a plasmonic metamaterial," *Appl. Phys. Lett.*, vol. 96, no. 25, pp. 251104, Jun., 22, 2010. [DOI: https://doi.org/10.1063/1.3442904].

[41] D. Ye, Z. Wang, K. Xu, H. Li, J. Huangfu, Z. Wang, and L. Ran, "Ultrawideband Dispersion Control of a Metamaterial Surface for Perfectly-Matched-Layer-Like Absorption," *Phys.*

Rev. Lett., vol. 111, no. 18, pp. 187402, Oct., 29, 2013. DOI: 10.1103/PhysRevLett.111.187402.

[42] Q. Feng, M. Pu, C. Hu, and X. Luo, "Engineering the dispersion of metamaterial surface for broadband infrared absorption," *Opt. Lett. 37*, vol. 37, no. 11, pp. 2133-2135, Jun., 1, 2012. [DOI: https://doi.org/10.1364/OL.37.002133].

[43] D. Ramaccia, C. Guattari, F. Bilotti and A. Toscano, "Metamaterial split-ring resonators for retrieval of soil electromagnetic properties," *2013 7th International Congress on Advanced Electromagnetic Materials in Microwaves and Optics*, 2013, pp. 121-123, DOI: 10.1109/MetaMaterials.2013.6808973.

[44] Y. Wen, H.-W. Zhang, Y.-S. Xie, Q.-H. Yang and Y. Liu, "Dual band terahertz metamaterial absorber: design, fabrication, and characterization," *Appl. Phys. Lett.*, vol. 95, no. 24, pp. 241111, Dec. 2009. DOI: 10.1063/1.3276072.

[45] X. Shen, T. J. Cui, J. Zhao, H. F. Ma, W. X. Jiang and L. Hui. "Polarization-independent wide-angle triple-band metamaterial absorber," *Optics Express*, vol. 19, no, 10, pp. 9401–9407, Apr. 2011. [DOI: https://doi.org/10.1364/OE.19.009401].

[46] H. Li, L. H. Yuan, X. P. Shen and Q. Cheng, "Ultrathin multiband gigahertz metamaterial absorbers," *Journal of Applied Physics*, vol. 110, no. 1, pp. 014909, Jul., 12, 2011. [DOI: https://doi.org/10.1063/1.3608246].

[47] Q. Ye, Y. Liu, M. Li and H. Yang. Multi-band metamaterial absorber made of multi-gap SRRs structure. *Applied Physics A*, vol. 107, no. 1, pp.155–160, Feb., 11, 2012. DOI 10.1007/s00339-012-6796-7.

[48] L. Huang and H. Chen, "Multi-Band and Polarization Insensitive Metamaterial Absorber," *Progress In Electromagnetics Research*, vol. 113, pp. 103-110, 2011. DOI:10.2528/PIER10122401.

[49] R. Yahiaoui and H. H. Ouslimani, "Broadband polarization independent wide-angle and reconfigurable phase transition hybrid metamaterial absorber," *Journal of Applied Physics*, vol. 122, no. 9, pp. 093104, Sep., 7, 2017. DOI: 10.1063/1.4989933.

[50] T. Beeharry, R. Yahiaoui, K. Selemani, and H. H. Ouslimani, "A Co-Polarization Broadband Radar Absorber for RCS Reduction," *Materials*, vol. 11, no. 9, pp.1668, Sep., 9, 2018. DOI: 10.3390/ma11091668.

[51] Z. Zhou, K. Chen, J. Zhao, P. Chen, T. Jiang, B. Zhu, Y. Feng and Y. Li, "Metasurface Salisbury screen: achieving ultra-wideband microwave absorption," *Opt. Express*, vol. 25, no. 24, pp. 30241-30252, Nov., 17, 2017. DOI: 10.1364/OE.25.030241.

[52] F. C. Seman, R. Cahill, V. F. Fusco and G. Goussetis, "Design of a salisbury screen absorber using frequency selective surfaces to improve bandwidth and angular stability performance," *IET Microwaves, Antennas & Propagation*, vol. 5, no. 2, pp. 149-156, Jan., 31, 2011. DOI: 10.1049/iet-map.2010.0072.

[53] G. W. Zhang, J. Gao, X. Y. Cao, L. Sijia and H. H. Yang, "Wideband Miniaturized Metamaterial Absorber Covering L-Frequency Range," *Radioengineering*, vol. 27, no. 1, pp. 154-160, 2018. DOI: 10.13164/re.2019.0154.

[54] W. Zuo, Y. Yang, X. He, C. Mao and T. Liu, "An Ultrawideband Miniaturized Metamaterial Absorber in the Ultrahigh-Frequency Range," *IEEE Antennas and Wireless Propagation Letters*, vol. 16, pp. 928-931, Sep., 30, 2016. DOI: 10.1109/LAWP.2016.2614703.

[55] W. Zuo, Y. Yang, X. He, D. Zhan and Q. Zhang, "A Miniaturized Metamaterial Absorber for Ultrahigh-Frequency RFID System," *IEEE Antennas and Wireless Propagation Letters*, vol. 16, pp. 329-332, Jun., 01, 2017. DOI: 10.1109/LAWP.2016.2574885.

[56] M. D. Banadaki, A. A. Heidari and M. Nakhkash, "A Metamaterial Absorber With a New Compact Unit Cell," *IEEE Antennas and Wireless Propagation Letters*, vol. 17, no. 2, pp. 205-208, Feb. 2018. DOI: 10.1109/LAWP.2017.2780231.

[57] Y. Kim, Y. Yoo, J. Hwang, and Y. Lee, "Ultra-broadband microwave metamaterial absorber based on resistive sheets," *Journal of Optics*, vol. 19, no. 1, 2017.DOI: 10.1088/2040-8986/19/1/015103

[58] A. Poddubny, I. Iorsh, P. Belov and Yuri Kivshar, "Hyperbolic Metamaterials," *Nature photonics*, vol. 7, pp. 948–957, Nov., 28, 2013. [DOI:https://doi.org/10.1038/nphoton.2013.243].

[59] X. Li, M. Pu, X. Ma, Y. Guo, P. Gao and X. Luo, " Dispersion engineering in metamaterials and metasurfaces," *J. Phys. D: Appl. Phys*, vol. 51, pp. 054002, Jan., 12, 2018. DOI: https://doi.org/10.1088/1361-6463/aaa233.

[60] Y. Cui, K. H. Fung, J. Xu, H. Ma, Y. Jin, S. He and N. X. Fang, "Ultrabroadband Light Absorption by a Sawtooth Anisotropic Metamaterial Slab," *Nano Lett.*,vol. 12, no. 3, pp. 1443-1447, Feb., 6, 2012. DOI: 10.1021/nl204118h.

[61] C. A. Balanis, *Antenna Theory: Analysis and Design*, 4th edition, Hoboken, NJ, USA, Wiley, 2016.

[62] F. Ding, Y. Cui, X. Ge, F. Zhang, Y. Jin, and S. He, "Ultra-broadband microwave metamaterial absorber," Appl. Phys. Lett., vo. 100, no. 10, pp. 103506, Mar., 09, 2012. [DOI: https://doi.org/10.1063/1.3692178].

[63] C. Long, S. Yin, W. Wang, W.Li, J. Zhu and J. Guan, "Broadening the absorption bandwidth of metamaterial absorbers by transverse magnetic harmonics of 210 mode," Sci. Rep., vo. 6, pp. 21431, Feb., 18, 2016. [DOI: https://doi.org/10.1038/srep21431].

[64] X. Yin, C. Long, J. Li, *et al.*, "Ultra-wideband microwave absorber by connecting multiple absorption bands of two different-sized hyperbolic metamaterial waveguide arrays," *Sci Rep*, vol. 5**,** pp. 15367, Oct., 19, 2015. DOI: 10.1038/srep15367.

[65] Y. Liu, W. Guo, and T. Han, "Ultra-broadband absorption with gradient pyramidal metamaterials," Progress In Electromagnetics Research, vol. 78, pp. 217–224, 2017. DOI:10.2528/PIERC17081107.

[66] C. M. Watts, X. Liu, and W. J. Padilla, "Metamaterial electromagnetic wave absorbers," Adv. Mater., vo. 24, no. 23, June, 24, 2012, pp. OP98-OP120. DOI: 10.1002/adma.201200674.

[67] Y. Ra'Di, C. R. Simovski, and S. A. Tretyakov, "Thin Perfect Absorbers for Electromagnetic Waves Theory, Design, and Realizations," Phys. Rev. Applied, vo. 3, no. 3, pp. 037001-1-37, Mar., 17, 2015. DOI:10.1103/PhysRevApplied.3.03700.

[68] R. Czarny et al., "High Permittivity, Low Loss, and Printable Thermoplastic Composite Material for RF and Microwave Applications," 2018 IEEE Conference on Antenna Measurements & Applications (CAMA), Vasteras, 2018, pp. 1-4. DOI: 10.1109/CAMA.2018.8530660.

[69] Preperm, https://www.preperm.com/products/stock-shapes/#filaments

[70] Electrifi, https://www.multi3dllc.com/about-electrifi/.

[71] R. Panwar, S. Puthucheri, D. Singh, and V. Agarwala, "Design of Ferrite–Graphene-Based Thin Broadband Radar Wave Absorber for Stealth Application", *IEEE Transactions on Magnetics*, vol. 51, no. 11, Jul., 9, 2015. DOI: 10.1109/TMAG.2015.2454431.

[72] F. M. Espiau and G. P. Le Sage, "3D Printed Radio Frequency Absorber," U.S. patent 2016/0263823 A1, Sep., 15, 2016.

[73] R. Kronberger and P. Soboll, "New 3D printed microwave metamaterial absorbers with conductive printing materials," *2016 46th European Microwave Conference (EuMC)*, London, 2016, pp. 596-599. DOI: 10.1109/EuMC.2016.7824413.

[74] D. Zhou, X. Huang, and Z. Du, "Analysis and Design of Multilayered Broadband Radar Absorbing Metamaterial Using the 3-D Printing Technology-Based Method," *IEEE Antennas and Wireless Propagation Letters*, vol. 16, pp. 133-136, Feb. 2017. DOI: 10.1109/LAWP.2016.2560904.

[75] W. Jiang, L. Yan, H. Ma, Y. Fan, J. Wang, M. Feng, and S. Qu, "Electromagnetic wave absorption and compressive behavior of a three-dimensional metamaterial absorber based on 3D printed honeycomb," *Sci Rep*, vol. 8, pp. 4817, Mar., 19, 2018. DOI:10.1038/s41598-018-23286-6.

[76] J. Ren, and J. Y. Yin, "3D-Printed Low-Cost Dielectric-Resonator-Based Ultra-Broadband Microwave Absorber Using Carbon-Loaded Acrylonitrile Butadiene Styrene Polymer," *Materials (Basel)*, vol. 11, no. 7, pp. 1249, Jul., 20, 2018. DOI: 10.3390/ma11071249.

[77] P. J. Bradley, M. O. M. Torrico, C. Brennan, and Y. Hao, "Printable all-dielectric water-based absorber," *Sci Rep*, vol, 8, pp. 14490, Sep., 27, 2018. DOI: DOI:10.1038/s41598-018-32395-1.

[78] J. Ren, and J.Y. Yin, “Cylindrical water resonator based ultra-broadband microwave absorber,” *Optical Materials Express*, vol. 8, no.8, pp. 2060-2071, Aug. 2018. [DOI: https://doi.org/10.1364/OME.8.002060].

[79] T. Liu and al., “Fabrication and absorbing property of the tower-like absorber based on 3D printing process,” *Physica B: Condensed Matter*, vol. 553, pp. 88-95, Jan.,15, 2019. [DOI: https://doi.org/10.1016/j.physb.2018.10.038].

[80] M. Petroff, J. Appel, K. Rostem, C. L. Bennett, J. Eimer, T. Marriage, J. Ramirez, and E. J. Wollack, “A 3D-printed broadband millimeter wave absorber,” *Review of Scientific Instruments*, vol. 90, no. 2, pp. 024701, Feb., 1, 2019. DOI: https://doi.org/10.1063/1.5050781.

[81] Q. Zhou, X. Yin, F. Ye, X. Liu, L. Cheng, and L. Zhang, “A novel two-layer periodic stepped structure for effective broadband radar electromagnetic absorption,” Materials & Design, vol. 123, pp. 46–53, June 5, 2017. [DOI: https://doi.org/10.1016/j.matdes.2017.03.044].

[82] Y. Shen, J. Zhang, Y. Pang, L. Zheng, J. Wang, H. Ma, and S. Qu, “Thermally tunable ultra-wideband metamaterial absorbers based on three dimensional water-substrate construction,” *Scientific reports*, vol. 8, no. 1, p. 4423, Mar., 13, 2018. DOI: 10.1038/s41598-018-22163-6.

[83] X. Begaud, A. Lepage, S. Varault, M. Soiron, and A. Barka, “Ultrawideband and wide-angle microwave metamaterial absorber,” Materials, vol. 11, no. 10, p. 2045, 2018. DOI: 10.3390/ma11102045.

[84] K.-L. Zhang, J.-Y. Zhang, Z.-L. Hou, S. Bi, and Q.-L. Zhao, “Multifunctional broadband microwave absorption of flexible graphene composites,” Carbon, vol. 141, pp. 608–617, 2019.

[85] J. Xie, S. Quader, F. Xiao, C. He, X. Liang, J. Geng, R. Jin, W. Zhu, and I. D. Rukhlenko, “Truly all-dielectric ultrabroadband metamaterial absorber: Water-based and ground-free,” IEEE Antennas and Wireless Propagation Letters, vol. 18, no. 3, pp. 536–540, March 2019.

[86] Z. Zhang, L. Zhang, X. Chen, Z. Wu, Y. He, Y. Lv and Y. Zou, “Broadband metamaterial absorber for low-frequency microwave absorption in the S-band and C-band,” *Journal of Magnetism and Magnetic Materials*, vol. 497, pp. 166075, Mar., 1, 2020. DOI: 10.1016/j.mmm.2019.166075.

[87] Y. Wu, H. Lin, J. Xiong, J. Hou, R. Zhou, F. Deng and R. Tang, “A broadband metamaterial absorber design using characteristic modes analysis,” *J. Appl. Phys.*, vol. 129, pp. 134902, Apr., 5, 2021. DOI: 10.1063/5.0043054.

[88] D. R. Smith, D. C. Vier, Th. Koschny, and C. M. Soukoulis, "Electromagnetic parameter retrieval from inhomogeneous metamaterials," *Phys. Rev. E*, vol. 71, pp. 036617, Mar., 22, 2005. DOI: 10.1103/PhysRevE.71.036617.

[89] X.-Y. Peng, B. Wang, S. Lai, D. H. Zhang, and J.-H. Teng, "Ultrathin multi-band planar metamaterial absorber based on standing wave resonances," *Opt. Express*, vol. 20, no. 25, pp. 27756-27765, Nov., 29, 2012. DOI: 10.1364/OE.20.027756.

[90] C. Qu, S. Ma, J. Hao, M. Qiu, X. Li, S. Xiao, Z. Miao, N. Dai, Q. He, S. Sun, and L. Zhou, "Tailor the Functionalities of Metasurfaces Based on a Complete Phase Diagram," *Phys. Rev. Lett. 115*, pp. 235503, Dec. 01, 2015. DOI: https://doi.org/10.1103/PhysRevLett.115.235503.

[91] D. Headland, Y. Monnai, D. Abbott, C. Fumeaux, and W. Withayachumnankul, "Tutorial: Terahertz beamforming, from concepts to realizations," *APL Photonics*, vol. 3, pp. 051101, Feb. 06, 2018. DOI: https://doi.org/10.1063/1.5011063.

[92] N. Fernez, L. Burgnies, J. Hao, C. Mismer, G. Ducournau, D. Lippens and É. Lheurette, "Radiative Quality Factor in Thin Resonant Metamaterial Absorbers," *in IEEE Transactions on Microwave Theory and Techniques*, vol. 66, no. 4, pp. 1764-1772, Apr. 2018. DOI: 10.1109/TMTT.2017.2784808.

[93] A. Sellier, “*Absorbants à métamatériaux: étude théorique et expérimentale*,” Thèse de doctorat Physique, Université Paris-Sud, Jun. 13, 2014. http://www.theses.fr/2014PA112111.

[94] N. Fernez, *“Structures périodiques et désordonnées pour l’absorption des ondes électromagnetiques,”* Ecole Doctorale Sicences pour l’Ingénieur de Nanotechnologie, Dec. 21, 2018. http://www.theses.fr/2018LILUI081.

[95] Hou-Tong Chen, "Interference Theory of Metamaterial Perfect Absorbers," *Opt. Express*, vo. 20, no. 7, pp. 7165-7172, Mar., 26, 2012. DOI: https://doi.org/10.1364/OE.20.007165.].
[96] A. Vora, J. Gwamuri, N. Pala et al. "Exchanging Ohmic Losses in Metamaterial Absorbers with Useful Optical Absorption for Photovoltaics," *Sci. Rep.*, vo. 4, pp. 4901, May, 9, 2015. DOI: https://doi.org/10.1038/srep04901.
[97] R. Grelot, "New concepts of dielectric metamaterials for high frequency applications (Dissertation)," Retrieved from http://urn.kb.se/resolve?urn=urn:nbn:se:kth:diva-278488
[98] Closed Boundary Quad-Ridge Horns | MVG (mvg-world.com)
[99] L. Pometcu, A. Sharaiha, R. Benzerga, R. D. Tamas and P. Pouliguen, "Method for material characterization in a non-anechoic environment," *Appl. Phys. Lett.*, vol. 108, no. 16, April, 22, 2016. [DOI: https://doi.org/10.1063/1.4947100.
[100] X. Lleshi, R. Grelot, T. Q. Van Hoang, B. Loiseaux and D. Lippens, "Wideband Metal-Dielectric Multilayer Microwave Absorber based on a Single Step FDM Process," 2019 49th European Microwave Conference (EuMC), Paris, France, 2019, pp. 678-681.
[101] Q. Lévesque, *" Conception de micro-optiques par structuration sub-longueur d'onde,"* Ecole Polytechnique Spécialité Physique, Oct, 17, 2014. http://www.theses.fr/2014EPXX0050.
[102] F. M. Smits, "Measurement of sheet resistivities with the four-point probe,*" The Bell System Technical Journal*, vol. 37, no. 3, pp. 711-718, May 1958. DOI: 10.1002/j.1538-7305.1958.tb03883.x.
[103] X. Lleshi, T. Q. Van Hoang, B. Loiseaux and D. Lippens, "Design and Full Characterization of a 3-D-Printed Hyperbolic Pyramidal Wideband Microwave Absorber," in IEEE Antennas and Wireless Propagation Letters, vol. 20, no. 1, pp. 28-32, Jan. 2021, doi: 10.1109/LAWP.2020.3037718.
[104] M. A. Stuchly and S. S. Stuchly, "Coaxial Line Reflection Methods for Measuring Dielectric Properties of Biological Substances at Radio and Microwave Frequencies-A Review," *IEEE Transactions on Instrumentation and Measurement*, vol. 29, no. 3, pp. 176-183, Sept. 1980. DOI: 10.1109/TIM.1980.4314902. (to use for the dielectric permittivity calculation)
[105] https://www.plastic2print.com/
[106] G. Isić, B. Vasić, D. C. Zografopoulos, R. Beccherelli, and R. Gajić, "Electrically Tunable Critically Coupled Terahertz Metamaterial Absorber Based on Nematic Liquid Crystals," *Phys. Rev. Applied*, vol. 3, no. 6, pp. 064007, Jun., 11, 2011. DOI: 10.1103/PhysRevApplied.3.064007.
[107] Closed Boundary Quad-Ridge Horns | MVG (mvg-world.com)
[108] J. P. Dunsmore, *"Handbook of Microwave Component Measurements: With Advanced VNA Techniques,"* Wiley, 2012. DOI:10.1002/9781118391242
[109] A. Goulas, S. Zhang, D. A. Cadman, J. Järveläinen, V. Mylläri, W. G. Whittow, J. C. Vardaxoglou, D. S. Engstrøm, "The Impact of 3D Printing Process Parameters on the Dielectric Properties of High Permittivity Composites," *Designs*, vol. 3, no. 50, Nov., 5, 2019. DOI: 10.3390/designs30400.
[110] W. Ben-Xin, H. Yuanhao, L. Pengcheng, X. Nianxi, W. Xiaoyi, W. Yanchao and C. Jianjun, "Multiple-Band Terahertz Metamaterial Absorber Using Multiple Separated Sections of Metallic Rectangular Patch," *Frontiers in Physics*, vol. 8, pp. 308, Aug., 13, 2020. DOI: 10.3389/fphy.2020.00308.
[111] J. Kim, K. Han and J.W. Hahn, "Selective dual-band metamaterial perfect absorber for infrared stealth technology," *Sci Rep*, vol. 7, pp. 6740, Jul., 27, 2017. DOI: https://doi.org/10.1038/s41598-017-06749-0
[112] M. D. Banadaki, A. A. Heidari and M. Nakhkash, "A Metamaterial Absorber With a New Compact Unit Cell," *IEEE Antennas and Wireless Propagation Letters*, vol. 17, no. 2, pp. 205-208, Feb. 2018. DOI: 10.1109/LAWP.2017.2780231.
[113] J. Kaiser, "The Archimedean two-wire spiral antenna," *IRE Transactions on Antennas and Propagation*, vol. 8, no. 3, pp. 312-323, May 1960. DOI: 10.1109/TAP.1960.1144840.
[114] K. Y. Lam, K. Luk, K. F. Lee, H. Wong and K. B. Ng, "Small Circularly Polarized U-Slot Wideband Patch Antenna," *in IEEE Antennas and Wireless Propagation Letters*, vol. 10, pp. 87-90, Feb., 04, 2011. DOI: 10.1109/LAWP.2011.2110631.
[115] https://empossible.net/wp-content/uploads/2020/04/Lecture-The-Grating-Equation.pdf

[116] Y. Cheng, B. He, J. Zhao and R. Gong, “Ultra-thin Low-Frequency Broadband Microwave Absorber Based on Magnetic Medium and Metamaterial,” *Journal of Elec Materi*, vol. 46, pp. 1293–1299, 2017. DOI: https://doi.org/10.1007/s11664-016-5115-z.

[117] L. Wangchang, L. Qing, W. Liwei, Z. Zuzhi, Z. Jingwu, Y. Yao, Q. Liang, Y. Jing, Q. Xiaojing and C. Shenglei, “Low frequency and broadband metamaterial absorber with cross arrays and a flaked iron powder magnetic composite,” *AIP Advances*, vol. 8, pp. 015318, Jan., 18, 2018. DOI: https://doi.org/10.1063/1.5010821.

[118] Y. Huang, Q. Fan, J. Chen, L. Li, M. Chen, L. Tang and D. Fang, “Optimization of flexible multilayered metastructure fabricated by dielectric-magnetic nano lossy composites with broadband microwave absorption,” *Composites Science and Technology*, vol. 191, pp. 108066, Feb., 9, 2020. DOI: https://doi-org.ressources-electroniques.univ-lille.fr/10.1063/1.2108158.

[119] Y. Huang, X. Yuan, M. Chen, W.-L. Song, J. Chen,Q. Fan, L. Tang and D. Fang, “Ultrathin Flexible Carbon Fiber Reinforced Hierarchical Metastructure for Broadband Microwave Absorption with Nano Lossy Composite and Multiscale Optimization,” *ACS Appl. Mater. Interfaces*, vol. 10, no. 51, pp. 44731 - 44740, Dec., 26, 2018. DOI: doi: 10.1021/acsami.8b16938.

[120] CST Microwave Studio 2019: CST Help, Material Overview.

[121] F. Costa, S. Genovesi, A. Monorchio and G. Manara, “A Circuit-Based Model for the Interpretation of Perfect Metamaterial Absorbers,” *IEEE Transactions on Antennas and Propagation*, vol. 61, no. 3, pp. 1201-1209, March 2013. DOI: 10.1109/TAP.2012.2227923.

[122] J. Fang, T. Liu, Z. Chen, Y. Wang, W. Wei, X. Yue and Z. Jianga, “A wormhole-like porous carbon/magnetic particles composite as an efficient broadband electromagnetic wave absorber,” *Nanoscale*, vol. 8, no. 16, pp. 8899 – 8909, Mar., 29, 2016. DOI: 10.1039/c6nr01863g.

[123] http://www.torwell3d.com/

[124] F. Costa, A. Monorchio and G. Manara, “Wideband Scattering Diffusion by using Diffraction of Periodic Surfaces and Optimized Unit Cell Geometries,” *Sci Rep*,vol. 6, pp. 25458, May, 16, 2016. DOI: https://doi.org/10.1038/srep25458.

[125] M. Skolnik, *Radar Handbook*, 3rd ed., NY, USA: McGraw-Hill, 2015.

[126] W. Chen, C. A. Balanis and C. R. Birtcher, "Checkerboard EBG Surfaces for Wideband Radar Cross Section Reduction," *in IEEE Transactions on Antennas and Propagation*, vol. 63, no. 6, pp. 2636-2645, Jun., 6, 2015. DOI: 10.1109/TAP.2015.2414440.

[127] A. Y. Modi, C. A. Balanis, C. R. Birtcher and H. N. Shaman, "Novel Design of Ultrabroadband Radar Cross Section Reduction Surfaces Using Artificial Magnetic Conductors," *in IEEE Transactions on Antennas and Propagation*, vol. 65, no. 10, pp. 5406-5417, Oct. 2017. DOI: 10.1109/TAP.2017.2734069.

[128] W. Li, Y. Zhang, T. Wu, J. Cao, Z. Chen and J. Guan, “Broadband Radar Cross Section Reduction by in-plane Integration of Scattering Metasurfaces and magnetic absorbing materials,” *Results in Physics*, vol. 12, pp. 1964-1970, Mar., 2019. DOI: https://doi.org/10.1016/j.rinp.2019.01.080.

[129] M. Paquay, J. Iriarte, I. Ederra, R. Gonzalo and P. de Maagt, "Thin AMC Structure for Radar Cross-Section Reduction," *in IEEE Transactions on Antennas and Propagation*, vol. 55, no. 12, pp. 3630-3638, Dec., 12, 2007, DOI: 10.1109/TAP.2007.910306.

[130] Y. Liu, Y. Hao, K. Li and S. Gong, "Radar Cross Section Reduction of a Microstrip Antenna Based on Polarization Conversion Metamaterial," in *IEEE Antennas and Wireless Propagation Letters*, vol. 15, pp. 80-83, Feb., 4, 2016, DOI: 10.1109/LAWP.2015.2430363.

[131] H. Dai, Y. Zhao, J. Chen, C. Yu and L. Xing, “Ultra-wideband radar cross-section reduction using polarization conversion metasurface,” *Int. J. RF Microw. Comput. Aided En.*, vol. 30, no. 2, Feb. 2020. DOI: 10.1002/mmce.22085.

[132] Y. Azizi, M. Soleimani and S. H. Sedighy, “Ultra-wideband radar cross section reduction using amplitude and phase gradient modulated surface,” *J. Appl. Phys.*, vol. 128, no. 20, pp. 205301, Nov., 30, 2020. DOI: 10.1063/5.0009651.

[133] D. Archer, “Artificial Resistive Card”, US Patent 5 126 716, Mesa, AZ Jun., 30, 1992.

[134] S. Kim, "Microwave Absorbing Properties of Magnetic Composite Sheets for Oblique Incidence Angles," *in IEEE Transactions on Magnetics*, vol. 47, no. 10, pp. 4314-4317, Oct., 10 2011, DOI: 10.1109/TMAG.2011.2157465.
[135] L. J. Du Toit and J. H. Cloete, "Electric screen Jauman absorber design algorithms," *in IEEE Transactions on Microwave Theory and Techniques*, vol. 44, no. 12, pp. 2238-2245, Dec. 1996. DOI: 10.1109/22.556452.
[136] Begaud, X.; Lepage, A.C.; Varault, S.; Soiron, M.; Barka, A. Ultra-Wideband and Wide-Angle Microwave Metamaterial Absorber," *Materials 2018*, vol. 11, pp. 2045. Oct., 20, 2018. DOI: 10.3390/ma11102045
[137] W. Samsul, "Maximally-Flat and Genetic Algorithm Solutions to Achieve Wideband Jaumann Absorbers" Doctor of Philosophy in the Department of Electrical and Computer Engineering in the Graduate School of Duke University, 2017.
[138] www.platefrome-canoe.com
[139] www.arkema.com
[140] www.neyco.fr
[141] T. Rydholm, "Measurement of Complex Permittivity and Permeability through a Cavity-Perturbation Method," Master's Thesis in Applied Physics, Chalmers Univerity of Technology, 2015, Sweden.
[142] J. Hsieh, Computed Tomography: Principles, Design, Artifacts, and Recent Advances, 2nd ed., Bellingham, WA, USA, Spie Press Book, 2009.
[143] K.S. Sree Harsha, *"Principles of Vapor Deposition of Thin Films,"* Elsevier Ltd, 2006. DOI: https://doi.org/10.1016/B978-0-08-044699-8.X5000-1.

Abstract

Electromagnetic (EM) absorbers have been widely used since the WWII in various applications to reduce radar cross section of aircrafts, to attenuate interferences between nearby antennas, in anechoic chambers to prevent reflections of spurious signals, etc. In the last twenty years, many studies on metamaterial absorbers, with low profile and can simultaneously satisfy multiple constraints as broadband absorption and good angular robustness have been done to achieve high performance EM absorbers. However, the strong growth in system density and the extensive use of wide frequency ranges require new innovative absorber structures able to cope with current and future challenges.

In the framework of this Ph.D., metamaterial-based absorbers are studied aiming at three objectives: i) reaching unitary absorption level, ii) giving guidelines to develop new absorbing materials with desired RF properties and iii) controlling the absorption level. The first study consist in maximizing the absorption level (above 90%) of the incoming wave's energy over a wide frequency band, for different polarizations and for different incident angles. Stair-like multilayer multi-material structures were analyzed for this purpose. The second study focuses on low-frequency absorbers that make use of metamaterials with magnetic properties. To achieve nearly unitary absorptivity, various solutions are proposed, such as combining dielectric resonators with magnetic materials or designing an absorber with electromagnetic properties not yet developed by industries. The third study focuses on controlling the absorption level from a few percent to 100% over a frequency range of interest. The resulting structures will enable us to obtain a surface with gradual absorptivity along the transverse directions of space, which allows for the possibility of reducing the Radar Cross Section.

Addressing these goals, the methodology to design and characterize various metamaterial absorbers, as well as the fabrication problems are analyzed in this dissertation.

Résumé

Les absorbants électromagnétiques ont été largement utilisés depuis la seconde guerre mondiale dans diverses applications: réduction de la signature radar d'avion, atténuation des effets d'interférence entre antennes proches ou prévention de la réflexion des signaux parasites dans les chambres anéchoïques. Depuis ces vingt dernières années, beaucoup d'études ont été consacrées aux absorbants de type métamatériaux. En effet ils sont très compacts, peuvent satisfaire simultanément de multiples contraintes et présenter de très hautes performances en termes de fenêtre d'absorption très large bande ou de grande robustesse angulaire. Cependant, l'accroissement actuel de la densification des éléments dans les systèmes, notamment rayonnants, ainsi que leur utilisation sur une très large gamme de fréquences, demande la recherche de nouvelles structures absorbantes innovantes capable de faire face à ces défis futurs.

Dans le cadre de ce travail de thèse, des métasurfaces absorbantes sont étudiées en visant trois objectifs: i) l'obtention d'un niveau d'absorption proche de l'unité, ii) donner des directives pour développer de nouveaux matériaux absorbants ayant les propriétés RF souhaitées et iii) le contrôle du niveau d'absorption. La première étude a trait à l'obtention d'un niveau d'absorption de l'énergie de l'onde incidente supérieur à 90% sur une bande très large (supérieure à une octave) pour différents états de polarisation et angles d'incidence. Dans ce but, des structures multi-matériaux de

forme pyramidale en marches d’escalier, ont été analysées. La deuxième étude porte sur les absorbeurs basse fréquence qui utilisent des métamatériaux aux propriétés magnétiques. Pour obtenir une absorptivité quasi unitaire, diverses solutions sont proposées, comme la combinaison de résonateurs diélectriques avec des matériaux magnétiques ou la conception d'un absorbeur aux propriétés électromagnétiques non encore développées par les industries. La troisième étude a pour but d’obtenir un niveau d’absorption quasi-constant dans la bande de fonctionnement entre quelques pourcents et 100%. Ces structures à réflexion partielles nous permettront de concevoir un profil graduel d’absorption dans les directions transversales à la direction de propagation de l’onde incidente, réduisant les effets de diffraction aux bords d’éléments métalliques.

Pour ces études sur les structures à réflexions partielle et totale, les aspects conception électromagnétique et de caractérisation, en particulier pour les mesures des spectres de réflectance en espace libre sont présentés et discutés.